Cell Fate Mechanisms in Colorectal Cancer

Sophie Kay

Keble College

D. Phil. in Systems Biology

Michaelmas Term, 2014

For Bump, who helped me to finish this

Acknowledgments

Many thanks to all those who, in small ways and large, have helped me towards the completion of this thesis.

First of all, to my supervisors: Prof. Helen Byrne, Prof. David Gavaghan and Dr. James Osborne, for their advice throughout my DPhil and their support during the ups and downs of the journey to the finish line; for the detailed comments on draft chapters; and for all their insights and guidance as the research progressed.

A debt of gratitude also to Trevor Dale at Cardiff University, and to Keith Brennan at the University of Manchester, whose experimental perspectives on my work and enthusiastic debates proved invaluable in shaping and refining the biochemical modelling presented here.

The applications of chemical reaction network theory in Chapter 4 would not have come about without the advice of Heather Harrington, who first introduced me to this fascinating field, and whose suggestions of useful literature and software helped me get to grips with the technical details.

My DPhil studies would not have been the same without the enjoyable office camaraderie over the years: thanks to all those who have aided and abetted with tea, cake and chat when the situation called for it – too many, alas, to name here. Beyond

the confines of my DPhil office, running the gauntlet of deadlines and paperwork was made immeasurably easier by some absolutely wonderful members of administrative staff: especial thanks to Julie Sheppard in the Department of Computer Science, Penn Bateman at Keble College and Sam Miles at the SysBio Doctoral Training Centre.

And of course to my wonderful family: Mum, Dad, Sam, Olivia and Tom, for their love and support throughout the years. In particular, to my parents, who will always be an inspiration; who have maintained an unwavering faith in me; and who instilled a love of reading in me during my early years, which undoubtedly came in useful when working through the 270 references in this thesis.

And most of all, to my husband Alastair, who has put up with me talking about my DPhil for far too long, who has made me laugh at myself when I needed it the most, and whose love, encouragement and unfailing support were instrumental in me making it through to the end.

Abstract

Thesis Title: Cell Fate Mechanisms in Colorectal Cancer

Name: Sophie Kay (née Kershaw)

College: Keble College

Degree Title: Doctor of Philosophy (D.Phil.) in Systems Biology

Submission Date: Michaelmas Term 2014

Page Count: 189 (excl. floats and bibliography)

Colorectal cancer (CRC) arises in part from the dysregulation of cellular proliferation, associated with the canonical Wnt pathway, and differentiation, effected by the Notch signalling network. In this thesis, we develop a mathematical model of ordinary differential equations (ODEs) for the coupled interaction of the Notch and Wnt pathways in cells of the human intestinal epithelium. Our central aim is to understand the role of such crosstalk in the genesis and treatment of CRC.

An embedding of this model in cells of a simulated colonic tissue enables computational exploration of the cell fate response to spatially inhomogeneous growth cues in the healthy intestinal epithelium. We also examine an alternative, rule-based model from the literature, which employs a simple binary approach to pathway activity, in which the Notch and Wnt pathways are constitutively on or off. Comparison of the two models demonstrates the substantial advantages of the equation-based paradigm, through its delivery of stable and robust cell fate patterning, and its versatility for exploring the multiscale consequences of a variety of subcellular phenomena.

Extension of the ODE-based model to include mutant cells facilitates the study of Notch-mediated therapeutic approaches to CRC. We find a marked synergy between the application of γ-secretase inhibitors and Hath1 stabilisers in the treatment of early-stage intestinal polyps. This combined treatment is an efficient means of inducing mitotic arrest in the cell population of the intestinal epithelium through enforced conversion to a secretory phenotype and is highlighted as a viable route for further theoretical, experimental and clinical study.

Contents

Introduction 1

A Literature and Methods 5

1 Crypt Biology 6

1.1 Crypt Homeostasis . . . 8

1.2 Colorectal Cancer . . . 13

1.3 Dynamic Evolution of Crypt Tissue . . . 14

1.4 Intestinal Biochemistry . . . 16

1.4.1 The Notch Pathway . . . 17

1.4.2 The Wnt Pathway . . . 23

1.5 Discussion . . . 27

2 Methods and Models 29

2.1 Notch Signalling . . . 30

2.1.1 The Model of Collier *et al.* (1996) . . . 30

2.1.2 Other Models of Juxtacrine Signalling . . . 33

2.1.3 Discrete & Rule-Based Models . . . 37

2.1.4 Models of Hes1 Oscillation . . . 38
2.1.5 Continuous Subcellular Models . . . 39
2.2 Wnt Signalling . . . 40
2.2.1 Lee *et al.* (2003) and Associated Literature . . . 40
2.2.2 Alternative Biochemical Models . . . 43
2.2.3 Crypt Embeddings . . . 44
2.3 Tools and Software . . . 45
2.4 Tissue Scale Modelling . . . 48
2.4.1 Tissue Modelling in Chaste . . . 50
2.5 Discussion . . . 54

B Model Development 56

3 A Coupled Notch-Wnt Model 57
3.1 Model Entities . . . 59
3.2 Experimental Evidence . . . 61
3.2.1 Further Comments . . . 66
3.3 Dimensional System . . . 67
3.3.1 Notch Pathway Submodel . . . 70
3.3.2 Wnt Pathway Submodel . . . 73
3.3.3 Network Motifs . . . 75
3.4 Nondimensionalised System . . . 76
3.5 Concluding Remarks . . . 79

4 Model Analysis 80
4.1 Dynamical Analyses . . . 80
4.1.1 Notch-Only System . . . 80
4.1.2 Wnt-Only Analysis . . . 88

4.1.3 Summary . . . 91
4.2 Chemical Reaction Network Theory . . . 92
4.2.1 A Formal Framework for CRNT . . . 93
4.2.2 Network Analysis . . . 100
4.3 Parametrisation . . . 102
4.3.1 Decay Rates . . . 103
4.3.2 Notch Model . . . 104
4.3.3 Wnt Model . . . 107
4.3.4 Parametrisation Findings . . . 111
4.4 Two-Cell Studies . . . 112
4.4.1 Timecourses of Hes1 and β-catenin . . . 113
4.4.2 Transcriptional Control of Hes1 . . . 113
4.4.3 Mutant Transformation . . . 115
4.4.4 Insights From Reduced and Full Systems . . . 121
4.5 Conclusions . . . 123

C Applications **125**

5 Comparison With Buske *et al.* (2011) **126**
5.1 Introduction . . . 126
5.2 A Tissue-Level Model for the Crypt . . . 128
5.3 Cell Cycle Model . . . 129
5.4 A Crypt Embedding of the NWODE Model . . . 130
5.5 A Crypt Embedding of the Buske Model . . . 133
5.6 Data Generation . . . 138
5.7 Runtime . . . 139
5.8 Robustness of Pattern Generation . . . 141

5.9 Simulation From Heterogeneous Initial Conditions 147
5.10 Cell Fate Parameters in the Buske Model 154
5.11 Cell Fate Parameters in the NWODE Model 163
5.12 Conclusions 170
5.12.1 Insights into ODE- and Rule-Based Paradigms 171
5.12.2 Applicability to Other Biological Scenarios 173
5.12.3 Final Comments 174

6 Clinical Treatments **175**
6.1 Introduction 175
6.2 Defining A Mutant Phenotype 177
6.3 Mutant Behaviour in a Crypt Setting 180
6.3.1 Observations of Mutant Cell Patches 181
6.3.2 Differences Between Healthy and Mutant Crypts 187
6.3.3 Comments 192
6.4 Exploring Clinical Treatments 193
6.5 Two-Cell Studies 196
6.6 Crypt Implementation 198
6.7 Mutant Phenotype with Regular Adhesion 200
6.8 Mutant Phenotype with Elevated Adhesion 209
6.9 Conclusions 217
6.9.1 Mutant Behaviour in the NWODE Model 218
6.9.2 Evaluation of Clinical Therapies 219

7 Conclusions **221**
7.1 Findings and Insights 222
7.2 Future Work 223
7.2.1 Biological Extensions 224

7.2.2 Mathematical and Computational Extensions 225
7.2.3 Further Studies 226
7.3 Closing Remarks 228

D Appendices **230**

Appendices **231**

A Model Parameters **231**
A.1 Parameter Sensitivity Analysis 236

B Point Dispersal Measures **241**
B.1 Subcellular Model 242
B.2 Point Dispersal Metrics in Two Dimensions 243
B.2.1 Ripley's Values 244
B.2.2 Pair Correlation Functions 247
B.2.3 Weighting at Domain Edges 249
B.2.4 Implementation 251
B.3 Static Monolayers 257
B.3.1 CPU Time and Metric Stepsize 258
B.3.2 Application to a Static Cell-Based Monolayer 263
B.4 Dynamic Simulations 266
B.4.1 Crypt Simulation Conditions 266
B.4.2 Graded Wnt Concentration 267
B.4.3 Results and Discussion 268
B.5 Discussion and Conclusions 275

C Additional Simulations **277**
C.1 Buske Model with Gamma-Distributed G1 Phases 277

C.1.1 Results and Discussion 278

Introduction

Cells of the mammalian gut are endowed with an incredible ability to grow, divide and organise themselves into coherent, functional structures. Remarkably, a single 'stem cell' – an unspecialised cell with the potential to develop into any cell type – taken from the intestinal lining (or *epithelium*) can, through its growth and division and that of its progeny, recapitulate entire test-tube shaped structures, or *crypts*, characteristic to the intestine. Furthermore, these artificially grown crypts contain the full range of specialised cell types, and display a contractility reminiscent of *in vivo* peristalsis around a fortnight after initial culturing. Over a relatively short time period, the original stem cell generates a self-organising structure endowed with both form and function [1, 2]. How does it achieve this? What processes are involved, and how do the growing cells coordinate and respond to spatial cues in order to generate and maintain such a structure?

Although the workings of *de novo* crypt generation are yet to be fully comprehended, much of our understanding rests on two major cellular processes: *proliferation* or *mitosis*, the division of a cell to produce 'daughter' cells; and *differentiation* or *cell fate specification*, the progressive specialisation a cell undergoes until it adopts a final, fixed function and set of behaviours.

However, the elegant coordination of proliferation and differentiation witnessed in *de novo* cryptogenesis also possesses a more sinister side: that of colorectal cancer. One of the most prevalent forms of cancer in the Western world, colorectal cancer (CRC) affects the colon and rectum at the end of the digestive tract and presents in the form of tiny outgrowths of the intestinal epithelium, the consequence of dysregulation of key cellular functions including proliferation and differentiation. Left unchecked, these *polyps* enter a phase of exponential growth and ultimately develop into aggressive tumours which generate secondary cancers in other organs, typically the liver and lungs. By this stage, the disease is invariably fatal [3, 4].

This presents a strong motivation for understanding the genesis of CRC through its governing processes. Inevitably this also requires us to understand the behaviour of healthy cells, and how these conditions can be perturbed into the aberrant behaviour characteristic to cancer cells.

Key Themes and Questions

Throughout this thesis, our main aim is to gain an understanding of the interplay of proliferation and differentiation in the cells of the intestinal epithelium, and ultimately to gain insights into how this crosstalk contributes to the development and treatment of CRC. We translate the underlying biology and biochemistry of the gut into a mathematical model which is then realised computationally. The resulting framework is subsequently used to explore and predict the behaviour of the healthy intestine, early stage cancerous development, and its response to proposed clinical treatments.

Development of such a framework requires an understanding of the function of the gut at subcellular, cellular and tissue level. Which biochemical processes guide mitosis and cell fate? The self-organisation witnessed in cryptogenesis experiments hints at spatial cues within the tissue: how are these spatial cues generated, and how

do cells of different types respond to these signals? How best can we represent these processes mathematically, and what level of detail is appropriate? Finally, can these mathematical and computational developments be employed to generate insights into, and predictions about, the behaviour of the crypt in the face of cancerous perturbation?

Overview of Contents

The story of this thesis is presented in three parts.

Part A addresses current developments in the experimental and theoretical sciences which influence and inspire the modelling work that follows in later Parts. There exists a vast biological literature underpinning our current awareness of the structure and function of intestinal tissue and its constituent cells; we provide an overview of the key areas in the biological review of Chapter 1. In many cases, this work has influenced and inspired investigation in the mathematical and computational modelling communities. Our research in this thesis will require us to employ various techniques and software discussed in the literature; we summarise these in Chapter 2, and survey current achievements in the mathematical modelling of the biochemical pathways associated with mitosis and cell fate selection.

Background influences addressed, we proceed to novel modelling work in *Part B*. One of the major contributions of this work is the model for subcellular biochemistry constructed in Chapter 3, which depicts the crosstalk between two cellular signalling networks: the canonical Wnt pathway, associated with proliferation, and the Notch pathway, a key effector of differentiation. This model is calibrated, parametrised and explored for two-cell systems in Chapter 4. This simple scenario demonstrates the main dynamical features of the model, illustrates the role of Notch-Wnt crosstalk in shaping the cell fate response, and enables preliminary examination of the possible consequences of the dysregulation of particular entities in the subcellular network.

Finally, *Part C* sees the application of our novel model to problems of computational and clinical relevance. In Chapter 5, we embed our model of the subcellular biochemistry into individual cells of a simulated tissue, providing a computational framework with which to explore the impact of subcellular perturbations upon higher scales of function. The performance of this embedding is compared to a competing model in the literature, namely that of Buske *et al.* [5], which uses a simple, rule-based formulation to depict proliferative and cell fate processes. Chapter 6 uses our embedding to explore the effects of two clinical treatments upon mutant cells in the crypt, providing proof-of-concept for the use of our framework as a test-bed for a variety of problems in the biological literature. Our findings are summarised in the Conclusions of Chapter 7.

And so...

Let us now start by examining the accumulated knowledge in the field up to this point, as we attempt to understand the interplay of proliferation and differentiation within the setting of the human gut.

Part A

Literature and Methods

1

Crypt Biology

Chapter Summary

Mathematical models are necessarily abstractions of the biological system; here we review experimental observations from the published literature. These address both cell- and tissue-level features of the intestinal epithelium, before progressing to a discussion of the biochemistry of our two pathways of interest, namely Notch (associated with cell fate selection) and Wnt (associated with control of proliferative processes).

An intricate landscape of geometry and function, the colonic epithelium forms a highly invaginated tissue, endowed with glandular structures and mucus-secreting goblet cells. It comprises millions of test-tube shaped structures called *crypts*, each consisting of up to 700 cells in mice [6] and 2000 in humans [7]. These structures feature in both the large and small intestine. Crypt size varies greatly according to colonic site, with the longest crypts occurring in the transverse (middle) colon; here murine crypts are typically 35 cells in height, compared to 19 cells in the ascending (early) colon [8].

A description of this intricate tissue can be found in the renowned medical text of 1858, Gray's Anatomy [9], detailing

> "*... minute tubular prolongations of the mucous membrane arranged perpendicularly, side by side, over its entire surface; they are longer, more*

> *numerous, and placed in much closer apposition than those of the small intestine; and they open by minute rounded orifices upon the surface, giving it a cribriform [sieve-like] appearance ...*"

A schematic of a typical crypt is provided in Figure 1.1, which demonstrates the arrangement of the epithelial lining into a finger-shaped projection extending into the gut wall.

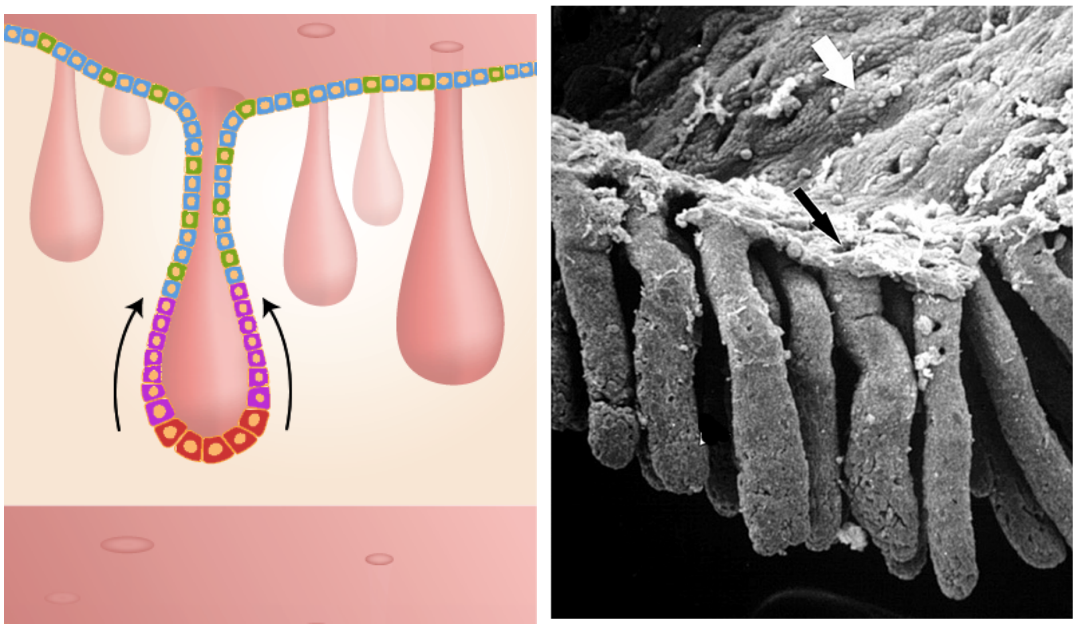

Figure 1.1: (L) Cross-section schematic of a crypt from the large intestine; image adapted from Reizel *et al.* [10]. Arrows denote the general direction of cell migration. Cells are coloured according to their type: red indicates a stem cell; purple indicates a proliferative progenitor or transit cell; secretory goblet cells are shown in green, and absorptive enterocytes are shown in blue. Full descriptions of these cell types are provided in Sections 1.1 and 1.4.1. (R) Electron micrograph of crypts in the murine intestine; the black arrow indicates the crypt orifice and the white arrow, the flat surface of the colonic lumen. Reproduced from van der Wath *et al.* [11]. Both sources originally published by PLoS and provided under a Creative Commons Attribution Licence, *CC-BY-2.5*.

The structure and function of the intestinal epithelium has long been a subject of interest to the biological community [12] and the attainment and maintenance of homeostasis in this tissue reflects a nuanced coordination of cell birth, migration and

death. This rich complexity raises many questions about the biochemical workings of intestinal epithelial cells and their integration into a coherent physical structure which unites form and function. It is this same epithelium that forms the site for colorectal cancer (CRC), in which disruption to the genetic profile or subcellular function of crypt cells can lead to polyp-like outgrowths of the intestinal tract, which develop into larger tumours. Our understanding of how normal cell processes falter during tumourigenesis is far from complete and thus invites further investigation, by both the experimental biologist and the applied mathematician. A timeline of key papers from the experimental and theoretical modelling communities is shown in Figure 1.2.

1.1 Crypt Homeostasis

The upward migration of cells known to occur in the crypt – Paneth cells excepted – was first identified by Friedman [13] in irradiative studies of rat intestine. Later experiments identified a population of putative stem cells in the lower regions of the crypt, displaying elevated proliferation rates [14]. Division of the stem cells yields transit-amplifying cells which occupy the middle regions, whose proliferative potential reduces on ascending the crypt. Ultimately cells adopt a terminally differentiated fate in the upper crypt, irreversibly specialised as either absorptive enterocytes or as mucus-secreting goblet cells [15]. The uppermost third of the crypt is thus devoid of mitotic activity [16]; here cells die and are sloughed into the gut lumen. Paneth cells are a special type of differentiated cell; only present in the small intestine, they migrate down to the crypt base and are thought to assist in crypt development and defence against microbes [17]. Location and function consequently hold a close association in intestinal tissue; an enumeration convention for cell location was therefore established by Cairnie *et al.* [16]. Under this system, a cell is said to be in the '$+n$ position' if it

sits atop $n-1$ cells, counting columnwise from the crypt base[1].

Mitosis

What induces the abrogation of mitosis in the upper crypt? What is meant by a 'stem cell' and how is this subpopulation maintained? The 'slow cut-off' model suggests that cells in the middle of the crypt experience a progressive decline in the probability of producing proliferative cells, owing to a gradient of extracellular factors along the length of the crypt, or an accumulation of intracellular components which arrests mitosis above some threshold value [18]. This spatial formulation is closely related to the idea of a *stem cell niche*, in which the local cell environment around the crypt base supplies growth factors which induce stemlike behaviour [19]. Away from this niche, cells have reduced exposure to such factors and do not show stemlike behaviour [20]. Under the niche model, 'stemness' arises from external cues associated with cell location.

Conversely, the '*generational*' or '*pedigree*' model assumes that cells progress through a strict hierarchy, such that stem cells give rise to transit cells endowed with a fixed number of divisions, prior to terminal differentiation. This approach accompanies the *divisional* model of stem cell proliferation, in which the size of the stem cell population is maintained through asymmetric division (yielding one transit and one stem cell) or symmetric division (yielding either two stem or two transit daughters with equal probability) [21]. These alternative models of stem cell maintenance are an important feature of the mathematical modelling work described in Section 2.4, whether niche-based [22, 5] or divisional [23, 24, 25].

[1]Longitudinal enumeration introduces greater uncertainty for later-numbered cells: the selection of the crypt base as the region of interest influenced the counting direction in this case, permitting more accurate assignment of location number in the proliferating regions.

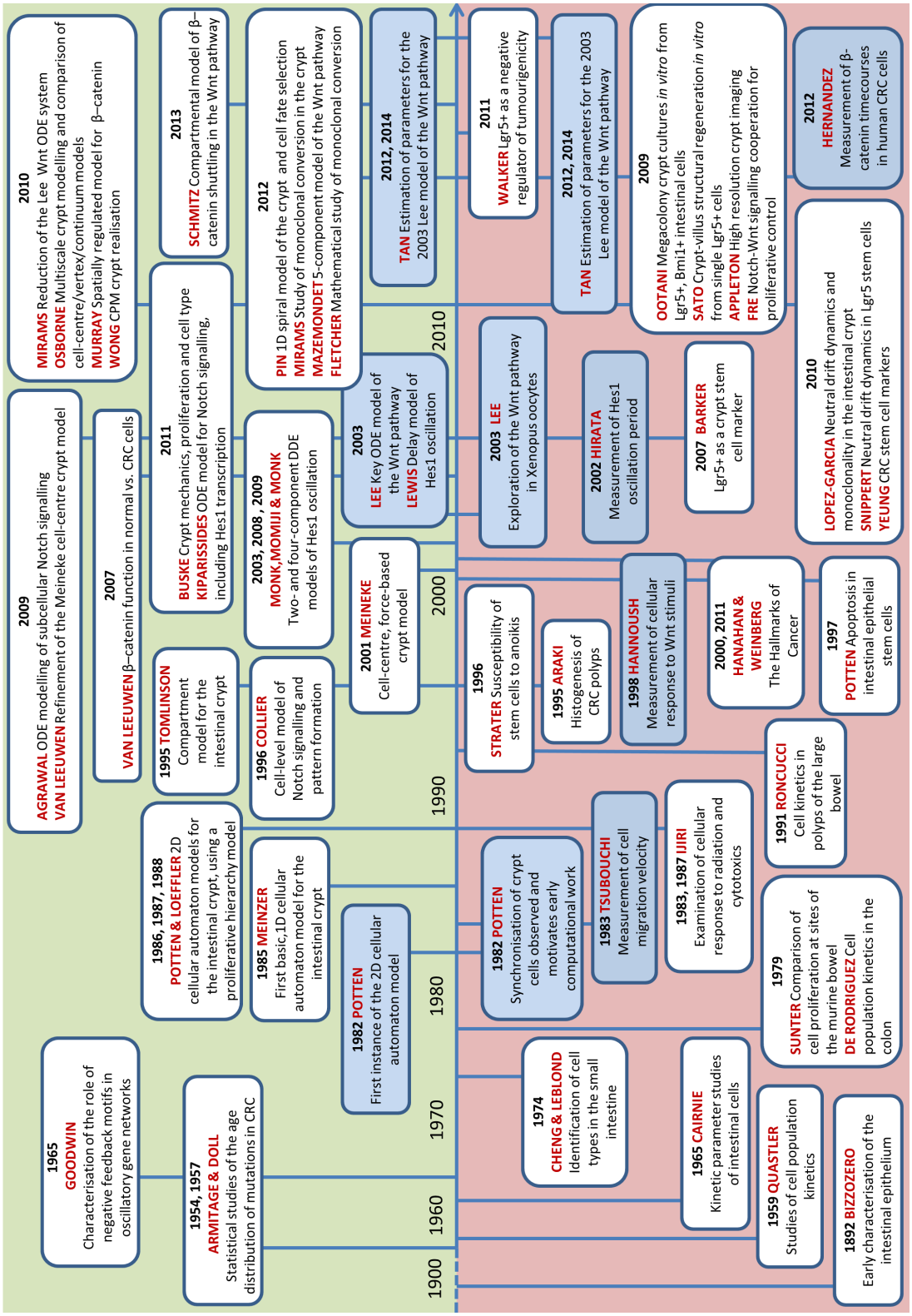

Figure 1.2: Timeline of developments in the (lower) experimental and (upper) mathematical literature. Crossover papers which combine mathematical and theoretical work, or which supply data for parametrisation of mathematical simulations, are shown in blue. For brevity only the name of the first author(s) is listed here; the timeline is not drawn to scale.

Stem Cells and Crypt Regeneration

Current definitions of stemness require an intestinal stem cell to exhibit *pluripotency* (the potential to develop into several distinct cell types) and the capacity to sustain epithelial regeneration in the crypt [26]. Barker *et al.* identified the putative stem cell marker *Lgr5* (also known as *Gpr49*) and observed actively cycling *Lgr5*+ cells near the base of the colonic crypt, displaying a clonal capacity to populate the entire crypt in lineage tracing experiments [26].

Successful *in vitro* crypt synthesis demonstrates the ability of *Lgr5*+ stem cells to generate the full spectrum of crypt cell types [1, 2]. The progeny of the *Lgr5*+ cells in these experiments spontaneously assemble into crypt geometries; furthermore, the resulting spheroidal megacolonies display a contractility reminiscent of *in vivo* peristalsis [2], apparently recapitulating crypt function as well as form. Much of this work supports the stem cell niche hypothesis; colony growth responds well to external proliferative cues. Sato *et al.* suggest that differential response to external cues, rather than differential exposure, is more important in cell proliferation [1]. *In vitro* crypt organoids may well prove useful for data assays in the future, as a test-bed for generating quantified measurements which can then be used to parametrise mathematical and computational models.

Although the *Lgr5* marker seems a good candidate for stem cell identification, it remains uncertain whether all such cells are functionally equivalent [27]. Studies point to *Bmi1* as an alternative marker in the small intestine [28], although it may delineate a subpopulation of less potent stem cells near the +4 position, rather than those at the crypt base. The over-expression of *Bmi1* in CRC cells is well documented [29, 30].

Intestinal stem cells populate and sustain the crypt by a process of 'Neutral Drift Dynamics' (NDD), in which a cell lineage exhibits randomised expansion or contraction over a period of time up to a point of universal dominance (crypt monoclonality) or extinction. If a stem cell dies, a neighbouring cell from the local population of

equipotent stem cells will expand to compensate for this loss. Lopez-Garcia *et al.* [31] identify NDD behaviour within intestinal crypts, outlining NDD and symmetric stem cell division as the chief means of realising a stable, dynamic equilibrium across the stem cell population. Snippert *et al.* corroborate this experimentally through striking use of multicoloured Cre-reporter fate mapping of *Lgr5+* stem cells [32], suggesting that a stochastic mechanism of stem cell expansion can yield monoclonality in the long term.

Cell Death Processes

Homeostasis owes its maintenance as much to cell death as it does to mitosis. Programmed cell death (apoptosis), in which the cytoplasm shrinks prior to disintegration of the cell, is predominantly restricted to upper crypt regions in colonic tissue [33, 34]. However, apoptosis is seen to occur at positions +4 to +5 of the small intestine. This is purported to act as a regulatory mechanism for the stem cell population and is not observed in crypts of the large intestine [34]. A specific form of apoptosis known as *anoikis* occurs in the uppermost regions of the crypt, when senescent cells detach from the basement membrane [35, 36]. Resulting dead cells are thus sloughed from the epithelium into the lumen of the gut. Anchoring of stem cells to the basement membrane *in vivo* serves a vital purpose, since such cells have been shown to exhibit particular susceptibility to anoikis *in vitro* [36].

Cell Migration

Migration also plays a role in homeostasis. Transit from crypt base to surface in the murine colon takes approximately two days [37], prior to desquamation into the lumen of the gut. Cell velocity increases linearly with crypt height before levelling out [16, 38, 39] and exhibits circadian variation [40]. Some theories suggest a coordinated movement amongst the crypt cells, whereby cell-cell connections induce unified mi-

gration of an epithelial layer [15]. Experiments measuring cell velocity have proven crucial in the development of spatially resolved mathematical and computational approaches, by providing data which can be used to calibrate models (e.g. [39], used in the computational study [41]).

Analysis of proliferative and migratory processes typically involves a cell labelling procedure, followed by longitudinal sectioning of the crypt. The angling of crypts within the tissue, along with the hexagonal packing arrangement of cells, can often lead to overestimation of crypt height [21]. This angling is visible in the electron micrograph image on the right-hand side of Figure 1.1. Stathmokinetic (mitosis-inhibiting) studies provide an insight into mitosis and migration in the intestinal epithelium, whether through use of cytotoxic agents [42, 43, 44], irradiation [43, 45], or both [45]. Cell movement is still observed during mitotic arrest; the authors of [45] therefore suggest that mitotic pressure may not be the sole cause of migration. Results from application of the protein synthesis inhibitor puromycin suggest that active mechanisms also contribute to cell movement up the crypt [42].

Cells of the intestinal crypt exhibit asynchronous cycling, with stochastic variation in cycle length [14], although some patches of apparent synchrony have been observed [46]. In healthy colonic tissue, stem cells reside at positions +1 to +2 [34]. At homeostasis the number of stemlike cells is thought to remain approximately constant; this could be achieved via maintenance of asymmetric division by each individual stem cell, or by a collective behaviour pattern across the population of stem cells [47].

1.2 Colorectal Cancer

Colorectal cancer has long been considered the canonical example of tumourigenesis under the traditional model of sequential mutation [48]. Nowadays this theory has largely been supplanted by the Cancer Stem Cell (CSC) hypothesis, in which the

tumour is generated by a small group of malignant stem cells which account for as little as 1% of the tumour mass [49]. It remains unclear whether such cells derive from stem cell mutations, or whether genetic hits occur in progenitor cells which subsequently regress to a stemlike phenotype. Nonetheless, CSCs seem to mirror the capabilities of their healthy counterparts in originating, maintaining and in some cases regenerating (in this case, cancerous) crypt tissue [50]. CSCs also show an improved ability for correcting DNA errors and experience a longer cell cycle than normal stem cells [49], even if cancer cells collectively exhibit a higher than average birth rate [51].

If the CSC hypothesis is valid, it holds considerable implications for the treatment of colorectal cancer, requiring the eradication of malignant stem cells that have few obvious morphological identifiers. Particular cell surface markers have, however, been associated with specific aspects of tumourigenic behaviour; for example, Dalerba *et al.* identify CD44+ CRC cells expressing the cell adhesion molecule $EpCAM^{high}$ [52] and apoptotic resistance in colon cancer stem cells has been observed *in vitro* in CD133+ cell lines [53].

The CSC hypothesis offers an intriguing cellular perspective on CRC: however, we are also interested in the maintenance of the entire tissue in CRC and the means by which it evolves.

1.3 Dynamic Evolution of Crypt Tissue

Disruption to mitotic processes frequently signals the onset of oncogenesis. Such considerations focus primarily on the cellular scale of interest; what can be said about how the appearance of the tissue as a whole changes during abnormal development?

Just as the kinetic behaviour of epithelial cells varies throughout the healthy intestine, so it does in abnormally proliferating tissue. Roncucci *et al.* observe considerable site-dependent variation in the labelling index of crypt cells throughout the colon and

rectum in human patients presenting with advanced polyp formation [54]. An increase in cell proliferation is particularly evident in the left colon and the rectum, with general expansion of the proliferative compartment featuring heavily in the adenomatous tissue under study.

Mutability of the proliferative response is not solely confined to hyperproliferative tissue. Far from being a static structure, the intestinal epithelium behaves as a dynamically evolving tissue [55]. Crypt production is maintained throughout life via a process of crypt branching or fission, the frequency of such occurrences reducing after birth and eventually falling to a low level in adulthood. Cairnie and Millen [56], through irradiative studies of crypt fission in mice, propose a model in which crypt size and number are maintained through feedback control and further support a spatial approach in commenting that '*every proliferating cell is a potential stem cell*' (the latter a development of the ideas of [57, 58]).

Crypt Fusion and Fission

It has been conjectured that intestinal polyps initiate from abnormal crypt fusion, followed by a series of crypt fission events. This behaviour is captured by the striking microscopy work of Araki *et al.* [59]. Heightened cell turnover in a polyp region appears to be confined to individual crypts: a hyperplastic crypt does not necessarily populate any neighbouring crypt structures. Such theories are consistent with observations of crypt fission events in the murine small intestine [56] and rat colon [60].

Crypt fission is also considered a key mechanism in the formation and regeneration of the intestinal epithelium. An elevated rate of crypt production has been observed in tissue samples from patients with intestinal disorders such as Crohn's disease, ulcerative colitis or multiple polyposis [55] and the existence of a crypt cycle is suggested, in which all healthy crypts (asynchronously) fissure every $9-18$ years. Control mechanisms such as chemical or electrical feedback from crypt cell gap junctions have been

proposed as a means of inducing plasticity in the crypt cycle [61].

Tissue Visualisation

Owing to the geometrically intricate and dynamically changing nature of the intestinal epithelium, accurate visualisation of crypt structures within the tissue has proved challenging. Electron microscopes (owing to their capacity to resolve distances as small as 10^{-10}m) can generate clear images [59], as can stained tissue sections [62]; these studies also capture static snapshots of crypt fission processes.

Nonetheless, the majority of studies infer three dimensional structure from two dimensional tissue sections: quite how representative such analysis can be is debatable. Advances in multiphoton microscopy and tissue preparation techniques have begun to address this, evincing the striking architecture of intestinal crypt structures and enabling the simultaneous imaging of up to 50 intact crypts [63].

1.4 Intestinal Biochemistry

Our focus on intestinal structure and function has been upon the cellular and tissue scales thus far. However, biochemical dysregulation is the first consequence of genetic mutation, and the means by which these aberrations propagate to the cellular scale. Indeed, Hanahan and Weinberg's characterisation of the 'Hallmarks of Cancer' [64, 65] describes the *programming of [tumourigenic] capabilities via intercellular circuitry* and an enabling characteristic, *genome instability and mutation*, as key aspects of malignant tissue growth and development.

Fearon & Vogelstein's so-called 'linear model of carcinogenesis' [48] dominated thinking in the early 1990s, emphasising sequential mutation as the cause of tumour development in the intestinal epithelium. Nowadays, the concept of a universal sequence of consecutive mutations is somewhat less popular. Distinctions have also

been drawn between active, 'driver' mutations and coexisting 'passenger' mutations, identified through extensive sequencing of cancer genomes [66].

In the interest of understanding the biochemistry of the intestinal epithelium and the implications for the genesis and treatment of CRC, we now describe our two pathways of interest: the Notch pathway, which is involved in cell fate selection, and the canonical Wnt pathway, which governs cell proliferation.

1.4.1 The Notch Pathway

The Notch pathway regulates cell development in the trajectory from fully undifferentiated to terminally differentiated cell and belongs to the class of *juxtacrine* signalling networks [67]. Juxtacrine signals are initiated by contact-based processes, in which two or more adjacent cells transfer a signal from one to the other via ligand binding events at their cell surface membranes [68].

Juxtacrine signalling in the Notch pathway involves three types of transmembrane protein: Delta ligand, Jagged ligand, and Notch receptor [69]. The extracellular portion of each participates in ligand-receptor binding events with receptors on neighbouring cells and is formed from a repeating series of epidermal growth factor (EGF) units, as well as a variety of other protein components, such as ankyrin (in Notch) or a cysteine-rich domain (in Delta and Jagged) [70]. Variation in the type and location of non-EGF proteins within the structure yields a family of homologues in vertebrates: three types of Delta, two types of Jagged and four types of Notch [71].

Initiation of a Notch cascade occurs when a Delta or Jagged ligand on a signalling cell binds to a Notch receptor on the recipient cell. Delta and Jagged ligands exhibit short-range action and only affect adjacent cells expressing the complementary Notch receptor [72, 73]. The following progression occurs, as depicted in Figure 1.3 [2]:

[2]This should be considered as a simplified description of the network. Owing to the complexity of the pathway, we delay full treatment and referencing until Chapter 3.

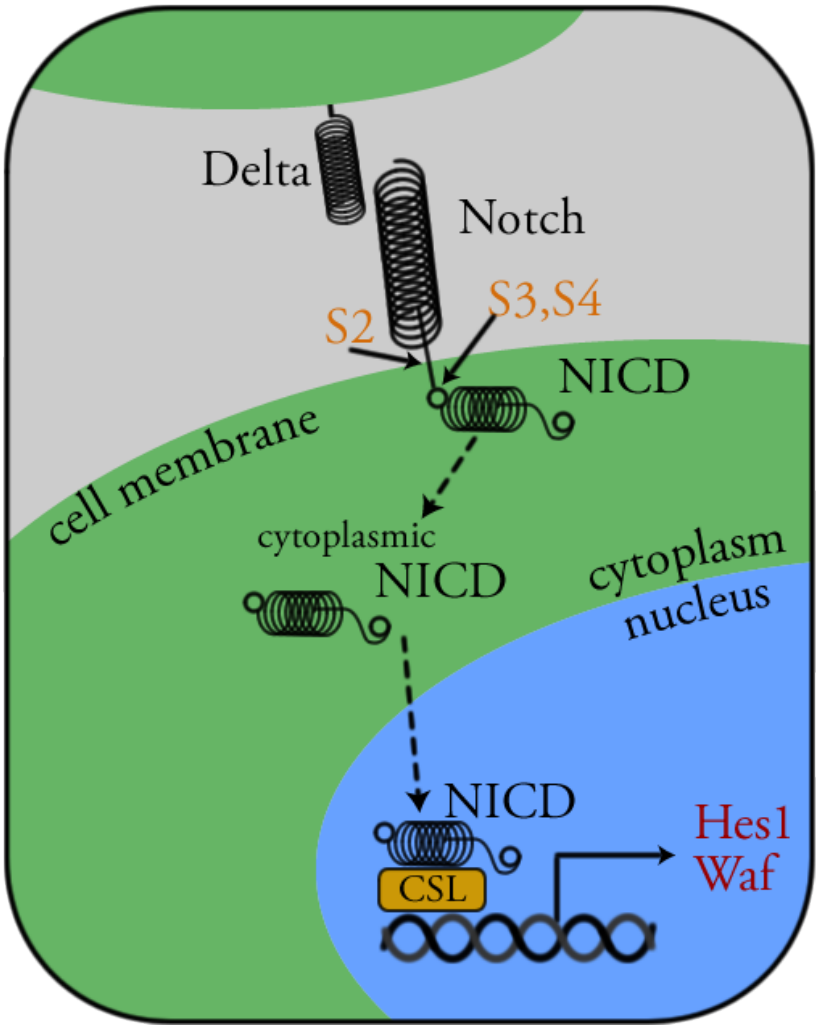

Figure 1.3: Simplified schematic of the Notch pathway described in Subsection 1.4.1. This depicts a ligand binding event at the cell membrane, passing a signal from the primary cell (binding using a Delta or Jagged ligand) to the recipient cell, which contributes a Notch ligand to the binding event. The cytoplasm is shown in green, the nucleus in blue, and the intercellular space in grey. Transcriptional targets of the pathway are listed in red.

1. Successful juxtacrine binding results in cleavage of Notch at three sites: S2 (located on the extracellular section of the molecule), S3 and S4 (intracellular loci) [69];

2. Notch receptor releases an intracellular fragment into the recipient cell, known as the Notch Intra-Cellular Domain (NICD) [74];

3. NICD translocates to the cell nucleus and binds to the transcription factor, CSL [75, 71];

4. NICD recruits a series of nuclear proteins to CSL, instigating transcriptional activation of Notch target genes [76, 71];

5. Transcriptional targets include: *Hes* (hairy enhancer of split) [77], itself involved in negative modulation of differentiation effectors such as *Ngn3* [78, 79]; and *Waf*, a cell-cycle regulator which initiates terminal differentiation [80];

6. Ligand expression of Jagged and Delta may also be up- or down-regulated by intermediate effectors such as *Ngn3* [81, 82], according to whether lateral inhibition or inductive signalling is operational (see Figure 1.4 for details).

Membrane-bound Notch acts as an extracellular receptor, whilst its intracellular fragment is a transcriptional regulator in the nucleus. The Notch pathway therefore functions as a signal transduction mechanism, allowing the cell to modulate its biochemical activity in response to the behaviour of neighbouring cells. A typical Notch cascade attains equilibrium within the timespan of the cell cycle [83].

Notch receptors were first isolated in *Drosophila* [84] and the pathway is conserved across many different species [71]. Nonetheless, it is highly context-dependent and its behaviour and transcriptional targets may vary according to the species and type of biological tissue [85, 86, 69]. The Notch pathway's diverse roles in cell fate selection

include *lateral inhibition* [67], *lineage specification* [69] and *inductive signalling* [87, 88], as illustrated in Figure 1.4.

Cell Fate Selection

There are four types of differentiated cell in the epithelium of the small intestine: goblet, Paneth, and enteroendocrine, which are secretory; and enterocytes, which are absorptive [89, 19]. Of these, only goblet cells and enterocytes feature in the large intestine. The Notch pathway is instrumental in selecting which of these four (or two) cell fates will be realised; this is achieved by the Notch target *Hes1*, and the protein *Hath1*, which is normally suppressed by *Hes1*.

Expression of *Hath1* (and conversely, suppression of *Hes1*) is associated with the selection of secretory phenotypes [90], whilst high *Hes1* expression is positively correlated with an absorptive fate. *In vivo* studies on the small intestine of *Hes1*-knockout mice have been shown to generate substantial numbers of all three secretory cell types [78]. Similarly, the inhibition of Notch signalling via γ-secretase yields an increased population of goblet cells [91]. Gain- and loss-of-function studies by Fre *et al.* [92] support this theory and suggest that Notch signalling via *Hes1* is responsible for early-stage cell fate selection.

Cellular transition towards terminal differentiation is brought about by an intricate coordination of the Notch and Wnt pathways, as shown in the cell hierarchy for fate specification in Figure 1.5. Notch is believed to select for absorptive/secretory function at an early stage of specification, when cells are residing in or near the stem cell niche and are actively dividing under high-Wnt conditions [19, 93]. As a cell travels up the crypt and is exposed to reduced Wnt levels, other pathways and cell regulators begin to act to coordinate a more refined selection of fate: for example, determining a specific fate for a cell already selected for secretory function.

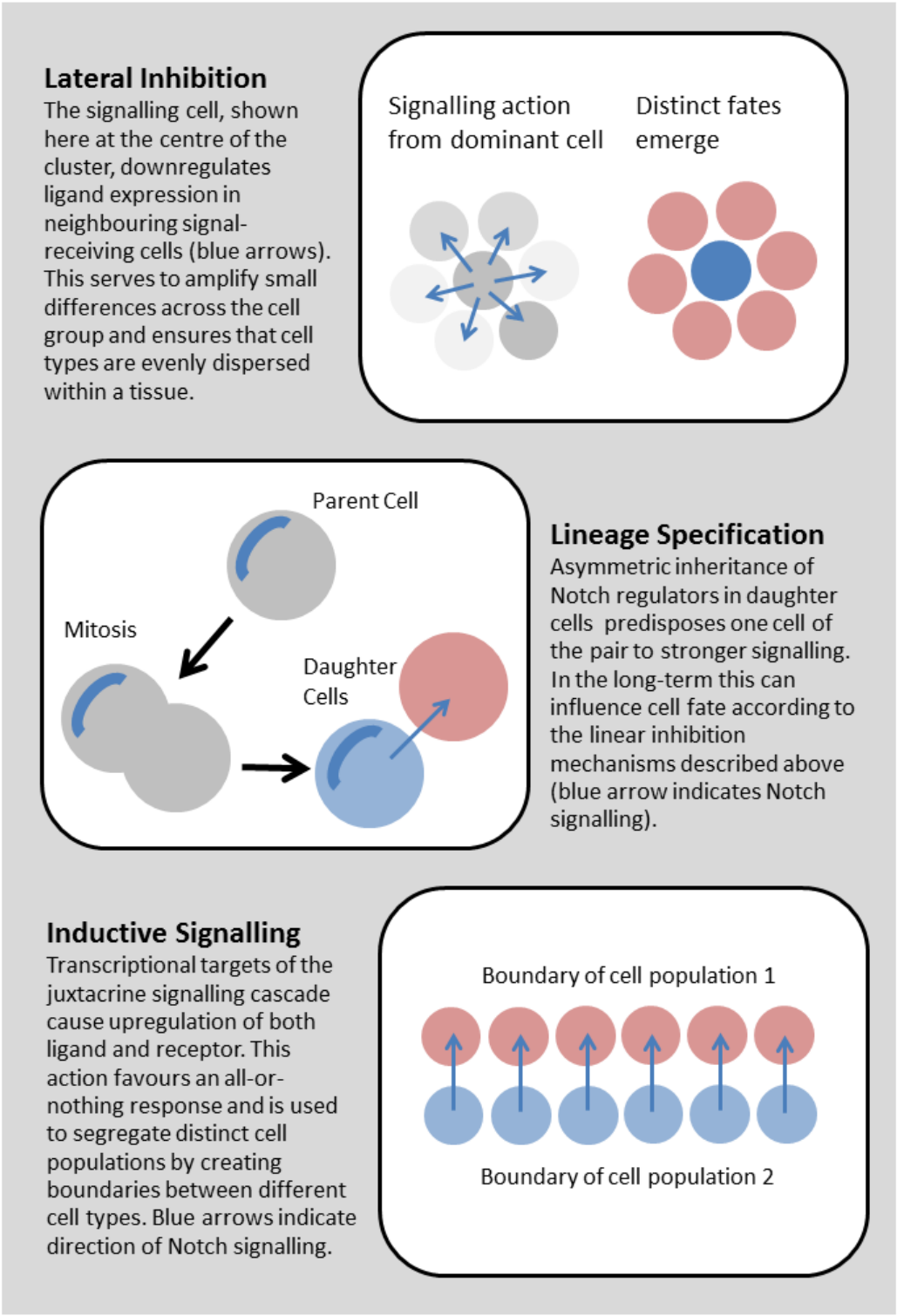

Figure 1.4: Notch roles in cell fate selection, inspired by schematics presented in Bray *et al.* [69].

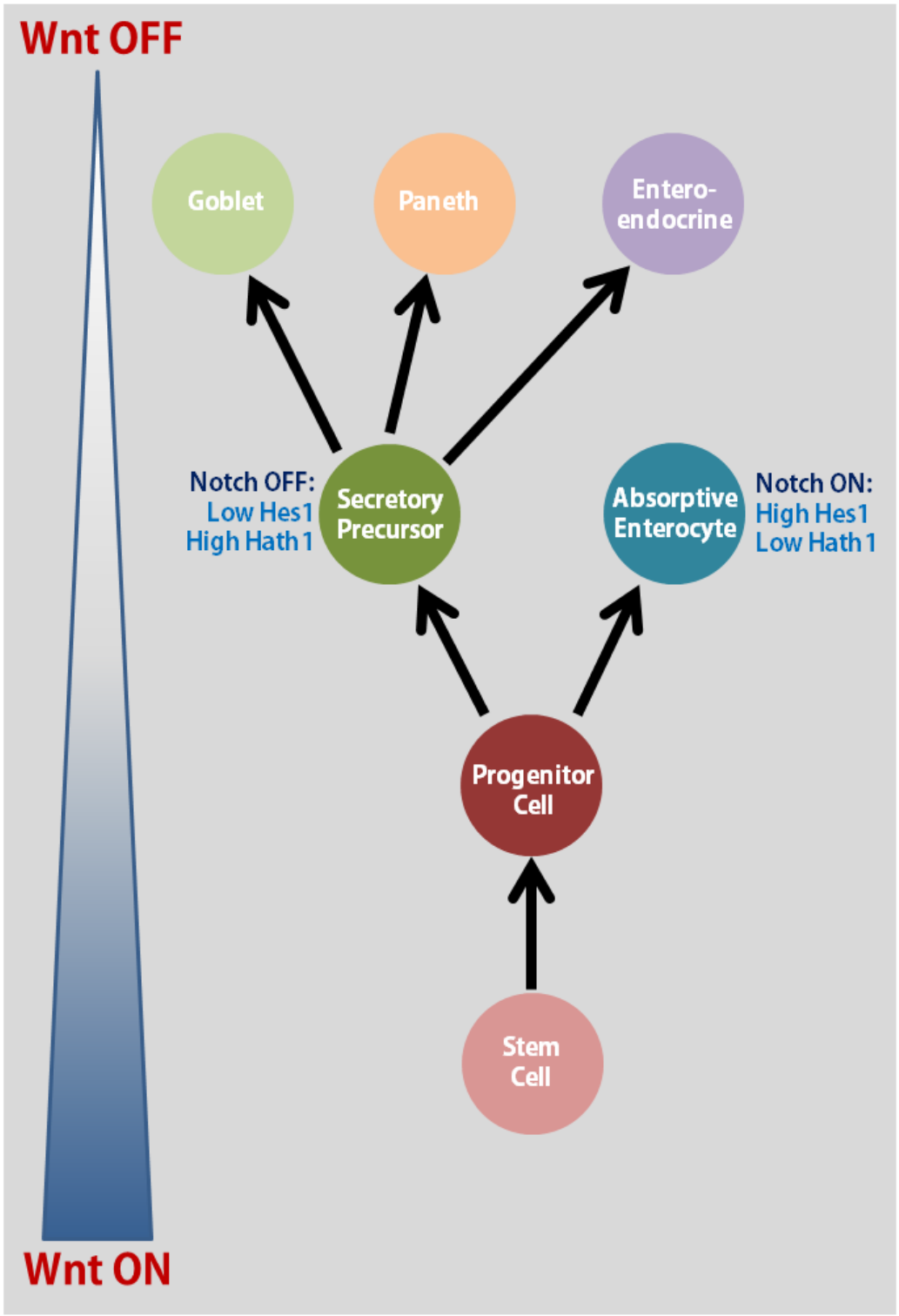

Figure 1.5: Hierarchy for cell fate selection in the intestinal epithelium, inspired by schematics in Yeung *et al.* [19] and Nakamura *et al.* [93]. Wnt expression is highest at the crypt base and diminishes on ascending the crypt.

1.4.2 The Wnt Pathway

The Wnt pathway is crucial in the development and maintenance of biological tissues. Its canonical form employs β-catenin to regulate transitions through the cell cycle [94] and centres on a mechanism for the control of cytoplasmic β-catenin levels. Dysregulation of the canonical Wnt pathway, typically through mutation of its constituent proteins, is strongly implicated in the development of colorectal cancer [95, 96, 94]. Mitotic disruption is a key feature of CRC, which displays a capacity for *self-sufficiency in growth signals*, *insensitivity to anti-growth signals*, and *limitless replicative potential* [64].

Non-canonical forms of Wnt signalling govern a variety of processes, including: integrin-mediated intercellular adhesion; planar cell polarity, and Wnt/calcium signalling [97]. In this study, we focus solely on the canonical pathway. Discussion of other modes of Wnt action can be found in the reviews [98, 99, 100, 101].

Origin of Wnt

Wnt proteins are a family of cysteine-modified growth factors, each approximately 40kDa in size [102]. Nineteen distinct Wnt genes are known to exist in the mammalian genome [103]. Lipid modifications to the Wnt molecular structure feature throughout the family. These lipid components are vital for signalling [104] but also cause hydrophobicity, which initially hindered attempts to characterise Wnt's properties [105, 106].

Lipid modification of Wnt is believed to occur in the endoplasmic reticulum. Assisted by trafficking complexes, Wnt is subsequently transported inside vesicles to the cell surface membrane, where it is secreted [103]. Although the Wnt pathway was traditionally believed to influence cells by medium-range interactions via morphogen gradients, recent findings are consistent with its involvement in short-range signalling between cells in close proximity [103].

Canonical Function

The canonical Wnt pathway is constitutively active in cells exposed to high levels of Wnt, and inactive when the local Wnt concentration is low.

When the extracellular Wnt stimulus is too weak, a '*destruction complex*' formed from – amongst others – APC, Axin and GSK3 binds to β-catenin and ubiquitinates it [107, 108, 109], as shown on the left-hand side of Figure 1.6. This effectively labels β-catenin for degradation by the proteasome [110], thus limiting the cytoplasmic concentration of β-catenin and preventing its nuclear translocation.

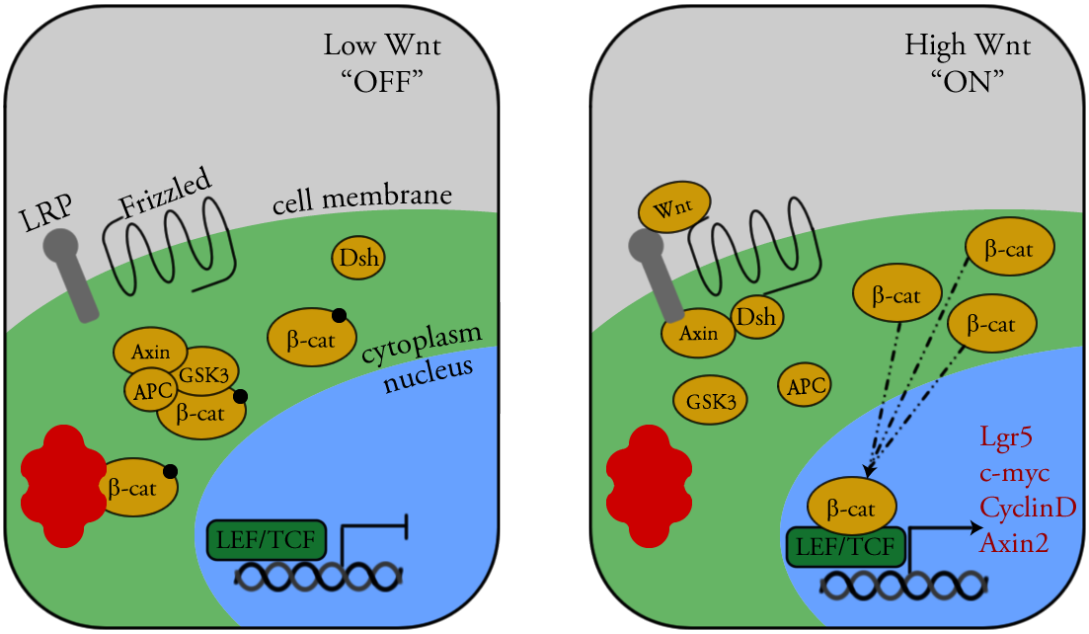

Figure 1.6: Simplified schematic of the Wnt pathway: (L) Pathway in the OFF state, when cell is subject to low extracellular Wnt; (R) Pathway in the ON state, when cell is subject to high extracellular Wnt. The proteasome is shown in red, whilst phosphorylated β-catenin is indicated by a tag. The nucleus is shown in blue, the cytoplasm in green, and the intercellular space in grey.

Activation of the Wnt signal occurs when extracellular Wnt molecules bind to Frizzled-LRP receptor complexes at the cell surface membrane, as on the right-hand side of Figure 1.6. This inhibits β-catenin degradation[3]:

[3]As with the Notch pathway in Section 1.4.1, we present a minimal explanation of the canonical

1. Signals from *Frizzled* receptors recruit cytoplasmic *Dishevelled* (*Dsh*) to the cell membrane [111];

2. In the absence of the destruction complex, cytoplasmic β-catenin accumulates and translocates to the nucleus, where it binds to the transcriptional activator, LEF/TCF [112];

3. Upregulation of Wnt target genes occurs. These include: *Lgr5*, the stem cell marker [26]; *cyclin D*, required in the cell cycle [113], *Axin*, involved in the β-catenin destruction complex, and *c-myc*, a cell growth regulator [114];

4. Secondary effects of Wnt target genes include downregulation of *Hath1*, involved in Notch signalling [115].

Recent observations by Li *et al.* [116] suggest that β-catenin binds with the destruction complex during periods of Wnt activation, but is not ubiquitinated in this interaction.

Mitotic Regulation

A mitotically active cell proceeds through four main phases during the cell cycle: $G1$, S, $G2$ and M, as shown in Figure 1.7. $G1$ and $G2$ are periods of growth; S is the synthesis phase, during which the cell builds the proteins necessary for proliferation; actively cycling cells undergo division during M, the mitotic phase [117]. Cell cycle regulators *c-myc* and *cyclin D1* are transcriptional targets of the Wnt pathway and determine whether the cell transitions through G1 phase or exits the cell cycle into a non-cycling, $G0$, phase [113, 114].

Downregulation of *c-myc* by disrupting β-catenin-TCF/LEF activity has been shown to cause G1 arrest during *in vitro* studies on CRC cell lines [94]. Wnt's proliferative control can be artifically upregulated *in vitro* via the Wnt agonist *R-Spondin1*

Wnt pathway here and delay full discussion until Chapter 3.

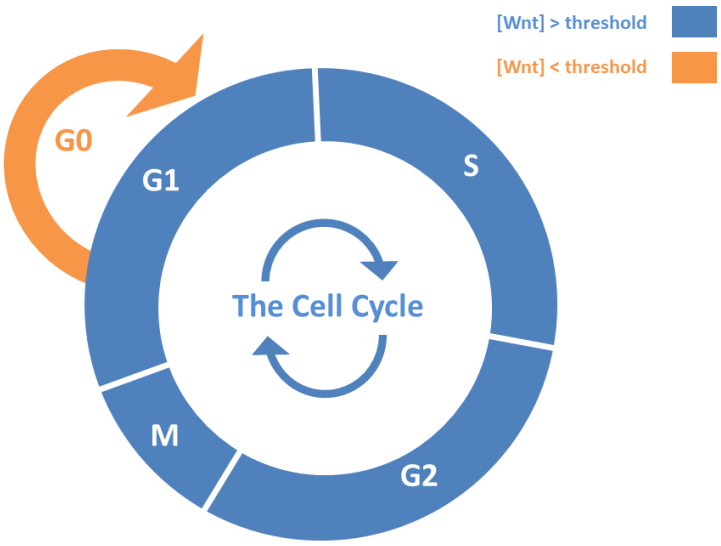

Figure 1.7: Partitioning of the cell cycle into four phases: M, $G1$, S, $G2$. Cells subject to sufficient stimulus from the extracellular Wnt concentration remain as cycling cells and divide during M phase. Cells exposed to a low-Wnt environment enter an arrested $G0$ phase. Cells in the $G0$ phase do not divide but may recover their cycling behaviour if their local Wnt concentration increases beyond a given threshold.

to induce crypt hyperproliferation, as in the *de novo* synthesis experiments of Ootani *et al.* [2].

Aberrant Wnt signalling in CRC presents in a variety of forms. The most common hereditary form of the disease arises from a mutated APC gene [118]. Loss of functional APC impairs the function of the β-catenin destruction complex; the resultant hyperproliferation of the intestinal epithelium produces polyps along the wall of the gut, which can acquire additional spontaneous mutations and develop into malignant growths. Notably, the majority of sporadic forms of CRC also involve loss of APC [119, 118]. Neoplastic cells frequently display 'addiction' to Wnt signalling [120] and *Lgr5* expression, the 'stemness' marker associated with Wnt pathway activity, is upregulated in colorectal tumour tissue [121].

An intricate pattern of cellular control is emerging as understanding increases of the interactions of the Wnt pathway with other networks, such as Notch [122] and EGF [123]. Interaction between the Wnt and Notch pathways has been implicated in colorectal cancer [124, 122] and a synergy between the two is believed to coordinate proliferative and differential processes in the crypt [93]. We explore the interactions with Notch in greater depth in Chapters 3 to 6.

1.5 Discussion

An understanding of the underlying biology is essential for the mathematical modelling process to follow. The review of the experimental literature presented here will prove invaluable in shaping decisions during the modelling and simulation process from Chapter 3 onwards.

Before progressing to build our subcellular model for Notch-Wnt crosstalk though, we first need to appraise the mathematical and computational literature. Existing representations of these systems, which we explore in Chapter 2, provide crucial in-

sights into the suitability of particular modelling approaches and help to summarise the understanding we have already gained of their qualitative behaviour.

2

Methods and Models

Chapter Summary

Investigation of the pathways discussed in Chapter 1 requires the use of quantitative methods. To this end, we summarize the relevant mathematical literature. This includes a synopsis of existing mathematical models for the Notch and Wnt pathways, along with an outline of key constructions for the tissue models used in the studies presented in later chapters.

Our review of the biological literature in Chapter 1 outlined the structure and function of the intestinal epithelium at the tissue, cellular and subcellular scales. This chapter aims to show how various features of the gut and its biochemistry can be explored theoretically, using examples from the mathematical and computational literature.

In Sections 2.1 and 2.2, we evaluate models for the Wnt and Notch pathways, in preparation for the subcellular modelling work of later chapters. In Section 2.3, we discuss the computational and simulation software used in this thesis, while Section 2.4 contains an outline of cell-based modelling techniques.

2.1 Notch Signalling

Mathematical models for the Notch pathway range from discrete models of ligand binding, to ODE models which account for subcellular activity and which may incorporate gene regulation events.

We begin by looking at some of the simplest models for the Notch pathway, namely those which address juxtacrine signalling. Such models account only for the ligand-receptor interaction at the cell surface membrane and do not attempt to model the subcellular biochemistry. Despite their apparent simplicity, juxtacrine models can offer useful insights into both lateral inhibition and lateral induction.

2.1.1 The Model of Collier *et al.* (1996)

The canonical ODE model for Delta-Notch signalling at the receptor-ligand scale is due to Collier *et al.* [125]. Its nondimensionalised form, in which time is scaled against the rate constant for decay of Notch, is shown in Equations (2.1) and (2.2). Given a cell P, the concentrations of Notch receptor, $N_P(\tau)$, and Delta ligand, $D_P(\tau)$, present in the cell at a time τ evolve as follows:

$$\frac{dN_P}{d\tau} = \frac{\overline{D(\tau)}^k}{a + \overline{D(\tau)}^k} - N_P(\tau), \tag{2.1}$$

$$\frac{dD_P}{d\tau} = \nu \left\{ \frac{1}{1 + bN_P(\tau)^h} - D_P(\tau) \right\}, \tag{2.2}$$

where $\overline{D(\tau)}$ represents the mean value of Delta across the immediate neighbours of cell P; the fixed parameters a, b, h, k are detailed in Table 2.1.

A 'neighbour' for juxtacrine signalling is defined to be any cell whose outer membrane is in direct contact with that of cell P which, in a biological setting, would allow the two cells to participate in ligand-receptor binding events at the cell surface. Notch in cell P responds to the Delta levels of its neighbours, while the Delta levels of cell

Parameter	Purpose	Standard Value
ν	Ratio of Notch:Delta decay	1.0
a	Hill dissociation constant	0.01
b	Delta denominator constant	100
h	Hill exponent for Notch synthesis	2.0
k	Exponent for Delta synthesis	2.0

Table 2.1: Standard parameter set for the model of Collier *et al.*, detailed in Equations (2.1) and (2.2).

P adjust according to the cell's own Notch levels.

A cell which actively inhibits its neighbours is termed the *primary* cell and is associated with high Delta expression, while cells subject to inhibition are said to adopt a *secondary* fate and have high Notch levels. The model of Collier *et al.* uses a positive feedback construction to explain *how* a primary fate cell is initially selected and *why* neighbours of this cell ultimately adopt the secondary, rather than primary, fate. Mathematically, these fates correspond to different stable states in the ODE system.

Model Dynamics

Since the model of Collier *et al.* forms one of the key influences on the development of our own model in Chapter 3, we now outline its dynamics in greater detail, using a two-cell embedding of the model as a simple case study. For brevity, we write the Notch and Delta production rates in Equations (2.1) and (2.2) thus:

$$Y(\bar{D}) \equiv \frac{\overline{D(\tau)}^k}{a + \overline{D(\tau)}^k}, \quad Z(N) \equiv \frac{1}{1 + bN(\tau)^h}\,. \tag{2.3}$$

Homogeneity and heterogeneity: In the *homogeneous* or *unpatterned* steady state, both cells have identical concentrations of Notch and identical concentrations of Delta, as shown on the right-hand side of Figure 2.1. Some parameter regimes also yield one or more pairs of *heterogeneous* or *patterned* steady states, in which

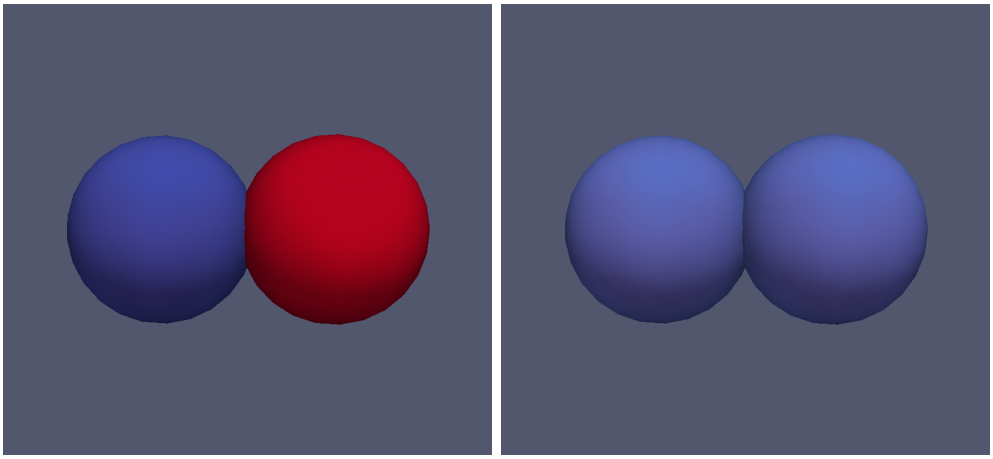

Figure 2.1: Steady states in a two-cell embedding of the Collier Notch model. Colours indicate Delta levels (dark blue indicates low Delta expression, dark red indicates high Delta). Left: The heterogeneous state, which teams a high-Delta primary fate cell with a low-Delta secondary fate cell. Right: The heterogeneous steady state, in which both cells adopt identical, low-Delta fates. Associated evolution plots for these images are shown in Figure 2.3.

one cell adopts a primary (high-Delta, low-Notch) fate, while the other settles on a secondary (high-Notch, low-Delta) fate.

Attraction to the homogeneous state: The monotonicity of the increasing Hill function Y and the decreasing term Z guarantees the existence of a single homogeneous steady state [125], whose stability depends on the parametrisation of the system. Heterogeneity develops when the homogeneous state is unstable [125, 126].

Role of positive feedback: Heterogeneous steady states in the model arise from a positive feedback loop, formed by the motif

$$\text{Delta} \rightarrow \text{Nbg.}\ \text{Notch} \multimap \text{Nbg.}\ \text{Delta} \rightarrow \text{Notch} \multimap \text{Delta}\,, \tag{2.4}$$

in which arrows ($\rightarrow$) and circular endcaps ($\multimap$) represent upregulation and downregulation respectively, and *Nbg.* indicates a concentration in the neighbouring

cell. The feedback loop yields heterogeneity by amplifying small differences in ligand expression between neighbouring cells. Higher values of the exponents h and k in Equation (2.3) strengthen each step in the motif (2.4) and, thus, increase the overall feedback strength, providing a stronger propensity for patterning. Indeed, the analysis presented in Collier *et al.* [125] confirms that the stability of a given steady state (n^*, d^*) depends upon the strength of this feedback. Denoting composition of functions by $\circ$ and the first-order derivative with respect to time τ by $'$, stable states can be shown to satisfy the inequality $(Y \circ Z \circ Y \circ Z)'(n^*) < 1$.

Attraction to the heterogeneous state: A dynamically changing phase plane, in which the nullclines for Delta and Notch rotate in opposite senses, causes an initial attraction to the homogeneous state until the nullclines coincide. As this continues and the nullclines move apart again, the system is pulled towards the heterogeneous state. Sketches of the rotating nullclines are shown in Figure 2.2. Movement towards the homogeneous state at the outset of simulation is clearly visible in the upper plot of Figure 2.3, before attraction to the patterned state begins to dominate.

The model of Collier *et al.* provides a simple, concise representation of the lateral inhibition process and has proven capacity for pattern generation. Nonetheless, the model is far from being the sole representation of juxtacrine signalling processes; consequently we now summarise some other examples.

2.1.2 Other Models of Juxtacrine Signalling

Owen *et al.* [127, 128] explore the role of lateral induction in pattern formation by following the changing totals of free ligand, free receptor, and bound ligand-receptor complex. The bound complex is assumed to have a saturating effect in upregulating

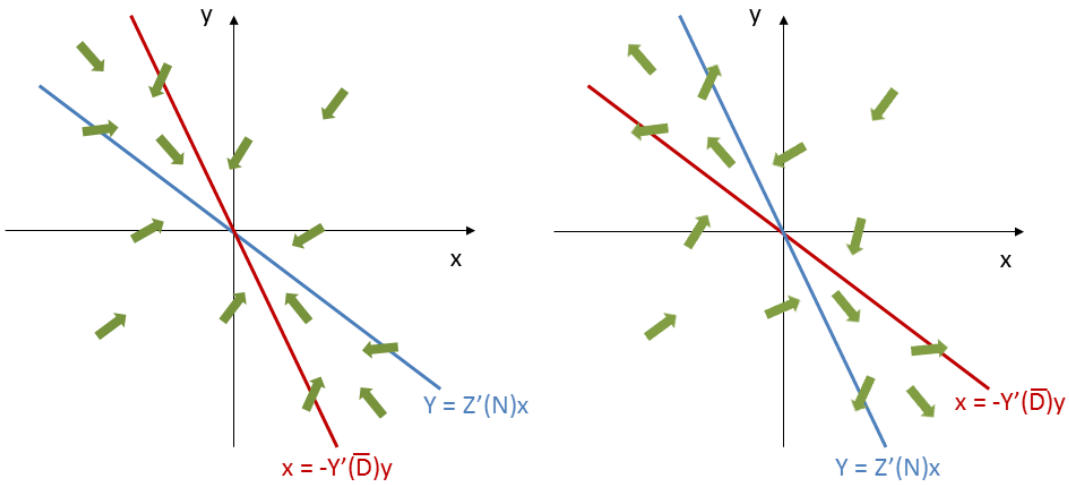

Figure 2.2: Rotation of nullclines in the dynamically changing phase plane of the model of Collier *et al.*, inspired by a sketch in the original paper [125]. (x, y) is a small perturbation about a homogeneous steady state, (n^*, d^*). (L) At the outset of simulation, attraction to the homogeneous steady state dominates. (R) As the nullclines rotate in the plane and eventually cross, the direction of attraction is reversed, and the system is pulled out towards one or other of the patterned, heterogeneous steady states.

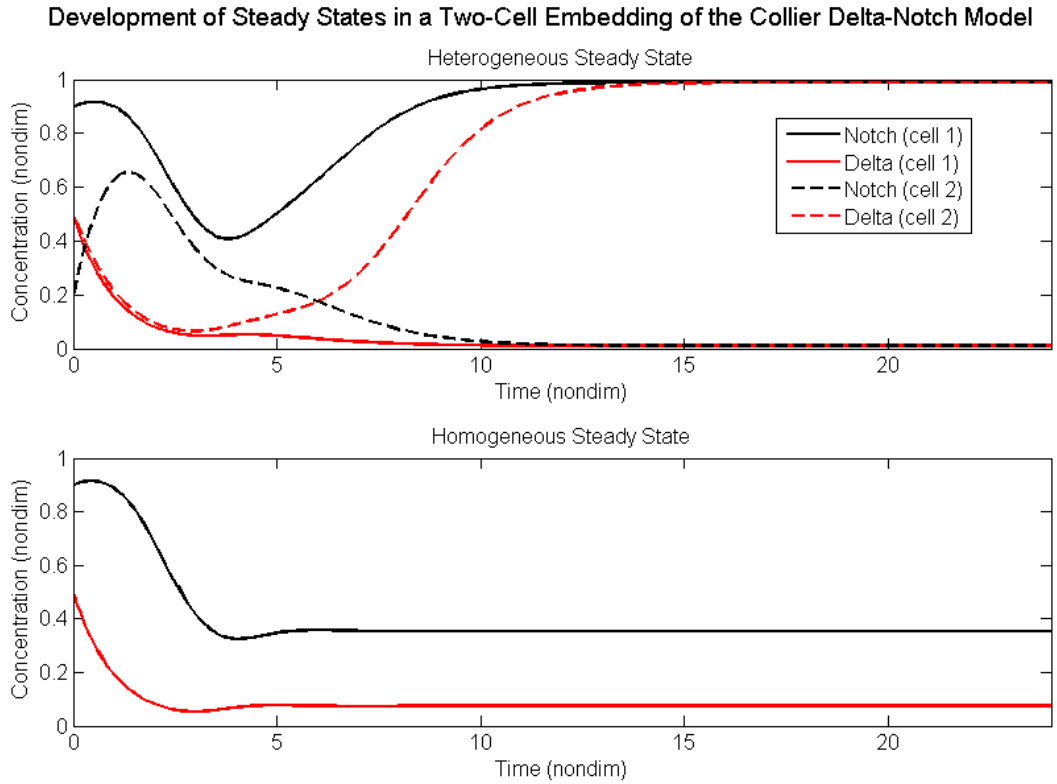

Figure 2.3: Time evolution of steady states for the cell pairs shown in Figure 2.1, using the nondimensional model of Equations (2.1) and (2.2) and parameters as in Table 2.1. The upper plot reaches a heterogeneous state, while the lower plot attains the homogeneous state. The two cells in the lower plot each start from the same initial conditions and evolve identically. *Upper Plot*: Patterned state arising from initial conditions $(0.9, 0.5)$, $(0.19, 0.5)$. *Lower Plot*: Unpatterned state arising from initial conditions $(0.9, 0.5)$, $(0.9, 0.5)$.

both ligand and receptor.

Lateral induction is a highly versatile pattern generator and the model of Owen *et al.* can exhibit spatially uniform behaviour, patterning or uncontrolled feedback. This appears to be a direct consequence of positive feedback, which can yield fast-growing modes at higher wavenumbers and hence generate longer scale patterns than a corresponding inhibitory model [129]. Embeddings of the model in a square lattice of non-dividing cells demonstrate a robust capacity for pattern generation of both spots and stripes [128]; comparison against a hexagonal array suggests that the square lattice provides the more robust patterning geometry [130]. Bifurcation analyses for the square case have since demonstrated that a wide variety of stable patterns exists for a given parameter set [131]. Notably, conditions have been derived under which the models of Collier *et al.* and Owen *et al.* exhibit the same homogeneous and heterogeneous steady states [130]. Equivalence occurs when receptor expression is held constant and low affinity binding is assumed.

Simulations on two-dimensional domains suggest that the model can generate patterning signals with arbitrarily large half-life [132] and control the size of cell clusters in a dynamic setting [133]. Inhomogeneity in the receptor and ligand distributions across the cell surface contribute to the propagation of long-range patterns [134].

An alternative model for ligand-receptor interaction has been developed by Sprinzak *et al.* [135]. This distinguishes between *cis*-Delta (Delta on a given cell) and *trans*-Delta on neighbouring cells, and similarly for Notch. Interactions between *cis*-Notch and *trans*-Delta generate an NICD signal in the recipient cell, which is used as a measure of cell fate, whilst binding between *cis*-Delta and *cis*-Notch causes mutual inactivation. The combination of *cis*-inhibition and *trans*-activation contributes to strong switch-like behaviour, in which a cell becomes either a signalling or receiving partner. This is shown to generate sharp pattern boundaries when embedded in a hexagonal cell lattice.

2.1.3 Discrete & Rule-Based Models

Inspired by a neural network model [136], Ghosh & Tomlin [137, 138] employ discrete states in a cellular automaton to capture Delta-Notch interactions. Each cell may take one of four states: Delta-expressing; Notch-expressing; expressing both; or neither. Transitions between these states occur according to an averaging process over neighbouring cells. Simulations on a hexagonal cell array develop a regular pattern with minor defects, similar to that of Collier *et al.*, but prove computationally quicker to implement.

Buske *et al.* [5] eschew explicit subcellular modelling in favour of a simpler, rule-based approach. In this model, a cell's Notch activity is either high or low and is influenced by neighbouring cell states; Wnt activity varies with the local curvature of the basement membrane. High Wnt and Notch levels maintain an undifferentiated phenotype; cells differentiate into either a secretory or an absorptive cell on attaining a low-Wnt state, with cell fate determined by a cell's Notch status at that instant. This approach generates the correct proportions of cell types but does not produce the 'salt-and-pepper' spatial arrangement characteristic to upper crypt regions in the intestinal epithelium.

Similarly, crypt embeddings performed by Pin *et al.* [139] determine Wnt and Notch activity using a rule-based approach, which averages over the behaviour of neighbouring cells. Although the crypt is modelled as a coiled, spiral string of cells and therefore differs from that of Buske *et al.*, the rule-based approach again fails to yield adequate dispersal of primary fate cells in the upper regions of the crypt.

The work of Buske *et al.* [5] is discussed further in Chapter 5, where its performance is compared against that of a framework which embeds an explicit biochemical model into each cell.

2.1.4 Models of Hes1 Oscillation

The role of negative feedback motifs in oscillatory gene networks was first characterised by Goodwin in 1965 [140]. The Goodwin model employs ordinary differential equations and augments a system of mRNA and protein with an unspecified intermediate in order to generate sustained oscillations [141]. Hirata *et al.* [142] propose a simple ODE model of Goodwin form to represent Hes1 oscillations and achieve an experimentally-validated, two hour oscillation period.

Such oscillations are now known to arise from delays in gene regulatory processes, such as transcription and protein folding. In light of this, Monk reformulates Goodwin's model using delay differential equations [143]. The transcriptional delay is of considerable functional importance, since the resulting two-equation model for *Hes1* mRNA and protein generates oscillations without the need for any intermediate and the mRNA half-life strongly influences the period of oscillation. Extension of this model to include Hes1 dimerisation [144] increases the oscillatory amplitude of *Hes1* protein, bringing it closer in line with experimental data.

Momiji and Monk subsequently couple two oscillating *Hes1* systems, enabling the investigation of in-phase and out-of-phase oscillations within lateral inhibition networks [145]. The authors explore the role of negative and positive feedback motifs in shaping the oscillatory dynamics of a two-cell system, ranging from a single cell subject to an autorepression loop, to two cells with *trans*-inactivating *Hes1* and *Ngn3*. Mutual inactivation is found to be important in generating oscillations, whilst the autorepression of *Hes1* aids the tunability of oscillations and dominates the system dynamics.

A similar approach to Monk [143] is adopted by Lewis [146], who uses two-cell systems to model mRNA-protein interactions in zebrafish *somitogenesis*, the generation of segments along an anatomical structure. Somitogenesis has inspired other studies of oscillation in the Notch pathway. For instance, the model of Goldbeter *et al.* [147]

couples simple representations of the Notch, Wnt and FGF pathways. However this model unites Wnt and Notch activity via the action of GSK upon NICD; current developments in the biochemical literature, discussed in Section 3.2, now appear to favour a β-catenin crosstalk hub. Murray *et al.* [148, 149] present a generalised model for coupled oscillations of gene expression in one-dimensional cell chains, using a PDE to characterise the spatial variation in oscillation phase. This framework explores the "*clock and wavefront*" model, in which a travelling wavefront along the cell chain determines the spatial location of particular development events, while a somitogenesis clock determines the periodicity with which these events occur. Coupling between cells serves to reduce the speed at which the travelling wavefront moves along the chain.

Few multicellular studies of the role of *Hes1* oscillations in cell fate exist at the present time. Oscillations of *Hes1* are thought to assist in the maintenance of cell-cycle processes as well as maintaining the flexibility of cell fate decisions within a cell population [150]. Two- and three-dimensional tissue embeddings of oscillatory models would serve as a valuable tool for exploring these hypotheses further.

2.1.5 Continuous Subcellular Models

The oscillating models described in Section 2.1.4 focus primarily on *Hes1* and its autoregulation, rather than the broader implications for Notch signalling. Agrawal *et al.* [151] and Kiparissides *et al.* [152] remedy this through the development of detailed subcellular models for the Notch pathway, incorporating Notch, *Hes1* and a CSL analogue. Both approaches include mRNA entities, enabling the generation of transcriptionally-driven oscillations without the need for a delay formulation. A compartmental approach allows for translocation between the cytoplasm and nucleus.

Variation in the transcriptional repression of *Hes1* enables the model of Agrawal *et al.* to transition between oscillation and bistable switching, suggesting that the cell regulates its behaviour by tuning the response of *Hes1*-associated processes [151].

Kiparissides *et al.* include terms for Mash1 (a *Hath1* analogue) and NICD to facilitate the study of differentiation processes. Damped oscillations in the model capture typical biological patterns of early cell-fate selection, but it is suggested that crosstalk with another pathway would be required to derive a terminally differentiated state [152].

A generalised model for Notch-Wnt interaction has also been explored [153, 154]. However, this provides an abstraction of cell fate entities and does not include a *Hes1* autoregulation motif. Coupling with Wnt via membrane-bound Notch allows inhibition of Wnt signalling to drive terminal differentiation in the cell.

2.2 Wnt Signalling

Mathematical modelling of the Wnt signalling pathway has generated a variety of interpretations in the literature. Some of these examine non-canonical forms of the Wnt pathway, such as its role in cadherin binding and cell-cell adhesion [155, 156, 157], or crosstalk with pathways other than Notch [158, 123]. Though interesting, these lie beyond the scope of this work and we shall restrict our attention to representations of the canonical pathway in this summary. Extensive reviews of the canonical and non-canonical Wnt modelling canon can be found in [159, 160].

2.2.1 Lee *et al.* (2003) and Associated Literature

The ODE system of Lee *et al.* [161] provided the first quantitative model of the Wnt pathway and has since been explored widely within the literature. Comprising fifteen coupled equations, the model includes a stepwise cycle for the phosphorylation and degradation of β-catenin and explicitly depicts the association and dissociation of elements in the β-catenin destruction complex, as shown in Figure 2.4. Use of ODEs is justified on the grounds that the majority of signal control occurs within the cytoplasm, which is assumed to be well-mixed: this contrasts with the shuttling

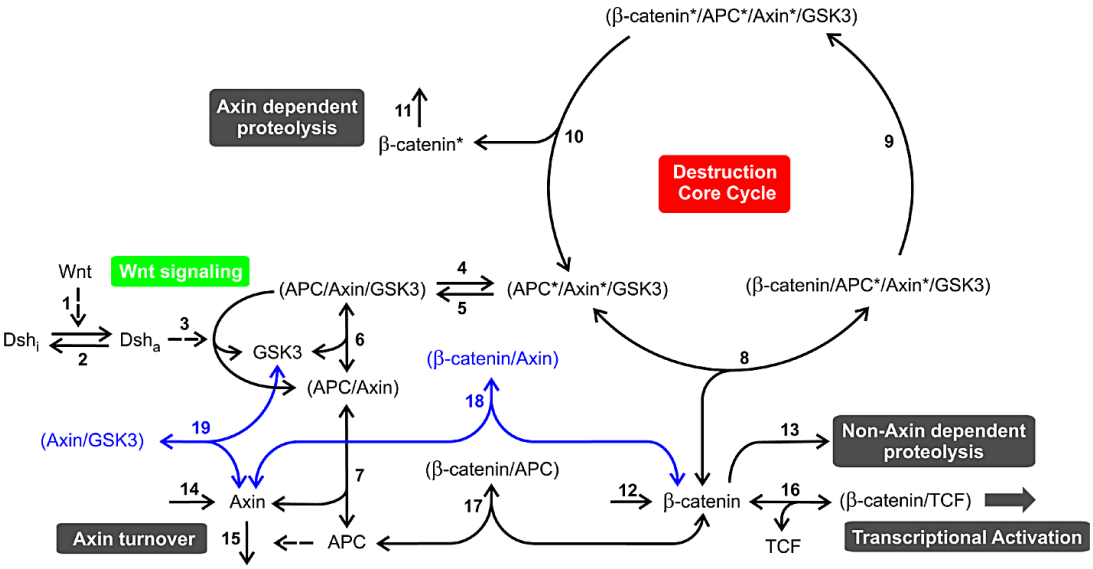

Figure 2.4: Network diagram for the model of Lee *et al.* [161], originally published by PLOS Biology and provided under a Creative Commons Attribution Licence, *CC-BY-2.5*. Protein complexes are enclosed in parentheses and labelled according to their component parts; phosphorylated agents are denoted with an asterisk. Arrows indicate the direction of reaction.

and/or compartmental approaches favoured by other models of the pathway [155]. Extracellular Wnt stimuli induce cytoplasmic signalling in Lee *et al.*'s model via *Dsh*, which is assumed to exist in both active and inactive forms.

The inherent difficulties in obtaining many biological parameters demand estimation of much of the parameter set. *In vitro* experiments on *Xenopus* oocytes provide values for six concentrations and three parameters; the remaining thirty-one parameters are either estimated from existing results in the biological literature, or adjusted to calibrate the model's numerical output against experimentally measured fluxes. However, a recent recalibration of the Lee *et al.* model for several human and canine cell lines [162] suggests that higher Axin and lower APC concentrations are required when applying the model in a mammalian context.

Numerical simulations of the Lee *et al.* model suggest that Axin, present in *Xenopus* at a substantially lower concentration than other components of the destruction

complex, acts as a rate-limiter in β-catenin degradation [161]. As such, it has been thought to provide a robust and effective means of regulating the strength of Wnt signalling within a cell [161]. Consistently low Axin levels may also serve to regulate crosstalk between Wnt and other pathways, by stabilising the levels of other members of the destruction complex such as APC and GSK3β, which might otherwise interact with other networks [163, 161].

A computational evaluation of the *Xenopus*-parametrised model of Lee *et al.*, performed by Goentoro *et al.* [164], has found the fold-change in β-catenin to be the most robust feature to parameter perturbations, given a fixed Wnt stimulus. By contrast, the absolute expression of β-catenin varies markedly in response to parameter perturbations. Robustness in fold-change may act as a means of overcoming biological noise, buffering the pathway's response against small fluctuations in rates and concentrations. Goentoro *et al.* also confirm these findings experimentally in human colorectal cell lines, which demonstrate a fold-change sensitivity to the synthesis rate of β-catenin [164].

Several systematic analyses of the Lee *et al.* model have yielded reductions to smaller ODE systems. Kruger and Heinrich [165] employ a series of conservation equations and fast equilibrium approximations to reduce the system to seven variables. The concentration of the β-catenin-TCF complex is found to be sensitive to fluctuations in the system parameters; this may result in the Wnt pathway becoming transcriptionally active even in the absence of extracellular stimulation. More recently, the asymptotic analyses of Mirams *et al.* [166] have separated the Lee *et al.* model into short, medium and long-term timescales. This has revealed conditions under which the model may be reduced to a single equation for β-catenin, capturing the long-term dynamics of the system. Nonetheless, Lloyd-Lewis *et al.* [160] highlight a conflict between the Mirams *et al.* estimate of $\sim 45h$ for this long-term timescale and that of Hernandez *et al.* [167], in which the half-life of active β-catenin is experimentally

measured at ~ 16 min.

Modifications to Lee *et al.* have captured other known properties of the biochemical network. Wawra *et al.* [168] formulate the model as a system of delay differential equations. Inspired by other model extensions which depict Axin as both a transcriptional target and inhibitor of the Wnt pathway [169, 158], two Wnt targets are added to the network, both inhibitors of Wnt signalling: Axin, and a hypothetical regulator which inhibits the action of *Dsh*. The resultant negative feedback loops generate oscillations in β-catenin, with period ranging from 2.5 to 6 hours according to the Axin and β-catenin flux through the system. The existence of oscillatory regimes in the Wnt system may provide a means of temporal coordination for its crosstalk with the Notch pathway, which also has a capacity for oscillation.

2.2.2 Alternative Biochemical Models

Mazemondet *et al.* [170] formulate a model involving only Wnt, Axin (phosphorylated and unphosphorylated) and β-catenin (nuclear and cytoplasmic). Stochastic and deterministic versions of the model explore the phenomenon of surges in Wnt expression after the differentiation process is complete. A compartmental approach is also employed by Schmitz *et al.* [171] to show that shuttling of the destruction complex between cytoplasm and nucleus may extend the persistence of the β-catenin-TCF complex and hence increase the strength of Wnt signalling on its transcriptional targets.

The thirteen-ODE system of Kogan *et al.* [172] focuses on the bound and free forms of the membrane-bound receptors Frizzled and LRP, in order to explore the influence of the pathway inhibitors *Dkk* and *sFRP*. Simulations indicate that combinations of the two inhibitors can produce a synergistic effect in reducing β-catenin accumulation, a finding which may have therapeutic implications for the treatment of CRC.

Other ODE models for Wnt biochemistry include Benary *et al.* [173], who compare

a 'minimal' model with a gene-expression augmented version under Wnt and APC gradients, and Song *et al.* [174], who examine the effects of mutations to APC and β-catenin.

2.2.3 Crypt Embeddings

Wnt signalling models have also been embedded into geometric models of the colorectal crypt, allowing the influence of spatial variation in the local tissue environment to be explored computationally.

van Leeuwen *et al.* [175] use a cell-based model of the crypt to carry out virtual microdissection and labelling experiments, studying problems such as niche succession. Cell type is defined on the basis of spatial location in the crypt, via an imposed gradient of the extracellular factor Wnt.

Mirams *et al.* [176] extend these simulations to study how the adhesion and location of mutant cells affect the capacity of a rogue progeny to dominate the crypt. Spatial proliferation cues are assumed via a Wnt gradient up the crypt; cells are endowed with a simple, stochastic cell cycle model; and mutant cells have a reduced adhesion and cell-cycle time, implemented through a variable threshold for proliferative cut-off. Results indicate that an ancestor cell need not remain in the crypt for monoclonal conversion to occur. Another extension of the van Leeuwen *et al.* framework has been used to show that the spatial 'stem cell niche' hypothesis is more likely than a stochastic generational model of stem cell division [177]. Spatially-determined cell fate selection significantly reduces the time taken to attain a monoclonal state and extension of the model's geometry to incorporate a rounded crypt base brings this time closer to experimentally observed values.

The continuum model of Murray *et al.* [22] explores the influence of spatially varying morphogen gradients upon cell density in the colorectal crypt. A one-dimensional partial differential equation (PDE) for cell density incorporates a 1D continuum ap-

proximation of the spring based mechanical model from [175] to describe cell movement up the crypt. An external Wnt gradient is defined which decays exponentially up the crypt axis, and is coupled to the cellular proliferative response by incorporating a single-equation reduction of Lee *et al.* [166] into the PDE. The model can predict the likely β-catenin distribution up the crypt from a given external Wnt gradient, by tracking the rate of change of local $\beta-$catenin. Under this model, cells proliferate if their local Wnt concentration exceeds a threshold and if the local cell density is sufficiently low. Mutations are simulated through parameter modification in the underlying Wnt model, allowing mutants to proliferate in lower Wnt conditions than healthy cells. Density tracking of mutant and healthy cells predicts colonisation of neighbouring crypts when the mutant population has both a proliferative advantage and an ability to evade apoptosis. A proliferative advantage alone is not enough, as mutant cells cannot achieve a sufficiently high velocity to invade neighbouring crypts.

A continuum approach to modelling the crypt is also adopted by Zhang *et al.* [178], who find that the scales of Wnt activation and inhibition may result in a Turing pattern [179] which could determine the dispersal of cell types in the crypt.

2.3 Tools and Software

The simulation of cell-based tissues with embedded biochemical models requires several software resources. All software used in this thesis is listed below, along with details of the algorithms employed. This leads naturally into the details of implementation at the cell and tissue scales, which are discussed in Section 2.4.

Chaste

Chaste (Cancer, Heart and Soft Tissue Environment) is an open-source software library and set of test suites for computational biologists, developed for the design and running

of multicellular tissue simulations [180]. These simulations may include user-defined specifics at the level of: subcellular reactions; whole-cell behaviour; cell-cell interaction or tissue-level function. *Chaste* is written in C++ and has a modularised, object-oriented structure.

Ordinary differential equations governing subcellular function are solved using a multistep solver from the external library CVODE [181]. Owing to the stiff system involved in our Notch-Wnt model, we implement Backward Differentation Formulas in fixed-leading coefficient form. Each integration step is solved using Newton iteration. Implementation specifics of tissue-scale processes in *Chaste* are detailed in Section 2.4.

We use *Chaste* in Chapters 5 and 6 and Appendix B to: explore a full crypt embedding of our model with an alternative model developed by Buske *et al.* [5]; simulate multicellular embeddings of our own subcellular model; to develop point dispersal metrics; and to construct multicellular embeddings of the Collier model.

Matlab and the Systems Biology Toolbox

MATLAB is a commercial software package for numerical computation, written in *C* but providing a high-level MATLAB language at the user front-end. All MATLAB calculations are performed using version *R2013a* of the software. These include: all two-cell studies (Ch. 4; Ch. 6; Appx. B), numerical studies of ordinary differential equations (Ch. 4; Appx. B) and data postprocessing for line and surface graphs (Chs. 4 – 6; Appx. B).

Numerical solution of ordinary differential equations in MATLAB uses the software's own suite of solvers. This includes algorithms for the solution of stiff ODEs, in which the presence of components varying over slow and fast timescales can cause numerical artefacts when using a regular solver. Consequently:

- Nonstiff problems are solved using the `ode45` solver, which implements an explicit Runge-Kutta $(4, 5)$ formula [182]. `ode45` uses the solution at $y(t_{n-1})$ to calculate

estimates at four increments within the stepsize interval. A weighted average of these values yields the value of $y(t_n)$;

- We employ the solver `ode15s` on stiff problems. This is a multistep, variable order solver: that is, it uses solutions from more than one previous timepoint to calculate the solution at the current time. Its algorithm is based upon the numerical differentiation formulas [182].

The *Systems Biology Toolbox* (SBT) is an add-on module for MATLAB [183] and is used for parameter sensitivity analyses in Chapter 4. Its methods for calculating parameter sensitivities for either oscillatory or fixed steady-state systems are described in Appendix A.

Chemical Reaction Network Toolbox

The *Chemical Reaction Network Toolbox* is a computational package for analysing the stability properties of chemical reaction networks, indicating whether a given network is capable of multiple stable states, or only one [184]. Chemical network representations differ from biological ones, which depict up- and down-regulation events but do not explicitly detail the chemical interactions involved.

The toolbox requires the user to specify the details of each reaction in the network of interest. Each inclusion takes the form $\mathrm{A} + \mathrm{B} \xrightarrow{\mathrm{E}} 2\,\mathrm{C} + \mathrm{D}$, where A and B are the reactants, C and D are the products, and E is either an inhibitor or a promoter of the reaction. The user has to provide stoichiometry information; for instance, specifying $2\,\mathrm{C}$ rather than just C as a product in the above example. However, the kinetics of each reaction do not need to be specified. Once the user has supplied details of all the reactions, the toolbox performs a sign-checking operation on two quantities derived from the network's stoichiometry [185] and then classifies the network according to its ability to exhibit multistationarity if allied with particular types of kinetics.

The toolbox is used in Chapter 4 to explore the stability of subgraphs in the Notch-Wnt reaction network; we therefore defer our explanation of the theory which supports this toolbox until Section 4.2. A detailed exposition of the algorithms underpinning the toolbox can be found in [185].

2.4 Tissue Scale Modelling

Armitage and Doll presented one of the earliest mathematical studies of cancer in the 1950s, with a statistical analysis of the age distribution of mutations in different organ systems [186, 187]. Ultimately this led to the linear model of carcinogenesis, involving sequential acquisition of mutations over an extended time period (discussed further in Section 1.4). These statistical approaches yielded estimates for the mutation rates in CRC, but could not explain its propagation throughout the colonic epithelium, owing to the absence of biophysical mechanisms. This created a demand for models of healthy crypt tissue, which could then be manipulated to address the problem of tumourigenesis.

Mathematical crypt models can be classified into one of three types.

Compartment models examine the behaviour of interdependent cell populations in the crypt but do not anchor these in a spatial domain [25]. Examples include Tomlinson and Bodmer's three-compartment model [188], which decomposes the crypt into stem, transit and differentiated compartments, each with fixed rates of death, differentiation and renewal. Extensions to this model have added stochastic fluctuations of renewal parameters [189], looked at the role of feedback between compartments in propagating mutations [190], and provided separate compartments for each cell generation in order to study cell cycle phase transitions [191].

Continuum models typically use systems of partial differential equations to charac-

terise the quantities of interest at all points in the tissue region, although some one-dimensional examples use ODEs [192]. Continuum models for the intestinal crypt have: developed means of studying the path of malignant cell clusters in the crypt [193]; examined compressibility and buckling of the epithelial cell layer [194] and compared their outputs against discrete analogues [195, 196].

Discrete models rely upon the representation of individual cells: this assumes that the dynamics of cell movement can be adequately described by a finite number of forces, protein concentrations and other quantities evaluated at a set of points in the domain. This class of model can be divided into two sub-types:

- *Lattice-based models*, in which cells are constrained to move on a fixed lattice. These include cellular automata (CA) and the cellular Potts model (CPM). CA represent each cell by a single lattice point and the rules for lattice updating may include such considerations as defining a cell's neighbourhood – and hence the nearby sites into which a cell can move – and defining a cell's probability of dividing or moving in a certain direction. CA have been studied in one [197, 198, 199] and two dimensions [200, 24, 201]. In a progression from the pointwise approach of CA, cells in the CPM are comprised of multiple, usually clustered, lattice points on a grid. Wong *et al.* [41] apply the CPM to the crypt, but the model proves highly sensitive to its starting configuration.
- *Off-lattice models*, which do not restrict cells to a predefined lattice and which may also allow the shape or position of the cell boundaries to evolve over time. This subclass of model is discussed further in Section 2.4.1.

Distinct modelling approaches may also yield different insights: not every model is appropriate for a given scenario. A full discussion of these issues is provided in the reviews [202, 203]. Our interest in cell fate selection in response to spatial cues naturally

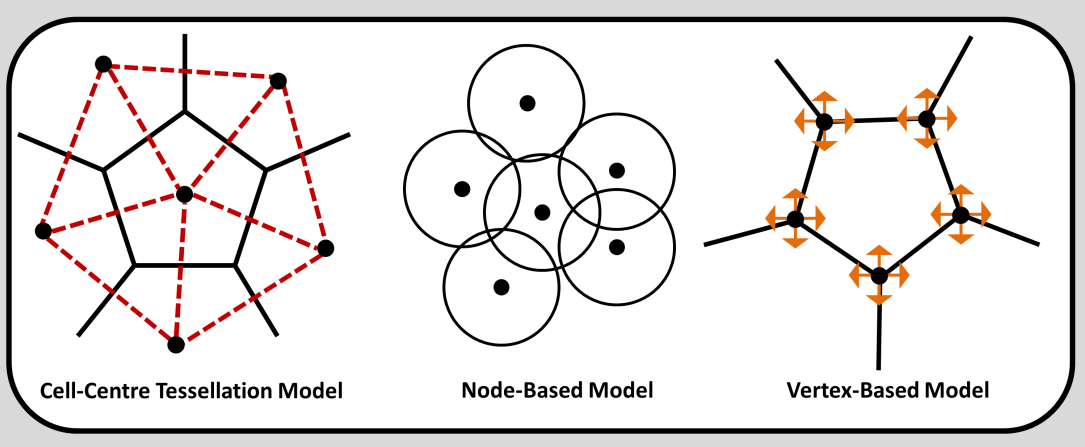

Figure 2.5: L-to-R: Cell-centre tessellation model, with cells formed from a Delaunay triangulation (red) and Voronoi tessellation (black); Cell-centre node-based model, with cells formed from overlapping spheres; Vertex dynamic model, in which cells are formed from a polygonal tessellation with moving vertices (orange).

leads us to use discrete, cell-based models. Moreover, the off-lattice models provide a more realistic representation of the packing and movement of cells within the crypt geometry. Consequently we restrict our attention to the three off-lattice approaches provided in Chaste, which we now describe.

2.4.1 Tissue Modelling in Chaste

All *Chaste* simulations in this thesis use one of three tissue-level models: *cell-centre tessellation based*, *cell-centre node based*, or *vertex based*. In each case, growth processes are modelled over a series of piecewise continuous timesteps, via an explicitly defined cell cycle model (CCM). This CCM may take the form of a discretised 'clock' or a more sophisticated series of continuous differential equations; we describe our CCM implementation fully in Chapter 5.

Cell-Centre Tessellation Model

In cell-centre dynamic models, the centrepoint of the cell entirely determines its location, as, for example, in Meineke *et al.* [204]. Cells move on a lattice-free surface and it is assumed that the motion of each cell can be adequately described by a finite number of forces, which arise from the interaction between a cell and its immediate neighbours.

Connectivity between cells is determined by forming a *Delaunay triangulation* comprising the lines between cell centres. This triangulation is then used to generate the cell boundaries by means of a *Voronoi tessellation*. The resulting polygonal lattice therefore defines the shape of the cell, as well as the location of its geometric centre. Elastic and adhesive interactions between cells are modelled by springs connecting the centres of adjacent cells; such an approach permits explicit mechanical control of cell motion. The cell-centre tessellation approach has led to several crypt-specific computational studies of note [175, 204, 195].

Implementation of the cell-centre method in *Chaste* updates each cell's position at a given timestep using the triangulation and tessellation methods described above. The total force, $\mathbf{F_i}$, on a cell, i, at time t, is calculated from the individual forces arising from connections with its neighbours, $j \in S_i$:

$$\mathbf{F}_i(t) = \sum_{j \in S_i} k_{ij}(|\mathbf{r}_i - \mathbf{r}_j| - s_{ij}(t)) \frac{(\mathbf{r}_j - \mathbf{r}_i)}{|\mathbf{r}_j - \mathbf{r}_i|}, \quad i = 1, \ldots, n, \tag{2.5}$$

where all quantities are defined in Table 2.2. The assumption of strong frictional forces between neighbouring cells implies that viscous forces dominate, allowing inertial influences to be neglected. The effective displacement of a cell over a small time

interval, Δt, is therefore an overdamped motion, governed by the drag coefficient, μ_i:

$$\begin{aligned} \mathbf{r}_i(t+\Delta t) &= \mathbf{r}_i(t) + \frac{1}{\mu_i}\mathbf{F}_i(t)\Delta t\,, \\ \frac{\mu_i(\mathbf{r}_i(t+\Delta t) - \mathbf{r}_i(t))}{\Delta t} &= \mathbf{F}_i(t)\,. \end{aligned} \tag{2.6}$$

As $\Delta t \to 0$ in (2.6), and substituting (2.5) for $\mathbf{F}_i(t)$, we obtain:

$$\mu_i \frac{d\mathbf{r}_i}{dt} = \sum_{j \in S_i} k_{ij}(|\mathbf{r}_i - \mathbf{r}_j| - s_{ij}(t))\frac{(\mathbf{r}_j - \mathbf{r}_i)}{|\mathbf{r}_j - \mathbf{r}_i|}, \quad i = 1, \ldots, n. \tag{2.7}$$

A typical cell representation for this cell-centre model is depicted on the left-hand side of Figure 2.5.

Parameter	**Specified Property**
$\mathbf{r}_i$	Spatial location of cell centre i
n	Total number of cells in the domain
k_{ij}	Strength of spring connecting cells i and j
$s_{ij}(t)$	Natural length of the spring connecting cells i and j
μ_i	Drag coefficient for cell i (dependent upon cell type)
t	Time
S_i	Set of cells neighbouring cell i

Table 2.2: A reference summary of the parameters for the off-lattice cell-centre model presented in [204].

Node-Based Model

The *cell-centre node-based model* uses the same force formulation as that of the cell-centre tessellation framework in Equation (2.7), but relies on an *overlapping spheres* method to determine cell connectivity, rather than the triangulation method of the cell-centre tessellation model [205]. This removes the requirement for regenerating the spatial mesh at each timestep and reduces the time required for simulation.

In this approach, cells are considered to interact if they lie sufficiently close, according to some predefined distance. In practice this is determined by the overlap, δ_{ij},

of the cell radii:

$$\delta_{ij} = R_i + R_j - \parallel r_i - r_j \parallel,$$

for R_i, R_j the predefined 'natural' radii of the two cells and $\parallel r_i - r_j \parallel$ their separation distance at the current timestep.

A typical cell representation for the node-based model is shown at the centre of Figure 2.5.

Vertex-Dynamic Model

In the vertex-dynamic model, a cell is defined by a series of moving points on its boundary and the free energy at these vertices is quantified through terms for deformation, surface tension and intercellular adhesion. Vertex models have been applied to crypt structures to a lesser extent than cell centre models, although some cases exist in the literature [195]. Polygonal tessellations generated by the vertex approach aim to replicate the packing arrangement of the intestinal crypt.

Our implementation of the vertex-dynamic model in *Chaste* employs the *Nagai-Honda model* [206], in which vertex movement is determined by

$$\begin{aligned}\eta_i \frac{d\mathbf{r_i}}{dt} &= -\nabla_i \sum_{j=1}^{n} (U_D^j + U_S^j + U_A^j), \\ &= -\nabla_i \sum_{j=1}^{n} \left(\alpha (A_j - A_{T,j})^2 + \beta (C_k - C_{T,j})^2 + \sum_{m=1}^{M_j} \gamma_m L_{j,m} \right),\end{aligned}$$

where all parameters are as stated in Table 2.3. A typical cell construction for this model is shown in the right-hand image of Figure 2.5. Alternatives to the Nagai-Honda model exist and are also provided within *Chaste*; these are discussed extensively in Fletcher *et al.* [207].

Parameter	Specified Property
$\mathbf{r}_i$	Spatial location of vertex i
η_i	Drag associated with vertex i
∇_i	Gradient w.r.t. $\mathbf{r}_i$
n	Total number of cells in the domain
U_D^j	Deformation energy for cell j
U_S^j	Membrane surface tension energy for cell j
U_A^j	Cell-cell adhesion energy for cell j
A_j	2D area of cell j
$A_{T,j}$	Target area of cell j
C_j	Perimeter of cell j
$C_{T,j}$	Target perimeter of cell j
M_j	Number of vertices on cell j
$L_{i,j}$	Straight-line distance between vertices i and j
α, β	Weighting constants for contributing energy terms
γ_m	Positive constant determined by site of external boundaries

Table 2.3: A reference summary of the parameters for the off-lattice, vertex-dynamic cell model presented in Nagai and Honda [206] and Osborne *et al.* [195].

2.5 Discussion

The extent to which the intestinal epithelium and the Notch and Wnt pathways have been explored in the experimental literature is apparent from the breadth of studies presented in Chapter 1. That these efforts have been matched by considerable interest from the mathematical and computational communities suggests that an investigation of Notch-Wnt crosstalk is not only timely but also scientifically relevant.

Furthermore, the majority of studies discussed in the review of Chapter 2 rely on rule-based representations of the Notch and Wnt pathways, or implement them as uncoupled subcellular models. Often, the resultant distribution of cell types fails to capture the true dispersal seen in the intestine [5, 139]. The development of a coupled model for Notch-Wnt interaction will allow us to assess whether such non-representative dispersal is a direct consequence of an oversimplified model of cell fate, and should provide insights into modelling approaches for differentiation processes.

Sections 2.3 and 2.4 have introduced the software used in this thesis and outlined

the modelling techniques they use in representing cell-based tissues. These techniques will be implemented from Chapter 4 onwards in exploring problems of biological relevance.

With these foundations now in place, we turn our attention to developing an ODE model of Notch-Wnt interaction in Chapter 3.

Part B

Model Development

3

A Coupled Model of Notch-Wnt Interaction

Chapter Summary

Using key results from the experimental literature, we develop a novel system of twelve ordinary differential equations (ODEs) to characterise the interaction between the Notch and Wnt networks.

Although the Collier model [125] discussed in Chapter 2 provides a useful depiction of the Notch feedback mechanisms arising from juxtacrine signalling at the cell surface, it cannot provide insights into crosstalk events between the Notch and Wnt pathways, since these occur inside the cell. An extended model depicting subcellular Notch and Wnt reactants is therefore required if we are to examine this interplay.

Our own ODE model, which we develop over the course of this chapter, unites diverse experimental results, some of which are being represented mathematically for the first time. We start in Section 3.1 by detailing the molecular entities involved; a diagram of the biological network is shown in Figure 3.1. Section 3.2 sees each path in the network justified with reference to the experimental literature, before these are realised as a dimensional system of twelve ordinary differential equations in Section 3.3. This system will be used in later chapters to study proliferation and cell fate specification in tissue-scale simulations.

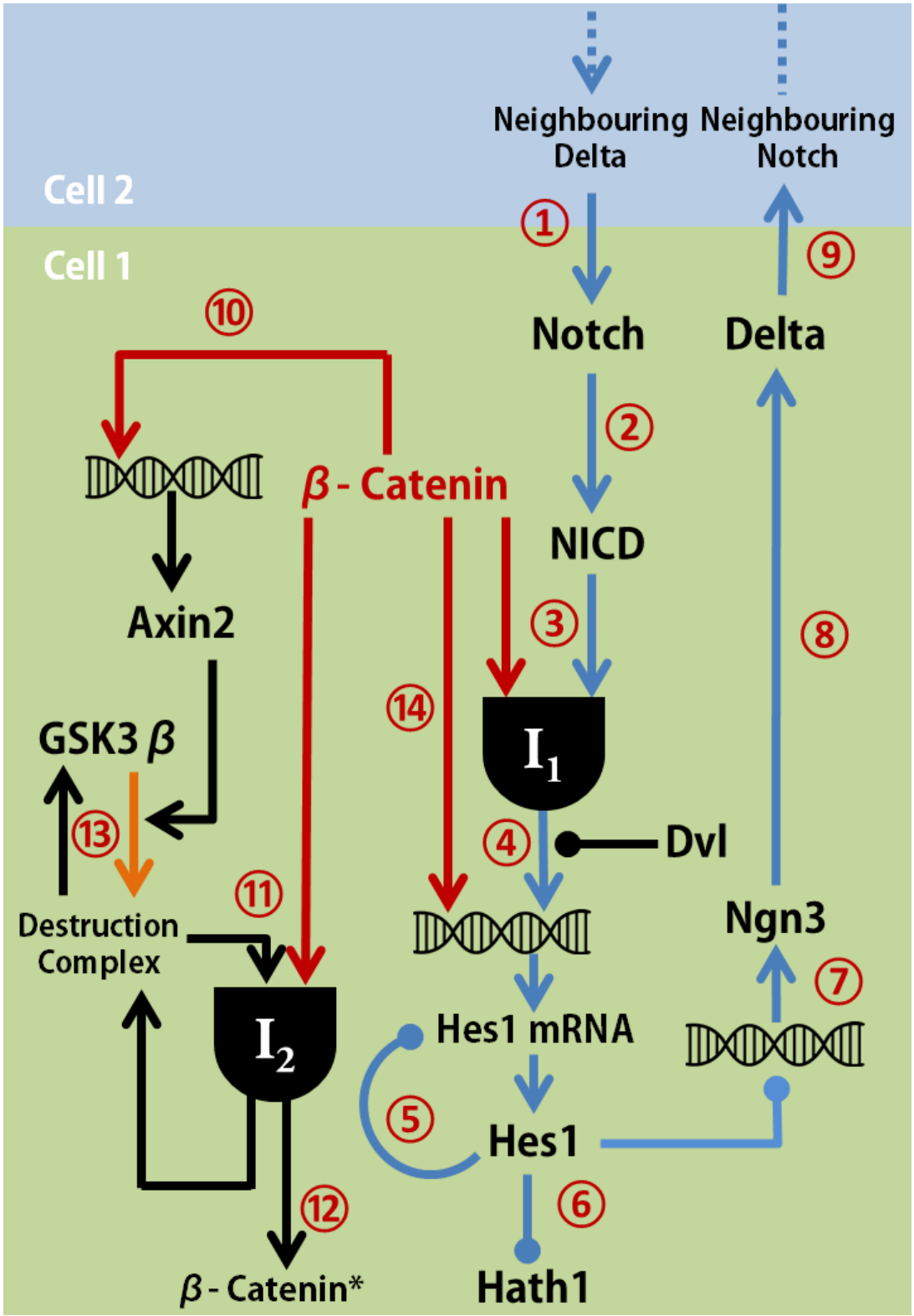

Figure 3.1: Network representation for our model of Notch-Wnt interaction: numbered steps are justified in the text in Section 3.2. Major steps in Notch function are shown in blue; those of the Wnt pathway in black; those involving the β-catenin crosstalk hub in red; Wnt-dependent steps in orange. Black AND gates signify the formation of intermediate complexes from two molecular partners. Circular end caps indicate inhibition steps; gene regulation events are indicated by DNA symbols.

3.1 Model Entities

The molecular entities in the model, depicted in Figure 3.1, are listed below; letters in parentheses indicate the variable name as it appears in our ODE model as presented in Section 3.3. Experimental evidence for the roles of these reactants is provided in Section 3.2.

Notch (N) refers to the Notch receptor, a long molecule anchored in the cell membrane and comprising a long section of EGF repeats extending outward from the membrane, linked to a shorter section which lies inside the cell [69]. In a departure from the model of Collier *et al.* [125], which deliberately avoided classifying Notch as being membrane bound or cytoplasmic, we here take N to represent the membrane-bound receptor only.

NICD (F) is a molecular fragment called the Notch Intra-Cellular Domain and is formed during cleavage of the Notch receptor, when the internal section of the receptor is released into the cytoplasm.

$\mathbf{I_1}$ (I_1) represents a molecular intermediate, formed from a complex of NICD and β-catenin.

Hes1 (H_1) is the *Hairy Enhancer of Split*, a name deriving from its association with bristle development in the *Drosophila* fruit fly [208] and body segmentation in insects and mammals [209]. Hes1 exhibits diverse patterns of expression in many different tissues and its incorporation in a model requires careful attention to the literature. For example, differences are apparent even between cell types in the nervous system, where boundary cells have persistent, high Hes1 expression, compared to a more variable production in compartmental cells [210]. Hes1 is considered to be a major target of Notch signalling and has a key role in cell fate specification, with Hes1-null tissue containing fewer absorptive enterocytes [92].

Ngn3 (P) is part of the Neurogenin family of proteins, associated with differentiation processes and, in some contexts, neural development, hence the term '*proneural protein*' in reference to neurogenins [211].

Delta ligand (D) is a complementary binding partner for Notch and similarly takes the form of an extracellular transmembrane protein [69]. As with our definition of N, all instances of D in our coupled model refer specifically to membrane-bound ligand.

Hath1 (H_2) is the human variant of a protein known as Atoh1 or Math1 in other organisms, and is confined to the lower gastrointestinal tract in humans [115]. Hath1 is strongly associated with control of differentiation processes [212]; indeed, high Hath1 levels have been shown to inhibit production of cyclin D1, thus pushing the cell into $G0$ phase [93]. High Hath1 expression is associated with a secretory cell phenotype, resulting in mucus-secreting goblet cells [115, 213]. Malignant colon tissue, in which Hath1 is suppressed, features fewer goblet cells than its healthy counterparts [115]. Application of γ-secretase inhibitors, which block cleavage of the Notch receptor and reduce Notch signalling, can enforce differentiation of proliferative crypt cells into goblet types [214]. Hath1 expression varies along the gut; human colonic tissue exhibits higher levels of Hath1 mRNA than tissue taken from earlier stages of the intestinal tract, such as the jejunum or ileum [213].

β-catenin (B) is a key effector of the canonical Wnt pathway and actively regulates the transcription of cell cycle proteins such as cyclin D [113]. As such, β-catenin is closely associated with proliferation events although, as the discussion of Section 3.2 will show, it also acts as a major crosstalk hub with other networks such as Notch.

GSK3β (G) is a protein kinase involved in the canonical Wnt pathway.

Destruction Complex (C) is formed under low-Wnt conditions, when cytoplasmic GSK3β binds with the proteins Axin2 and APC (in the interest of simplicity, the latter is not represented explicitly in our model). This destruction complex ubiquitinates β-catenin, ultimately leading to its proteasomal degradation [215].

Axin2 (A) is a gene target of the Wnt pathway; its transcription is upregulated by β-catenin, yet it also has a role in the degradation of β-catenin by acting as a scaffold protein for the β-catenin destruction complex [216, 97].

$\mathbf{I_2}$ (I_2) represents a molecular intermediate, formed from a complex of β-catenin and GSK3β when the cell is subject to a low degree of Wnt stimulation.

Having outlined the function of the main reactants in our model, we shall now justify our inclusion of the fourteen interactions depicted in Figure 3.1 with reference to the experimental literature.

3.2 Experimental Evidence

Our coupled model for Notch-Wnt interaction draws on a great deal of experimental work from current scientific literature. We now present the references which form the foundations of our model development. Each step in Figure 3.1 has been enumerated for clarity.

(1) **Neighbouring Delta binds to Notch:** A membrane-bound Delta ligand on a signalling cell can bind with a Notch receptor on a neighbouring cell [84], initiating a series of reactions in the latter cell which constitute a *Notch signalling cascade* [67]. Multiple forms of Delta have been identified, although it is not yet clear how their functions differ [69]. A further class of ligands, Jagged (Serrate in non-human mammals), is also complementary for Notch [217] and, like Delta, consists of a series of EGF repeats and a terminal DSL domain which mediates

binding [218]. For simplicity, we consider only Delta as the binding partner in our model; nor do we distinguish between the three distinct types of Delta ligand known to exist in mammals [69].

(2) **Fragmentation of the Notch ligand:** Ligand-receptor binding between Delta and Notch induces three cleavage events in the Notch ligand, known as $S2$, $S3$ and $S4$ [218]. These cleavages at the cell membrane are in part mediated by an enzyme complex, γ-secretase, and cause the internal NICD fragment to be released into the cytoplasm [91]. These three cleavages are treated as a single event in our model.

(3) **NICD forms a complex with β-catenin:** Direct binding of NICD with β-catenin is a key point of Notch-Wnt crosstalk. This interaction has been identified in vascular progenitor cells via reporter gene and immunoprecipitation studies, in which expression of NICD and/or β-catenin were activated [219]. NICD-β-catenin binding has also been demonstrated *in vitro* in human kidney cells [220]. NICD-mediated sequestering of β-catenin may provide a switching mechanism in the canonical Wnt pathway by diverting β-catenin from regulating Wnt target genes [220].

(4) **Transcriptional regulation of Hes1:** Following on from the evidence for Step (3), the study by Yamamizu *et al.* [219] demonstrates a synergy between NICD and β-catenin which amplifies the effect on the Hes1 promoter. A threefold increase in Hes1 promoter activity is observed in cells expressing both NICD and β-catenin, compared to those expressing NICD alone [219]. This upregulation has also been observed in human kidney cells [221], human colon cells [77] and murine fibroblasts [220]. *In vitro* studies of hamster ovarian cells identify Dishevelled as a key effector of Notch regulation at this point in the network, by measuring changes in Notch response when either Wnt, Dsh or β-catenin

production is induced [222]. Expression of either Wnt or Dsh results in a 0.4− to 0.5−fold change in Notch activity, yet expression of β-catenin results in a 1.2−fold change. Immunoprecipitation studies on the same cell line have confirmed the direct binding of Dsh to RBP-Jκ complexed with NICD. The same study also showed that blocking the Dsh signal allows human neuroblastoma lines to avoid Notch downregulation in the face of a Wnt stimulus [222].

(5) **Autoinhibition of Hes1:** Hes1 protein is known to dimerise and bind to its own promoter, thereby negatively regulating its own expression [223, 224, 225]. This motif is highly conserved between species, borne out by molecular analyses, *in vitro* and *in vivo* studies in mice [223, 226, 142], rats [227, 142] and *Drosophila* [223], amongst others. This autoinhibition causes oscillations in the levels of Hes1 mRNA and protein and has been addressed by Hirata *et al.* [142], who identify an oscillation period of around two hours in a variety of cell lines and estimate the half-lives of the mRNA and protein to be around 24.1 and 22.3 minutes respectively.

(6) **Hes1 destabilises Hath1:** Gene expression analyses on the gut tissue of Hes1-knockout mice have identified downregulation of Math1 by Hes1 [78, 214, 92, 228]. Tissue samples from the knockouts show elevated numbers of secretory cells, typically associated with Hath1 expression [78, 214]. Conversely, activation of Notch signalling (and hence Hes1 expression) in the murine gut [92] and in human CRC cell lines [229] represses the transcription of Math1/Hath1 and impairs the formation of goblet cell types. Whether this behaviour is more apparent in the early digestive tract [78] or prevalent throughout the gut [214] remains uncertain.

(7) **Hes1 downregulates Ngn3:** Hes1 binds directly to the Ngn3 promoter, thereby blocking its activity [78], although a destabilisation action of Hes1 on Ngn3 has

also been postulated [79]. This downregulation has been observed *in vitro* in mouse fibroblasts [230], *in vivo* in the murine gut [78, 230, 92], and has been further confirmed through sequence analyses of the Ngn3 promoter in humans and mice [230]. Hes1-mutant mice embryos have been shown to exhibit premature neuronal differentation, associated with increased expression of the Neurogenin protein family [231]; conversely, Ngn3-null mice exhibit diminished differentiation capacity in their intestinal cells [232]. Hes1-knockout, adult mice show an elevated expression of Ngn3 in the gut [228]. Experiments on human liver cells estimate the half-life of Ngn3 to be around 30 minutes [79].

(8) **Ngn3 upregulates Delta:** Upregulation of the Delta gene, *Dll*1, by Ngn3 has been demonstrated in the mouse pancreas, through microarray analysis of Ngn3-inducible cell lines [81, 82] and coexpression studies [79]. This pattern of action also appears to be highly conserved in non-mammalian species including *Xenopus* [211].

Steps (7) and (8) together link the strength of the Notch signal inversely with that of Delta expression. Cells of the murine intestine which test null for Hes1 also have high Delta expression [78]; similarly, Math1(+/+) mice have low Hes1 levels and express more Delta [90].

(9) **Delta binds to neighbouring Notch ligand:** This step is justified on the same grounds as Step (1) above; however, we note that the reaction cascade running from Notch to Delta via Hes1 in a given cell serves to downregulate Delta when a cell is expressing high levels of Notch. For this reason we would generally expect either Step (1) or Step (9) to dominate in any one cell, in cases where the cascade is driving lateral inhibition or cell type segregation.

(10) **Axin2 upregulated by Wnt signalling:** Axin2 is a scaffold protein and has a role in the action of the destruction complex on β-catenin [216, 97]. It is

also transcriptionally upregulated by β-catenin and as such forms a negative feedback loop, serving to regulate the Wnt pathway [216]. Induction of Axin2 in response to Wnt exposure has been documented in cell lines from mice [216], rats [233, 216] and human colon cancer [233].

(11) **Destruction complex binds to β-catenin:** Under low Wnt levels, GSK3β is present in complexed, rather than free, form, and (along with the proteins Axin2 and APC) is a key component of a destruction complex that binds to β-catenin and labels it for degradation [96, 234]. For the purposes of our model, we only represent a general "destruction complex" rather than accounting for its composite parts, and model the transition of GSK3β between the complexed and non-complexed states as a reversible reaction, $G \rightleftharpoons C$. This may be an oversimplification, given assertions in the literature that the concentration of Axin2 within the complex may have a central role in regulating the rate of this step in *Xenopus* oocytes [161]; however, *in vitro* experiments suggest that this is not the case for mammalian cell lines [162]. Although vesicular shuttling of GSK3β is believed to play an important role in the coordination of Wnt signalling [235], our ODE model is non-compartmental and therefore does not distinguish between the various sequestered forms of GSK3β.

(12) **Ubiquitination of β-catenin and subsequent degradation:** This process of β-catenin regulation is well described in the literature. Once β-catenin is bound to the destruction complex, its serine and threonine residues are phosphorylated [234], which ultimately leads to its ubiquitination and destruction by the proteasome [236].

(13) **Destruction complex formation:** GSK3β aggregates with other proteins under low Wnt levels, forming a destruction complex that binds to β-catenin and labels it for degradation [96, 234]. Under high Wnt levels, this complex is largely

disaggregated, yielding an increase in cytoplasmic β-catenin. Consequently, the ratio of the forward reaction $G \to C$ to that of the reverse reaction $C \to G$ is higher when the Wnt stimulus is low, and lower when the Wnt stimulus is high.

(14) **β-catenin directly upregulates Hes1:** Peignon *et al.* [77] have identified complementary binding sites on the β-catenin molecule and Hes1 promoter and infer direct regulation of Hes1 levels by β-catenin. This occurs independently of the Notch-dependent mechanism described in reaction (4) above.

3.2.1 Further Comments

The experimental findings detailed in Section 3.2 address Wnt-mediated control of Notch signalling via both β-catenin and Dishevelled. Examples of Notch regulating Wnt have been observed in *Drosophila*, such that activation of Notch near a compartment boundary induces expression of Wnt signalling molecules [237]; however, the complexity of the network in Figure 3.1, and our chosen focus on the mammalian gut, lead us to omit this interaction for now. Given that Wnt-Notch crosstalk occurs in both the upstream and downstream sections of each pathway, modification of downstream processes may offer a useful approach to treating CRC. Stabilisation of Hath1 might be advisable [77], in addition to the upstream γ-secretase inhibition typical of many existing clinical treatments. Exploration of this hypothesis remains a long-term goal of this work.

β-catenin is also involved in the direct upregulation of the ligand Jagged1; other ligands are also upregulated, but through secondary processes rather than active binding to a promoter [77]. In the interest of clarity, we shall consider only the Delta ligand in this model.

Finally, autoregulation appears to be a feature of both the Notch and Wnt pathways, whether through the transcriptional autoinhibition of Hes1, the negative feedback loop containing Axin2, or the extended positive feedback loop from Notch (ul-

timately) onto itself. These motifs could potentially generate oscillations or act as bistable switches; it is intended that our network model will be able to provide some insights into how and when these motifs influence the crosstalk between Notch and Wnt.

3.3 Dimensional System

We now present our dimensional system of ODEs for the Notch-Wnt interaction network, starting with the Notch pathway, allied with a simple model of Wnt signalling. We adopt a slight abuse of notation in these equations, such that the letter denoting reactant X is also used to signify "the concentration of reactant X", which would more conventionally be written as $[X]$.

The system comprises twelve equations: six for the Notch pathway, four for the Wnt pathway, and two intermediate complexes which either mediate interactions between the two pathways (I_1) or which respond to the strength of extracellular Wnt signalling to regulate the level of active β-catenin in the cell (I_2). Listings for the variables can be found in Table 3.1, while the parameters are listed in Table 3.2.

Throughout this model, we represent the extracellular Wnt stimulus by a time-dependent, nondimensional quantity, $W(t)$. For now we refrain from specifying the form of W (e.g. constant, pulsatile/oscillatory).

Labelling Conventions

Our ODE model for Notch-Wnt interaction adopts the following labelling conventions for variables and parameters:

- *Time* is written as either t (dimensional) or τ (nondimensional);
- *Exponents* are indicated by the lower-case Arabic letters, m and n;

Variable	Description	Units	Scaling
t	Time	min	$\tau = \mu_N t$
N	Membrane-bound Notch receptor	nM	$N = \frac{\theta_1}{\mu_N} N'$
F	Notch Intracellular Domain (NICD)	nM	$F = \frac{\theta_1}{\mu_F} F'$
H_1	Hes1	nM	$H_1 = \frac{\xi_2}{\mu_{H_1}} H_1'$
P	Ngn3	nM	$P = \frac{\xi_3}{\mu_P} P'$
D	Delta ligand	nM	$D = \frac{\theta_4}{\mu_D} D'$
H_2	Hath1	nM	$H_2 = \frac{\xi_5}{\mu_{H_2}} H_2'$
G	GSK3β	nM	$G = \frac{\theta_1}{\mu_G} G'$
C	Destruction complex	nM	$C = \frac{\theta_1}{\mu_C} C'$
B	Active β-catenin	nM	$B = \frac{\theta_1}{\mu_N} B'$
A	Axin2	nM	$A = \frac{\theta_6}{\mu_A} A'$
I_1	Intermediate 1 (NICD/β-catenin)	nM	$I_1 = \frac{\theta_1}{\mu_{I_1}} I_1'$
I_2	Intermediate 2 (GSK3β/β-catenin)	nM	$I_2 = \frac{\theta_1}{\mu_{I_2}} I_2'$

Table 3.1: Variable listings for our coupled Notch-Wnt model as described in Section 3.3. The independent variable, time, is presented first, followed by the twelve dependent variables representing the reactants in the network.

- *Variables* are written as upper-case Arabic letters (e.g. A, B, C);
- *Functions* are written using upper-case Greek letters (e.g. Ψ, Φ, Θ);
- *Parameters* are represented in the lower-case Greek alphabet (e.g. μ, θ, ξ).

Nondimensional variables and parameters are indicated by the dash notation $'$, except where specified otherwise.

Intermediate formation

The pathway diagram of Figure 3.1 incorporates two AND gates, each representing complexes between protein entities in the reaction network. In each case we have assumed a 1-1 stoichiometry, in the absence of evidence to the contrary in the literature:

- Binding of β-catenin and NICD to form I_1: $B + F \rightleftharpoons BF\,(= I_1)$;
- Binding of the destruction complex to β-catenin to form I_2: $B + C \rightleftharpoons BC\,(= I_2)$.

Equilibrial constants for these reactions are not available in the literature; however, given the strong experimental evidence for such binding, we make the simplifying assumption of dominant fast forward kinetics and reduce the reaction schemes to $B + F \to I_1$ and $B + C \to I_2$. A first-order mass action law is then used to derive the reaction rates for intermediate formation, namely $\alpha_1 B \cdot F$ and $\alpha_3 B \cdot C$. The subsequent dissociation of these intermediates adopts a simple linear form, with decay rate constants μ_{I_1} and μ_{I_2} respectively.

Wnt- and Axin2-Dependence

Several rates within our model depend on the strength of the extracellular Wnt stimulus, $W(t)$ and/or the cellular Axin2 levels, $A(t)$.

In particular, β-catenin destruction regulated by the canonical Wnt pathway relies upon the state of equilibrium of $G \rightleftharpoons C$. Owing to its dependence upon the local Wnt stimulus and the cellular Axin2 levels, we abbreviate the rate function for the forward reaction to $\Psi_{W,A}$.

The functional form of $\Psi_{W,A}$ has been informed by steady-state analyses on the decoupled, Wnt-only system, outlined in Section 4.1.2. The approach has been to select the simplest function which ensures agreement with known properties of the biochemical system at steady-state (for example, the response of particular reactant concentrations to Wnt stimulation). Values for the exponents and multiplying parameter have been determined by matching the Wnt response of the system to the experimental data of Hernández *et al.* [167], as described in Section 4.3.

We therefore suppose the forward reaction to be Wnt- and Axin2-dependent, of

rate

$$\Psi_{W,A} = \Psi(W(t), A(t)) \equiv \frac{1.4A(t)^2}{1 + (1 + W(t))^4} \,. \tag{3.1}$$

That is, the rate increases with Axin2 levels and decreases with Wnt stimulus. The reverse reaction $C \to G$ is assumed to occur at constant rate μ_C.

As discussed in Section 3.2, the transcription of Hes1 is inhibited by Dishevelled. For simplicity we do not represent Dsh explicitly. Given that Dsh activity is high when the Wnt stimulus is high, we simply scale the transcription of Hes1 according to a Wnt-dependent function, which we denote Ψ_W:

$$\Psi_W = \Psi(W(t)) \equiv \frac{\sigma_K}{\sigma_K + W(t)} \,, \tag{3.2}$$

where σ_K is an inhibition constant to be specified. Ψ_W attenuates the expression of Hes1 in response to a strong extracellular Wnt stimulus.

3.3.1 Notch Pathway Submodel

The use of Hill-type and hyperbolic functional forms in this model has been influenced by a four-component, non-delay model by Shepherd [238], which is itself an adaptation of a delay model due to Momiji and Monk [145], discussed in Section 2.1.4. The model by Shepherd is capable of generating oscillations from a non-delay formulation and can be solved numerically without recourse to more complicated delay solvers.

Production of Notch receptor, N, incorporates a similar Hill-form production term to that suggested by Shepherd [238] and Collier *et al.* [125]. The linear decay term represents the fragmentation of Notch to release NICD:

$$\frac{dN}{dt} = -\mu_N N + \underbrace{\frac{\theta_1 \bar{D}^{m_1}}{\kappa_1^{m_1} + \bar{D}^{m_1}}}_{\text{Steps } (1) \text{ and } (9)} \,, \tag{3.3}$$

where $\bar{D}$ is the mean Delta level expressed by neighbouring cells and μ_N the rate constant of ligand fragmentation. The Hill function has dissociation constant κ_1, maximal rate θ_1 and Hill coefficient m_1.

The Notch Intracellular Domain (NICD) is a fragment, F, of the original membrane-bound Notch ligand, N; its production is assumed to scale with the rate of Notch fragmentation, as $\alpha_{\text{frag}}\mu_N N$. The nondimensional constant α_{frag} represents the proportion of Notch which results in generation of NICD; it is determined in Chapter 4 via parameter fitting against experimental data. $\alpha_{\text{frag}} < 1$ acknowledges that loss of Notch in Equation (3.3) is due to natural decay as well as to the NICD fragmentation process. The rate of removal of NICD is assumed to depend on the rate at which it binds with β-catenin, as described in Section 3.3, along with a small decay component:

$$\frac{dF}{dt} = -\mu_F F + \underbrace{\alpha_{\text{frag}}\mu_N N}_{\text{Step } (2)} - \underbrace{\alpha_1 B \cdot F}_{\text{Step } (3)}, \tag{3.4}$$

where μ_F, α_1 are rate constants for NICD decay and β-catenin/NICD binding respectively.

NICD forms an intermediate, I_1, with β-catenin; its formation requires the presence of both entities. We therefore model the production rate using the first-order law of mass action and assume linear decay. Both of these steps are justified in Section 3.3:

$$\frac{dI_1}{dt} = -\mu_{I_1} I_1 + \underbrace{\alpha_1 B \cdot F}_{\text{Step } (3)}, \tag{3.5}$$

where μ_{I_1} is the rate constant for dissociation of the intermediate.

Hes1, H_1, is subject to three separate sources of transcriptional regulation, namely β-catenin, I_1, and H_1, as depicted in Figure 3.1. Transcription of Hes1 is assumed to have a maximal rate, ξ_2. β-catenin and I_1 each upregulate Hes1 transcription and their respective actions on the Hes1 promoter are modelled as Hill functions in

Equation (3.6). These two entities are assumed to have an additive effect upon the promoter[1]. The relative contributions of I_1 and B to the upregulation are described by the non-negative, nondimensional constants θ_2, θ_7 and the sum of the two Hill functions is constrained to lie in the range $[0, 1]$, by imposing the restriction $\theta_2 + \theta_7 = 1.0$. Hes1 transcription is also modulated by Hes1 autorepression, which is modelled by a hyperbola in H_1, with exponent n_2 and inhibition constant σ_2. Combining these assumptions with linear decay of Hes1, we derive the following ODE for evolution of Hes1:

$$\frac{dH_1}{dt} = -\mu_{H_1} H_1 + \Psi_W \left(\underbrace{\frac{\theta_2 I_1^{m_2}}{\kappa_2^{m_2} + I_1^{m_2}}}_{\text{Step } (4)} + \underbrace{\frac{\theta_7 B^{m_7}}{\kappa_7^{m_7} + B^{m_7}}}_{\text{Step } (14)} \right) \underbrace{\frac{\xi_2 \sigma_2^{n_2}}{\sigma_2^{n_2} + H_1^{n_2}}}_{\text{Step } (5)}, \tag{3.6}$$

where μ_{H_1} is the rate constant of Hes1 decay. The Hill functions decribing the actions of B and I_1 on the Hes1 promoter have exponents m_2, m_7 and Hill coefficients κ_2, κ_7.

Proneural protein, P, is transcriptionally inhibited by Hes1. Its synthesis is therefore modelled by a hyperbola in H_1, with maximal rate ξ_3, exponent n_3 and inhibition constant σ_3. Linear decay of Ngn3 is also assumed. This yields the following equation for evolution of proneural protein:

$$\frac{dP}{dt} = -\mu_P P + \underbrace{\frac{\xi_3 \sigma_3^{n_3}}{\sigma_3^{n_3} + H_1^{n_3}}}_{\text{Step } (7)}, \tag{3.7}$$

where μ_P is the rate constant of Ngn decay.

The rate of change of Delta ligand, D, is modified from the analogous Collier *et al.* [125] expression, akin to the approach of the Shepherd model [238], such that the production term depends upon the proneural protein, P. Synthesis of Delta is modelled

[1]The decision to combine the two upregulation effects by an additive law is the result of extensive discussion with experimental collaborators, and is further supported by the separate promoter binding sites known to exist for I_1 and β-catenin [77].

by a Hill form in P, with maximal rate θ_4, Hill coefficient m_4 and dissociation constant κ_4.

$$\frac{dD}{dt} = -\mu_D D + \underbrace{\frac{\theta_4 P^{m_4}}{\kappa_4^{m_4} + P^{m_4}}}_{\text{Step } (8)}, \tag{3.8}$$

where μ_D is the rate of linear decay of Delta.

We consider Hath1 to be downstream of Hes1 and therefore label it H_2. Hath1 production is inhibited by Hes1, yielding a fractional synthesis term with maximal rate ξ_5, exponent n_5 and inhibition constant σ_5. Linear decay of Hath1 is assumed, with rate constant μ_{H_2}:

$$\frac{dH_2}{dt} = -\mu_{H_2} H_2 + \underbrace{\frac{\xi_5 \sigma_5^{n_5}}{\sigma_5^{n_5} + H_1^{n_5}}}_{\text{Step } (6)}. \tag{3.9}$$

H_2 decouples from the rest of the system; we retain Equation (3.9) nonetheless, as it will be required in later work to specify cell fate once the ODE model is embedded in a cell population.

3.3.2 Wnt Pathway Submodel

First we present the equation for GSK3β. Loss of GSK3β arises partly from linear decay and partly from transfer to the β-catenin destruction complex, C. Growth terms are associated with Wnt-dependent production and freeing of GSK3β from the destruction complex.

$$\frac{dG}{dt} = -\mu_G G + (1 + W(t))\alpha_2 + \underbrace{\mu_C C - \alpha_5 \Psi_{W,A} G}_{\text{Step } (13)}, \tag{3.10}$$

where μ_G is the rate constant of decay of G, μ_C the rate of dissociation of the destruction complex C and α_5 the rate constant for GSK3β incorporation into the destruction complex. The term $(1 + W(t))\alpha_2$ represents the Wnt-dependent rate of GSK3β production[2].

The destruction complex, C, is also dependent on rates $\Psi_{W,A}$ and μ_C, but in the reverse manner to that of Equation (3.10). The latter two terms in Equation (3.11) represent: the release of C from the intermediate complex, I_2; and a mass-action rate for binding with β-catenin:

$$\frac{dC}{dt} = \underbrace{-\mu_C C + \alpha_5 \Psi_{W,A} G}_{\text{Step } (13)} + \mu_{I_2} I_2 - \underbrace{\alpha_3 B \cdot C}_{\text{Step } (11)}, \tag{3.11}$$

where α_3 is the rate constant of $B - C$ binding and μ_{I_2} the rate constant of decay of I_2.

The regulation of β-catenin, B, is subject to the two binding reactions that form the intermediates I_1, I_2, yielding the evolution equation

$$\frac{dB}{dt} = -\mu_B B + (1 + W(t))\alpha_4 - \underbrace{\alpha_1 B \cdot F}_{\text{Step } (3)} - \underbrace{\alpha_3 B \cdot C}_{\text{Step } (14)}, \tag{3.12}$$

where $(1+W(t))\alpha_4$ represents a background production rate of β-catenin[3]. The latter two terms relate to the respective rates of formation of the intermediate complexes outlined in Section 3.3. β-catenin is also assumed to undergo linear decay, with rate constant μ_B.

As with the other intermediate, the rate of formation of I_2 is assumed to follow

[2]The functional form of $(1 + W)\alpha_2$ has been determined using steady-state analyses of the decoupled, Wnt-only system, detailed in Section 4.1.2. This reflects the simplest function which yields characteristic, qualitative steady-state behaviour for GSK3β.

[3]Just as for the background rate of production of GSK3β, the background rate of β-catenin production has been suggested by steady-state analysis of the decoupled Wnt system, choosing the simplest function which yields realistic steady-state behaviour.

first-order mass action kinetics, whilst its decay rate is linear, with rate constant μ_{I_2}. That is,

$$\frac{dI_2}{dt} = -\mu_{I_2} I_2 + \underbrace{\alpha_3 B \cdot C}_{\text{Step } (11)} . \tag{3.13}$$

Our final reactant is Axin2, A. Synthesis of Axin2 is assumed to exhibit a Hill function dependence upon B, with maximal rate θ_6, Hill coefficient m_6 and dissociation constant κ_6, while its decay is assumed to be linear, with rate constant μ_A:

$$\frac{dA}{dt} = -\mu_A A + \underbrace{\frac{\theta_6 B^{m_6}}{\kappa_6^{m_6} + B^{m_6}}}_{\text{Step } (10)} . \tag{3.14}$$

Although phosphorylated β-catenin is formed during the dissociation of I_2, its evolution is assumed to have no bearing on the rest of the system, as the phosphorylated form is subsequently degraded by the proteasome, without participating in any other reactions. Consequently our model does not explicitly account for the evolution of phosphorylated β-catenin.

3.3.3 Network Motifs

Network motifs can often aid us in understanding the function or likely outcomes of a system of reactants. In our Notch model, for example, the path leading from Notch to Hes1 and back to Notch via activity in neighbouring cells provides an extended *positive feedback loop*, allowing Notch to stimulate its own upregulation in the long term. Such behaviour typically yields a sigmoidal response curve and can also drive bimodal variation in a population [239]. As such, it is a suitable mechanism for cell fate selection.

Motifs can also provide insights into our representation of Wnt and Notch crosstalk.

For example, β-catenin upregulates Hes1 via two different routes. The first of these is a direct upregulation on the Hes1 promoter, while the action mediated via I_1 provides an indirect activation. This structure serves as a *coherent type 1 feed-forward loop* [240], in which both branches of the loop achieve activation, but through different effectors. Such a motif commonly acts as a persistence detector, which could enable Hes1 transcription to be briefly maintained if the signal from β-catenin were stopped [239].

3.4 Nondimensionalised System

Our initial ODE system given by Equations (3.3) - (3.14) was presented in dimensional form; we shall now nondimensionalise it. Nondimensionalisation is routinely performed to reduce the number of parameters in the system and to facilitate estimation of the relative importance of the different reactions within the network. Table 3.2 lists the parameters in our ODE model, along with their units and the scalings applied in the nondimensionalisation.

In Section 3.3, we observed that Equation (3.9) for Hath1 decouples from the rest of the system. Nonetheless, the concentration of Hath1 will later be required to determine cell fate in tissue embeddings of the model and so we retain Equation (3.9) in the following rescaling.

Time is scaled against μ_N^{-1}, the timescale for decay of the Notch receptor; we define a nondimensional time, τ, such that $\tau = \mu_N t$. Over the course of nondimensionalisation, we also introduce a group of parameters labelled ν_X, for X a given reactant. These represent decay ratios with Notch; that is, $\nu_X = \frac{\mu_X}{\mu_N}$. Nondimensionalised equivalents for the dependent variables can be found in Table 3.1.

	Parameter	Units	Scaling
Dissociation Constants	κ_1	nM	$\kappa_1 = \frac{\theta_4}{\mu_D}\kappa_1'$
	κ_2	nM	$\kappa_2 = \frac{\theta_1}{\mu_{I_1}}\kappa_2'$
	κ_4	nM	$\kappa_4 = \frac{\xi_3}{\mu_P}\kappa_4'$
	κ_6	nM	$\kappa_6 = \frac{\theta_1}{\mu_N}\kappa_6'$
	κ_7	nM	$\kappa_7 = \frac{\theta_1}{\mu_N}\kappa_7'$
Inhibition Constants	σ_2	nM	$\sigma_2 = \frac{\xi_2}{\mu_{H_1}}\sigma_2'$
	σ_3	nM	$\sigma_3 = \frac{\xi_2}{\mu_{H_1}}\sigma_3'$
	σ_5	nM	$\sigma_5 = \frac{\xi_2}{\mu_{H_1}}\sigma_5'$
	σ_K	dim'less	-
Decay Constants	General μ_X	min^{-1}	-
Decay Ratios	General $\nu_X = \frac{\mu_X}{\mu_N}$	dim'less	-
Maximal Rates	θ_i, $i = 1, 4, 6$	nM min^{-1}	-
	θ_i, $i = 2, 7$	dim'less	-
	ξ_i, $i = 2, 3, 5$	nM min^{-1}	-
Other Rate Constants	α_1	$\text{nM}^{-1}\text{min}^{-1}$	$\alpha_1 = \frac{\mu_N^2}{\theta_1}\alpha_1'$
	α_2	nM min^{-1}	$\alpha_2 = \theta_1\alpha_2'$
	α_3	$\text{nM}^{-1}\ \text{min}^{-1}$	$\alpha_3 = \frac{\mu_N^2}{\theta_1}\alpha_3'$
	α_4	nM min^{-1}	$\alpha_4 = \theta_1\alpha_4'$
	α_5	$\text{nM}^{-1}\ \text{min}^{-1}$	$\alpha_5 = \frac{\mu_G\mu_A}{\theta_6}\alpha_5'$
	α_{frag}	dim'less	-
Exponents	m_i, $i = 1, 2, 4, 6, 7$	dim'less	-
	n_i, $i = 2, 3, 5$	dim'less	-

Table 3.2: Parameters for the coupled Notch-Wnt ODE model presented in Section 3.3.

$$\frac{dN'}{d\tau} = -N' + \frac{\bar{D}'^{m_1}}{\kappa_1'^{m_1} + \bar{D}'^{m_1}}, \tag{3.15}$$

$$\frac{dF'}{d\tau} = \nu_F \left\{ -F' + \alpha_{\text{frag}} N' - \frac{\alpha_1'}{\nu_F} B' \cdot F' \right\}, \tag{3.16}$$

$$\frac{dI_1'}{d\tau} = \nu_{I_1} \left\{ -I_1' + \frac{\alpha_1'}{\nu_F} B' \cdot F' \right\}, \tag{3.17}$$

$$\frac{dH_1'}{d\tau} = \nu_{H_1} \left\{ -H_1' + \Psi_W \left(\frac{\theta_2 I_1'^{m_2}}{\kappa_2'^{m_2} + I_1'^{m_2}} + \frac{\theta_7 B'^{m_7}}{\kappa_7'^{m_7} + B'^{m_7}} \right) \frac{\sigma_2'^{n_2}}{\sigma_2'^{n_2} + H_1'^{n_2}} \right\}, \tag{3.18}$$

$$\frac{dP'}{d\tau} = \nu_P \left\{ -P' + \frac{\sigma_3'^{n_3}}{\sigma_3'^{n_3} + H_1'^{n_3}} \right\}, \tag{3.19}$$

$$\frac{dD'}{d\tau} = \nu_D \left\{ -D' + \frac{P'^{m_4}}{\kappa_4'^{m_4} + P'^{m_4}} \right\}, \tag{3.20}$$

$$\frac{dH_2'}{d\tau} = \nu_{H_2} \left\{ -H_2' + \frac{\sigma_5'^{n_5}}{\sigma_5'^{n_5} + H_1'^{n_5}} \right\}, \tag{3.21}$$

$$\frac{dG'}{d\tau} = \nu_G \left\{ -G' + C' + (1 + W(\tau))\alpha_2' - \alpha_5' \Psi_{W,A'} G' \right\}, \tag{3.22}$$

$$\frac{dC'}{d\tau} = \nu_C \left\{ -C' + I_2' + \alpha_5' \Psi_{W,A'} G' - \frac{\alpha_3'}{\nu_C} B' \cdot C' \right\}, \tag{3.23}$$

$$\frac{dB'}{d\tau} = \nu_B \left\{ -B' + (1 + W(\tau))\alpha_4' - \frac{\alpha_1'}{\nu_F} B' \cdot F' - \frac{\alpha_3'}{\nu_C} B' \cdot C' \right\}, \tag{3.24}$$

$$\frac{dI_2'}{d\tau} = \nu_{I_2} \left\{ -I_2' + \frac{\alpha_3'}{\nu_C} B' \cdot C' \right\}, \tag{3.25}$$

$$\frac{dA'}{d\tau} = \nu_A \left\{ -A' + \frac{B'^{m_6}}{\kappa_6'^{m_6} + B'^{m_6}} \right\}. \tag{3.26}$$

For brevity, we hereafter drop the dash notation from our nondimensional variables. For the meantime, all representations of variables and parameters are assumed to refer to the nondimensional version unless otherwise stated.

3.5 Concluding Remarks

Equations (3.15)–(3.26) form our nondimensional ODE system for modelling the interaction between the Notch and Wnt pathways. This chapter has focused on the construction of, and justification for, each element of the reaction network and ODE model, and for this reason we have avoided discussion of the numerical values for parameters and concentrations. Similarly, we defer the definition of Delta averaging – $\bar{D}$ in Equation (3.3) or $\bar{D}'$ in Equation (3.15) – until later, when we address two-cell simulations of the model in Chapter 4, and multicellular embeddings in Chapter 5.

Before the system can be applied in a multicellular setting, it first needs to be analysed, parametrised and calibrated against experimental data. All of these tasks will be performed in Chapter 4. In the meantime, full parameter and concentration listings for our Notch-Wnt ODE model, as well as suggested initial conditions, can be found in Tables A.1 to A.5 of Appendix A.

In the next chapter, the Notch and Wnt components will be decoupled and analysed separately in two-cell simulations. This enables us to confirm the behaviour of each pathway and to ascertain the effects of crosstalk once the system is again considered as a whole.

4 Analysis of the Notch-Wnt Model

Chapter Summary

Mathematical analysis of the model presented in Chapter 3 demonstrates a good qualitative match with known features of the corresponding biological system. Comparison of the numerical output against experimental results facilitates estimation of the model's parameters, allowing us to perform preliminary investigations of its behaviour in a two-cell system.

If the effects of Notch-Wnt crosstalk in our system are to be fully comprehended, we must first examine the two pathways separately. To this end, the Notch and Wnt modules of the ODE system described by Equations (3.15) – (3.25) will now be decoupled for separate analysis.

4.1 Dynamical Analyses

4.1.1 Notch-Only System

Decoupling Notch from Wnt leaves the coloured components of Figure 4.1, represented by the ODEs (4.1) – (4.7). For clarity, we abbreviate the Hill functions and hyperbolas

as follows:

$$\Phi_i(X) = \frac{X^{m_i}}{\kappa_i^{m_i} + X^{m_i}}, \quad \Theta_i(X) = \frac{\sigma_i^{n_i}}{\sigma_i^{n_i} + X^{n_i}},$$

where all parameters are defined as in Table 3.2 and $X \equiv X(\tau)$ is a reactant concentration in the system at time τ. Since Φ is monotonic increasing and Θ monotonic decreasing on $\mathbb{R}^+$, it follows that $\Theta'(X) < 0 < \Phi'(X)$, $\forall X \in \mathbb{R}^+$, where $'$ denotes the derivative with respect to X. To simplify analysis further, we initially restrict attention to the homogeneous case, for which the cell population evolves in a uniform state. Consequently the Delta average $\bar{D}$ over neighbouring cells can be replaced with D in Equation (4.1).

Although the Notch module defined below has been decoupled from the Wnt system, β-catenin still features at points where crosstalk would usually occur. B is therefore treated as an input parameter throughout the Notch-only analysis. Under these assumptions, the nondimensional, homogeneous sub-system can be expressed as:

$$\frac{dN}{d\tau} = -N + \Phi_1(D), \tag{4.1}$$

$$\frac{dF}{d\tau} = \nu_F \left\{ -F + \alpha_{\text{frag}} N - \frac{\alpha_1}{\nu_F} B \cdot F \right\}, \tag{4.2}$$

$$\frac{dI_1}{d\tau} = \nu_{I_1} \left\{ -I_1 + \frac{\alpha_1}{\nu_F} B \cdot F \right\}, \tag{4.3}$$

$$\frac{dH_1}{d\tau} = \nu_{H_1} \left\{ -H_1 + \Psi_W \Big(\theta_2 \Phi_2(I_1) + \theta_7 \Phi_7(B) \Big) \Theta_2(H_1) \right\}, \tag{4.4}$$

$$\frac{dP}{d\tau} = \nu_P \left\{ -P + \Theta_3(H_1) \right\}, \tag{4.5}$$

$$\frac{dD}{d\tau} = \nu_D \left\{ -D + \Phi_4(P) \right\}, \tag{4.6}$$

$$\frac{dH_2}{d\tau} = \nu_{H_2}\Big\{ - H_2 + \Theta_5(H_1)\Big\}. \tag{4.7}$$

The complexity of Equations (4.1) – (4.7) prohibits their systematic analysis. Equation (4.7) for the evolution of Hath1 readily decouples from the other Notch entities and will be temporarily omitted until Section 4.2.

Reduction to Four Equations

Assuming B to be a constant input parameter yields linearity in the steady states of (4.2) and (4.3). This guides us to suppose that $\nu_F, \nu_{I_1} \gg 1$, such that F and I_1 can be assumed linearly proportional to N[1]. That is, $F = \gamma N$ and $I_1 = \omega F = \eta N$, where $\gamma, \omega, \eta \in \mathbb{R}^+$. Under this assumption, the Notch-only model reduces to four ODEs:

$$\frac{dN}{d\tau} = -N + \Phi_1(D), \tag{4.8}$$

$$\frac{dH_1}{d\tau} = \nu_{H_1}\Big\{ - H_1 + \Psi_W\Big(\theta_2\Phi_2(\eta N) + \theta_7\Phi_7(B)\Big)\Theta_2(H_1)\Big\}, \tag{4.9}$$

$$\frac{dP}{d\tau} = \nu_P\Big\{ - P + \Theta_3(H_1)\Big\}, \tag{4.10}$$

$$\frac{dD}{d\tau} = \nu_D\Big\{ - D + \Phi_4(P)\Big\}. \tag{4.11}$$

The system (4.8) - (4.11) represents an extended version of Momiji *et al.*'s network [145], but without the positive feedback on P. However, the Momiji *et al.* framework involves only two components (analogous to H_1 and P), as its main objective is to examine the role of feedback loops in lateral inhibition.

Although our model utilises similar feedback motifs, its objectives are different:

[1]This reduction is performed to facilitate analysis of the system dynamics. This approach is suggested by the structure of Equations (4.2) and (4.3), which do not involve the functions Φ, Θ and can hence be solved at steady state to yield I_1 in terms of N.

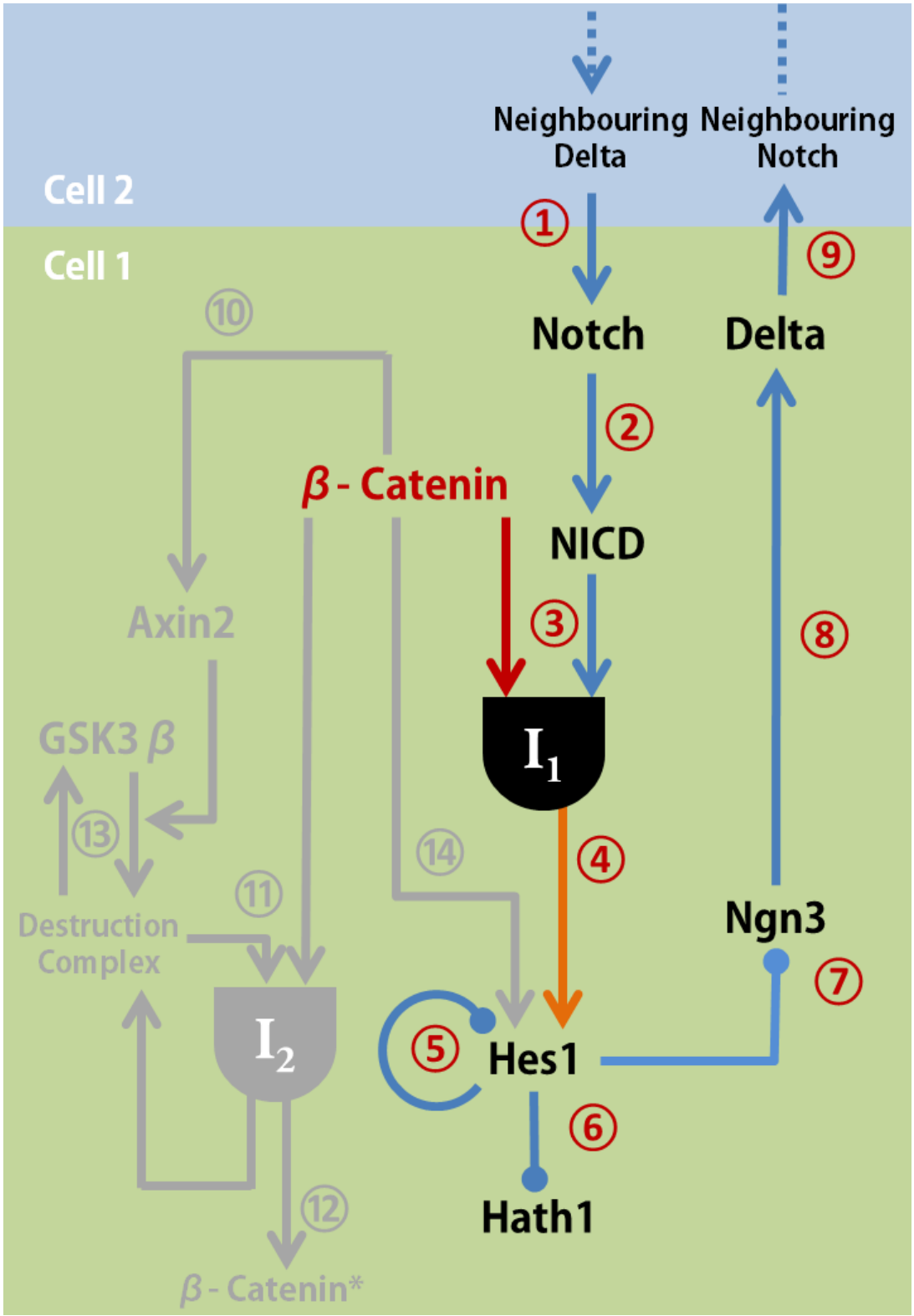

Figure 4.1: Schematic of the reactions involved in the Notch-only system of Equations (4.1) – (4.7). The reactions involved are the same as described in Chapter 3; however, DNA events have been removed from the depiction to aid clarity.

additional components are required in our model to study the intervention of β-catenin and Wnt at distinct points between the initiation of a Notch cascade at the cell surface and the transcriptional regulation of Hes1 in the nucleus. The emphasis which our model places on the ratio of Notch to Wnt intervention in regulating Hes1 transcription represents a key development with regard to the literature.

Steady State Analysis

Steady states of the system (4.8) - (4.11) are obtained by setting $\frac{d}{d\tau} = 0$ in each evolution equation; this enables us to eliminate N, P and D and obtain the following implicit expression for the steady state concentration of Hes1, $H_1 = H^*$ say:

$$H^* = \Psi_W\Big(\theta_2\Phi_2(\eta\Phi_1 \circ \Phi_4 \circ \Theta_3(H^*)) + \theta_7\Phi_7(B)\Big)\Theta_2(H^*)\,. \tag{4.12}$$

Since Φ_i is an increasing and Θ_i a decreasing function for $H^* \in \mathbb{R}^+$,$\forall i$, the composition $\Phi_2(\eta\Phi_1 \circ \Phi_4 \circ \Theta_3(H^*))$ is decreasing in $\mathbb{R}^+$. The right-hand side of (4.12) is therefore a decreasing, positive-valued function of H^* on $\mathbb{R}^+$, because $\Phi(x), \Theta(x) > 0$ for $x > 0$. Equality with the left-hand side, which is trivially increasing in H^*, guarantees the existence of a unique biologically realistic steady state for Hes1.

Linear Stability Analysis

Linear stability analysis can be used to explore the dynamical response of the four-component Notch system to small perturbations. Taking the system (4.8) – (4.11), we construct its Jacobian matrix $J = \left[\frac{\partial a_i}{\partial b_j}\right]$, in which the $(i,j)^{th}$ component is the partial derivative of the i^{th} evolution equation, a_i, with respect to the j^{th} variable, b_j.

Eigenvalues λ of the linearised system are the solutions to $|J - \lambda I| = 0$, for I the

identity matrix. This yields the following characteristic polynomial in λ:

$$|J - \lambda I| = \quad \lambda^4 + J_3\lambda^3 + J_2\lambda^2 + J_1\lambda + J_0\,, \tag{4.13}$$

where

$$\begin{aligned}
J_3 =& \Big\{1 + \nu_H y + \nu_P + \nu_D\Big\}\,,\\
J_2 =& \Big\{\nu_P\nu_D + \nu_P + \nu_D + (\nu_D + \nu_P + 1)\nu_H y\Big\}\,,\\
J_1 =& \Big\{\nu_D\nu_P + (\nu_D\nu_P + \nu_D + \nu_P)\nu_H y\Big\}\,,\\
J_0 =& \nu_D\nu_P\nu_H y - \nu_H\nu_P\nu_D\Psi_W\Phi_1'(D)\Phi_2'(\eta N)\Theta_2(H)\Theta_3'(H)\Phi_4'(P)\,,
\end{aligned}$$

and where

$$y = (1 - \Psi_W(\theta_2\Phi_2(\eta N) + \theta_7\Phi_7(B))\Theta_2'(H))\,.$$

Given that $\theta_7 = 1 - \theta_2$, θ_2 encapsulates the ratio of $B : I_1$-mediated action upon the Hes1 promoter and features heavily in the eigenvalue equation (4.13). Figure 4.2 shows the influence of θ_2 upon the eigenvalues λ.

The system has four eigenvalues. Observation of these in a non-negative range, as shown in Figure 4.2, suggests the existence of two negative reals, and a pair of complex conjugates with negative real part. Negativity of the real parts of all four eigenvalues generates stable steady states in the system.

The complex conjugate eigenvalues arise from a supercritical Hopf bifurcation in θ_2, visible on the lower-right plot of Figure 4.2. That this occurs for $\theta_2 = 0$ suggests that the action of β-catenin upon the Hes1 promoter serves to stabilise Notch and dampen oscillations. Figure 4.3 shows the steady state values for Hes1 in the nondimensional

system. At lower levels of B, Hes1 steady states increase with the amount of Notch-mediated transcriptional control (i.e. high θ_2 values). Sufficiently high β-catenin expression forces Hes1 into a lower steady state and can overcome the strength of Notch-mediated Hes1 promotion.

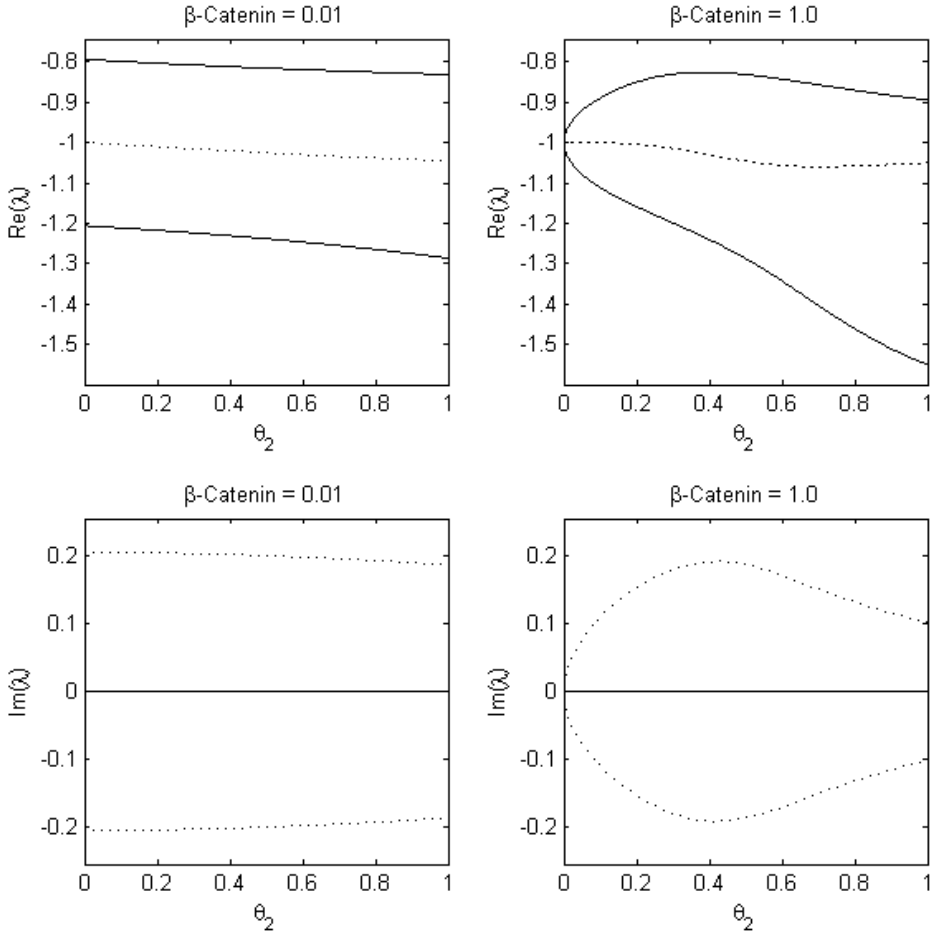

Figure 4.2: Dependence of the eigenvalues λ from Equation (4.13) upon θ_2, separated into real (upper plots) and imaginary (lower plots) components. Complex conjugate eigenvalues are depicted with dashed lines and we have $\nu_H = \nu_P = \nu_D = 1.0$; $\Psi_W = 1.0$; $\eta = 0.5$. All exponents $m_i, n_i = 3$; $\kappa_i = 0.5$ for $i = 1, 2, 4$; $\sigma_2 = 0.5$; $\sigma_3 = 0.1$; and $N, H, P, D = 0.75$.

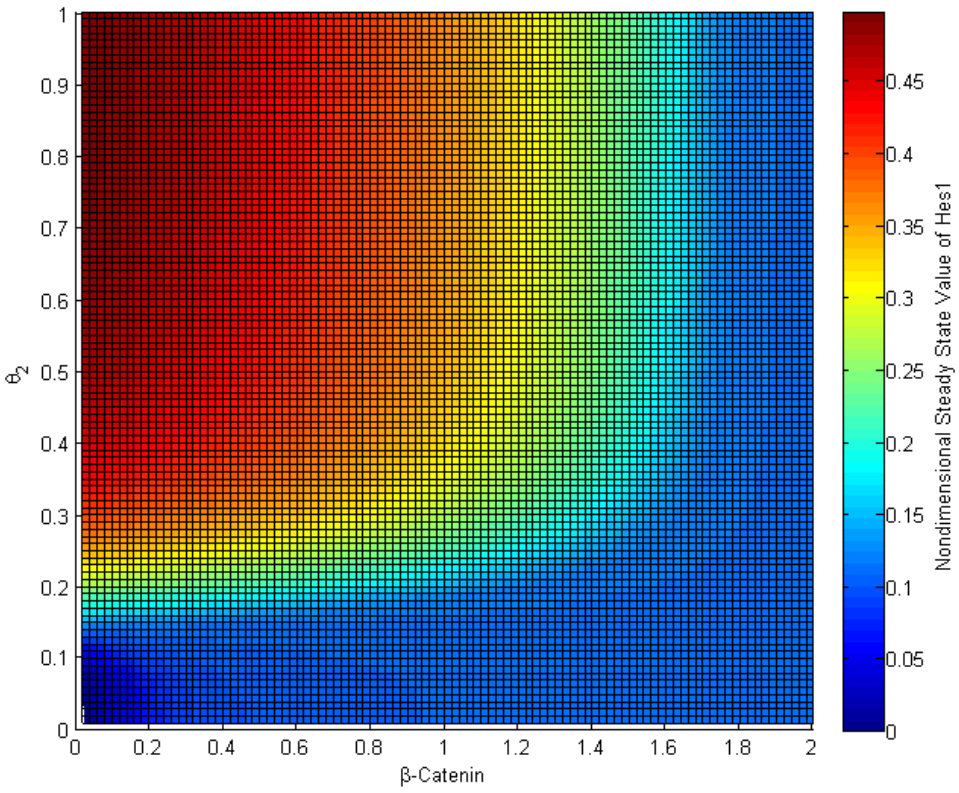

Figure 4.3: Surface plot showing variation in the Hes1 steady state in the nondimensional system (4.8) - (4.11), in response to changes in θ_2 and β-catenin.

4.1.2 Wnt-Only Analysis

Retaining the notation of Section 4.1.1, we proceed to an analysis of the decoupled Wnt system, described by the following equations:

$$\frac{dG}{d\tau} = \nu_G \left\{ -G + C + (1 + W(\tau))\alpha_2 - \alpha_5 \Psi_{W,A} G \right\}, \tag{4.14}$$

$$\frac{dC}{d\tau} = \nu_C \left\{ -C + I_2 + \alpha_5 \Psi_{W,A} G - \frac{\alpha_3}{\nu_C} B \cdot C \right\}, \tag{4.15}$$

$$\frac{dB}{d\tau} = \nu_B \left\{ -B + (1 + W(\tau))\alpha_4 - \frac{\alpha_1}{\nu_F} B \cdot F - \frac{\alpha_3}{\nu_C} B \cdot C \right\}, \tag{4.16}$$

$$\frac{dA}{d\tau} = \nu_A \left\{ -A + \Phi_6(B) \right\}, \tag{4.17}$$

$$\frac{dI_2}{d\tau} = \nu_{I_2} \left\{ -I_2 + \frac{\alpha_3}{\nu_C} B \cdot C \right\}. \tag{4.18}$$

Concentration of the Notch entity NICD (F), which interacts with β-catenin, is assumed to take a constant value for the purpose of these analyses, and is treated as a parameter of the system.

Steady State Analysis

Given a constant Wnt stimulus, W, and setting $\frac{d}{d\tau} = 0$ as in Section 4.1.1, the decoupled Wnt system (4.14) – (4.18) yields the following steady states, expressed in terms

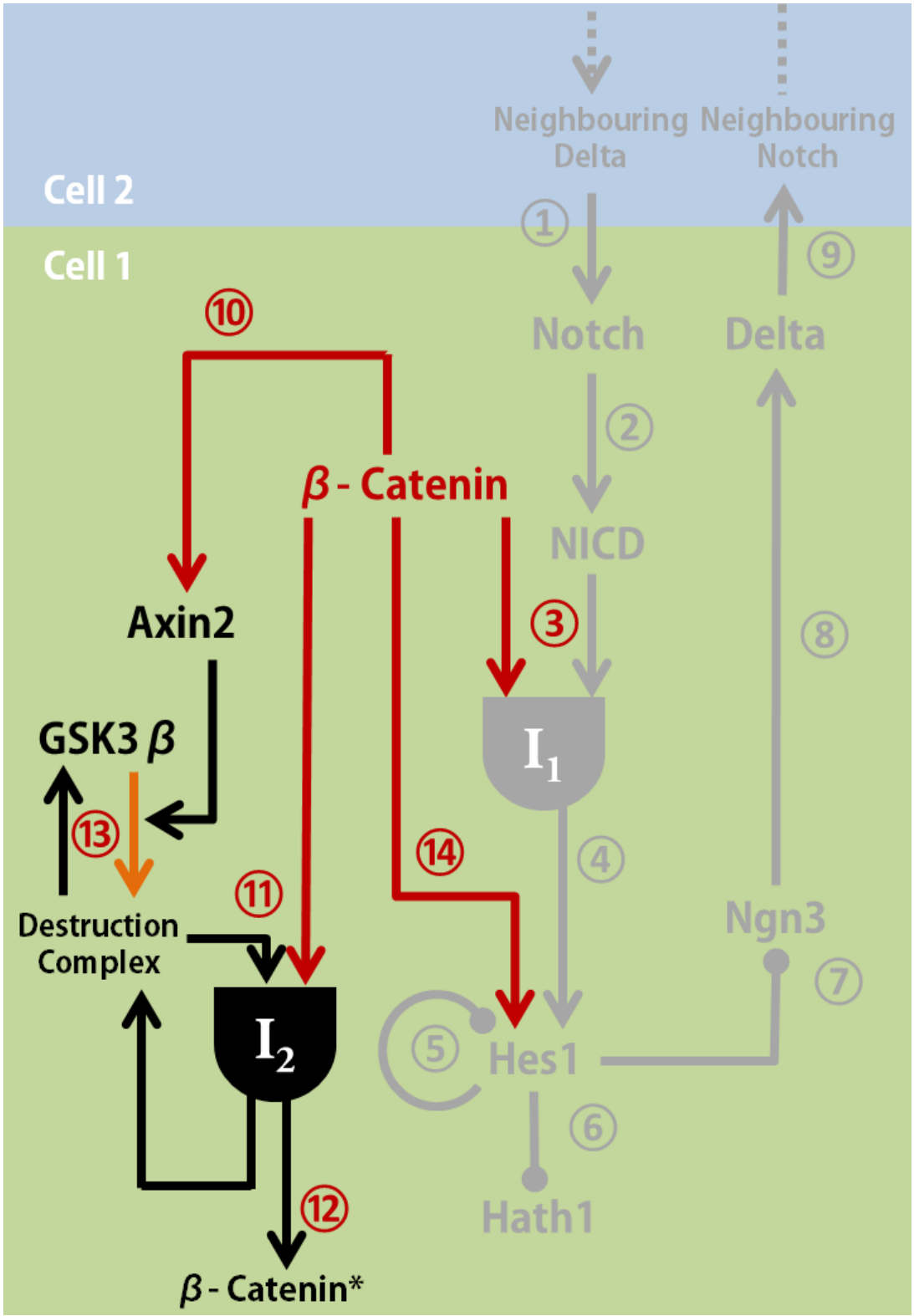

Figure 4.4: Schematic of the reactions involved in the Wnt-only system of Equations (4.14) – (4.18). The reactions involved are the same as described in Chapter 3; however, DNA events have been removed from the depiction to aid clarity.

of equilibrial β-catenin, $B = B^*$:

$$\begin{aligned} G^* =& (1+W)\alpha_2, \quad A^* = \Phi_6(B^*), \\ C^* =& 1.4\,\alpha_2\alpha_5 \frac{1+W}{1+(1+W)^4}\,\Phi_6(B^*)^2, \\ I_2^* =& \frac{1.4\,\alpha_2\alpha_3\alpha_5}{\nu_C}\frac{1+W}{1+(1+W)^4}\,B^*\Phi_6(B^*)^2, \end{aligned}$$

along with an implicit equation for B^*,

$$\frac{\alpha_4}{B^*} = \frac{1}{1+W}\left(1+\frac{\alpha_1}{\nu_F}F\right) + \frac{1.4\,\alpha_2\alpha_3\alpha_5}{\nu_C}\frac{1}{1+(1+W)^4}\,\Phi_6(B^*)^2. \tag{4.19}$$

The left-hand side of (4.19) is decreasing in B^*, whilst the right-hand side is increasing in B^*, owing to the Hill function $\Phi_6(B^*)$. This produces exactly one biologically realistic (i.e. in $\mathbb{R}^+$) solution for B^*. This is clear from the graph sketch of Figure 4.5, which shows the single intersection of the left- and right-hand side functions in the first quadrant.

Inspection of (4.19) and Figure 4.5 confirms that B^* exhibits qualitatively appropriate behaviour within the Wnt system. For example, the steady state value B^* will be increased by:

- increasing the Wnt stimulus, $W(\tau)$;
- increasing α_4, the production rate of β-catenin;
- decreasing α_5, the rate constant for formation of the destruction complex, C;
- decreasing α_3, the rate at which C binds with β-catenin ;
- decreasing the interaction of β-catenin with the Notch system (involving elements of the group $\frac{\alpha_1}{\nu_C}F$).

Strong interaction with NICD attenuates the response of β-catenin to variation in Wnt levels, as shown in Figure 4.6. As the quantity $\alpha_1 F$ increases, the gradient with

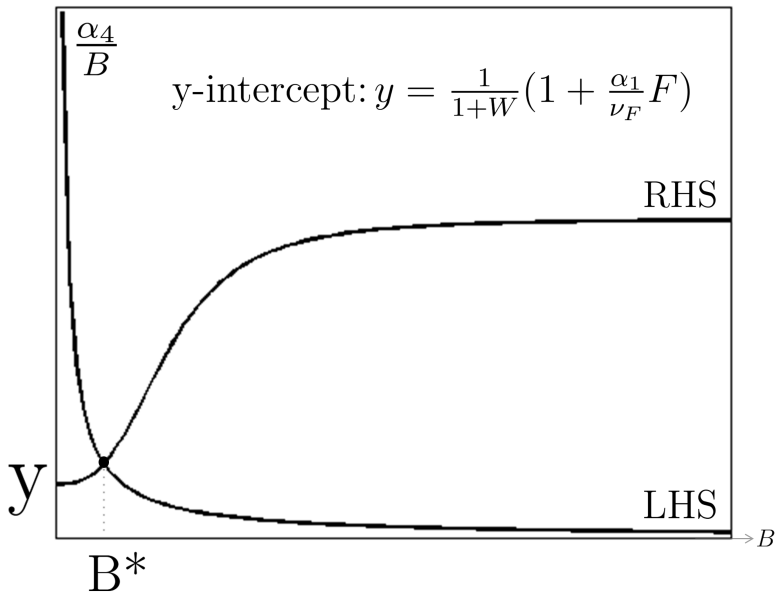

Figure 4.5: Steady state solution of β-catenin in the decoupled Wnt system. Sketches of the left- and right-hand sides of Equation (4.19) are plotted; their intersection yields one steady state in the biologically realistic regime.

respect to Wnt stimulus tends to zero. Indeed on the sketch of Figure 4.5, a high value of $\alpha_1 F$ gives the RHS function a high y-intercept, bringing the intersection of the two graphs into a regime where the asymptotic behaviour of $\frac{\alpha_4}{B}$ near $B = 0$ dominates. When the crosstalk with Notch is reduced, B^* increases with the Wnt signal.

4.1.3 Summary

Our studies of the decoupled Notch and Wnt systems in Sections 4.1.1 and 4.1.2 have confirmed the existence of biologically realistic steady states and, in the case of Notch, parameter regimes which yield damped oscillations.

We now turn to chemical reaction network theory to gain a broader perspective on the impact of Notch-Wnt coupling upon the stability properties of the system.

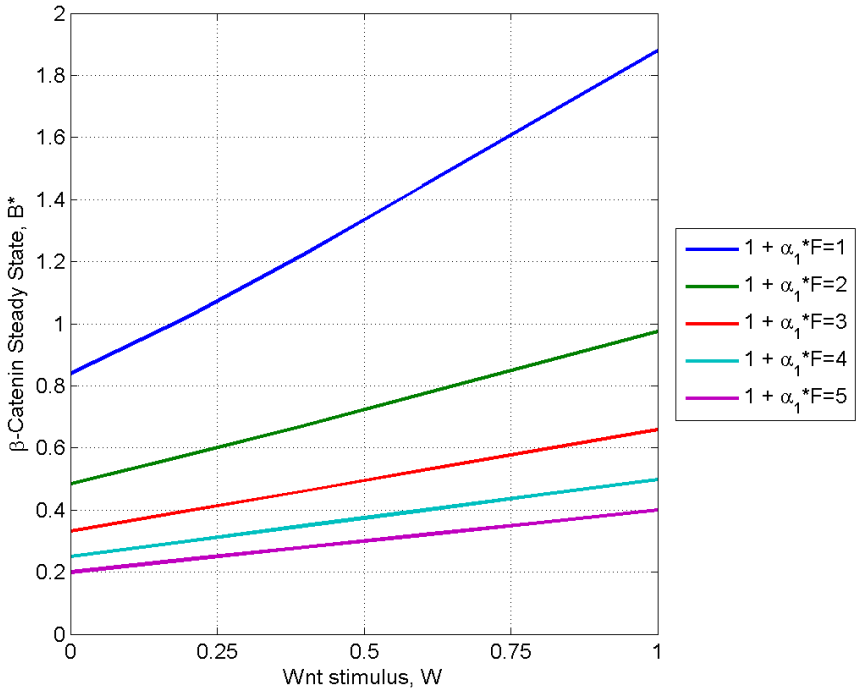

Figure 4.6: Response of B^* to variation in Wnt signal and strength of the Notch interaction, $\alpha_1 F$. Numerical solutions of (4.19) were generated from parameter values $\alpha_2 = \alpha_3 = \alpha_4 = 1.0$, $\alpha_5 = 0.4$ and $\nu_F = \nu_C = 1.0$.

4.2 Chemical Reaction Network Theory

The complexity of our Notch-Wnt system makes extensive dynamical analysis difficult, owing to the sizable parameter space (involving 41 parameters, as listed in Table 3.2) and the number of reactants. Chemical reaction network theory (CRNT) provides a means of determining the multistationarity properties of the network without specifying parameter values or explicit dynamical laws and without recourse to the system reduction employed in Section 4.1.1.

4.2.1 A Formal Framework for CRNT

Due to the extensive notation in this field, we present a minimal list below and refer readers to Shinar and Feinberg [241] for a full treatment of the subject. Except where stated otherwise, the wording of our definitions and propositions is adopted from Shinar and Feinberg [241].

A biochemical network consists of two aspects: a *network structure* $\{\mathcal{S}, \mathcal{C}, \mathcal{R}\}$, where:

- $\mathcal{S}$ is the set of all *chemical species* in the network;
- $\mathcal{C}$ is the set of *combinations*[2]. $\mathcal{C}$ comprises reactant or product expressions which express the stoichiometric linking of elements of $\mathcal{S}$, such as $F+B$, N, and $B+C$ – i.e., any expression which forms the entire right- or left-hand side of a reaction equation;
- $\mathcal{R} \subset \mathcal{C} \times \mathcal{C}$ is the set of *reactions*. Reactions satisfy two properties: first, that $(y, y) \notin \mathcal{R}$ for any $y \in \mathcal{C}$; secondly, that for each $y \in \mathcal{C}$, there exists $y' \in \mathcal{C}$ such that $(y, y') \in \mathcal{R}$ or $(y', y) \in \mathcal{R}$;

and a *kinetics*, $\mathcal{K}$, which assigns a functional form to each of the reaction rates associated with elements of $\mathcal{R}$.

Conventions and Definitions

We begin by establishing formal definitions for the *influence specification*, $\mathcal{I}$, and *stoichiometric subspace*, $\mathcal{E}$, of a reaction network, and for the properties of *injectivity* and *concordance*. All definitions adopt the following conventions of notation:

- $\mathbb{R}^I$, where I is a set, denotes the vector space of real-valued functions with

[2] In CRNT, $\mathcal{C}$ is actually called a *complex*. Here we call it a *combination* to avoid confusion with the true biochemical complexes we discussed in Chapter 3.

domain I. This removes the restriction of enumerating vector entries as in $\mathbb{R}^N$ (for $N \in \mathbb{N}$); instead vector entries are indexed over the elements of I;

- Those vector functions which take only positive values form the subset $\mathbb{R}^I_+ \subset \mathbb{R}^I$; those which take non-negative values are indicated by the set $\overline{\mathbb{R}}^I_+ \subset \mathbb{R}^I$;
- The *support* of $\underline{x} \in \mathbb{R}^I$, $supp(\underline{x})$, is the set of indices $i \in I$ for which $x_i \neq 0$;
- For $y \in \mathbb{R}$, $sgn(y)$ denotes the sign of y; for $y \in \mathbb{R}^I$, $sgn(\underline{y})$ indicates the function such that $(sgn(\underline{y}))_i := sgn(y_i)\,, \forall i \in I$.

Having established these notation conventions, we may proceed to some formal definitions. Key definitions are demonstrated for two simple networks in Figures 4.7 and 4.8.

Definition 4.2.1. *An influence specification $\mathfrak{I}$ for a reaction network $\{\mathcal{S}, \mathcal{C}, \mathcal{R}\}$ is an assignment to each reaction $y \to y'$ of a function $\mathfrak{I}_{y\to y'} : \mathcal{S} \to \{1, 0, -1\}$ such that*

- $\mathfrak{I}_{y\to y'}(s) = 1, \quad \forall s \in supp(y)$,
- *if $\mathfrak{I}_{y\to y'}(s) = 1$ [resp. -1], then species s is an inducer [inhibitor] of reaction $y \to y'$;*
- *if $\mathfrak{I}_{y\to y'}(s) = 0$, then species s has no influence on the rate of the reaction $y \to y'$.*

The *influence specification* therefore assigns each species a 1, 0 or -1 for every reaction in a network, according to whether the species is an inducer, neutral or an inhibitor of a given reaction. This construct permits the study of networks involving

autoregulatory components and allows reactions to be modulated by species other than their products or reactants.

Definition 4.2.2. *The stoichiometric subspace $\mathcal{E}$ of a reaction network $\{\mathcal{S}, \mathcal{C}, \mathcal{R}\}$ is the linear subspace of $\mathbb{R}^{\mathcal{S}}$ defined by*

$$\mathcal{E} := span\{y' - y \in \mathbb{R}^{\mathcal{S}} | \, y \to y' \in \mathcal{R}\}.$$

Two vectors $\underline{c}, \underline{c}^* \in \overline{\mathbb{R}}^{\mathcal{S}}_+$ are said to be stoichiometrically compatible if $\underline{c}^* - \underline{c} \in \mathcal{E}$.

It is clear from Definition 4.2.2 that elements of $\mathcal{E}$ are summations of the linear expressions which arise from rearranging reaction expressions to the form $(products - reactants)$. We also define a linear map $L : \mathbb{R}^{\mathcal{R}} \to \mathcal{E}$ by

$$L\underline{\gamma} := \sum_{y \to y' \in \mathcal{R}} \gamma_{y \to y'}(y' - y)\,, \tag{4.20}$$

for $\gamma_{y \to y'} \in \mathbb{R}$ the entries of $\underline{\gamma}$. The map L is used in Definition 4.2.5 to outline concordance. The kernel of L is the set $kerL = \{\underline{x} \in \mathbb{R}^{\mathcal{R}} : L(\underline{x}) = \underline{0}\}$.

All elements of $\mathcal{E}$ can be expressed in the form (4.20). However, the standard approach is to write $\underline{\sigma} \in \mathcal{E}$ as a vector in $\mathbb{R}^{\mathcal{S}}$.

Definition 4.2.3. *A kinetics $\mathcal{K}$ for a reaction network $\{\mathcal{S}, \mathcal{C}, \mathcal{R}\}$ is weakly monotonic with respect to influence specification $\mathcal{I}$ if, for every pair of elements $\underline{c}^*, \underline{c}^{**} \in \overline{\mathbb{R}}^{\mathcal{S}}_+$, the following implications hold for each reaction $y \to y' \in \mathcal{R}$ such that $supp(y) \subset supp(\underline{c}^*)$ and $supp(y) \subset supp(\underline{c}^{**})$:*

- $\mathcal{K}_{y \to y'}(\underline{c}^{**}) > \mathcal{K}_{y \to y'}(\underline{c}^*) \implies \exists$ *species s such that* $sgn(c_s^{**} - c_s^*) = \mathcal{I}_{y \to y'}(s) \neq 0$,

- $\mathcal{K}_{y\to y'}(\underline{c}^{**}) = \mathcal{K}_{y\to y'}(\underline{c}^{*}) \implies$ *either:*

  (a) $c_s^{**} = c_s^* \quad \forall s \in supp(y)$, *or:*

  (b) $\exists$ *species* s, s' *with* $sgn(c_s^{**} - c_s^*) = \mathcal{I}_{y\to y'}(s) \neq 0$ *and* $sgn(c_{s'}^{**} - c_{s'}^*) = -\mathcal{I}_{y\to y'}(s') \neq 0$.

Weakly monotonic kinetics therefore admit - amongst others - Hill kinetics, mass-action kinetics and hyperbola functions. Our Notch-Wnt ODE model satisfies the conditions for weakly monotonic kinetics subject to its influence specification $\mathcal{I}$.

Definition 4.2.4. *A kinetic system $\mathcal{K}$ is injective if, for each pair of distinct, stoichiometrically compatible elements $\underline{c}^*, \underline{c}^{**} \in \overline{\mathbb{R}}_+^{\mathcal{S}}$, at least one of which is positive,*

$$\sum_{y\to y'\in\mathcal{R}} \mathcal{K}_{y\to y'}(\underline{c}^{**})(y'-y) \neq \sum_{y\to y'\in\mathcal{R}} \mathcal{K}_{y\to y'}(\underline{c}^{*})(y'-y).$$

Remark 4.2.1. *An injective kinetic system cannot admit two distinct, stoichiometrically compatible equilibria, at least one of which is positive. That is, injectivity may be equated with monostability.*

The following definition of concordance relies upon the linear mapping L, detailed in Equation (4.20).

Definition 4.2.5. *A reaction network $\{\mathcal{S}, \mathcal{C}, \mathcal{R}\}$ with stoichiometric subspace $\mathcal{E}$ is concordant with respect to influence specification $\mathcal{I}$ if there do not exist $\underline{\gamma} \in ker L$ and a non-zero $\underline{\sigma} \in \mathcal{E}$ having the following properties:*

- *For each* $y \to y'$ *such that* $\gamma_{y\to y'} > 0$, *there exists a species* s *for which* $sgn(\sigma_s) = \mathcal{I}_{y\to y'}(s) \neq 0$;
- *For each* $y \to y'$ *such that* $\gamma_{y\to y'} < 0$, *there exists a species* s *for which* $sgn(\sigma_s) = -\mathcal{I}_{y\to y'}(s) \neq 0$;
- *For each* $y \to y'$ *such that* $\gamma_{y\to y'} = 0$, *either:*
  (a) $\sigma_s = 0 \quad \forall s \in supp(y)$, *or:*
  (b) $\exists$ *species* s, s' *for which* $sgn(\sigma_s) = \mathcal{I}_{y\to y'}(s) \neq 0$ *and* $sgn(\sigma'_s) = -\mathcal{I}_{y\to y'}(s') \neq 0$;

Figures 4.7 and 4.8 depict two simple networks and derive expressions for $\mathcal{E}$ and $kerL$. The example in Figure 4.7 has trivial kernel and is therefore concordant according to Definition 4.2.5. However, the network in Figure 4.8 has a non-trivial kernel and a case can be found of a non-zero $\underline{\sigma} \in \mathcal{E}$ and $\underline{\gamma} \in kerL$ which satisfy the conditions listed in Definition 4.2.5. The network shown in Figure 4.8 is therefore discordant. Neither example need be allied with specific reaction rates during this analysis; concordance is a property of the underlying network $\{\mathcal{S}, \mathcal{C}, \mathcal{R}\}$ and is independent of the kinetics $\mathcal{K}$.

Our definitions now established, we turn to the main theoretical result of interest.

Concordant Networks with Weakly Monotonic Kinetics

The following proposition provides us with a means of determining when our Notch and Wnt networks (or indeed the full coupled system) are monostable.

Proposition 4.2.1. *A kinetic system* $\{\mathcal{S}, \mathcal{C}, \mathcal{R}, \mathcal{K}\}$ *is injective whenever there exists an influence specification* $\mathcal{I}$ *such that:*

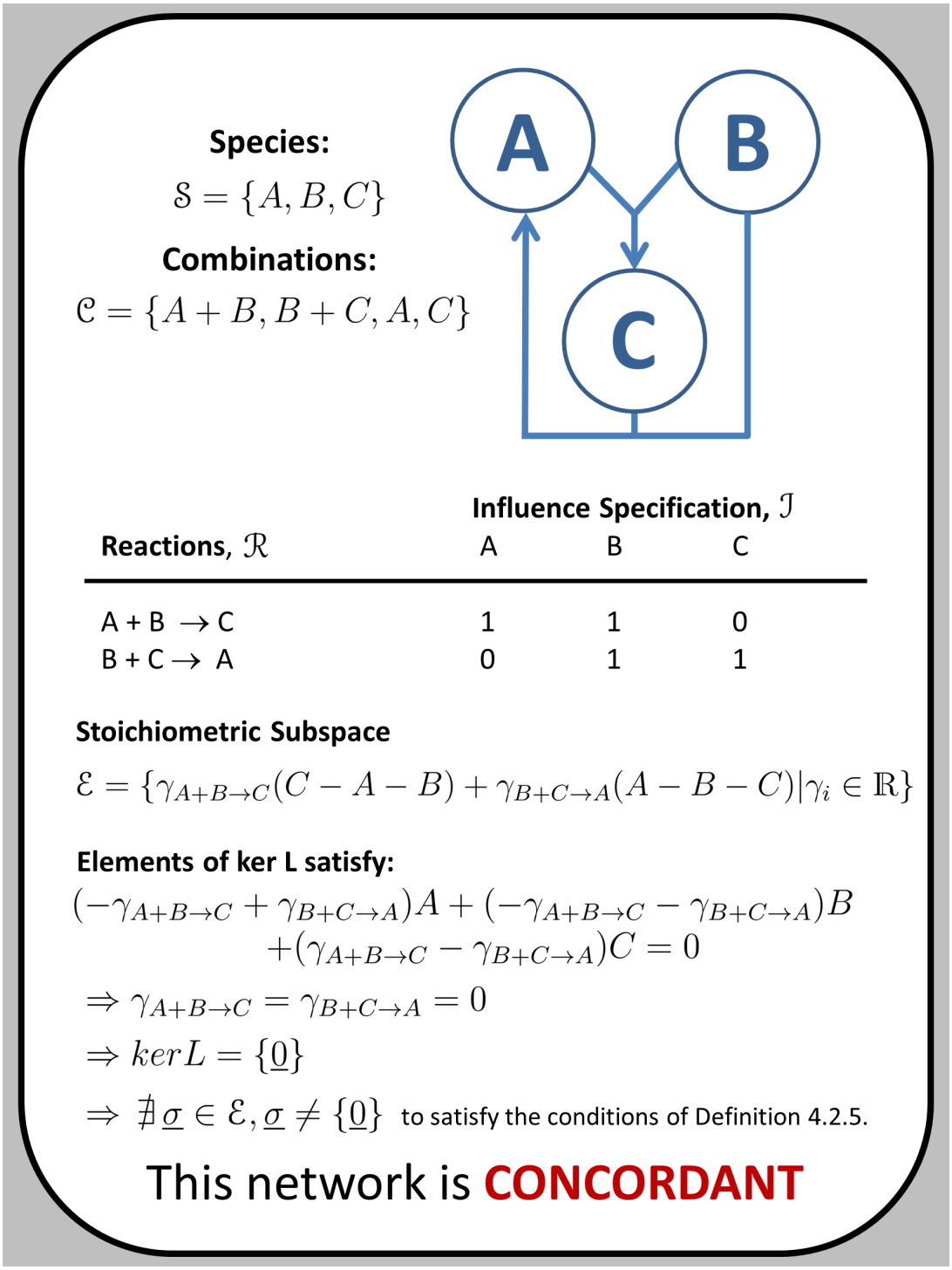

Figure 4.7: A simple example of a concordant network, indicating the sets $\mathcal{S}, \mathcal{C}, \mathcal{R}, \mathcal{I}$ and $\mathcal{E}$. In this case, the linear mapping L has trivial kernel and there does not exist a suitable $\underline{\sigma} \in \mathcal{E}$ to satisfy the properties listed in Definition 4.2.5. Consequently this network is concordant.

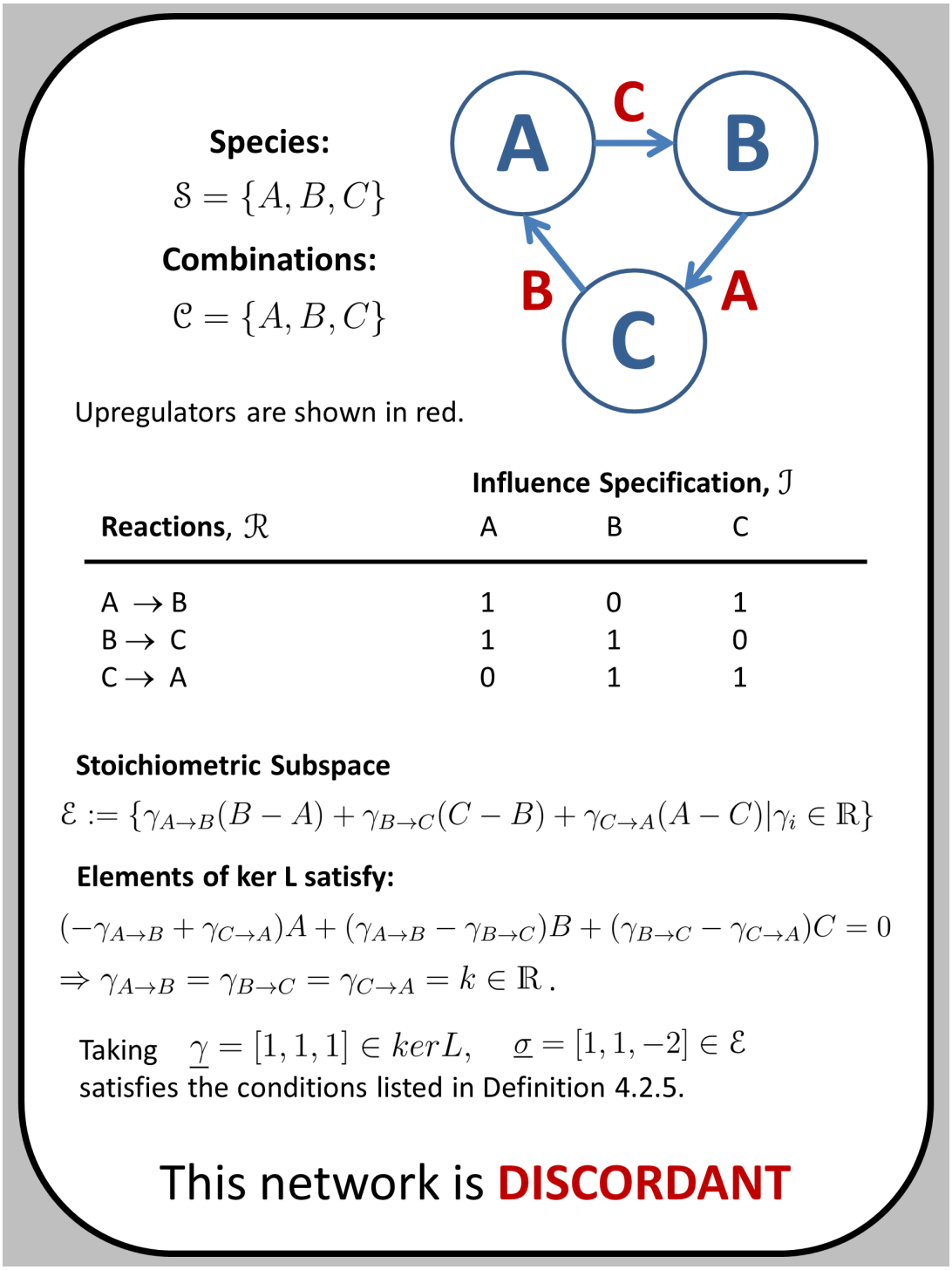

Figure 4.8: A simple example of a discordant network, indicating the sets $\mathcal{S}, \mathcal{C}, \mathcal{R}, \mathcal{I}$ and $\mathcal{E}$; regulators of a given reaction are indicated in red. In this case, the linear mapping L has non-trivial kernel and it is possible to find a $\underline{\gamma} \in kerL$ and $\underline{\sigma} \in \mathcal{E}$ to satisfy the properties listed in Definition 4.2.5. Consequently this network is discordant.

- *The kinetics* $\mathcal{K}$ *is weakly monotonic with respect to* $\mathcal{I}$*;*
- *The underlying network* $\{\mathcal{S}, \mathcal{C}, \mathcal{R}\}$ *is concordant with respect to* $\mathcal{I}$*.*

Our Notch-Wnt system has a valid influence specification according to Definition 4.2.1 and satisfies Definition 4.2.3 of weakly monotonic kinetics. Proposition 4.2.1 and Remark 4.2.1 together imply that any concordant network or sub-network in our model should be injective and hence monostable. Conversely, a discordant network or sub-network will exhibit more than one steady state and may be capable of switch-like behaviour or other interesting dynamics.

The associated reaction network in our case is large and complex; a concordance assessment of our Notch-Wnt network will therefore require automated analysis.

4.2.2 Network Analysis

The *Chemical Reaction Network Toolbox* described in Section 2.3 calculates whether or not a network is concordant. This requires us to supply the species and network connectivity of the (non-reduced) Notch-only, Wnt-only and fully coupled networks, along with the influence specification for up- or down-regulation of each interaction. Owing to the bifurcation behaviour detected in the Notch system in Section 4.1.1, we supply two versions of the Notch-only and whole network: the first containing both Hes1 regulation actions (⑭ via B and ④ via I_1) and the second involving only the I_1-mediated step.

It is not possible to analyse states of the heterogeneous system, owing to the excessively large computation time for a system of this complexity; consequently, all our CRNT results relate to a homogeneous Notch pathway, in which we assume $D = \bar{D}$. Crosstalk species B and F in the decoupled systems are represented as full reactants with their own inflows and outflows. Results from the chemical network analysis are

shown in Table 4.1.

Model	Active Coupling Points	Wnt ON	Wnt OFF
Notch Only	(4), (14)	✔	✔
	(4) only	✔	✘
Wnt Only	N/A	✔	✔
Full System	(4), (14)	✔	✔
	(4) only	✘	✘

Table 4.1: Concordance results for decoupled and whole networks in a homogeneous ($D = \bar{D}$) system, analysed using the CRN Toolbox. A tick indicates a concordant network and a cross, a discordant network. The second column indicates which β-catenin crosstalk points were included in each network. β-catenin is not used up in interaction 14 and so the comparison of the two coupling points does not apply to the Wnt-only system.

Discussion of CRNT Results

Comparisons between the decoupled and full systems provide valuable insights into the origins of the behaviour of the coupled Notch-Wnt network:

β-catenin acts as a stabilising force: Action of β-catenin upon the Hes1 promoter (networks involving (14)) always yields an injective, and hence monostable, network. This reinforces our impression of β-catenin as a stabilising force in the Notch system and echoes the findings of Section 4.1.

Discordance arising from Wnt response: In the absence of the stabilising influence of β-catenin and in the presence of a Wnt stimulus, the full network generates multistationarity from two monostable subnetworks. Harrington *et al.* [242] demonstrate that in such cases, the rate of shuttling of crosstalk species determines the region of parameter space in which multistability occurs.

Multistability in Notch influences the full system: Sub-networks can transmit discordance to the full network, as shown by Shiu [243]. Some of the discordance in the full Notch-Wnt network (④ only, Wnt off) can be attributed to the equivalent discordance in the Notch system.

The stability properties of the full system therefore depend not just on the presence or absence of a Wnt stimulus, but also on the mechanisms governing transcription of Hes1. This motivates particular focus upon the parameter θ_2 and the Wnt stimulus W in Section 4.4.

4.3 Parametrisation

The parameter set for the dimensional model of Equations (3.3) – (3.14) includes decay rates, maximal transcription rates and exponents as well as binding and dissociation rates for complexes and intermediates. Some of these quantities, such as decay rates, are readily amenable to experimental measurement, whilst others, such as binding rates, are not. Consequently, experimental estimates are not available for every parameter in our model at the present time.

The following priority ordering was employed when selecting parameter estimates:

1. Estimates derived from human cell lines, in particular intestinal epithelial lines, have been used wherever possible;

2. In the absence of data for human cell lines, values from mammalian lines have been employed;

3. Otherwise, non-mammalian readings or values from published mathematical models have been used as initial estimates for parameter fitting studies, as described in sections 4.3.2 and 4.3.3.

Here the principal focus is on the qualitative features of the model within biologically sensible regimes, rather than aiming to deliver high-precision matching with experimental data. Global parameter analysis therefore lies beyond the scope of the present work; one might hope that qualitative predictions from our model could provide the stimulus for an experimental estimation of its parameters within a single, human intestinal cell line.

All *in vitro* experiments cited here take readings over a population of cells; the resulting estimates therefore represent a population average. Furthermore, the non-compartmental structure of our model assumes that the cytoplasm is 'well-stirred', with reactant species present at a uniform concentration throughout the cell.

Decoupled Notch and Wnt models are used during the parametrisation process of Sections 4.3.2 and 4.3.3. The recoupled, full system is used to explore the emergent properties of the model in the two-cell simulations of Section 4.4.

4.3.1 Decay Rates

All degradation reactions in our system take the form $X \rightarrow \varnothing$, for X a chemical species. Application of a first-order mass action law yields a decay rate of $\mu_X X$, for μ_X the corresponding rate constant.

Experimental literature specifies the half-life of a species. The half-life, $t_{1/2}$, of species X is defined as the period of time, measuring from $t = 0$, for the concentration of X to fall to half its initial value, X_0. Assuming exponential decay in all cases yields:

$$\frac{X_0}{2} = X_0 e^{-\mu_X t_{1/2}}$$

$$\implies \mu_X = \frac{ln2}{t_{1/2}} \approx \frac{0.693}{t_{1/2}}\,.$$

Once the half-life $t_{1/2}$ is known, the decay rate constant can be calculated directly. Parameter values in the final column of Table A.1 were derived using this approach.

4.3.2 Notch Model

Our objective in parametrising the Notch system defined by Equations (3.3) – (3.9) is to approximate the period of oscillations obtained by Hirata *et al.* [142]. Initial parameter fitting was performed by solving for the homogeneous state of a two-cell system, in which both cells adopt a uniform state.

Exponents m_i, n_i for the Hill functions and hyperbolas are set at $m_i = 3$, for $i = 1, 2, 4, 6, 7$ and $n_i = 3$, for $i = 2, 3, 5$. This reflects the strength of feedback required to generate oscillations in the absence of a delay-driven formulation.

Hirata *et al.* (2002)

The experiments of Hirata *et al.* [142] characterise the oscillation period, Hes1 decay rate, and several qualitative features of the Notch pathway. The authors demonstrate that stimulation of murine myoblast cells with a Hes1 inducer yields three to six cycles of oscillation in both Hes1 mRNA and protein. These decaying oscillations persist over a six to twelve hour timespan and have a mean period of around two hours. This behaviour is also observed when the myoblasts are exposed to Delta-expressing cells.

Although a quantified oscillation period does not in itself yield parameters directly, it provides an excellent target measurement for use in parameter fitting, which we describe below.

Fitting Procedure

Parameters which could not be estimated from the literature were approximated by the following method.

An oscillatory regime was located within the nondimensionalised form of the decoupled Notch model[3], described by Equations (4.1) – (4.7). The parametrisation for

[3]Nondimensional simulations on a similar, four-component system by Shepherd [238] provided useful information regarding possible parameters to use as a starting point in this investigation.

this oscillatory regime was redimensionalised, applying the scaling detailed in Table 3.2 and using the biological estimate for the Notch decay rate, $\mu_N = 0.017$ min^{-1} from Logeat *et al.* [244]. The resulting values were used as initial values for missing parameters in the parameter fitting exercise. Initial conditions were chosen to be of the same order as in the model of Agrawal *et al.*, and were set to $0.5nM$.

1. *Sensitivity analysis:* A sensitivity analysis was performed on the Notch parameter set to determine the influence of each parameter upon the length of the Hes1 oscillation period. This analysis was carried out using the Systems Biology Toolbox in MATLAB and involves increasing each parameter in turn and measuring the resulting change in the Hes1 oscillation period. Expressions for the normalised oscillation period sensitivity are discussed in Appendix A, Section A.1.

2. *Fitting order:* Results from the sensitivity analysis were used to create a prioritised parameter sequence, in which parameters were listed in decreasing order of oscillation period sensitivity. This ordering allows the most sensitive parameters to be fitted first, before the less sensitive ones. The priority ordering is listed in Section A.1 of Appendix A and can also be seen in the ordering of parameters on Figure A.1.

3. *Test range:* Parameter fitting was performed using MATLAB. Each parameter in turn was modified over a ±100% tolerance; the ODE model was simulated for 1000 evenly spaced values within this parameter range and the resulting mean period of the oscillations was measured for 12 hours after stimulation. For the purpose of the fitting algorithm, the oscillation period was defined as the difference between two successive oscillatory peaks, which can be located by identifying local maxima on the *Hes1* timeseries vector. In each case, the parameter was revised to the value which provided the closest match to the two

hour oscillation period observed by Hirata *et al.* [142]. This revised value was accepted into the parameter set and the fitting algorithm moves on to the next parameter in the priority set.

4. *Repeat iteration:* Several complete cycles of modification were employed to improve the parameter approximations. The stopping point of the iterations was reached when the difference between the oscillation period at two successive iterations fell below a given tolerance.

Although this unsophisticated method does not necessarily locate the globally optimal parameter set, it provides a quick means of approximating unknown parameters in a context such as ours where qualitative behaviour, rather than high-precision quantitative matching, is the overall goal. Parameter estimates have been taken from the biological literature wherever possible. Furthermore, all the numerically fitted parameters remain close to the literature approximations used as initial values in the fitting, and indeed are of the same order of magnitude.

Nonetheless, the parametrisation of our Notch-Wnt model would undoubtedly benefit from further investigation, whether by recourse to new experimental work or by improving the numerical methods used in the parameter fitting process – or, indeed, a combination of both. Such work lies beyond the scope of the present study however, and we defer its discussion until the outline of future work detailed in Chapter 7, Section 7.2.

Application of Fitted Parameters to a Heterogeneous System

The homogeneity restriction was then relaxed and the fitted parameter set tested in a heterogeneous, two-cell system to examine the variation in oscillation period with initial conditions. Initial conditions in each cell were varied independently over the range $[0.0, 1.0]$. The surface plot in Figure 4.9 depicts the resulting variation in the

oscillation period of the first cell; non-oscillating results show up as a period of zero.

Where oscillations occur, the period generally lies in the $2-4$ hour range. This offers a reasonable match to the estimate of Hirata *et al.* but with a slight tendency to overestimate the period. Slight overestimation is to be expected for a non-delay model of this kind; the inclusion of Hes1 mRNA and dimerisation processes has been shown to assist in matching oscillations to the experimental data [143, 144]. Such modifications might provide the basis for more extensive investigation in the future but lie outside the scope of the present work.

4.3.3 Wnt Model

Data for parameter fitting in the Wnt model described by Equations (3.10) – (3.14) were drawn from Hernández *et al.* [167], which supplies a β-catenin timecourse for *RKO* cells, a human colon cell line.

Hernández *et al.* (2012)

Hernández *et al.* [167] perform *in vitro* experiments on the human colon carcinoma cell line, *RKO*, measuring the phosphorylated and unphosphorylated concentrations of β-catenin following stimulation with 100 ng/ml Wnt. Membrane-bound β-catenin involved in intercellular adhesion is removed from these measurements through the use of trapping beads and subsequent centrifugation.

Our ODE model for the Wnt pathway does not include phosphorylated β-catenin, owing to the assumption that its removal from the system is instantaneous following ubiquitination by the destruction complex. Nonetheless, Hernández *et al.* find that "*[almost] all β-catenin is unphosphorylated*". In light of these findings, we believe that the resulting timecourse for total β-catenin provides good target data for the β-catenin timecourse of our ODE model.

The Hernández *et al.* timecourse is characterised by a transient accumulation

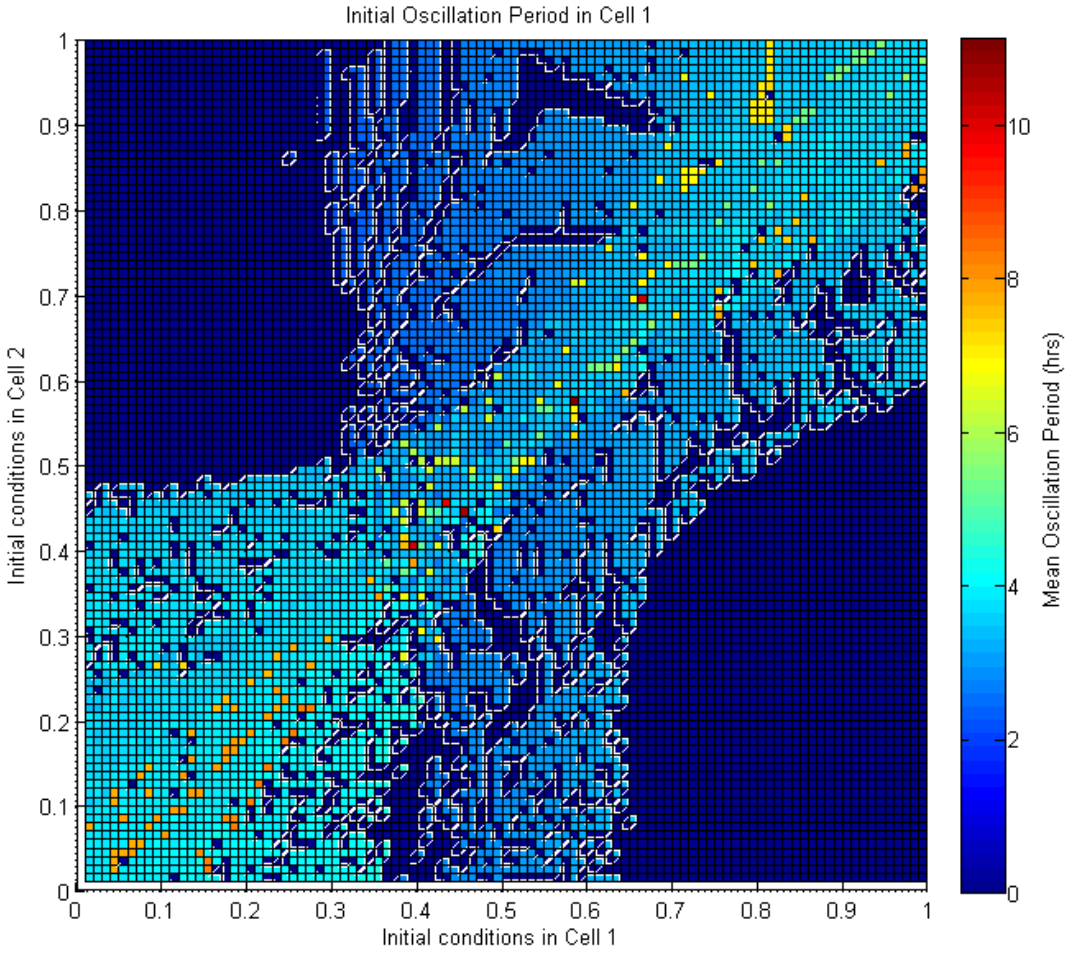

Figure 4.9: Response of oscillation period to variations in initial conditions in a two-cell system. Owing to the symmetry of the problem, only the oscillations in Cell 1 were measured; results for Cell 2 correspond to a reflection of this surface in the line $y = x$. An amplitude filter was applied during generation of the plot, so as to disregard any small-amplitude oscillations (< 0.001) arising from the computational solution process, rather than true oscillations of the ODE model.

phase during the first two hours after Wnt stimulation, followed by a plateau over the next four hours. During this time, the concentration of the destruction complex changes relatively little and can be assumed constant for the purpose of calculating initial estimates for parameters α_3 and α_4. The concentration of NICD is treated as an input parameter.

Applying a steady-state assumption to Equation (3.12), the time-dependent evolution for β-catenin, we generate simultaneous equations for α_3 and α_4:

$$\dot{B} = (1+W)\alpha_4 - B(\alpha_1 \cdot F + \alpha_3 \cdot C + \mu_B)\,,$$

$$0 = 2\alpha_4 - 54(40\alpha_3 + 0.007)\,, \tag{4.21}$$

$$0.5 = 2\alpha_4 - 9(40\alpha_3 + 0.007)\,. \tag{4.22}$$

Here, $W = 1$ because we derive estimates for α_3, α_4 from the data of Hernández *et al.* [167], which we interpret as the reference state for the Wnt concentration. The substitution $\alpha_1 F = 0.007 min^{-1}$ is based upon typical values from the decoupled Notch system at steady state. The steady-state concentration of C is estimated using data from Tan *et al.* [162]. The solution of Equations (4.21) and (4.22) yields initial estimates of $\alpha_3 = 1.028 \times 10^{-4}$ and $\alpha_4 = 0.3$ for use in parameter fitting.

Lee *et al.* (2003) and Tan *et al.* (2012)

Initial estimates for the remaining parameters were approximated using the mathematical model of Lee *et al.* [161], whose rate parameters are derived from experiments on *Xenopus* oocytes. As this is non-mammalian data, these estimates were used as initial values for parameter fitting, rather than being adopted wholesale into the model. Parameters $\mu_C, \mu_{I_2}, \theta_6$ and α_5 were approximated in this way.

Initial conditions for β-catenin were matched to those in the Hernández *et al.*

data [167]. The experimental findings of Tan *et al.* [162] allow us to approximate the initial concentrations for the remaining species. Tan *et al.* provide volume-scaled measurements of the concentration of Wnt pathway components in three human cell lines from the intestinal epithelium. Measurements for each cell line are similar and we take the species mean across the three cell lines as a guideline for the initial conditions in our Wnt system.

Concentrations of G and A are available directly from the data; we equate the destruction complex, C, with the concentration of APC. The concentration of destruction complex bound to β-catenin is not measured, but we assume its initial conditions to be similar to those of G and C. A list of initial conditions can be found in Table A.5.

Fitting Procedure

All Wnt stimuli have been nondimensionalised against a reference value of 100 ng/ml. The unstimulated state, $W = 0$ in our model, equates to 0 ng/ml; the reference value represents $W = 1$. All other values scale linearly with this, with values $W > 1$ representing a hyperstimulated state.

Simulations of the dimensional, decoupled Wnt system were run to obtain 3-hour timecourses for β-catenin, in order to compare against the data of Hernández *et al.*. The mean squared error (MSE) of the model's performance, $\hat{X}$, against the experimental data, X, was calculated in each case:

$$MSE = \frac{1}{n}\sum_{1}^{n}(\hat{X} - X)^2\,, \tag{4.23}$$

where $n = 6$, the total number of observations.

The parameter fitting procedure for the Wnt system was almost identical to the method described for the Notch system in Section 4.3.2, as follows:

1. *Sensitivity analysis:* As with the Notch fitting procedure, a sensitivity analysis

was performed using the Systems Biology Toolbox in MATLAB. However, the Wnt system does not display oscillatory behaviour and so the sensitivity analysis measures each parameter's impact upon the stable steady state of β-catenin within the system, rather than using an oscillation period. The equations for this calculation are discussed at length in Section A.1, Appendix A.

2. *Fitting order:* The same priority ordering concept was used as for the Notch system. The parameter ordering for the Wnt system is listed in Section A.1 of Appendix A and can also be seen on Figure A.2.

3. *Test range:* Parameter fitting was performed in MATLAB. Each parameter in the Wnt-only model was varied in turn over 1000 evenly-spaced values within a $\pm 100\%$ tolerance of the initial guess, before being corrected to the value which minimised the mean-squared error (4.23).

4. *Repeat iteration:* Several complete cycles of modification were employed to improve the parameter approximations. The stopping point of the iterations was reached when the MSE fell below a given tolerance.

The resulting fit of our model against the β-catenin timecourse of Hernández *et al.* [167] is shown in Figure 4.10. A full parameter list of the fitted values is provided in Tables A.1 - A.4 of Appendix A.

4.3.4 Parametrisation Findings

The β-catenin evolution of our model, shown in the upper plot of Figure 4.10, provides a close fit to the data of Hernández *et al.* [167].

Comparisons of our decoupled models against experimental data indicate that they capture the qualitative features of the Notch and Wnt systems and do so within a biologically sound regime. This enables us to apply the full, coupled model to problems of biological and biochemical interest.

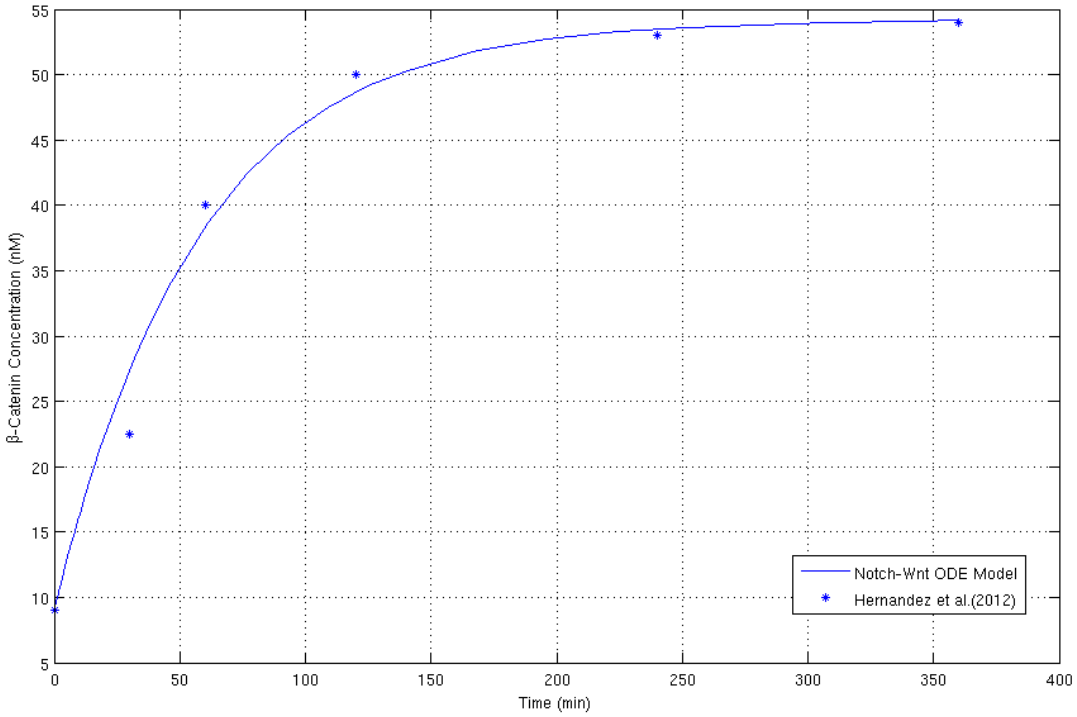

Figure 4.10: Timecourse for β-catenin evolution in the dimensional, decoupled Wnt model (line graph), compared against the experimental readings of Hernández *et al.* [167] (point data).

4.4 Two-Cell Studies

The remaining simulations in this chapter remove the restriction of homogeneity and focus on the dynamics of two coupled cells.

All cells start from the standard Wnt conditions detailed in Table A.5. For the healthy cell pairs of Section 4.4.1, the first cell of the pair adopts conditions of $0.5nM$ for all its Notch components, whilst the Notch entities of the second cell start from $0.51nM$. This difference permits the emergence of heterogeneous states. Initial conditions for mutant cell simulations are stated in the relevant sections.

4.4.1 Timecourses of Hes1 and β-catenin

Figure 4.11 demonstrates the effect of increasing Wnt levels upon the expression of both Hes1 and β-catenin in each member of the cell pair.

The second cell, which starts from slightly higher initial Notch conditions, has the higher Hes1 expression at all Wnt stimuli. Although the difference between the two cells' β-catenin levels is slight, higher Hes1 levels correlate with a marginally lower β-catenin expression for the cases $W = 0$ and $W = 1$.

The stronger the Wnt stimulus, the more β-catenin is expressed, but the qualitative form of the timecourse remains the same. Hyperstimulated Wnt conditions ($W = 2$) serve to dampen oscillations in Hes1 and promote homogeneity in Hes1 expression.

4.4.2 Transcriptional Control of Hes1

Transcription of Hes1 is promoted through two different routes: the first occurs via the intermediate I_1 and is primarily Notch-mediated; the second is Wnt-mediated and involves β-catenin binding directly to the Hes1 promoter. In our model, the ratio of Notch- to Wnt-mediated control is encapsulated in the parameter θ_2. $\theta_2 = 1.0$ indicates that all upregulation is performed by I_1; when $\theta_2 = 0.0$, all regulation occurs via β-catenin; and $0 < \theta_2 < 1$ denotes a combination of the two.

Analysis of our network in Sections 4.1 and 4.2 indicated that the regulatory mechanisms of Hes1 play a major role in shaping the dynamics of the Notch system. Figures 4.12 and 4.13 show the response of Hes1 to changes in θ_2, for Wnt stimulus present and absent. These simulations employ standard initial conditions and parametrisations in both cells and were run at $W = 0.0$ and $W = 1.0$, for a range of values $\theta_2 \in [0.0, 1.0]$.

Oscillations are associated with values $\theta_2 > 0.5$, where the majority of Hes1 transcription is regulated by I_1. Substantial involvement of β-catenin at lower values of θ_2 dampens oscillations and forces the cells to settle rapidly on a constant steady state.

Comparison between Figures 4.12 and 4.13 indicates that a higher Wnt stimulus

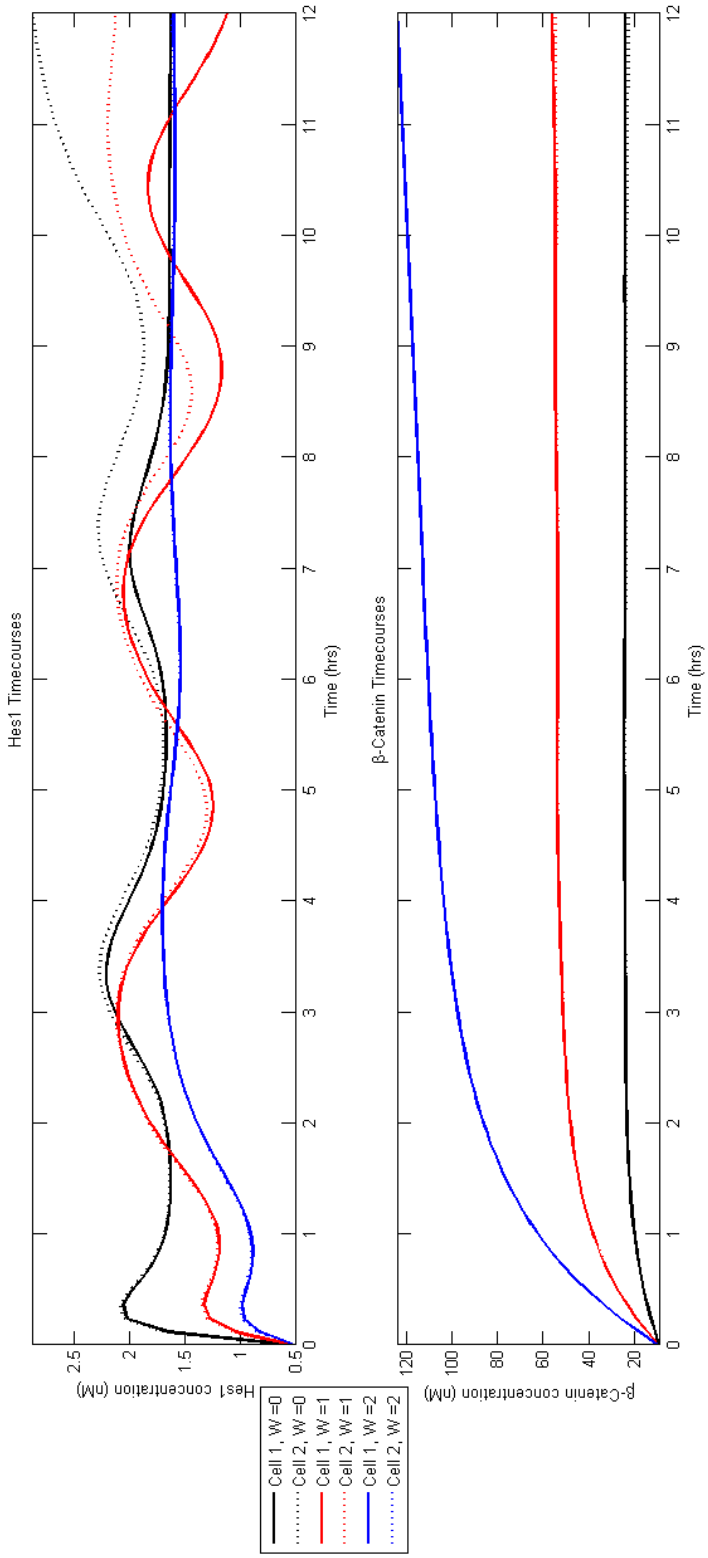

Figure 4.11: Wnt response of Hes1 and β-catenin in a heterogeneous, two-cell system. The timecourses show (top) Hes1 and (bottom) β-catenin expression for three cell pairs, exposed to a low ($W = 0$), high ($W = 1$) or hyperstimulated ($W = 2$) Wnt concentration. The standard initial conditions, listed in Table A.5, are used for each of the cells.

reduces the overall expression of Hes1, as well as reducing the amplitude of any oscillations. The overall steady state of β-catenin is unaffected by the interaction with the Notch pathway, although some simulations at low-Wnt, high-θ_2 develop small-amplitude oscillations about the steady state in response to the oscillations in the Notch system.

These results support the idea that Notch signalling maintains flexibility in cell fate decisions [150]. Cells could regulate this by preserving a Notch-mediated monopoly over the transcriptional regulation of Hes1, until a β-catenin intervention at a specified time.

4.4.3 Mutant Transformation

Thus far, we have examined the behaviour of healthy cells. However, our original motivation was to understand cell fate selection in the context of colorectal cancer.

An APC Mutant

We begin by examining a mutant phenotype originally discussed in Section 1.4.2, that of an APC mutant in which the function of the β-catenin destruction complex is either partially or wholly impaired. We discuss the implementation of this phenotype in detail in Chapter 6; for now it suffices to note that we modify the term $\alpha_5 \Psi_{W,A} G$ for formation of the destruction complex, scaling this value by 0.5 to represent a single-hit mutation, and removing it altogether to depict a two-hit mutant.

Results for two-cell simulations of these mutant cells are shown in Figures 4.14 and 4.15. Both cells are healthy at $t = 0h$ and are set off from homogeneous conditions. The second cell acquires a single APC mutation at $t = 8h$ and a second hit at $t = 16h$, indicated by the vertical gridlines.

The first hit causes separation of the previously identical trajectories for the two cells and these differences are magnified still further once the second hit appears. As

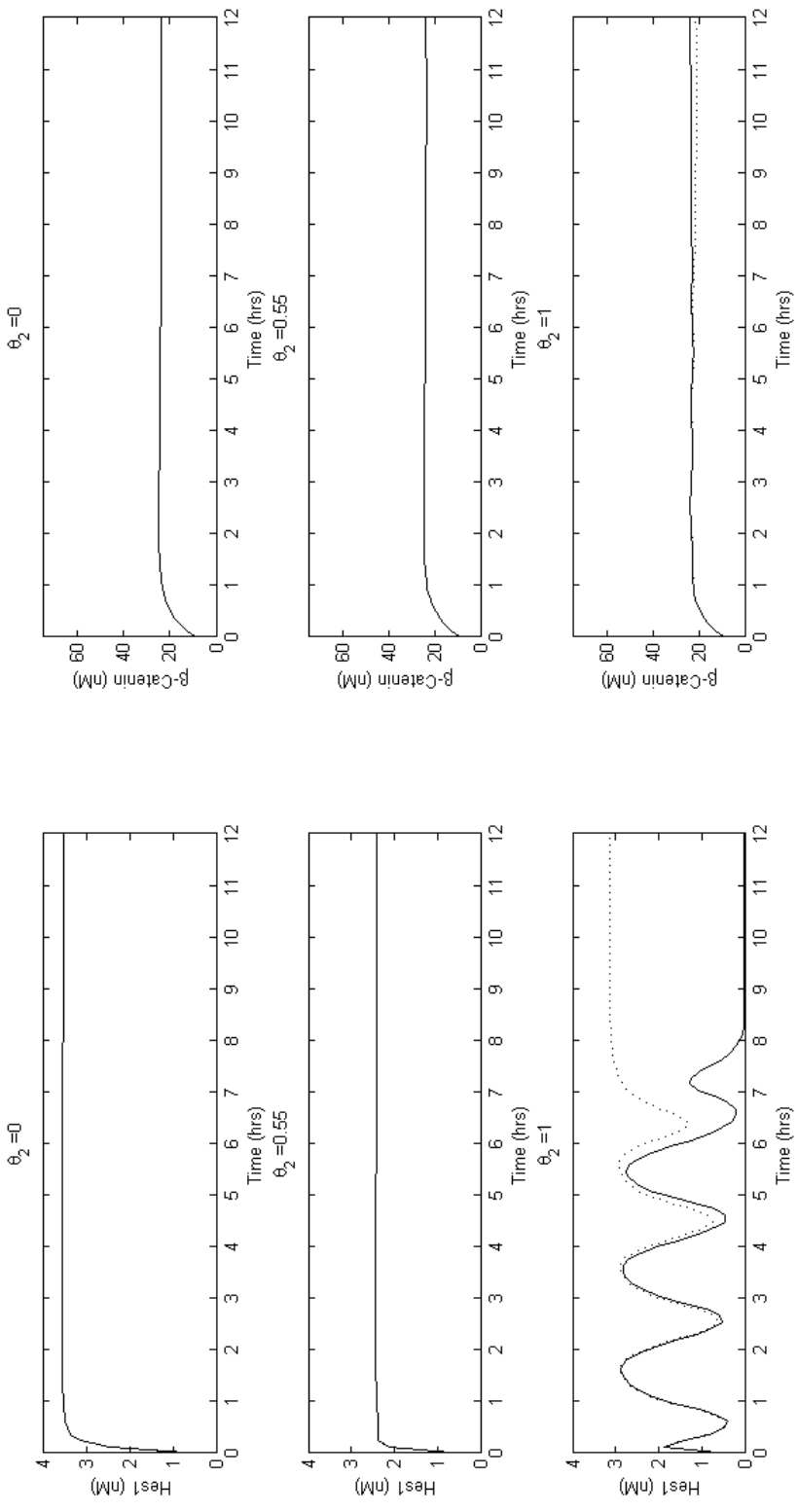

Figure 4.12: Influence of θ_2 upon the Hes1 steady state at $W = 0.0$. The timecourses show (left) Hes1 and (right) β-catenin expression for three cell pairs, using values of θ_2 ranging from (top) $\theta_2 = 0$ to (bottom) $\theta_2 = 1$. Standard initial conditions, listed in Table A.5, are used for each of the cells. Timecourses for the first cell are shown with a solid line; those for the second cell are indicated with a dotted line. Ultimately β-catenin settles upon a constant steady state at long times.

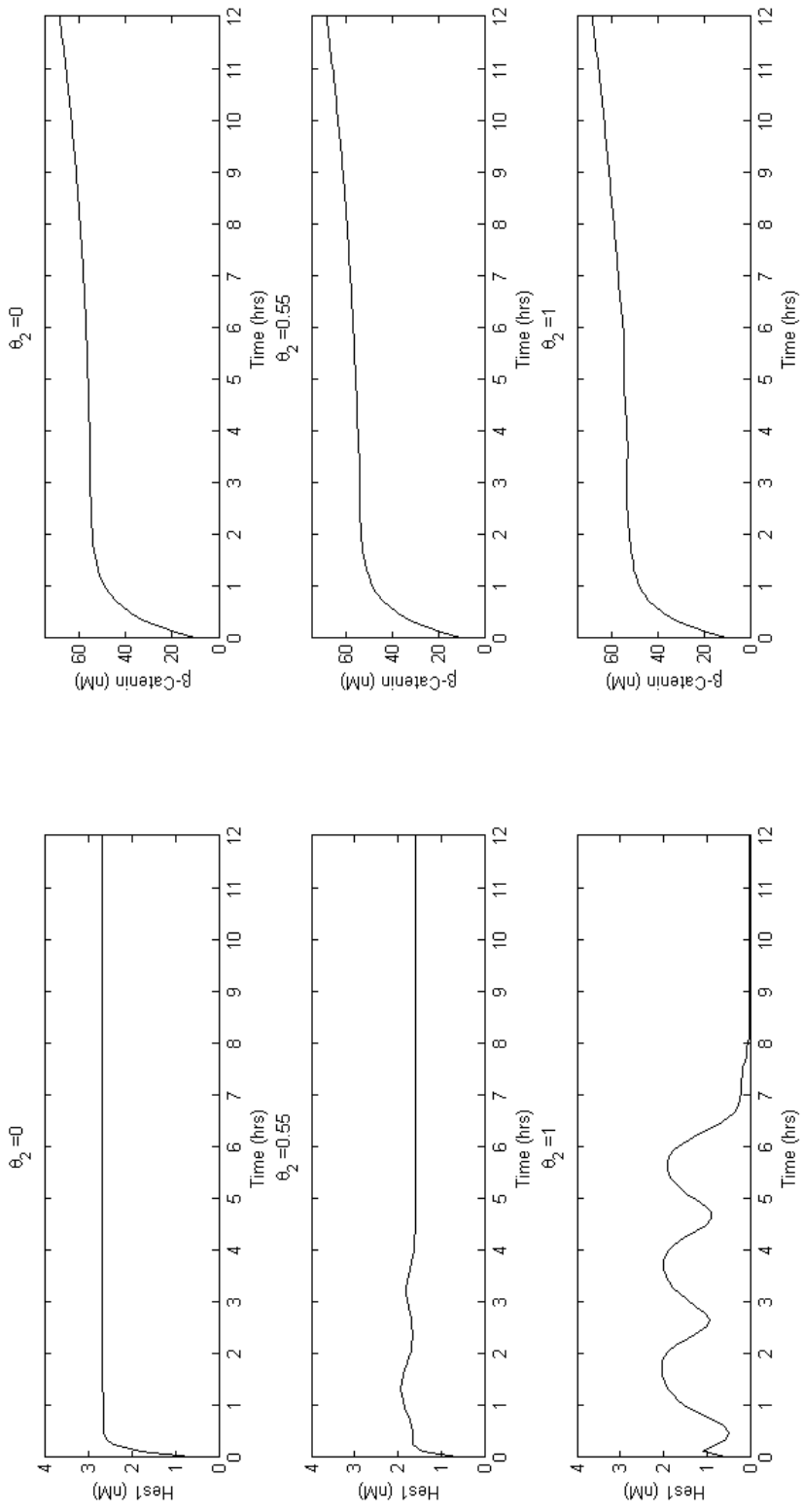

Figure 4.13: Influence of θ_2 upon the Hes1 steady state at $W = 1.0$. The timecourses show (left) Hes1 and (right) β-catenin expression for three cell pairs, using values of θ_2 ranging from (top) $\theta_2 = 0$ to (bottom) $\theta_2 = 1$. Standard initial conditions, listed in Table A.5, are used for each of the cells. Timecourses for each cell pair coincide in these simulations. Ultimately β-catenin settles upon a constant steady state at long times.

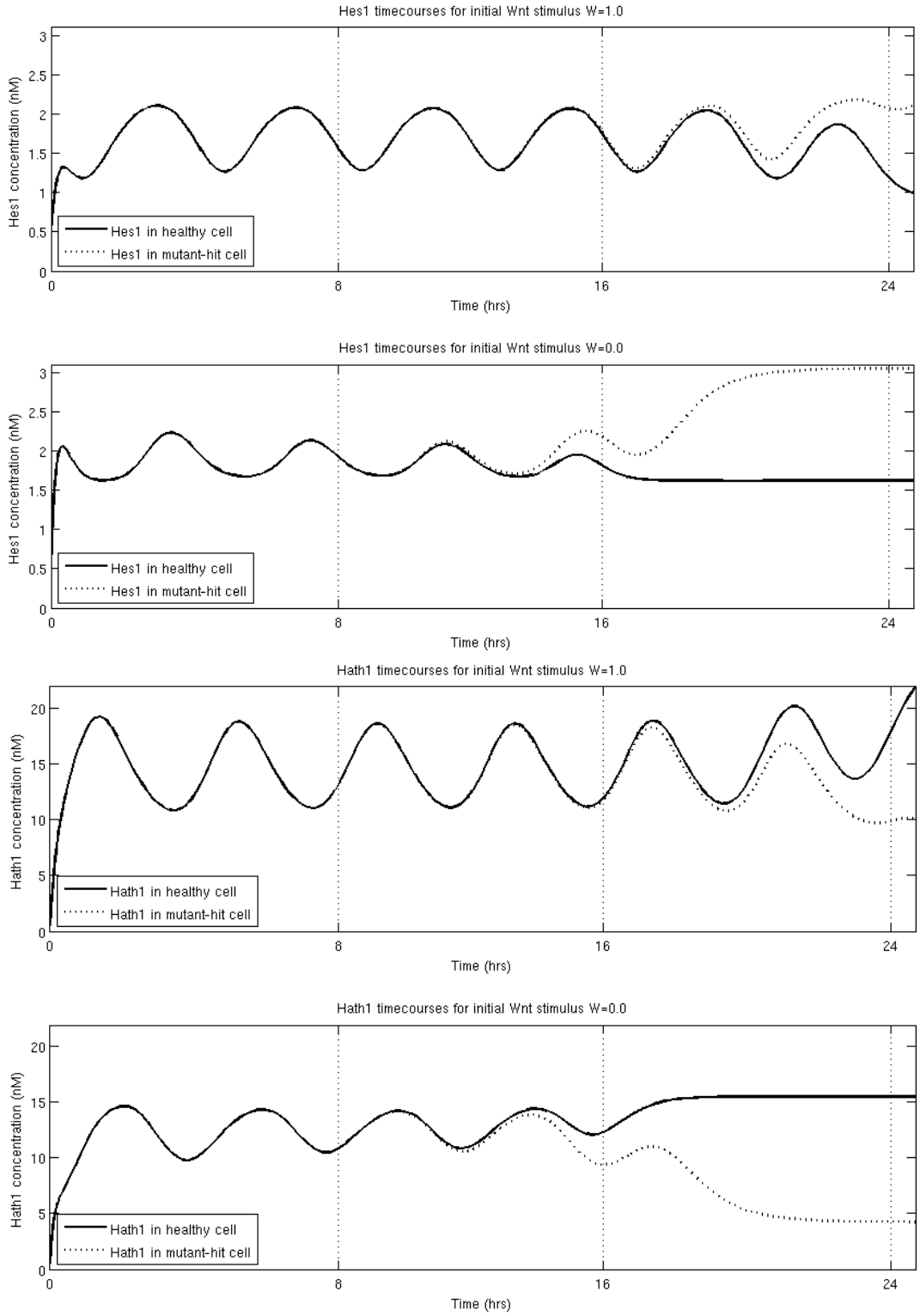

Figure 4.14: Timecourses for a cell pair, started from homogeneous initial conditions. Both cells are initially healthy; the second cell mutates over the course of the simulation, acquiring its first APC knockout at $t = 8h$ and its second at $t = 16h$.

is clear from Figure 4.15, the acquisition of APC mutation(s) reduces the destruction of β-catenin, thereby increasing its expression within the cell. Impairment of the destruction complex allows the mutant phenotype to express higher levels of Hes1, associated with prolonged mitotic activity, and reduced levels of Hath1, associated with cell-cycle exit, as shown in Figure 4.14. This is due to the interaction between the Notch and Wnt pathways around the β-catenin/Hes1 crosstalk hub. Elevated levels of β-catenin serve to upregulate Hes1, both through the direct binding of Step (14) and the indirect, NICD-mediated route of Step (4). This also causes damping of Notch oscillations, forcing the system to settle on a constant steady state.

Hyperstimulated Response to Extracellular Wnt

We now examine the consequences of mutations which confer a hyperstimulated Wnt state. This approach is based upon suggestions in the literature that differential response to Wnt stimuli, rather than differential exposure, is a major influence upon cell proliferation [1]. Figure 4.16 shows the outcome of mutation events in a cell pair; the lower plot in each case is devoid of Wnt stimulus ($W = 0.0$), whilst the upper plot evolves under a stimulus $W = 1.0$. Using standard initial conditions and parameters, simulations are run for 12 hours (720 min) with healthy cells. Thereafter, the second cell mutates to a hyperstimulated Wnt state, behaving as if $W = 2.0$, and the two-cell system is allowed to evolve for a further twelve hours.

Irrespective of whether the background Wnt stimulus is on or off, the healthy Hes1 timecourse in Figure 4.16 oscillates and demonstrates mild divergence by the twelve hour mark. At this point, the second cell has the higher Hes1 expression. Once this cell mutates, there is an abrupt change in the pattern of Hes1 expression; Hes1 levels in the mutant cell fall sharply, while the healthy cell increases its Hes1 expression. Oscillations do not occur post-mutation; the Hes1 timecourses intersect and the cells settle on a constant steady state, with a high-Hes1 healthy cell and a low-Hes1 mutant.

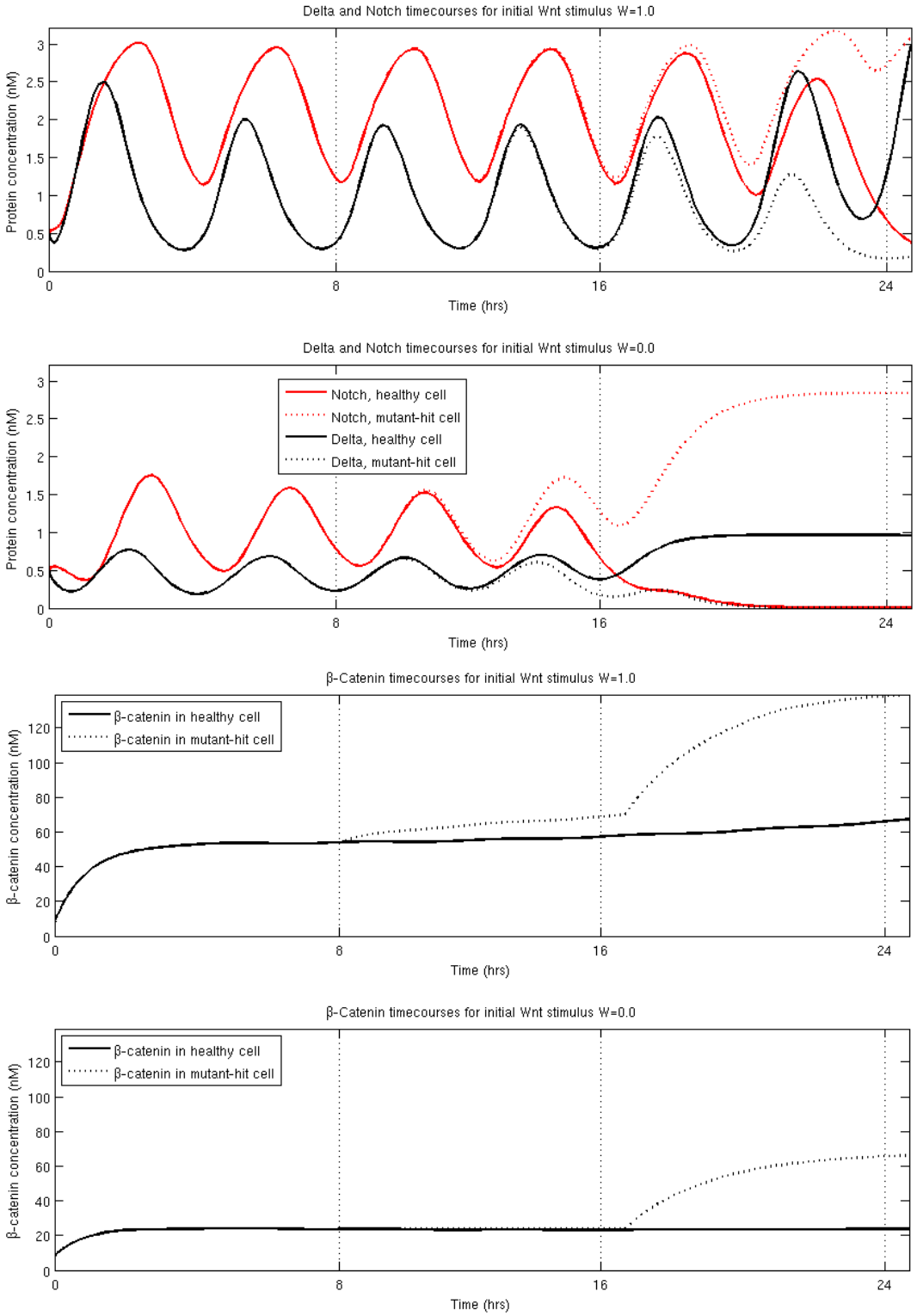

Figure 4.15: Expression of (top) Delta and Notch and (bottom) β-catenin in a two-cell system where the second cell acquires two successive APC mutations: a single APC mutation at $t = 8h$ and a second hit at $t = 16h$, indicated by the vertical gridlines. The homogeneous initial conditions are as for Figure 4.14.

Hyperstimulation of the Wnt pathway in the mutant cell enables it to invert the cell fate decision of its neighbour, forcing it from a primary to a secondary fate. Although this pattern of behaviour is evident in both the Wnt-on and Wnt-off scenarios, the transitions post-mutation are more pronounced and occur over shorter times in the low-Wnt scenario. This reversal of roles affects the entire Notch pathway, as confirmed by Figure 4.16, which shows the Delta and Notch expression of the healthy and mutant cells. Crossing of the timecourses for the two cells occurs as a result of the mutation event and the mutant cell begins to express high levels of Delta.

Given that Hes1 expression is associated with maintaining a proliferative phenotype, the ability of a mutant cell to invert cell fate decisions might stimulate surrounding cells to continue in a mitotically active state for longer. The elevated β-catenin expression of hyperstimulated mutants is also believed to help maintain active cycling. Consequently, mutation events might generate mitotically active clusters which are only partly composed of aberrant cells.

4.4.4 Insights From Reduced and Full Systems

The reduced systems presented in Sections 4.1.1 and 4.1.2 identify oscillatory regimes for the homogeneous steady state of the Notch subnetwork, governed by the relative strengths of β-catenin- and Notch-mediated Hes1 transcription. These are also observed in the whole system and the two-cell embedding. Indeed, CRNT analysis of the whole model in Section 4.2 suggests that the direct action of β-catenin upon the Hes1 promoter can confer monostability upon the system, while the two-cell embedding demonstrates the damping of Hes1 oscillations by the action of β-catenin.

Nonetheless, the CRNT results indicate that the reduced Notch system is not a good predictor of the stability of the whole system when all Hes1 transcription is Notch-mediated, in the presence of a Wnt stimulus. The nuanced interactions of β-catenin and Dishevelled with the Hes1 promoter play an important part in shaping the

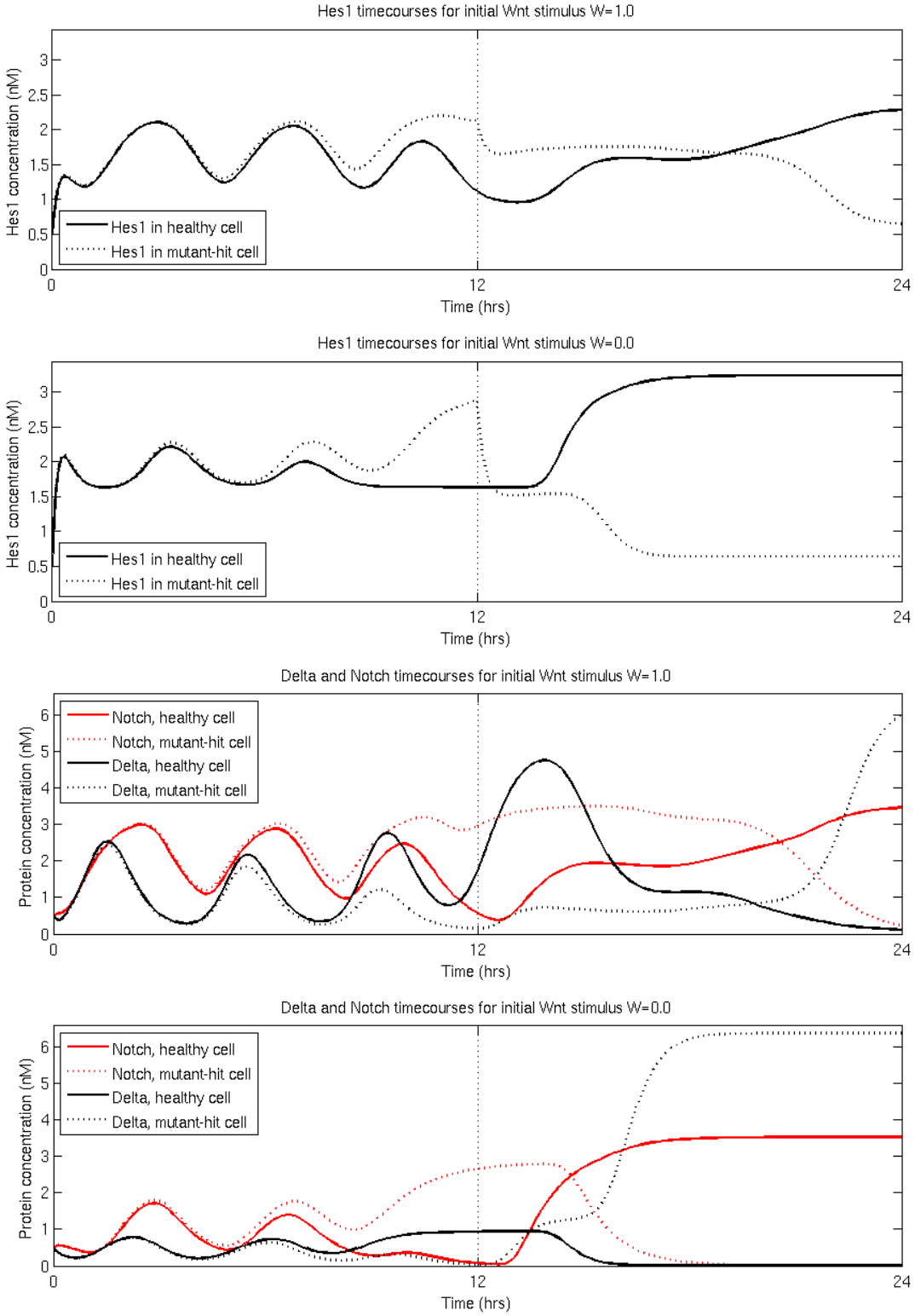

Figure 4.16: (Top) Hes1 and (Bottom) Delta-Notch timecourses for a coupled cell pair. Both cells remain healthy for the first 12 hours; at this point, the second cell (dashed line) mutates to a hyperstimulated Wnt cell and behaves as if $W = 2.0$.

dynamics of the biochemical cell fate selection mechanism, and justify our approach of studying Notch and Wnt as interacting systems, rather than disjoint networks.

Some features of the simple analyses carry through to the two-cell scenario: for example, the APC mutant phenotype displays elevated β-catenin expression owing to a reduced rate of formation of the destruction complex; this damps Hes1 oscillations more rapidly. However, the focus of the reduced models upon the homogeneous steady state precludes exploration of the cell-fate switching imposed by the Wnt-hyperstimulated phenotype upon a cell pair. This motivates the use of multicellular embeddings to capture the dynamics of cell fate selection at the tissue scale.

4.5 Conclusions

Several independent analyses in this chapter have confirmed that our model for Notch-Wnt interaction reproduces the main qualitative features of each pathway, such as the Notch pathway's capacity for damped oscillations, and provides good agreement with the available experimental data. The following principal findings have emerged:

Wnt acts upstream of Notch: Side-by-side timecourses for Hes1 and β-catenin show significant qualitative variation in Hes1, but little change in the expression pattern of β-catenin. This supports the idea of the Wnt pathway acting as an upstream regulator of Notch.

Wnt stabilises Notch: Direct action of β-catenin on the Hes1 promoter confers a single steady state on a homogeneous Notch-Wnt network. Increasing concentrations of β-catenin also reduce the final steady state of Hes1 via this direct transcriptional control. β-catenin crosstalk seems primarily to stabilise the output of the Notch pathway and to reduce the flexibility of fate decision which would otherwise be conferred by oscillations.

Actions on the Hes1 promoter shape Notch dynamics: Simulations in this chapter indicate that the presence or absence of oscillations is associated with control of the Hes1 promoter. Regulation of Hes1 transcription via the Notch intermediate I_1 helps to maintain oscillations, while Wnt-mediated regulation via direct β-catenin binding dampens them and induces the cell to settle on a constant steady state. Cells might regulate the relative contribution of these two transcription routes in order to coordinate the timing of cell fate selection.

Wnt hyperstimulation determines the fate of neighbouring cells: The mutation scenarios explored here suggest that cellular transformation to a hyperstimulated Wnt state drives neighbouring cells to adopt a secondary, low-Delta fate. This might enable the mutant cell to maintain neighbouring healthy cells in a mitotically active state and could have some relevance to the Cancer Stem Cell Hypothesis discussed in Section 1.2.

Analytic work in Section 4.1 suggests that a high binding rate between NICD and β-catenin could attenuate the response of the Wnt pathway to extracellular Wnt stimuli. Analysis of NICD timecourses from later simulations suggests that NICD attains equilibrium quickly and has a relatively small value at steady state. This may be an interesting line of enquiry for therapeutic interventions in hyperstimulated cells.

We shall explore the consequences of mutation at the tissue scale in Chapter 6. In anticipation of this, we begin by embedding our Notch-Wnt ODE model in a dynamic, cell-based crypt in Chapter 5.

Part C

Applications

5

Comparison With Buske et al. (2011)

Chapter Summary

In this chapter, we develop a multiscale, crypt-based embedding of our ODE model for Notch-Wnt crosstalk, endowing each cell in the simulated tissue with a set of continuous differential equations which govern the processes of proliferation and cell fate specification. Simulations of this embedding are compared with those of an alternative, rule-based approach proposed by Buske *et al.* [5]; both models predict the same spacing of secretory cells in the upper crypt, but the ODE-based approach is found to offer more robust pattern generation in the mid-crypt region.

5.1 Introduction

The opening discussion of this thesis asked how the processes of proliferation and cell fate selection interact within the environment of the intestinal epithelium. From the perspective of computational science, how should one reconcile the coupling of the relevant subcellular biochemistry – embodied by our ODE system for Notch-Wnt interaction presented in Chapter 3 – with events at higher spatiotemporal scales, such as the tissue-scale cell fate patterning of the crypt? Are certain modelling approaches preferable as regards their suitability for depicting the balance of cell division and fate determinance in the gut?

If we are to gain an understanding of the origins and treatment of CRC via computational modelling, then it is essential that we first understand the strengths and limitations of the modelling framework we are using, and compare its performance with that of alternative approaches in the modelling canon. Consequently, this chapter focuses upon modelling homeostasis in a healthy intestinal crypt.

A Modelling Comparison

Our own model for proliferation and cell fate selection in the crypt (hereafter referred to as the Notch-Wnt ODE-based model, or *NWODE model* for brevity) adopts the parameterised, dimensional system of ODEs formed by Equations (3.3) – (3.14), developed during Chapters 3 and 4. This system is embedded into individual cells of a cell-based tissue representing the intestinal crypt epithelium, which is described in Sections 5.2 and 5.3. The attendant issues of coupling the subcellular equations to higher-level processes are described and discussed in Section 5.4.

Not all approaches to crypt modelling require embedded equations: in particular, the rule-based representation of Buske *et al.* [5] (hereafter referred to as the *Buske model* for brevity) avoids the use of subcellular equations in favour of considering discrete states for each cell, in which the Wnt and Notch pathways are either constitutively active, or not. Implementation of this model is discussed in Section 5.5.

The computational studies of Sections 5.8 and 5.9 contrast the performance of the NWODE and Buske models. The rule-based formulation of the Buske model, being computationally simpler, provides an interesting counterpoint to the more complex ODE construction involved in the NWODE model. Comparison between these two models should inform us as to which method is preferable for a given modelling scenario. We subject the Buske and NWODE models to closer scrutiny in Sections 5.10 and 5.11, by examining their response to variation in their respective cell fate parameters for determining conversion to the secretory phenotype.

We now outline the tissue and cell cycle models used in the simulations to follow.

5.2 A Tissue-Level Model for the Crypt

All crypt simulations are carried out using a cell-centre tessellation tissue model in *Chaste*, as described in Section 2.4.1. The crypt epithelium is modelled as the two-dimensional surface of a cylinder in three-dimensional space, with laterally periodic boundary conditions. A zero-flux boundary condition is implemented at the crypt base, such that any cells moving below the boundary are pushed back into the crypt, thus preventing movement through the bottom of the domain. Cells which move beyond a given upper height are removed from the simulation, mimicking the sloughing processes which occur *in vivo*. Each crypt measures 22 cell diameters in height at the start of simulation, with a circumference of 10 cell diameters [195, 175].

A fixed linear gradient of the extracellular factor Wnt is imposed on the domain. Wnt is assumed to be at its highest concentration at the crypt base, where it adopts the (nondimensional) value $W = 1.0$, and declines up the crypt, to a value of $W = 0.0$ at the top. This decreasing, vertical Wnt gradient is consistent with current experimental observations [245]. Vasculature is not represented in the tissue model; instead the crypt environment is assumed to be nutrient-rich. This approach is similar to existing modelling work in the computational literature [195, 175].

All simulations in this chapter assume the crypt to be comprised only of healthy cells, of either transit, absorptive or secretory phenotype. Since we are modelling the colorectal epithelium, rather than earlier parts of the intestinal tract, we do not include Paneth cells in our representation. We also note that the model presented in Buske *et al.* employs a curved crypt base; we omit this here in favour of a simple, flat truncation to the cylinder, in the interest of focusing upon the cell fate mechanisms, but consider it a worthwhile area for extended studies in the future.

5.3 Cell Cycle Model

Both the Buske and NWODE embeddings utilise the same basic cell cycle model described in Figure 1.7, in which the lengths of the M, $G2$ and S phases are fixed, totalling 14 hours, and the $G1$ phase length is assigned at the point of cell birth, varying stochastically with a mean of approximately 2 hours. Cells can divide if they are mitotically active and have completed their cell cycle; this latter condition is determined by the age of the cell. Whether or not a cell is mitotically active depends upon the constraints of the individual model; we defer this detail until Section 5.4.

To facilitate fair comparison of the Buske and NWODE models, the cell cycles of both embeddings generate their $G1$ phase lengths from the normal distribution $N(2, 1)$, truncated to exclude negative or very small values (those less than 0.01 hours). This yields a mean cell cycle time of approximately 16 hours.

Nonetheless, the original published version of the Buske model assumed a Gamma-distributed phase length. Appendix C presents results from a series of Buske simulations in which the $G1$ phase lengths are drawn from the distribution Gamma$(4, 0.5)$, again truncated to exclude negative or very small values, to see whether the model yields the same behaviour. The graphs shown in Figures C.1 and C.2 show negligible difference between the outcomes when using Gamma- or normally-distributed G1 phase lengths: the timecourses for patterning behaviour in each case are indistinguishable, and the pattern metrics on ascending the crypt at dynamic equilibrium are almost identical. This provides sufficient grounds for adopting a truncated normal distribution throughout the comparisons in this chapter.

Cell growth during M phase is modelled by increasing the rest length of the springs between a cell, i, and its neighbours, j, in the underlying tissue model. This involves a change from $s_{ij} = 0.1$ to $s_{ij} = 1.0$ during the final hour of a cell's cycle, for the force summation shown in Equation (2.5). Outside this time window, a cell's spring

rest lengths are all set to $s_{ij} = 1.0$. After mitosis, the resulting daughter cell is placed 0.1 cell diameters away from cell i, in a randomly chosen direction. This approach is consistent with existing studies in the literature [195].

5.4 A Crypt Embedding of the NWODE Model

A crypt embedding of the system of ODEs described in Chapter 3 requires us to consider: how the behaviour of the Wnt system will be coupled to the cell cycle; how the pathway components will be inherited by daughter cells; and how the underlying Notch model should perform cell fate selection. Details of proliferative zones, inheritance and cell fate selection rules for the NWODE model are summarised in Figure 5.1 and Table 5.1, alongside those of the Buske model for comparison.

Wnt and Notch Signalling

Signalling and crosstalk for the Wnt and Notch pathways are modelled by the dimensional ODE system described by Equations (3.3) – (3.14). The value of the nondimensional Wnt stimulus, W, is taken directly from the local extracellular Wnt stimulus at the cell's location in the domain. For the purpose of calculating $\bar{D}$, the mean Delta concentration of neighbouring cells, a neighbouring cell is defined as one which shares a spring connection with a given cell, according to the construction of the underlying cell-centre tessellation tissue model. This is discussed at length in Section B.2.4 of Appendix B.

The Wnt system components of the model adopt initial conditions close to their steady state values at $W = 1$, listed in Table A.5 of Appendix A. Except where stated otherwise, the Notch components adopt randomised initial conditions drawn from the uniform interval $[0.475, 0.525]nM$.

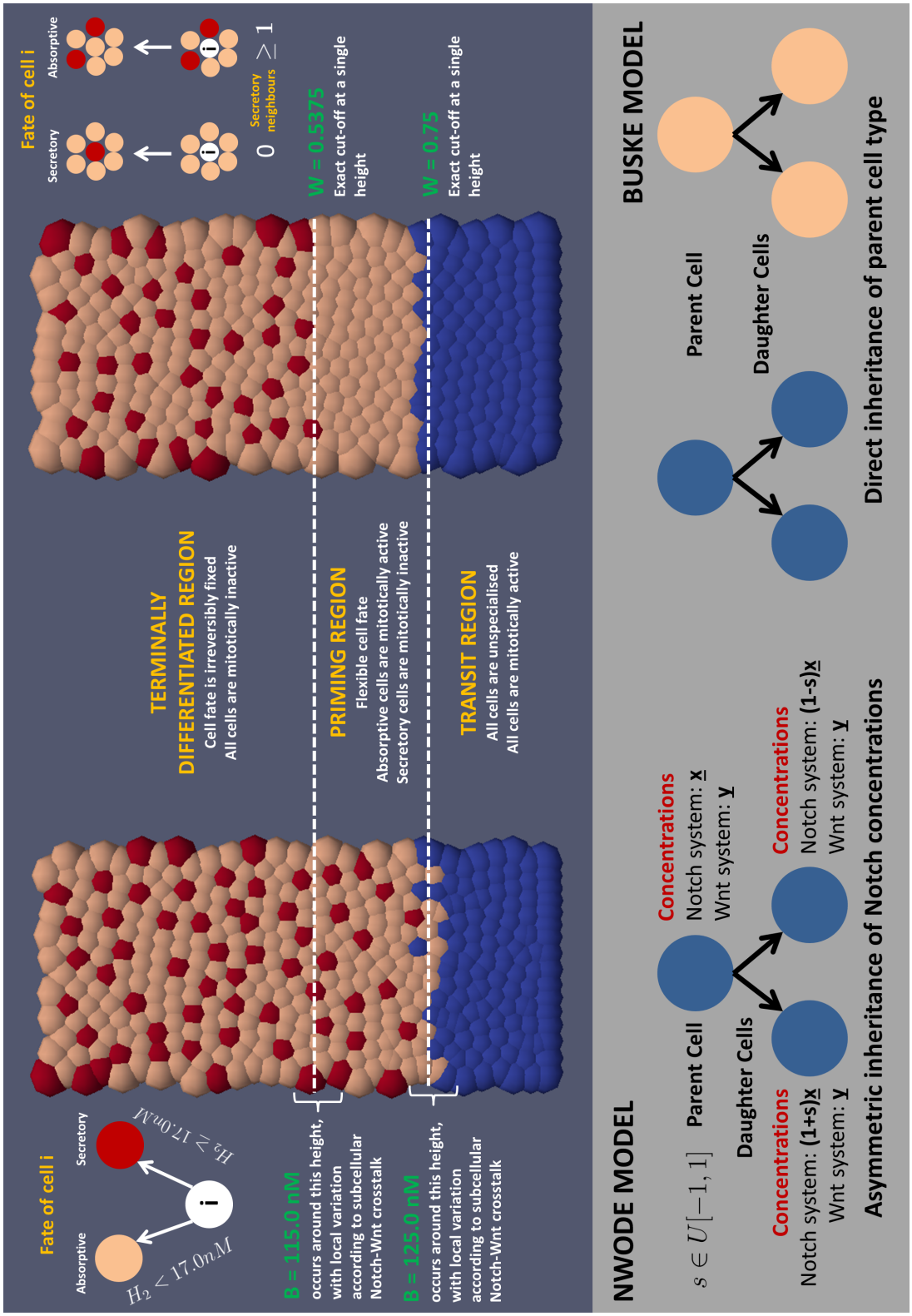

Figure 5.1: Crypt schematic for (L) the NWODE model, and (R) the Buske model. The upper part of the figure demonstrates the proliferative cut-off for each zone of the crypt, along with an illustration of the cell fate selection mechanisms used in the priming region. Lower diagrams indicate the inheritance models at mitosis.

Cell Phenotypes and Mitotic Activity

Proliferation and cell fate specification in the NWODE embedding are governed by two key thresholds of β-catenin expression: a transit cell threshold $b_{tr} = 125.0nM$, and a terminal differentiation threshold, $b_{td} = 115.0nM$. Whether or not a cell is mitotically active therefore depends upon its β-catenin concentration, B.

Cells in the lowest region of the crypt attain a state $B \geq b_{tr}$ and are mitotically active *transit cells*. The Wnt concentration, and hence the β-catenin state of cells, falls on ascending the crypt. The middle region of the crypt is characterised by concentrations $b_{tr} > B \geq b_{td}$ and is referred to as the *priming region*. The process of cell fate selection is assumed to begin here but these decisions remain flexible whilst cells remain within the priming region.

The NWODE model follows the biological tenet that Hes1 expression is associated with the formation of absorptive enterocytes [92] and Hath1 with the genesis of secretory goblet cells [91]. Given the reciprocal relationship between Hes1 and Hath1 [19], we use Hath1 expression to determine cell fate; once a cell is in the priming region, $H_2 \geq 17.0$ selects a cell for the secretory fate[1]. Otherwise, the cell adopts an absorptive type. Absorptive cells are assumed to be mitotically active, but secretory cells exit the cell cycle and are mitotically inactive. This agrees with the results of Hes1 knock-out studies in the literature, in which murine crypts devoid of Hes1 experience a significant increase in goblet cell numbers and a reduction in the size of the proliferative compartment [91].

The uppermost region of the crypt is exposed to the lowest Wnt stimulus and the β-catenin states adjust accordingly, such that $B < b_{td}$; this adjustment can be seen in the homogeneous, two-cell simulation in the lower graph of Figure 5.2. Beyond this threshold, cells become *terminally differentiated* as either secretory or absorptive

[1]This value was selected following inspection of the Hath1 concentration range in an NWODE crypt over 300 hours of simulation.

types, and are mitotically inactive. Proliferation is thus restricted to the lower regions of the crypt and cells become progressively more specialised on ascending the crypt, in line with experimental observations [13].

The values of the thresholds b_{tr} and b_{td} are determined from simulations of a homogeneous implementation of the ODE system (3.3) – (3.14). The upper plot of Figure 5.2 shows the variation in the β-catenin steady state with the local Wnt stimulus. These steady-state results are used to calibrate the thresholds to bring the crypt proportions into agreement with the biological findings discussed in Chapter 1.

Inheritance

Daughter cells inherit the Wnt pathway concentrations of the parent cell at the point of cell division and sample the Wnt concentration of their local environment prior to further solution of their associated ODE systems; as far as we are aware, there is no evidence at the present time to indicate asymmetric inheritance in the Wnt pathway. Notch pathway components from the parent are shared asymmetrically between the daughter cells, in agreement with observations in the experimental literature [69].

Asymmetric inheritance is determined by a 'skewness factor' $s \sim U[-1, 1]$, generated anew for each division event. The two daughter cells inherit multiples $(1 + s)$ and $(1 - s)$ respectively, of the concentrations of Notch components in the parent cell. This ensures conservation of Notch during each division event. The spatial location of either daughter does not influence which receives higher or lower concentrations of Notch components from the parent cell.

5.5 A Crypt Embedding of the Buske Model

The Buske model adopts a far simpler approach to modelling Notch and Wnt activity. Rather than using embedded ODEs, Buske *et al.* endow each cell with two binary fate

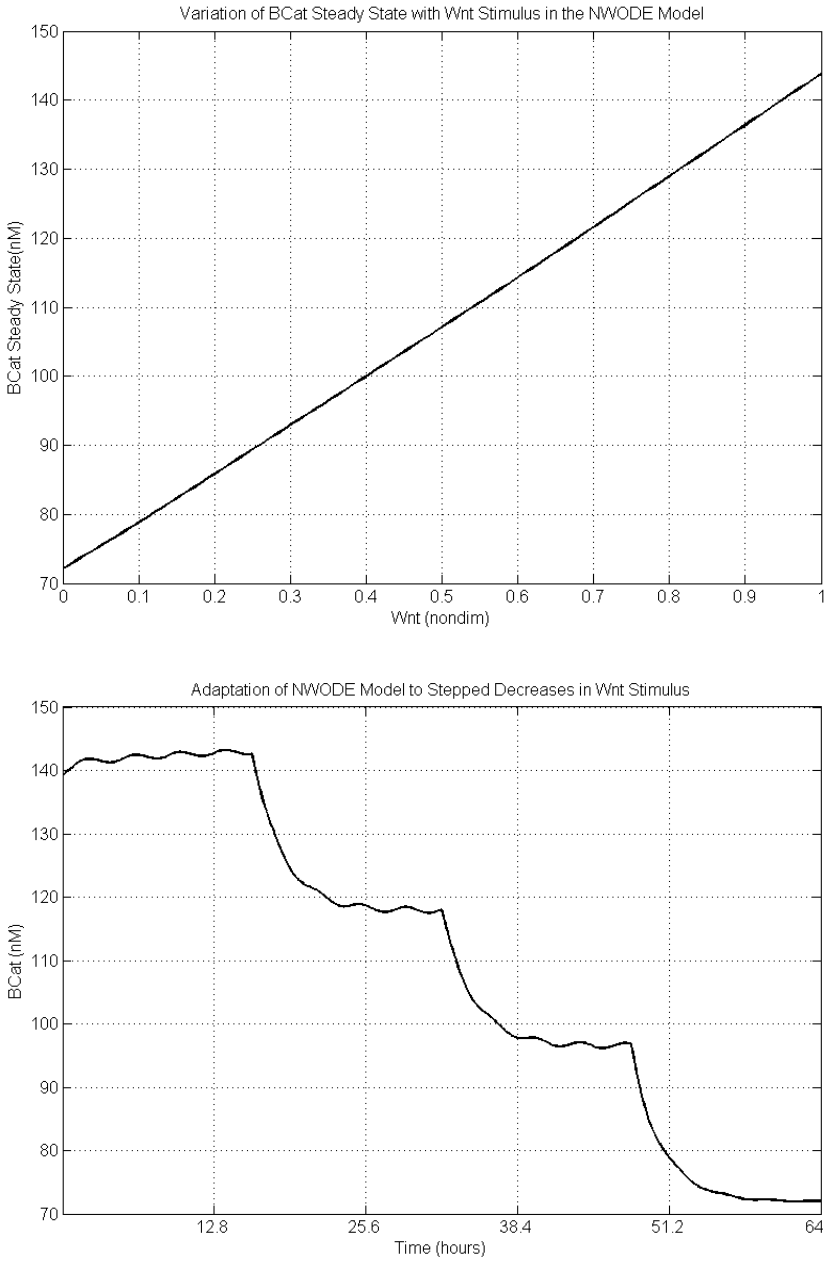

Figure 5.2: Behaviour of the β-catenin homogeneous steady state in the Notch-Wnt ODE model: (Top) Variation of the β-catenin steady state with the external Wnt stimulus; (Bottom) Demonstration of β-catenin adjustment within a cell in response to stepped decreases in Wnt stimulus. Initially the cell is subject to a $W = 1.0$ stimulus; this falls to $W = 0.65$ at $t = 16h$, $W = 0.35$ at $t = 32h$ and $W = 0.0$ at $t = 48h$. Initial conditions are a homogeneous version of the crypt values stated in Table A.5 of Appendix A, i.e. using non-randomised Notch conditions.

NWODE Model	Attribute	Buske Model
Embedded ODE system, Equations (3.10) – (3.14) 5 biochemical entities represented	**Wnt signalling**	Binary status: Wnt pathway either ON or OFF No explicit biochemical representation
Embedded ODE system, Equations (3.3) – (3.9) 7 biochemical entities represented	**Notch signalling**	Binary status: Notch signal either ON or OFF No explicit biochemical representation
Direct inheritance of Wnt components Asymmetric inheritance of Notch components Daughters inherit multiples $(1+s)$, $(1-s)$ of the parent Notch concentrations respectively, for $s \sim U[-1,1]$	**Inheritance**	Direct inheritance of cell type from parent cell
Cells are mitotically active for $B \geq 125.0nM$	**Proliferation**	Cells are mitotically active for $W \geq 0.75$
Fate priming occurs for $B < 125.0nM$ Secretory cells develop when $H_2 > 17.0nM$ in the underlying ODE system bsorptive cells develop otherwise	**Fate selection**	Fate priming occurs for $W < 0.75$ Secretory cells develop for Notch OFF (i.e. no secretory neighbours) Absorptive cells develop otherwise
Occurs for $B < 110.0nM$	**Terminal differentiation**	Occurs for $W < 0.5375$

Table 5.1: Summary of the differences between the Buske and NWODE crypt embeddings.

statuses: one for Notch, and one for Wnt. Pathway activity is therefore either ON or OFF in each case; there are no intermediate states or explicit Notch-Wnt crosstalk.

Although this approach in its current form precludes explicit study of subcellular pathway interactions, the studies of Section 5.6 aim to determine whether or not this simpler, rule-based approach may prove advantageous in particular modelling scenarios. Table 5.1 summarises the differences between the Buske and NWODE approaches and a schematic of the two models is shown in Figure 5.1. Except where otherwise stated, we adopt the parameter values described in Buske *et al.* [5] to maintain continuity with the literature.

Wnt and Notch Signalling

The absence of an embedded ODE representation from the Buske model yields a simpler representation of Notch and Wnt signalling. The Wnt activity status of a cell is determined by the strength of the local Wnt stimulus, W, in relation to the priming threshold, w_{tr} and the terminal differentiation threshold, w_{td}. Wnt activity status is drawn directly from the spatial location of the cell and does not account for local variability in the Wnt activity of individual cells at a given height up the crypt.

Notch behaviour in a given cell is determined by a contact-based analysis which examines the phenotype of neighbouring cells. That is, the Notch activity level of a cell i is determined by

$$\text{Notch}_i = \sum_{j \in J} \text{Status}_j \,, \tag{5.1}$$

$$\text{for } \text{Status}_j \in \{0, 1\}, \text{Notch}_i \in \mathbb{N}.$$

where J is the set of cells neighbouring cell i (defined, as before, according to cell-cell connections in the associated tissue model) and Status_j depends upon the phenotype

of cell j: $\text{Status}_j = 1.0$ for secretory cells and 0.0 for transit and absorptive cell types.

Cell Phenotypes and Mitotic Activity

Partitioning of the crypt into active transit, priming and terminally differentiated regions is similar to that of the NWODE model, but with thresholds determined directly by the local Wnt stimulus. Whether or not a cell is mitotically active therefore depends upon a priming threshold, w_{tr} and a terminal differentiation threshold, w_{td}.

Crypt base: Cells for which $W \geq w_{tr}$ are mitotically active *transit cells*.

Priming region: The priming region is bounded by the thresholds $w_{tr} > W \geq w_{td}$. *Absorptive cells* in this region are assumed to be mitotically active, while *secretory cells* exit the cell cycle;

Upper crypt: All cells for which $W < w_{td}$ are *terminally differentiated* as either secretory or absorptive types, and are mitotically inactive.

For comparison with the NWODE model, the thresholds w_{tr} and w_{td} are set to the Wnt values which yield the homogeneous β-catenin steady state thresholds b_{tr}, b_{td} implemented in the NWODE model.

Cell type updating in the Buske model is determined by the summation rule of Equation (5.1). If $\text{Notch}_i \geq 1.0$, cell i becomes an absorptive cell at the next timestep; otherwise it becomes a secretory cell. Consequently, any cell which neighbours a secretory cell will always become absorptive in the priming region; conversely, transformation to a secretory cell can only occur where a cell has no secretory neighbours.

Except where stated otherwise, initial conditions for the Buske model set cells below $W = w_{tr}$ to be of transit type. Cells above this height are randomly assigned either secretory or absorptive phenotypes, such that a cell has probability 0.2 of being a secretory cell, in line with the proportions reported in Buske *et al.* [5].

Inheritance

Owing to the absence of embedded ODEs, daughter cells in the Buske model inherit their parent's cell type directly. This is always either a transit or an absorptive type, since these are the only two mitotically active phenotypes. Cell types are updated at every timestep, according to the summation rule stated in Equation (5.1).

5.6 Data Generation

Implementation of both the Buske and NWODE models relies upon random number generation, whether to determine an initial distribution of cell types (as in the Buske model) or to specify randomised initial conditions for an underlying ODE system (for the NWODE model). Both models also utilise random numbers throughout the simulation process in order to generate G1 phase lengths. Consequently, all simulations are performed for 100 random number seedings; this enables settling of the means and standard deviations, whilst remaining computationally feasible. Results reflect the mean/standard deviation of these 100 outcomes, except where stated otherwise.

Output Metrics

Our comparison between the Buske and NWODE models focuses upon their cell fate selection mechanisms: how many of each cell type are produced, and how are the differentiated cells distributed? Consequently this chapter examines three main metrics: total counts for each cell phenotype; mean spacing between secretory cells, expressed in terms of mean cell diameters; and the Ripley H-Value for dispersal of secretory cells. These outputs enable not just the tracking of the proportions of the various cell types, but also of the spatial distribution of primary fate cells generated by the Buske and NWODE models.

The Ripley H-Value [246] is a statistical measure used to measure point dispersal in

2D space, or on a 2D surface as in our crypt simulations. Ripley's H-Value lies on the interval $[-1, 1]$; -1 represents perfect dispersal and 1 perfect clustering, while a value of zero indicates purely random scattering commensurate with a Poisson distribution. This measure is discussed in full in Appendix B and is demonstrated for a simple crypt embedding of the model of Collier *et al.* [125] in Figures B.10 and B.11. An evaluation of its performance on cell-centre tessellation, node-based and vertex dynamic tissue models is provided in Section B.3.1.

Partitioning of the Crypt

We partition the crypt surface into distinct zones in order to provide a more fine-grained Ripley analysis of the domain. These zones are shown in Figure 5.3; each is of equal area and its bounds remain fixed throughout simulation. The first four zones are used for the Ripley timecourses of Figures 5.8, 5.14 and 5.15; however, the graphical summaries of behaviour at dynamic equilibrium, shown in Figures 5.9 and 5.16, use results from all seven zones, in order to provide a more detailed impression of the variation in Ripley value on ascending the crypt.

5.7 Runtime

Crypt embeddings of the Buske and NWODE models are established and run until dynamic equilibrium is attained. Runtime is determined by measuring the number of processor seconds required to run a crypt at dynamic equilibrium for 200 hours of crypt time. Timings reflect the outcome when running as a single-threaded program on an Intel Core 2 Quad CPU 8300, 2.5GHz processor.

This assessment includes mechanical updates to the underlying tissue mesh, cell birth, death and fate selection processes, and – where relevant – solution of equations by external solver libraries. No output metrics (e.g. Ripley analysis, cell counts) are

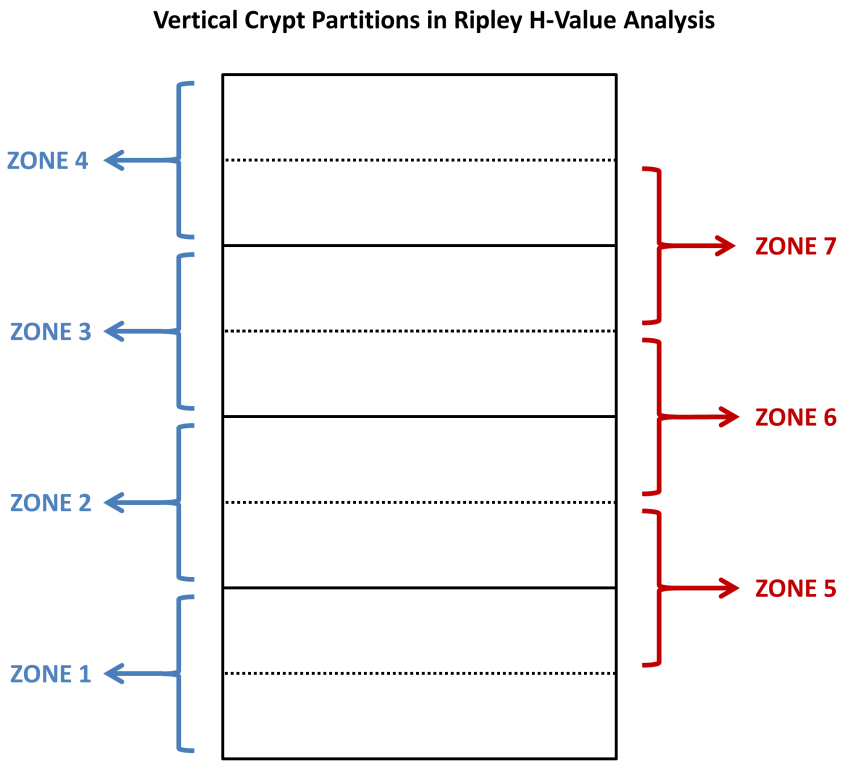

Figure 5.3: Subdomain partitioning for Ripley analysis of the crypt domain. The 2D cylindrical surface (shown here rolled out into a rectangle) is split into four main zones, numbered $1-4$ low-to-high, and the H-Value is assessed for each zone. Three further subdomains, numbered $5-7$, are of equal height to Zones $1-4$ but are staggered to start and end at the midpoints of the first four zones. This provides seven distinct zones for pattern analysis up the crypt.

performed during the runtime analysis.

The NWODE model takes 2353 seconds (39.2 minutes) to simulate 200 hours of crypt time. The Buske model is over three times faster, taking 707 seconds (11.8 minutes), as its reliance on rule-based cell fate selection does not require calls to an ODE solver. The computational simplicity of the Buske formulation therefore offers significant advantages with regard to runtime.

5.8 Robustness of Pattern Generation

First, we test the robustness of pattern generation using a simple case study: a crypt with unpatterned initial conditions. Both the Buske and NWODE crypts are established as described in Section 5.2. Instead of providing randomised initial conditions to the ODEs of the NWODE model, all equations are set off from a homogeneous state[2], in which the expression of Hath1 is uniformly low. An analogous setup is employed for the Buske model, such that all cells in the priming and differentiated regions are defined to be absorptive cells.

For the purposes of investigating the pattern generation properties, cell totals and Ripley analyses are output for every timestep of the simulation (equivalent to 18 seconds of crypt time), as opposed to the simulations of Section 5.9, in which metrics are read out one per half hour of crypt time. This requires a long runtime (several days to simulate 200 crypt hours) and so we present results for a single, representative simulation here.

Snapshots of crypt evolution at consecutive timesteps are shown in Figure 5.4, while Figure 5.5 shows the resulting dynamic equilibrium. Figure 5.6 depicts timecourses for the totals of secretory, absorptive and transit phenotypes for both the NWODE and Buske models.

Comments on the Buske Model

The upper row of screenshots shown in Figure 5.4 depicts the Buske model at consecutive timesteps, early in the equilibration phase. Cells in the priming region oscillate *en masse* between absorptive and secretory phenotypes at consecutive timesteps (each equivalent to 18 seconds of crypt time).

This artefact is not discussed in Buske *et al.* [5] and could be due to the choice of output timestep for their data collection. Block oscillations occur over consecu-

[2] i.e., using non-randomised versions of the initial conditions stated in Table A.5 of Appendix A.

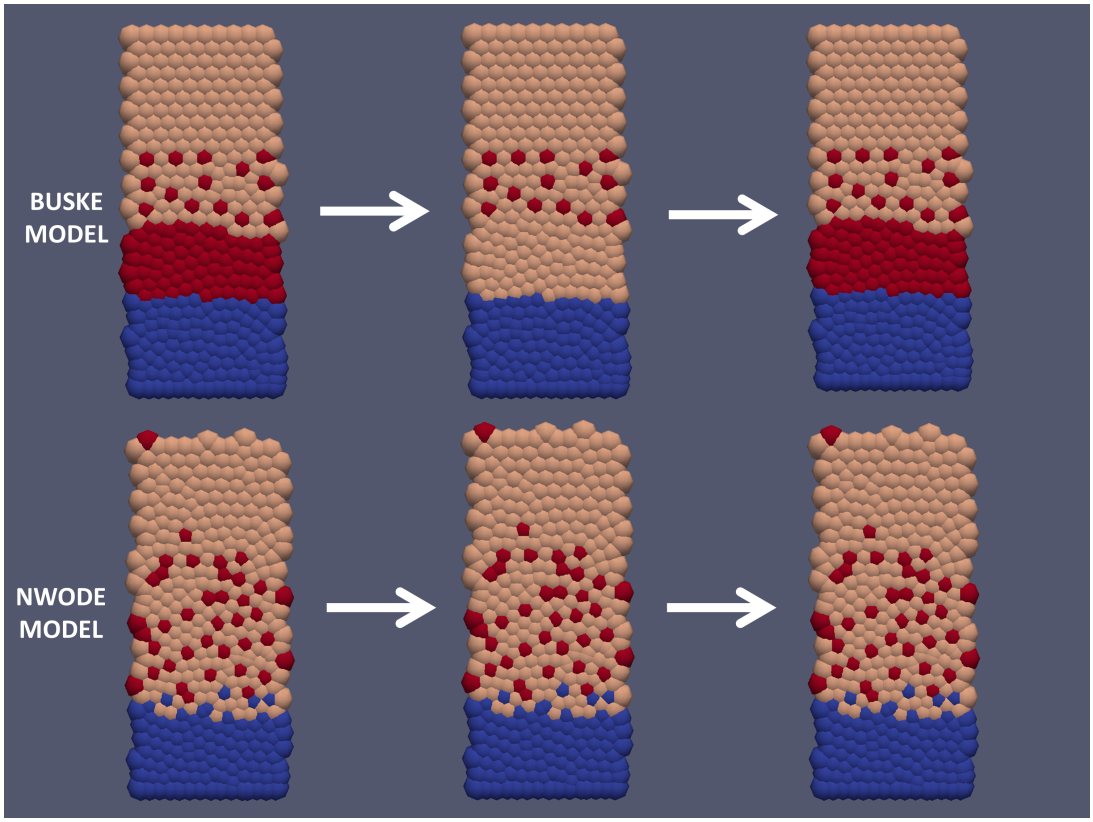

Figure 5.4: Screenshots of the Buske and NWODE models at successive timesteps during the equilibration phase, using unpatterned initial conditions. The Buske embedding displays block oscillations in which the priming region alternates between absorptive (peach) and secretory (red) phenotypes; transit cells are shown in blue. Such oscillation is an artefact of the rule-based approach to cell fate selection described by Equation (5.1). By contrast, the NWODE embedding is not susceptible to this behaviour, owing to its use of an ODE model to determine cell fate.

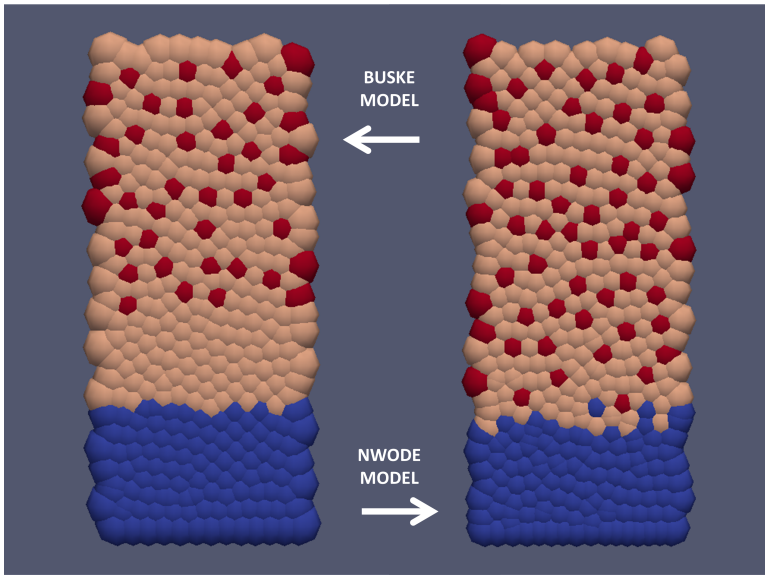

Figure 5.5: Crypts at dynamic equilibrium in the (L) Buske and (R) NWODE models, generated from unpatterned initial conditions. The Buske crypt still displays block oscillation of the priming region at this stage, and is shown for the absorptive phase of oscillation in this snapshot.

tive simulation timesteps in the Buske model, so if the simulation and data output timesteps do not coincide, the block oscillations cannot be detected. Our own simulations of the Buske model in Section 5.9 do not detect this behaviour for the same reason, because they employ a longer output timestep which always observes the crypt in the same phase of oscillation.

Oscillation of the priming region is a consequence of the discrete Notch summation described by Equation (5.1) and the secretory conversion threshold $\text{Notch}_i \geq 1.0$: any cell which has even one secretory neighbour will become an absorptive cell at the next timestep. Use of unpatterned initial conditions therefore predisposes the priming zone to alternate between absorptive and secretory phenotypes. The role of cell fate parameters in Equation (5.1) merits further study and we shall evaluate the influence of the secretory conversion parameter, $Status_j$, on cell fate patterning in Section 5.10. Buske *et al.* also explore alternative parametrisations and find that

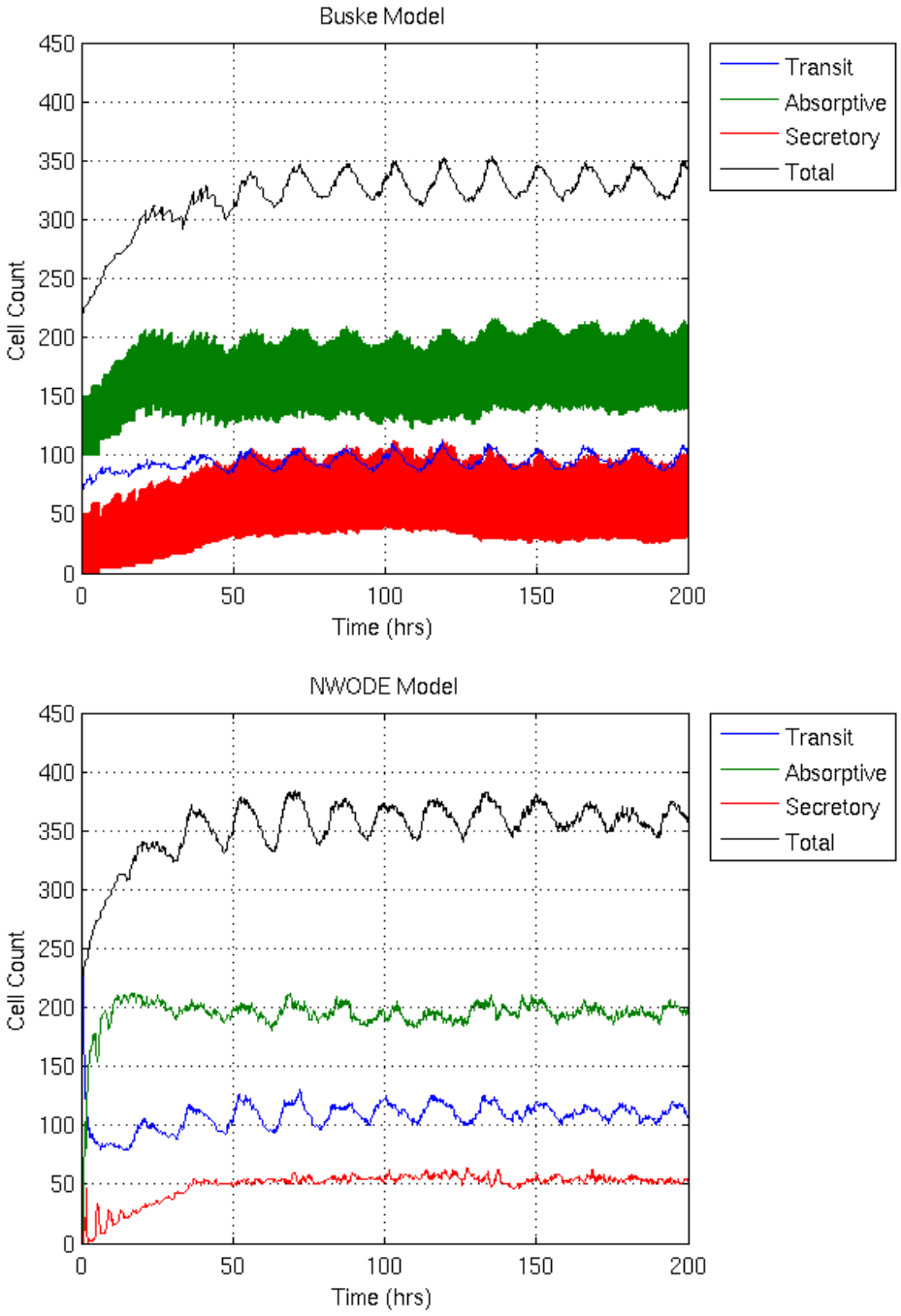

Figure 5.6: Cell totals for the different cell types over the course of a single simulation run, started from unpatterned initial conditions. (Upper) Cell totals for the Buske model; lines for the absorptive and secretory cell types appear densely packed, owing to block oscillations occurring in the priming region, as illustrated in Figure 5.4. (Lower) Cell totals for the NWODE model. Transient oscillations at the start of simulation are due to spatiotemporal oscillations in the underlying Notch system as the domain equilibrates.

increasing the secretory conversion threshold for $Notch_i$ increases the secretory cell count and reduces the number of undifferentiated and absorptive cells.

Block oscillation of the priming zone does not impede the development of patterning in the differentiated region, as shown by the dynamic equilibrium image of Figure 5.5. The fixed upper regions of the crypt display a dispersed pattern of secretory phenotypes, because individual cells are gradually pushed up into the terminally differentiated region by the mitotic pressure generated from cell division in the lower crypt regions. A given cell may cross the threshold w_{td} in either the absorptive or secretory phase of oscillation and its fate is fixed thereafter. If such a cell has adopted a secretory type, it induces Notch activation in neighbouring cells which are still in the priming region; these cease oscillating, and later become absorptive cells when they are pushed out of the priming region. Transit cells do not contribute to the Notch status of neighbouring cells and so the Buske model has no prepatterning facility in the lower crypt when used to model the crypt epithelium of the large intestine, since there are no Paneth cells to induce Notch activation.

Simulation of the Buske model from unpatterned initial conditions does not preserve a strict size ordering of the three phenotype populations: a Buske crypt may contain more secretory cells than transit cells, or *vice versa*, depending on the phase of oscillation at a given timestep. Experimentally observed samples of intestinal tissue do not report this level of variation [201, 214, 122]. However, current laboratory techniques do not permit the observation of crypt tissue in continuous time and so it is difficult to obtain accurate biological approximations of cell total timecourses against which to compare these results.

Comments on the NWODE Model

Homogeneous initial conditions represent an unstable steady state of the NWODE model, as for the model of Collier *et al.* [125] discussed in Section 2.1.1. Asymmetric

inheritance of Notch components at mitosis is a vital driver of cell fate selection in this tissue-level embedding, by perturbing the NWODE model from the homogeneous state to facilitate the emergence of heterogeneity. A distributed pattern of secretory cells within the priming region has already developed in the snapshots shown in Figure 5.4 and propagates up the crypt to achieve patterning of both the priming and differentiated regions at dynamic equilibrium, as in Figure 5.5.

The continuous[3] ODEs provided by the NWODE model allow for nuanced changes to a group of neighbouring cells, over a series of timesteps. This permits gradual progression towards a patterned state; the stills shown in Figure 5.4 show no cell type changes over three timesteps, which represent 36 seconds of crypt time. This is consistent with observations of Notch pathway equilibration timescales *in vitro* [83].

Some transient oscillations occur during the first ten hours of simulation, as can be seen from Figure 5.6, arising from equilibration of the Notch pathway. They are the multicellular analogue of the oscillations seen in the two-cell simulations of Figure 4.12 and have a wavelength of many, rather than consecutive, timesteps. Once the system has attained dynamic equilibrium, these oscillations cease and small heterogeneities across the priming region permit the emergence of a fully patterned state. The NWODE model maintains a strict ordering of the population size of the different cell phenotypes: absorptive cells are the most numerous, followed by transit cells, with secretory cells fewest in number.

Inspection of Hath1 and Hes1 concentrations in movies of NWODE crypt simulations indicate that the use of ODEs to implement cell fate decisions generates subcellular heterogeneity in the transit region of the crypt. Although the mitotic activity of this region prevents a full prepattern from emerging, Hath1 concentrations of cells and their neighbours begin to diverge prior to entering the priming region. This may assist the development of priming region patterning in the NWODE crypt embedding.

[3] That is, piecewise continuous, viewed from a computational perspective.

5.9 Simulation From Heterogeneous Initial Conditions

All the remaining simulation results reflect the outcome of crypts started from heterogeneous initial conditions. Runtime considerations induce us to write out metric data once per half hour of crypt time. Block oscillations of the Buske model still occur throughout these simulations but are not apparent in Figures 5.7 – 5.10, as the output timestep observes the priming region in the same oscillatory phase on each occasion.

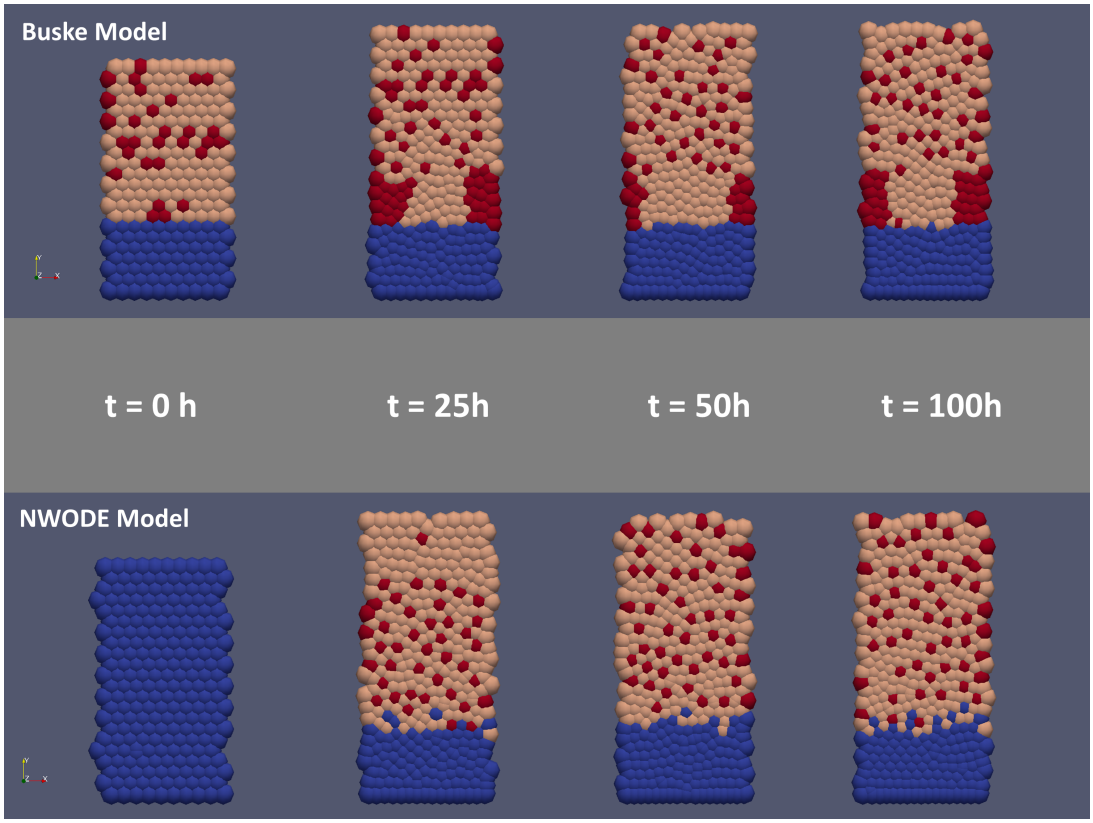

Figure 5.7: Evolution timecourses for (top) the Buske model, and (bottom) the NWODE model, showing the progression through the equilibration process until a dynamic equilibrium is attained around $t = 50h$. Transit cells are shown in blue; absorptive cells are peach and secretory cells are red. The Buske model has to be directly set up with secretory and absorptive phenotypes already specified. The NWODE model bases its cell fate decisions on the concentration of Hath1 in its subcellular ODEs; consequently all cells are initially labelled as transits and the cell type is updated in the first simulation timestep, immediately following the initial snapshots at $t = 0$.

Features of the Secretory Cell Distribution

Both the rule-based and ODE methods produce a similar mean spacing of secretory cells in the upper crypt regions of Zones 3 and 4, as shown by Figure 5.8. In particular, they both predict a secretory cell pattern of approximately 2.2 cell diameters, with an associated Ripley H-value of $H = -0.4$, indicating dispersal. Zone 1 consists solely of transit cells and therefore returns a zero Ripley value throughout the simulations.

This is an interesting result and suggests that a more sophisticated ODE approach is not essential for generating the specific secretory cell distribution seen here. The observed pattern lengthscale may arise from the method of determining the "nearest neighbours" with which a given cell interacts; the contact-based nature of Notch processes may therefore be instrumental in regulating the extent of secretory cell dispersal. Dependence of patterning on neighbour selection has already been demonstrated for the juxtacrine signalling model of Webb and Owen [134] on regular and irregular hexagonal and square lattices of cells[4]; similar analysis of the Buske and NWODE models could prove a useful area for further study.

Substantial differences between the models arise in Zone 2; this is a mitotically active region, and the one in which initial cell fate selection occurs. The Ripley H-values shown in Figure 5.8 indicate clustering of the secretory cells in Zone 2 of the Buske model (Ripley's H-Value > 0). This distribution is also visible in the priming region of the Buske snapshots in Figure 5.7. Such clustering deviates significantly from qualitative expectation, as the biological literature only reports dispersed patterns of secretory cells [201, 214, 122]. The NWODE model consistently produces a dispersed pattern of around two cell diameters in the same region.

The line graphs of Figure 5.9 summarise the secretory cell spacing and associated Ripley H-Values for the Buske and NWODE models at dynamic equilibrium. Both

[4]Webb and Owen find that a hexagonal array has a smaller region of parameter space for which patterning is possible. Irregularities of the underlying mesh can drive the development of defects within the dominant patterning regime.

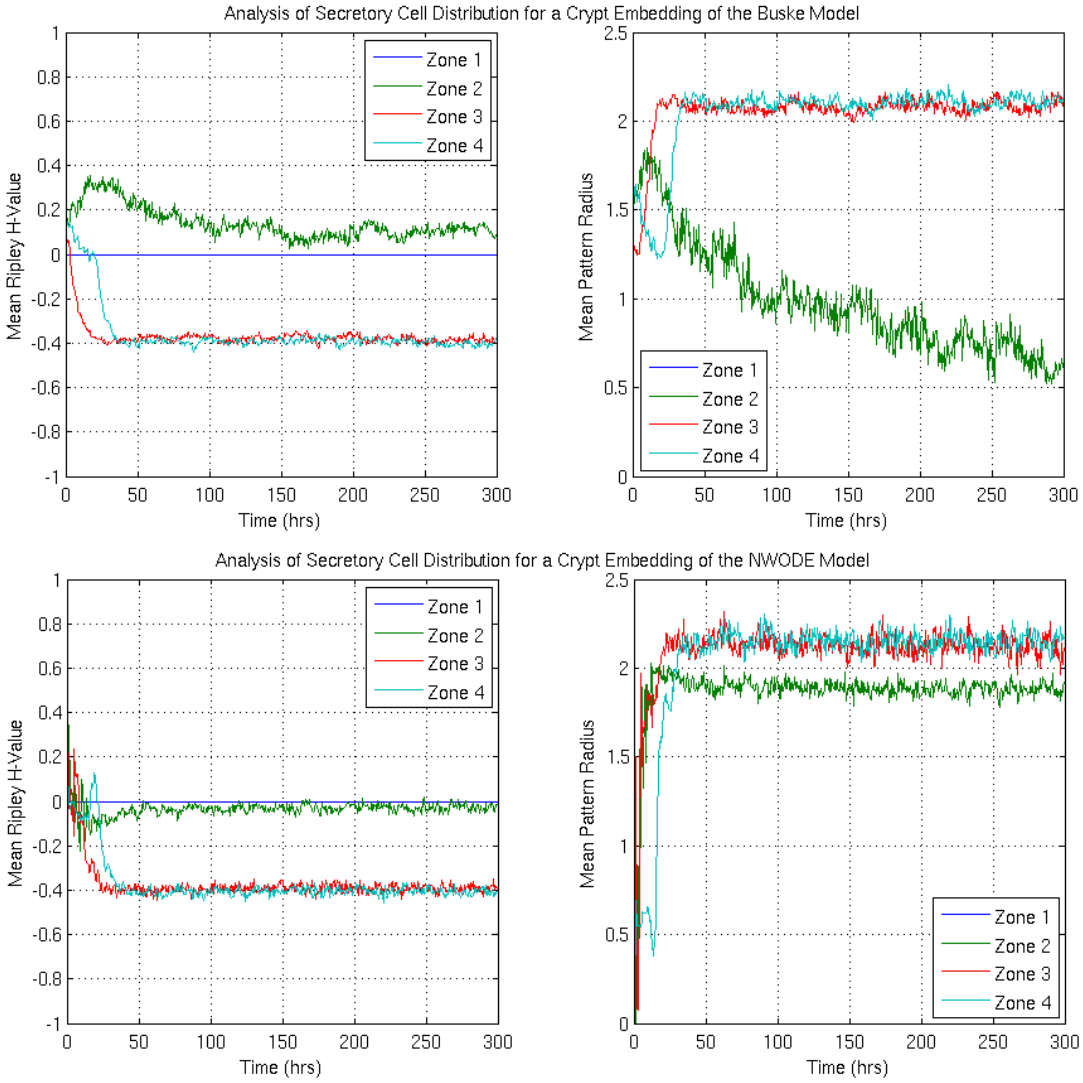

Figure 5.8: Distribution of secretory (goblet) cells within four height bands of the crypt, numbered from lowest (Zone 1) to highest (Zone 4); results for the Buske model are shown on the upper plots, and those for the NWODE model on the lower. Left-hand plots depict Ripley H-Values for each of the zones, whilst those on the right provide timecourses for the mean pattern radius of secretory cells. Pattern radius readings for Zone 1 always remain at zero, as this is the transit zone and does not contain secretory cells.

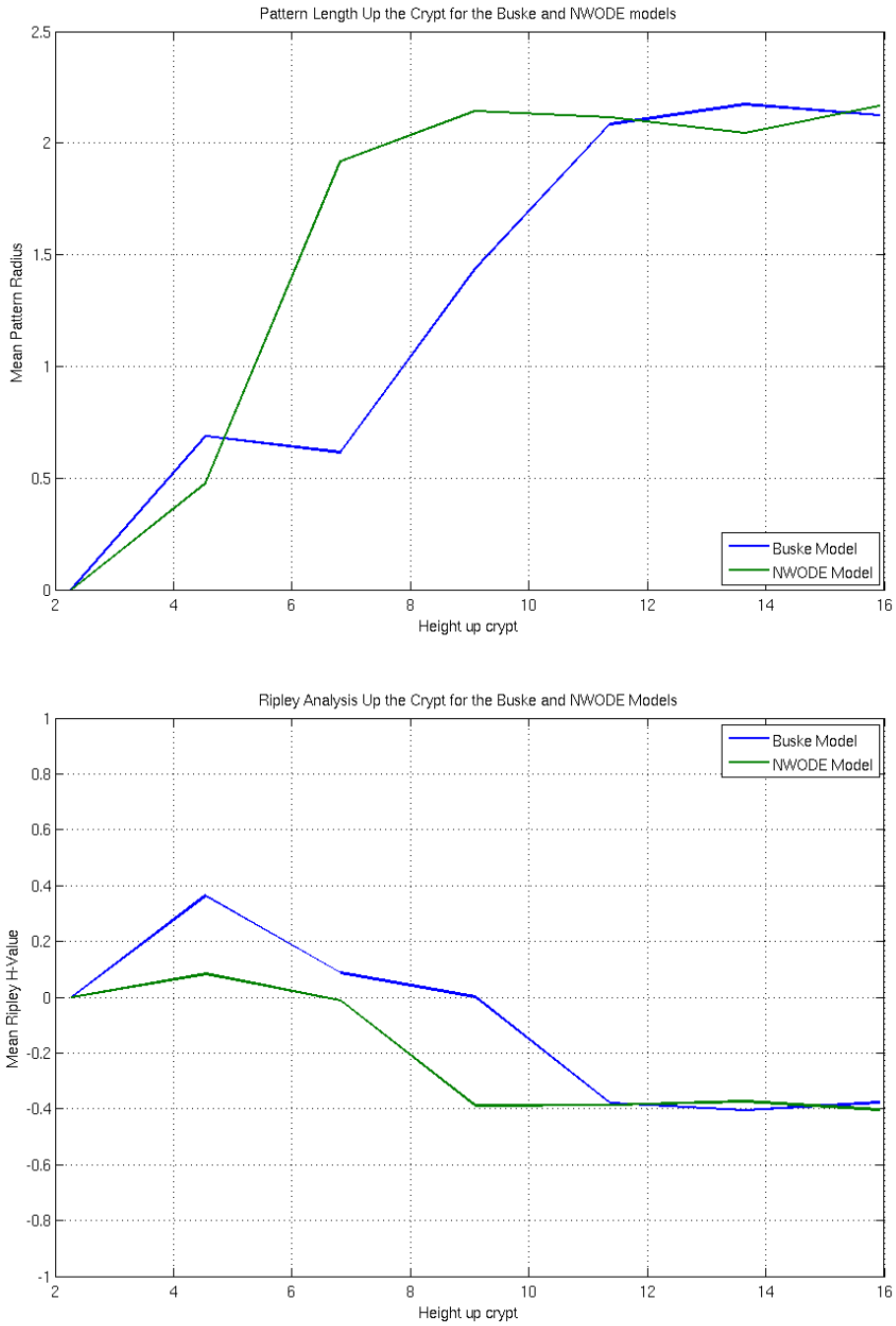

Figure 5.9: (Upper) Mean pattern radius and (Lower) Mean Ripley H-Values on ascending the crypt, for both the Buske and NWODE crypt models at dynamic equilibrium. Data have been drawn from all seven assessment zones shown in Figure 5.3.

models return a positive, clustered Ripley H-Value for Zone 5 (about a quarter of the way up the crypt) because this zone lies on the divide between the unpatterned transit region and the priming region, where initial cell fate selection occurs.

The pattern lengthscales for both models increase through the middle region of the crypt; some secretory cells are eliminated at this stage, producing a slightly longer pattern length in the upper crypt. The NWODE model attains its final spacing further down the crypt than the Buske model, as a result of the former's robust patterning in the priming region.

Features of the Cell Totals

Timecourses for cell totals of secretory, transit and absorptive phenotypes are shown in Figure 5.10. Ideally, additional experimental work should be carried out to estimate parameters accurately for both the Buske and NWODE models, if a rigorous quantitative analysis is to be performed. Consequently this discussion focuses on a qualitative comparison of the results.

Both cell fate models demonstrated long-wavelength oscillations in the cell populations of Figure 5.6; this is still evident in the heterogeneous case shown in Figure 5.10. This effect is stronger in the NWODE than the Buske model and is also more pronounced in the mitotically active phenotypes; it is a consequence of the initial conditions and may be more pronounced in the NWODE model owing to its use of a biochemical cut-off to determine the transit and priming regions, rather than the fixed spatial bound used in the Buske model. These oscillations are substantially reduced by averaging over larger numbers of simulations and additional runs should eradicate them altogether.

Cell totals for the NWODE model display a small standard deviation, suggesting relatively weak dependence on initial conditions. This is consistent with the high degree of patterning robustness observed in Section 5.8 and seen in similar models

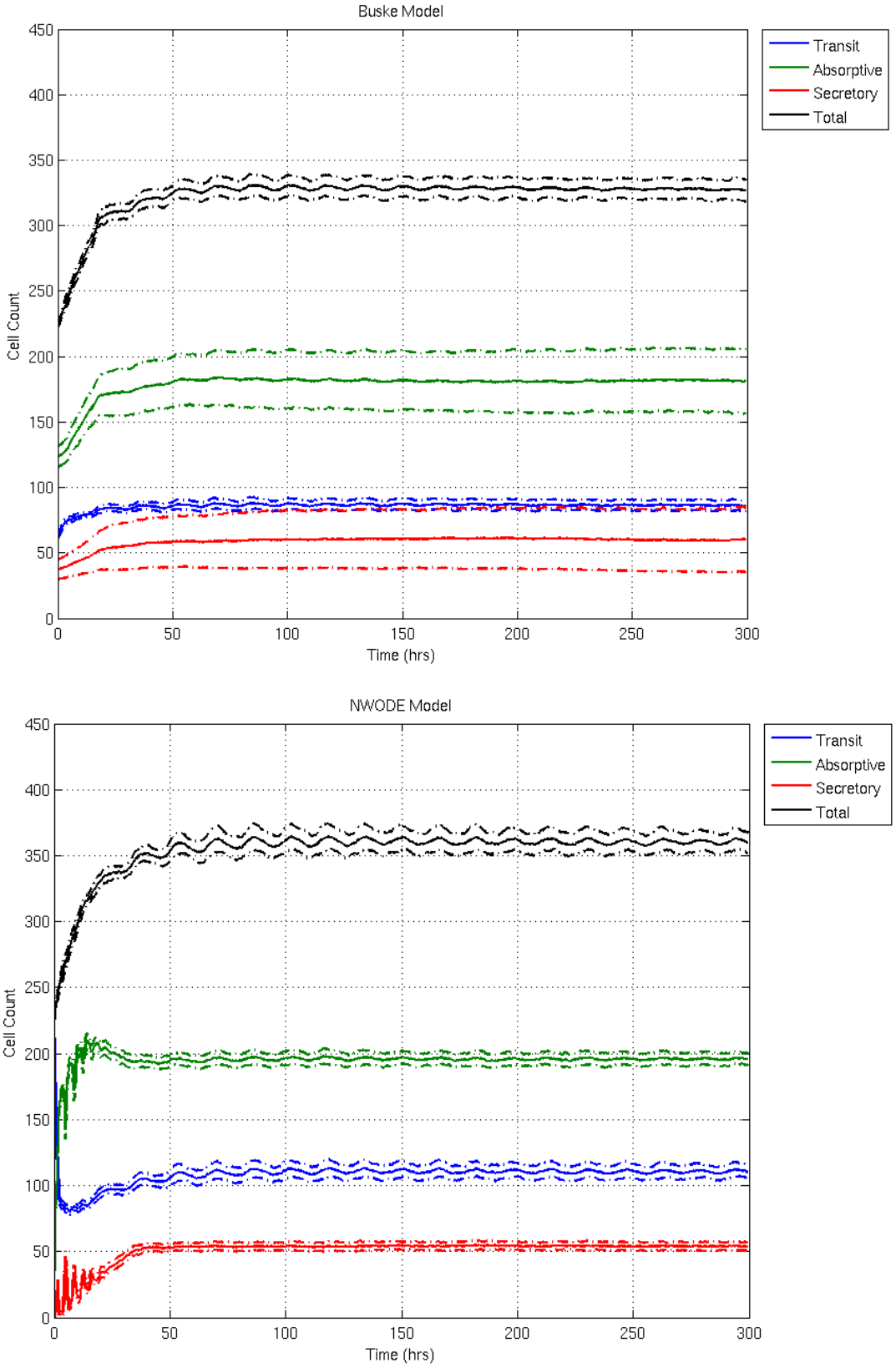

Figure 5.10: Cell totals for each of the main cell types over the course of a simulation. Solid lines represent mean values taken over 100 simulations; dotted lines indicate standard deviations for each cell type.

in the literature, such as that of Collier *et al.* [125, 126]. For the NWODE model to be extensively deployed as a model for the colorectal crypt, further experimental investigation would need to confirm that existing observations of cell fate [201, 214, 122] are consistently representative of subpopulation proportions in the biological setting, and provide suitable data for accurate calibration of the model parameters to match against this regime.

Discussion of pattern robustness for the Buske model in Section 5.8 suggested that cell fate in the priming region of the crypt is strongly dependent on the initial conditions. This is certainly borne out by the absorptive and secretory cell totals of Figure 5.10, which yield a larger standard deviation than their NWODE counterparts. If further experimental investigations were to suggest a larger degree of variation in crypt cell counts, it might be possible to adapt the Buske model to suitably model this, given further investigation of its dependence on initial conditions.

The ODE-based crypt model contains more transit cells at dynamic equilibrium than the rule-based framework. The Buske model derives mitotic activity status directly from the local Wnt stimulus. This produces a clear horizontal boundary between the transit and priming regions, which is visible in the simulation snapshots of Figure 5.7. By contrast, the NWODE model uses β-catenin to determine the proliferation cutoff. Although the β-catenin concentration of a cell is influenced by the local Wnt stimulus, it is also subject to local variation in Notch activity, due to the crosstalk between the two pathways. This results in a more graduated transition between the transit and priming zones; indeed, isolated blue transit cells can be seen above the main transit-priming divide in Figure 5.7. This may explain why the NWODE model yields more transit cells at dynamic equilibrium.

5.10 Cell Fate Parameters in the Buske Model

Simulations presented in Sections 5.8 and 5.9 reflect the behaviour of the Buske model when using the parameter set of Buske *et al.* [5]. We now extend the study to examine the impact of the cell fate selection parameter, $Status_{sec}$. This parameter is involved in the Notch activity summation expressed by Equation (5.1), in which the Notch activity status of the current cell is determined by its number of secretory neighbours.

The published parametrisation of the Buske model assigns a value $Status_{sec} = 1.0$ to a secretory cell, and $Status_{non-sec} = 0.0$ to non-secretory types. Summation of the neighbour statuses yields the Notch activity status, $Notch_i$; $Notch_i \geq 1.0$ induces the cell to become absorptive at the next timestep, otherwise it becomes secretory. That is, a cell becomes secretory only if it has no secretory neighbours, as detailed in the schematic of Figure 5.1.

It is therefore the relative, rather than absolute, values of the parameter $Status_{sec}$ and the threshold for $Notch_i$ which determine the cell fate behaviour of the Buske model. We now present additional simulations of the Buske model, which retain the secretory conversion threshold $Notch_i \geq 1.0$ but adopt $Status_{sec} = 1.0, 0.5, 0.34$ or 0.25. Cells in these simulations will become secretory if they have no, at most one, at most two or at most three secretory neighbours respectively. All simulations adopt the conditions described in Sections 5.2 – 5.6.

Ideally we would compare the performance of both the Buske and NWODE models as their cell fate parameters are varied. However, the two models adopt very different approaches to cell fate selection and it is not possible to form a meaningful equivalence between their respective parameter sets. Consequently we focus solely on the Buske model in this section and address the NWODE secretory threshold separately in Section 5.11.

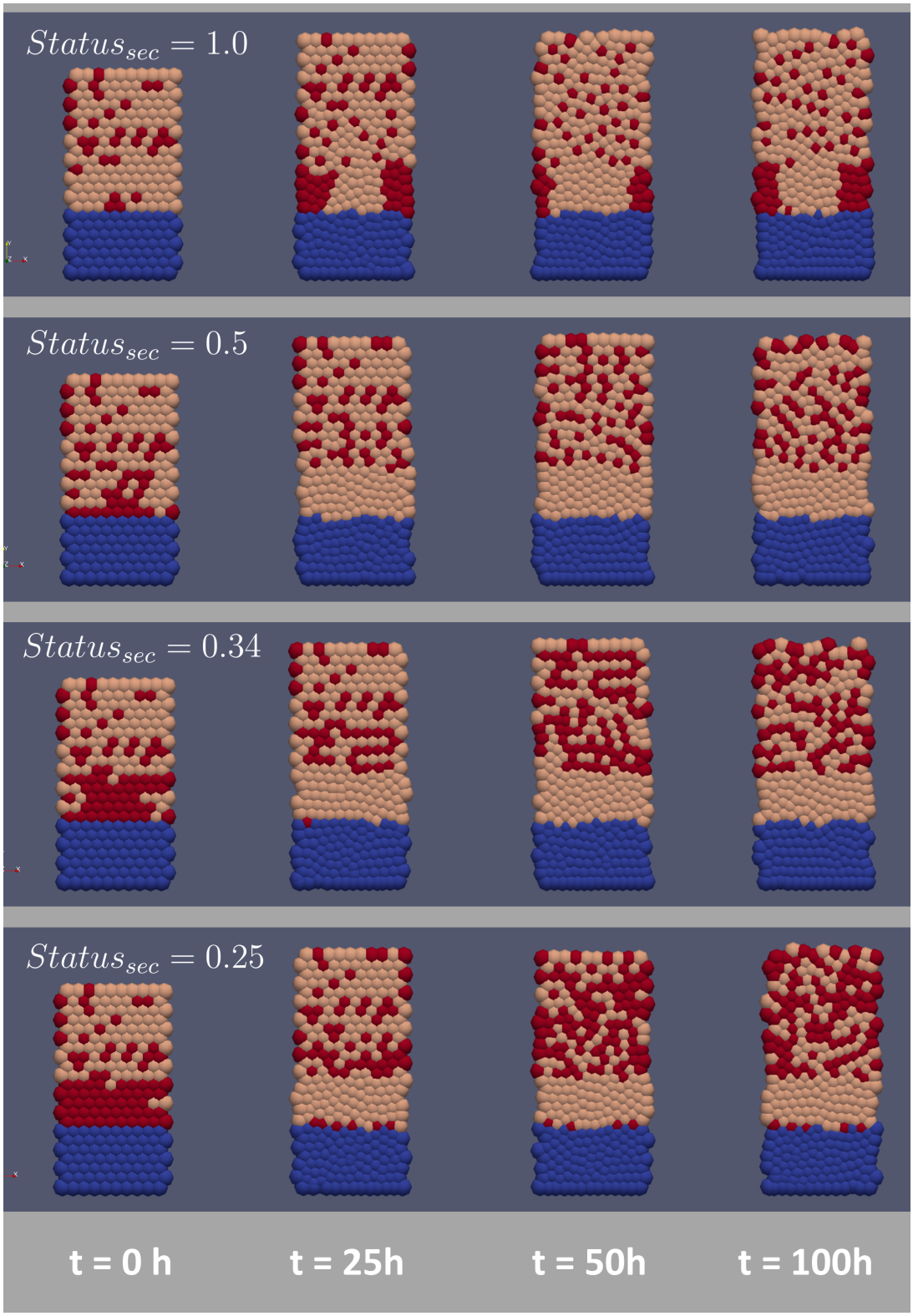

Figure 5.11: Snapshots of crypt evolution for four different instances of the Buske model, each for a different value of $Status_{sec}$. Transit cells are shown in blue, absorptive cells are peach and secretory cells are red. Differences between the $t = 0$ snapshots are the result of the first round of cell type updating; all cases have been run using identical initial conditions and the same random number seeding.

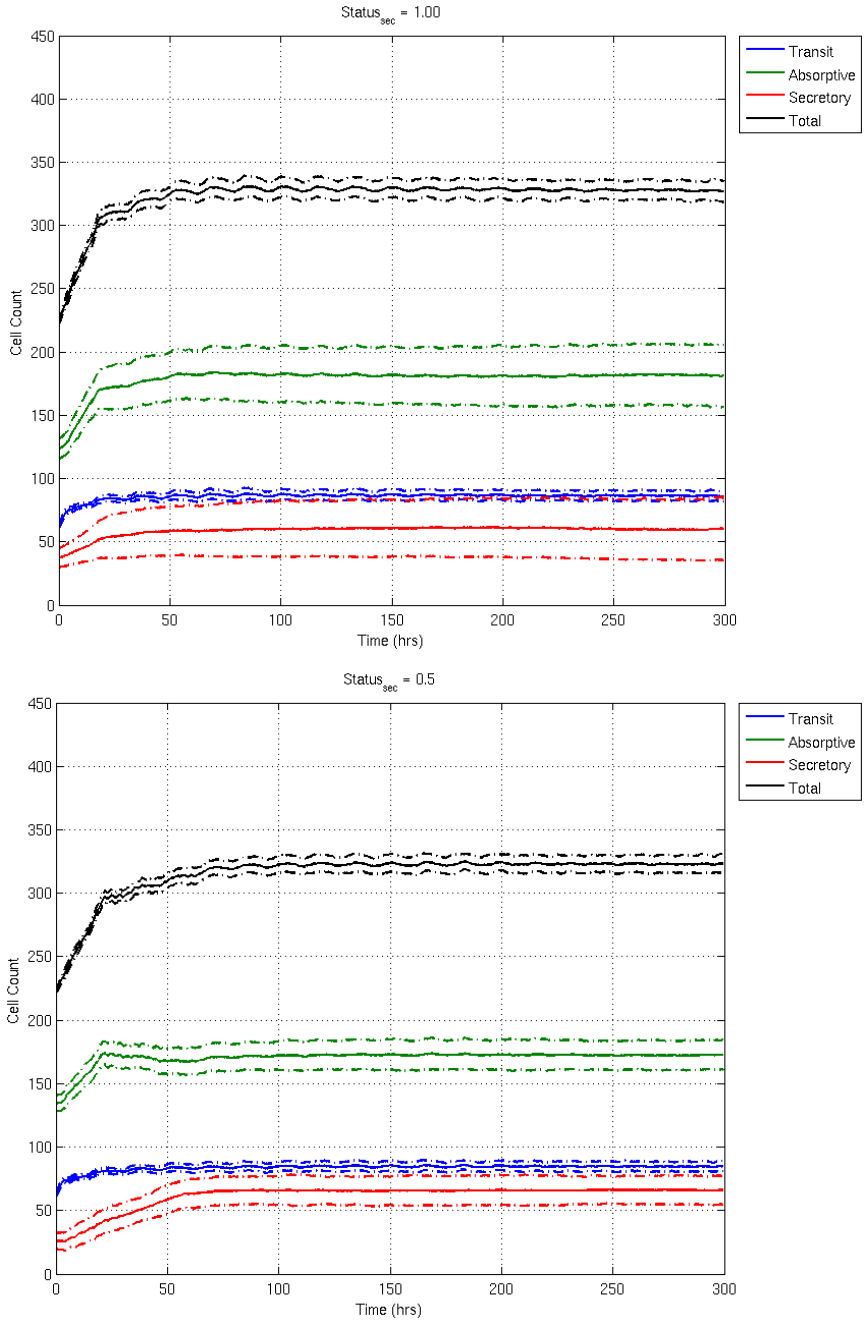

Figure 5.12: Cell totals for each of the main cell types over the course of a simulation, shown for the parametrisations $Status_{sec} = 1.0$ and $Status_{sec} = 0.5$. Solid lines represent mean values taken over 100 simulations; dotted lines indicate standard deviations for each cell type.

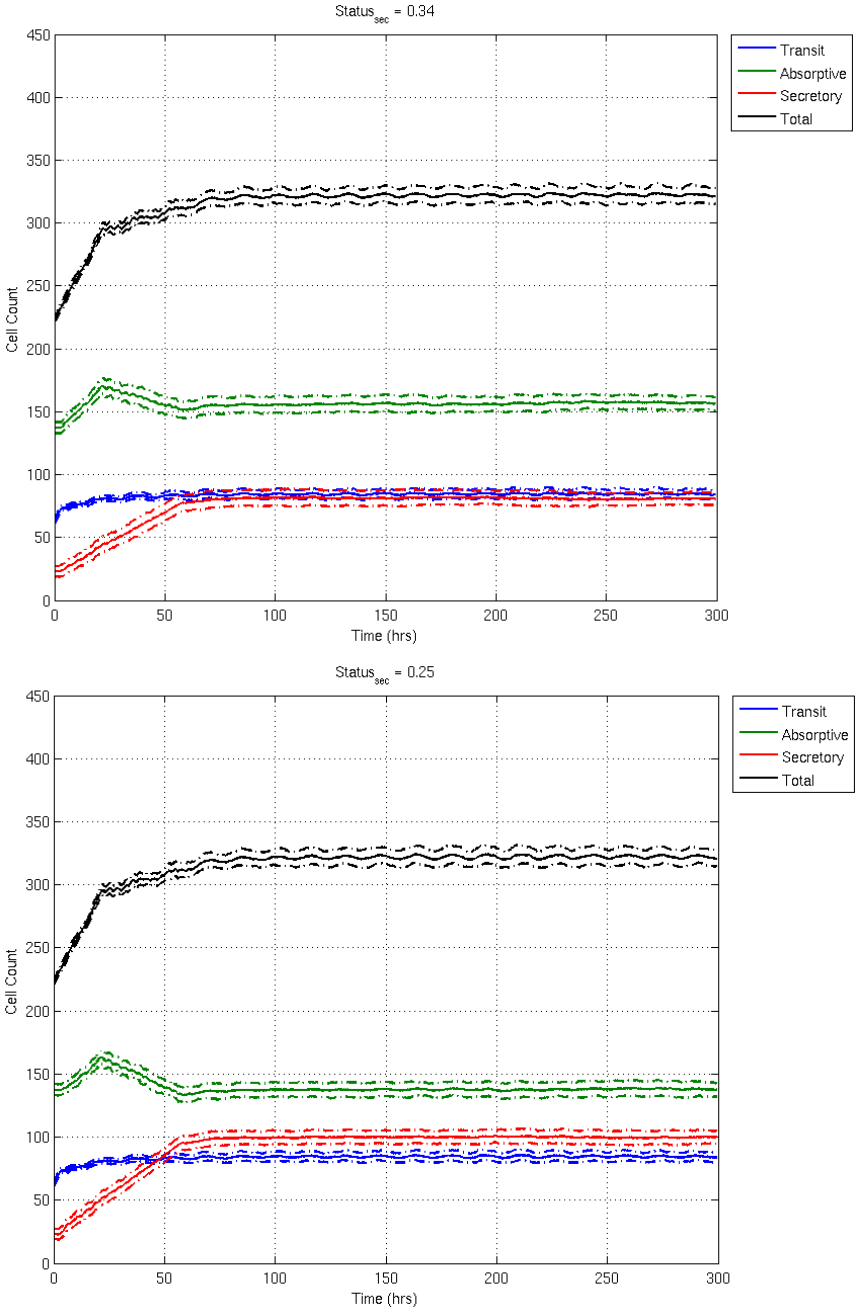

Figure 5.13: Cell totals for each of the main cell types over the course of a simulation, shown for the parametrisations $Status_{sec} = 0.34$ and $Status_{sec} = 0.25$. Solid lines represent mean values taken over 100 simulations; dotted lines indicate standard deviations for each cell type.

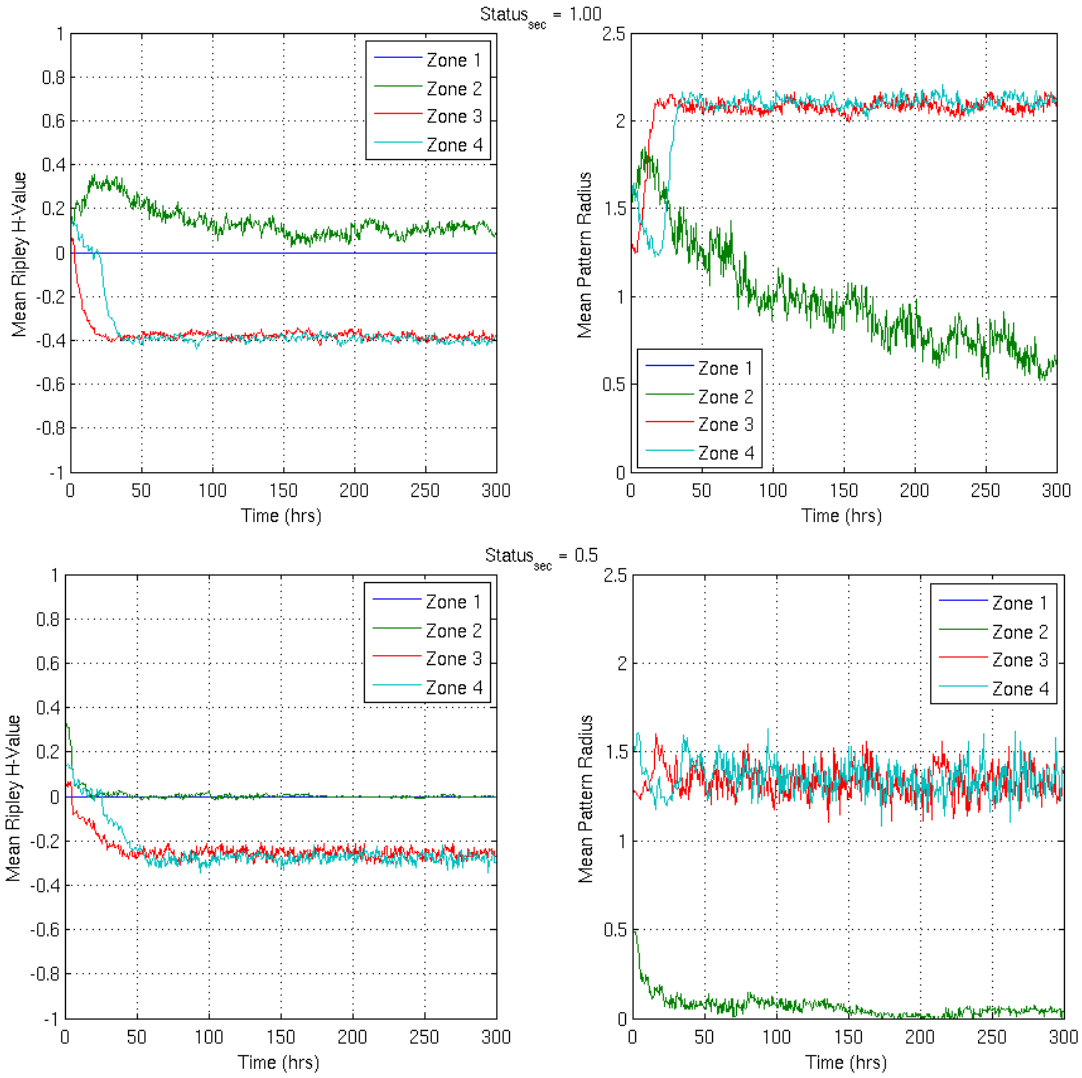

Figure 5.14: Distribution of secretory (goblet) cells within four height bands of the crypt, numbered from lowest (Zone 1) to highest (Zone 4), shown for the parametrisations $Status_{sec} = 1.0$ and $Status_{sec} = 0.5$. Left-hand plots depict Ripley H-Values for each of the zones, whilst those on the right provide timecourses for the mean pattern radius of secretory cells.

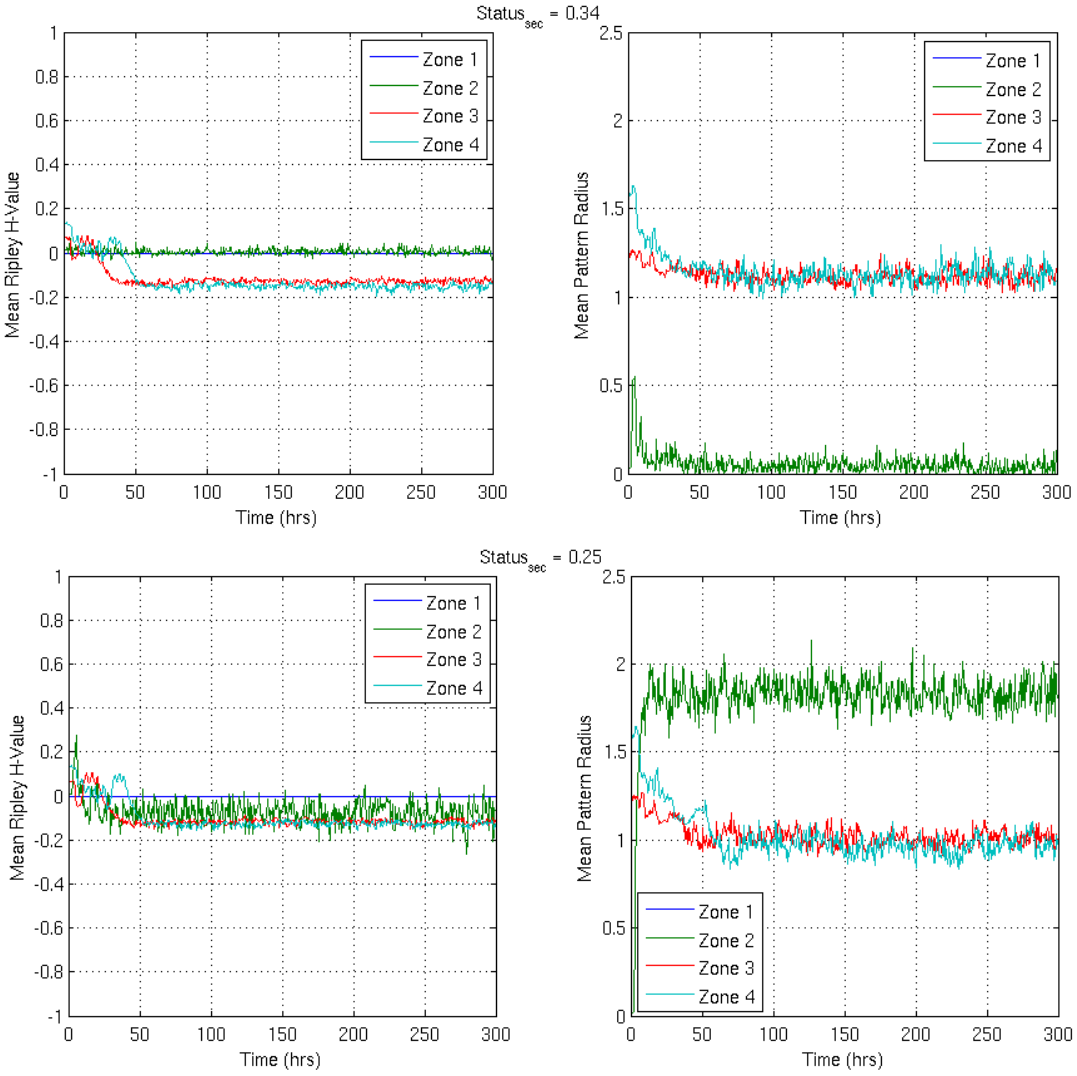

Figure 5.15: Distribution of secretory (goblet) cells within four height bands of the crypt, numbered from lowest (Zone 1) to highest (Zone 4), shown for the parametrisations $Status_{sec} = 0.34$ and $Status_{sec} = 0.25$. Left-hand plots depict Ripley H-Values for each of the zones, whilst those on the right provide timecourses for the mean pattern radius of secretory cells.

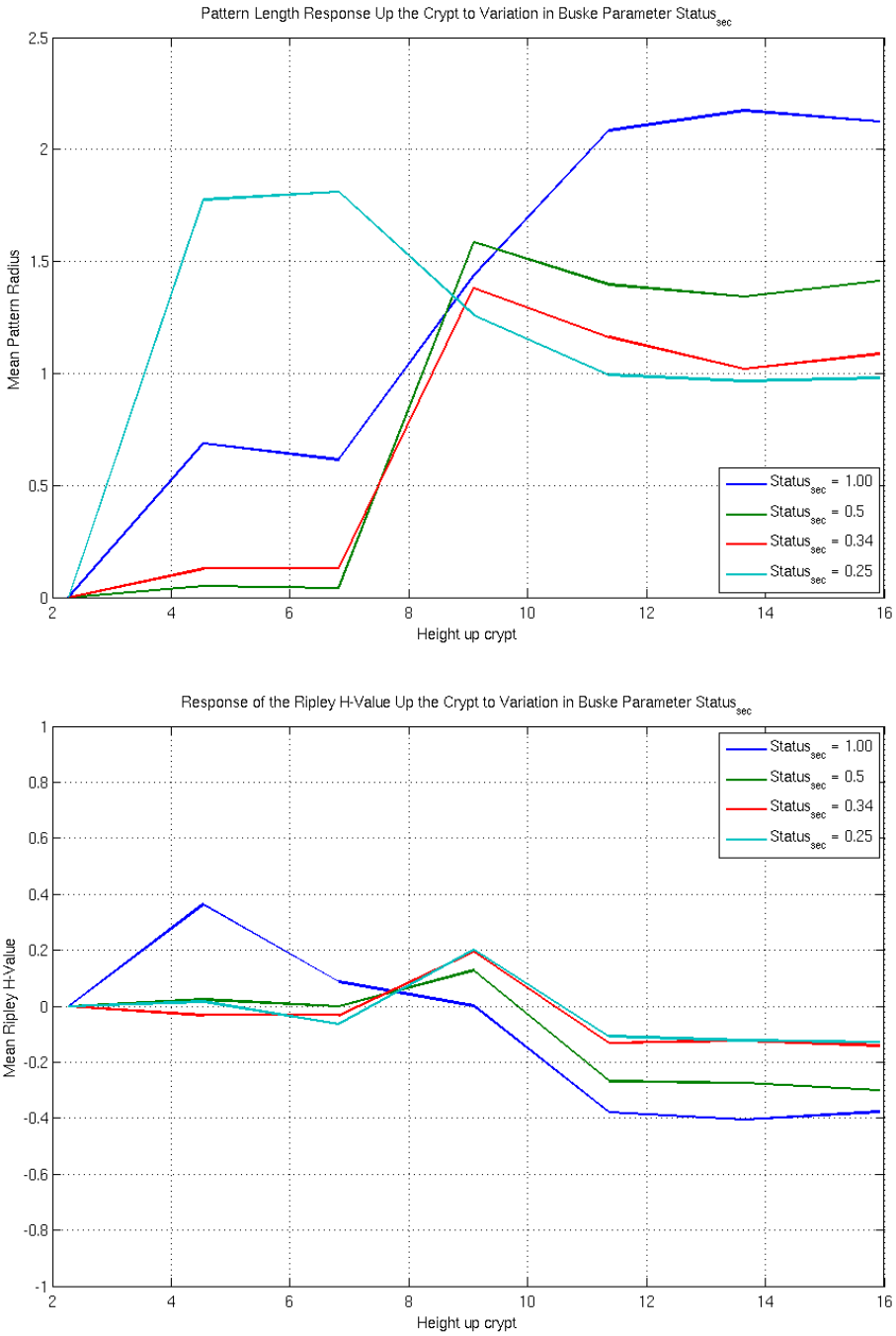

Figure 5.16: (Upper) Mean pattern radius and (Lower) Mean Ripley H-Values on ascending the crypt, for four parametrisations of the Buske crypt model, shown at dynamic equilibrium. Data have been drawn from all seven assessment zones shown in Figure 5.3.

Screenshots of Domain Evolution

Figure 5.11 presents a series of snapshots of Buske crypts for the four tested values of $Status_{sec}$, shown for a series of times during the equilibration process. All cases have been run using the same random number seeding and initial conditions.

Decreasing the value of $Status_{sec}$ increases the production of secretory cells, resulting in a highly clustered pattern in the upper, terminally differentiated region of the crypt. However, the priming zone remains largely or completely unpatterned in all cases, as a result of the high dependence on initial conditions in the Buske model: the discrete construction of the Notch summation of Equation (5.1) either tends to remove all patterning from the priming region (as in the case $Status_{sec} = 0.5$), or to drive the region towards a block pattern (as in the case $Status_{sec} = 1.0$). Only for very specific starting configurations does a distributed pattern appear to be retained: for example, some secretory cells are retained at the lower end of the priming region in the case $Status_{sec} = 0.25$.

Cell Totals

Supplementary simulations by Buske *et al.* [5] vary the threshold for $Notch_i$ in a manner analogous to our variation of $Status_{sec}$, and find that increasing the threshold for secretory cell conversion (equivalent to reducing $Status_{sec}$) increases the secretory cell count and reduces the absorptive cell count. Parameter variation in the Buske summation only produces demonstrable changes beyond particular thresholds, owing to the discrete construction of the summation in Equation (5.1).

Our simulations agree with these findings: a reduction in $Status_{sec}$ increases the number of secretory cells (from around 60 to 100 in the graphs of Figures 5.12 and 5.13) and decreases the number of absorptive cells (from around 175 to 140). The transit cell count is trivially unaffected by the parameter change.

There is also a substantial reduction in the standard deviation of the absorptive and

secretory cell counts for lower values of $Status_{sec}$; this is not discussed in Buske *et al.* [5]. As for our earlier studies, more experimental data would be required to determine how these results relate quantitatively to the variation seen in the biological scenario.

Ripley Analysis

Timecourses of pattern lengthscale and Ripley H-Value are shown in Figures 5.14 and 5.15. Zone 1 remains unpatterned throughout the simulations, because it contains only transit cells. Zones 3 and 4 in the upper crypt develop clear patterning; decreasing the value of $Status_{sec}$ decreases the pattern lengthscale, and produces a less negative Ripley H-Value, indicating a less dispersed, more random appearance to the pattern of secretory cells. Zone 2 includes the cutoff between the transit and priming regions. Ripley analysis of this zone indicates clustered patterning for $Status_{sec} = 1.0$ and minimal or no patterning for the other values.

Analyses for the secretory cell distribution at dynamic equilibrium are shown in Figure 5.16. Each of the four cases display established patterning in the upper half of the crypt, although the pattern lengthscale decreases with $Status_{sec}$, in agreement with the $t = 100$ screenshots shown in Figure 5.11. The lowest values of $Status_{sec}$ have a mean lengthscale close to zero, suggesting that each cell in the terminally differentiated region neighbours a secretory cell.

Ripley H-Values for these zones indicate a transition from a more dispersed pattern to a less dispersed one as $Status_{sec}$ is reduced. The cases $Status_{sec} = 0.5, 0.34, 0.25$ exhibit little or no patterning in the priming zone. This is evident from the positive Ripley H-Value in the mid-crypt, where the transition between the priming and differentiated zones occurs, and the lack thereof at the boundary between the transit and priming zones. By contrast, the $Status_{sec} = 1.0$ case has a positive Ripley value at the transit-priming boundary, indicating patterning within the priming region, but no such peak on the priming-differentiated boundary.

Certainly the appearance of the differentiated region in the case $Status_{sec} = 1.0$ seems more consistent – qualitatively speaking – with experimentally-captured images of cell fate spacing in the gut epithelium [201, 214, 122]; substantial clustering of primary fate cells has not been reported in the literature to date. This would seem to support the use of $Status_{sec} = 1.0$ in the Buske model, in agreement with Buske *et al.* [5], as opposed to smaller parameter values. Nevertheless, it would seem expedient to explore possible functional alternatives to the Notch summation used in the Buske model, to see whether patterning could be extended across the priming region of the Buske model for a wider range of initial conditions.

5.11 Cell Fate Parameters in the NWODE Model

Simulations presented in Sections 5.8 and 5.9 reflect the behaviour of the NWODE model when using a fixed parameter set. We now examine the impact of the secretory selection threshold for Hath1, H_2. Cells in the priming region adopt a specialised phenotype according to their subcellular concentration of Hath1: if this expression is below the given threshold, they become absorptive cells; otherwise they become secretory cells, as shown in the crypt schematic of Figure 5.1. H_2 is a continuous, real-valued variable; we restrict ourselves to cases in the range $[12.0, 30.0]nM$, in the region of the 17.0nM 'standard' value stated in Section 5.4.

The NWODE model relies on a subcellular ODE embedding of the Notch-Wnt model presented in Chapter 3. Studies of cell pairs in Chapter 4 indicate the presence of a homogeneous steady state and one or more pairs of heterogeneous steady states, in which one cell adopts a high, and the other a low, concentration of Hath1. This is consistent with the behaviour of other Notch pathway models which employ similar motifs and functional forms, such as those of Collier *et al.* [125] and Shepherd [238].

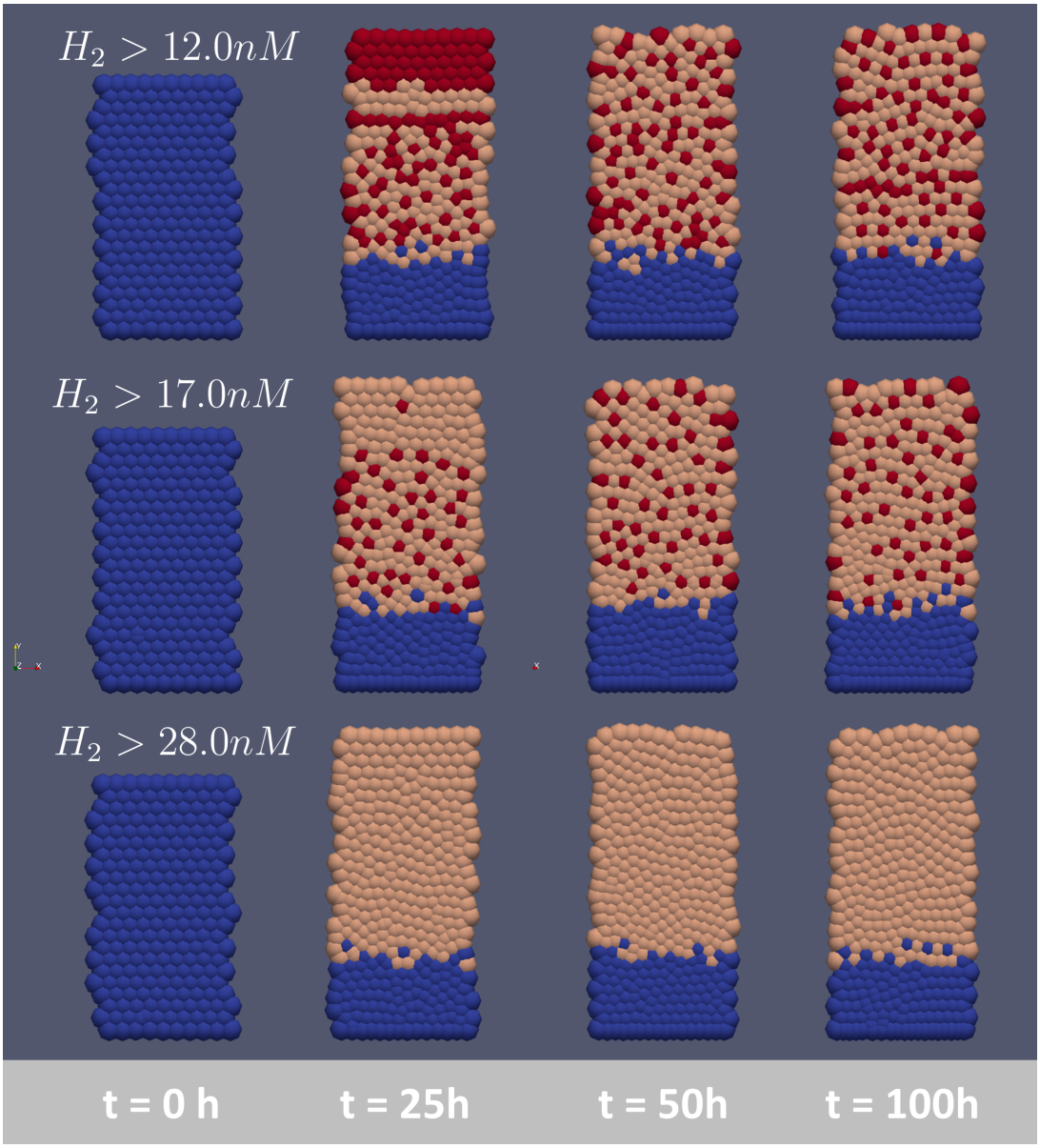

Figure 5.17: Snapshots of crypt evolution for three different instances of the NWODE model, for the secretory thresholds $H_2 > 12.0$nM ('low'), $H_2 > 17.0$nM ('standard') and $H_2 > 28.0$nM ('high'). Transit cells are shown in blue, absorptive cells are peach and secretory cells are red. All cases have been run using identical initial conditions and the same random number seeding.

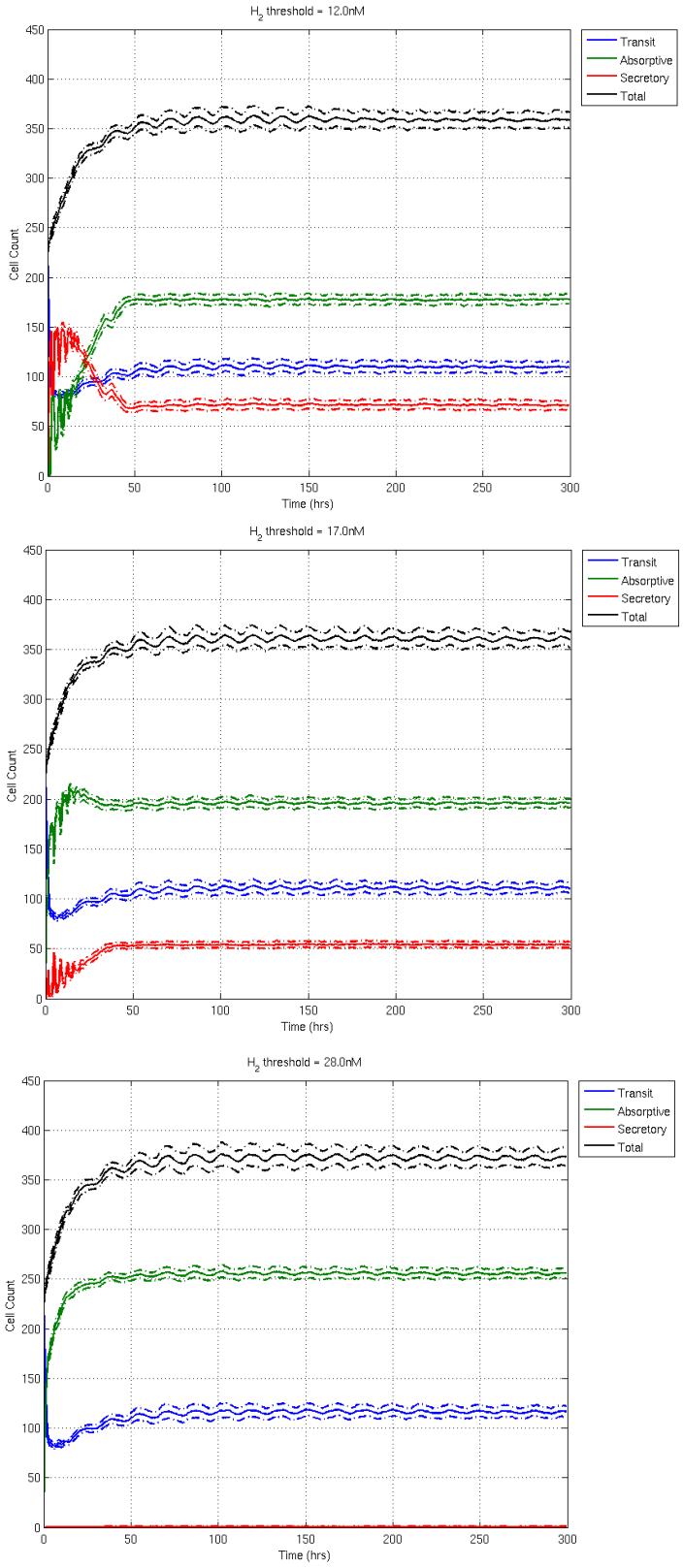

Figure 5.18: Cell population counts over the course of a simulation, shown for the NWODE thresholds $H_2 > 12.0$nM , $H_2 > 17.0$nM and $H_2 > 28.0$nM. Solid lines represent mean values; dotted lines indicate standard deviations.

Screenshots of Domain Evolution

Figure 5.17 presents a series of snapshots of NWODE crypts for three values of the secretory threshold, shown for a series of times during the equilibration process.

Small changes to the Hath1 threshold (of the order of $\pm 1 - 2$nM) do not change the patterning substantially. If the threshold is increased beyond the maximum range of the underlying ODE model (as in the $H_2 > 28.0$nM case), all cells above the transit zone adopt an absorptive phenotype. On the other hand, if the threshold is reduced sufficiently (as in the $H_2 > 12.0$nM case), more secretory cells are produced, disrupting the dispersed pattern seen in the $H_2 > 17.0$nM case.

Cell Totals

The long-term behaviour of the NWODE model preserves the relative ordering of its cell type populations over the tested range of Hath1 thresholds: the secretory cell population is smallest, followed by transit cells, and finally absorptives.

Nonetheless, if the Hath1 threshold is reduced to 12.0nM, the crypt initially produces more secretory cells but does not sustain this to dynamic equilibrium, as can be seen from the upper plot of Figure 5.18. Even so, the low-threshold case generates fewer absorptive cells than the standard $H_2 > 17.0$nM case (180 vs. 200). By contrast, the high-threshold case $H_2 > 28.0$nM does not produce any secretory cells at all, as the ODE system does not surpass this value in a healthy crypt.

Ripley Analysis

The NWODE model displays very little variation in its patterning behaviour for small changes to the Hath1 threshold (of the order of $\pm 1.0nM$), owing to its reliance on an embedded ODE system with robust patterning involving high-Hath1/low-Hath1 pairs of stable states. A more substantial change is required to alter the cell fate outcome.

Timecourses for the high, standard and low cases are shown in Figure 5.19. The low-threshold and standard-threshold cases generate similar Ripley timecourses, indicating similar patterning at dynamic equilibrium, but the low-threshold case demonstrates greater variation in its pattern lengthscale. This suggests that the low-threshold case exhibits greater pattern variation over its 100 simulations. The high-threshold case is noticeably different; the lack of secretory cells prevents patterning, producing zero Ripley values. This is also borne out by Figure 5.20, showing the pattern radius and Ripley values up the crypt at dynamic equilibrium, for six different values of the Hath1 threshold. The low- and medium-range values show very little difference in the differentiated region of the crypt, although the $H_2 > 12.0$nM case exhibits a slightly closer pattern; reduction of the threshold beyond this point is likely to produce substantially more secretory cells.

The two-cell studies of Chapter 4 show a separation of fates in the heterogeneous steady state: one cell becomes high-Hath1 (and low-Notch), and the other, low-Hath1 (high-Notch). Although this scenario cannot provide quantitative insight into the steady state values of the multicellular crypt setting, the qualitative separation of Hath1 concentrations still applies. Small variations in the Hath1 selection threshold are unlikely to cause significant changes to the resulting pattern. If the threshold were substantially reduced below the typical "low-Hath1" state (below 12.0nM), the majority of cells would adopt a secretory phenotype; alternatively, if the threshold exceeds the typical "high-Hath1" state (e.g. 28.0nM), cells retain an absorptive type. Thresholds between these transition values generate varying degrees of pattern.

Some local variation in Hath1 concentrations is to be expected, due to Notch-Wnt crosstalk effects and the asymmetry of Notch inheritance at mitosis. This might permit fate change of a small number of cells in response to slight variation in the Hath1 threshold, but is unlikely to significantly change the large-scale behaviour of patterning throughout the crypt.

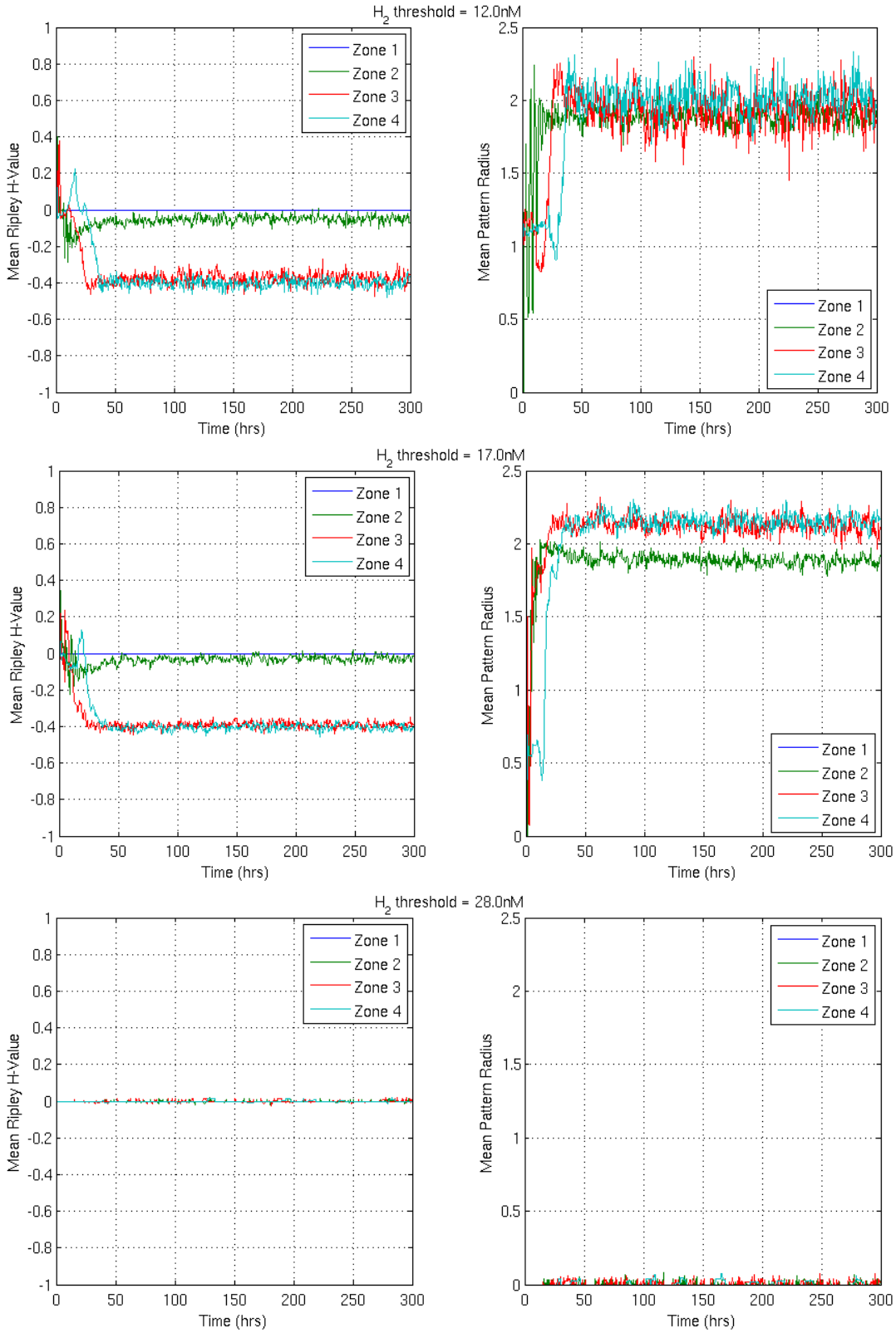

Figure 5.19: Ripley timecourses for zones $1-4$ of the crypt, generated from 100 simulations of the NWODE model using a secretory selection threshold of (top) $H_2 > 12.0nM$, (middle) $H_2 > 17.0nM$ and (bottom) $H_2 > 28.0nM$.

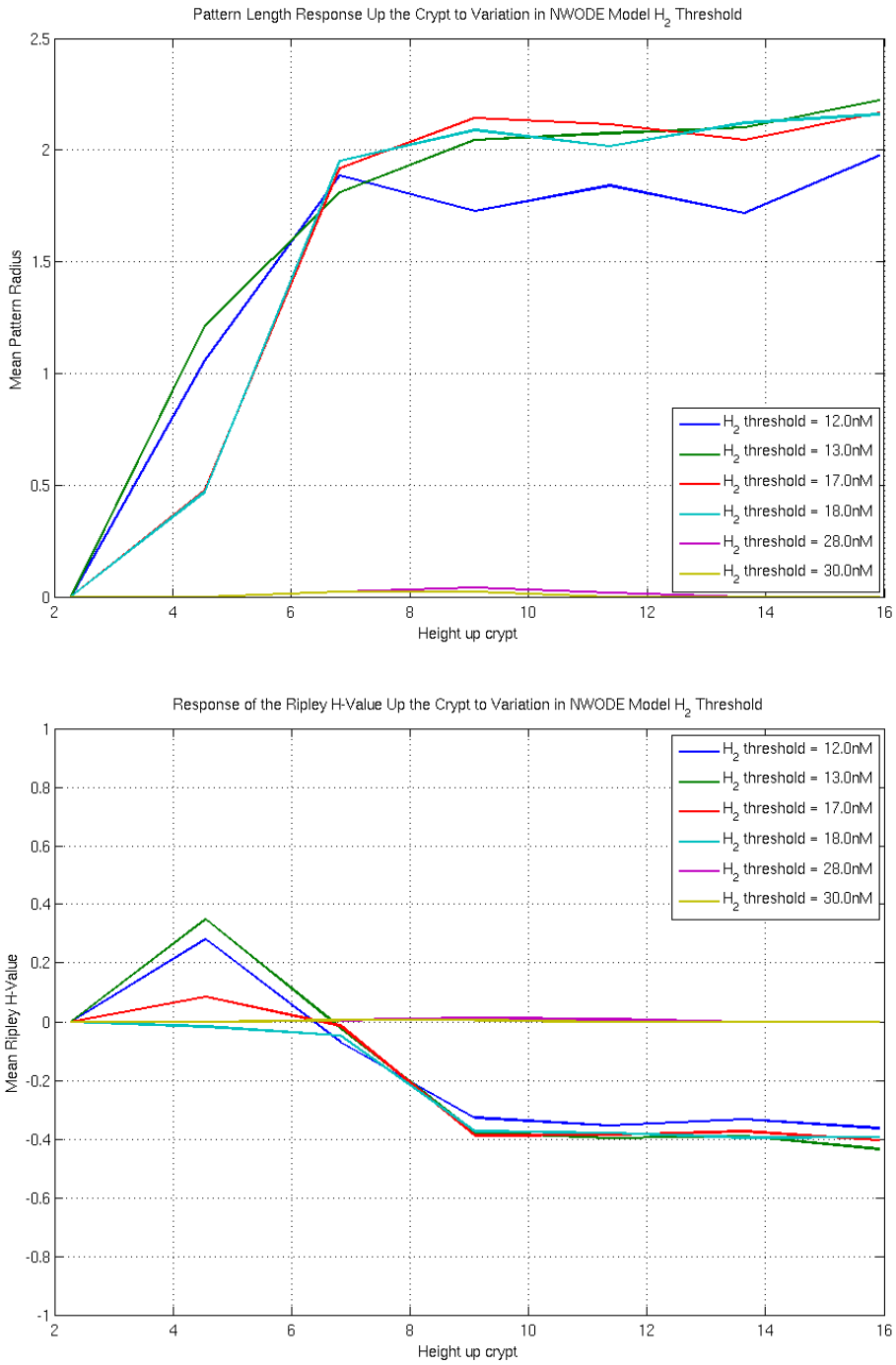

Figure 5.20: (Bottom) Ripley and (Top) pattern length analyses for NWODE crypts at dynamic equilibrium, shown for simulations using a range of secretory selection thresholds from $H_2 > 12.0nM$ to $H_2 > 30.0nM$. Crypt subregions used to generate these results are as shown in Figure 5.3.

5.12 Conclusions

Existing crypt models in the literature either involve simple ODE embeddings of Delta-Notch signalling, without deriving cell fate directly from these concentrations [247] or use a less complex, rule-based approach to modelling Notch activity [5, 139]. The NWODE model presented here is, to the best of our knowledge, the first case of a detailed system of subcellular ODEs being used to model coupled Notch-Wnt interaction in the crypt and to derive cell fate directly from this information; it represents a substantial advance on the current literature and offers a wealth of possibilities for further study and development.

Simulations in this chapter have characterised the cell fate behaviour of the Buske and NWODE models in a cylindrical crypt and have established a computational framework for quantifying the spatial output of such models, using the Ripley H-Value to assess cell dispersal. This simple geometry is a necessary starting point for preliminary comparison; a natural extension would be to employ a dynamically changing crypt geometry with a spherical base cap, akin to a deformable test-tube, of the kind employed by Mirams *et al.* [247], Fletcher *et al.* [177] or Buske *et al.* [5], amongst others. This may mitigate compression effects associated with having a rectangular region of transit cells in the cylindrical geometry, reported by Osborne *et al.* [195].

A key area for further work is to obtain additional experimental data relating to the number and distribution of different cell types in the colorectal epithelium, against which the performance of the Buske and NWODE models can be compared. Such data would need to include multiple stills of individual crypts, with clear staining of goblet cells to determine their number and distribution.

5.12.1 Insights into ODE- and Rule-Based Paradigms

Comparison of cell patterning capabilities in the Buske and NWODE models have provided a number of insights into the use of rule-based and ODE embedding approaches.

Robustness of Pattern Generation

Robustness of the pattern generating capacity is one of the key differences between the rule-based and ODE-based approaches. The NWODE model is less dependent on the initial conditions and exhibits a pattern robustness commensurate with similarly-structured Notch models in the literature [125]. The Buske model is capable of a greater range of patterning behaviours in the priming region and exhibits a greater dependence on the starting conditions. A capacity to generate subcellular heterogeneity at mitosis is an important factor in pattern development for the NWODE model, as shown by the snapshots of Figure 5.6.

Existing observations in the biological literature suggest that a dispersed pattern of secretory cells in the upper half of the intestinal crypt is the accepted behaviour for this tissue [201, 214, 122]. Certainly the NWODE model is more consistent at modelling dispersal of secretory fate cells throughout the specialised regions of the crypt, but further investigations would be required to determine how closely this robustness reflects the biological setting. Additional mathematical investigation may be required to determine whether the Buske and NWODE models can be suitably parametrised or adapted to match quantified dispersal measurements from biological tissue.

Influence of Neighbour Selection and Mesh Geometry

Remarkably, both the Buske and NWODE models predict the same pattern lengthscale of 2.2 cell diameters for secretory cells in the upper crypt, despite their differences in behaviour in the priming region. This suggests that an ODE approach is not essential for capturing cell fate expression in the terminally differentiated region. The juxtacrine

nature of Notch signalling is intrinsically reliant upon the definition of the 'nearest neighbours' with which a cell makes contact and it is possible that this, coupled with any bistable switching mechanism, will at least approximate this lengthscale in a crypt embedding, irrespective of the method used to generate subcellular heterogeneity, given suitable parametrisation[5].

Additional computational studies might extend analyses in the literature. Work by Webb and Owen [134] has already examined the patterns arising from juxtacrine signalling on fixed lattices, in both square and hexagonal, regular and irregular geometries. All the crypt studies in this chapter model a dynamically growing cell-based tissue, in which the number of cell neighbours varies across the population, as well as for any given cell over time. These involve an irregular, dynamically changing polygonal mesh; a formal analysis would require extension of these existing static studies for specific polygonal geometries.

Moreover, the Buske model in its current form does not adjust its calculation of Notch stimulus (defined in Equation (5.1)) to account for dynamic changes to cell neighbour counts. Computational exploration of neighbour selection processes may lead us to modify the Buske Notch calculation by using an averaging process, rather than direct summation alone.

Timescales

The block oscillations characteristic of the Buske model have not been observed experimentally; they should be considered a model artefact as they occur over consecutive simulation timesteps. Cell fate *in vivo* is known to evolve over much longer timescales than the 18 second windows represented by successive timesteps in the crypt simulations. Typical timescales for gradual equilibration of the NWODE model from homo-

[5]We note that the Buske parameter studies of Section 5.10 demonstrate a much-reduced spacing of secretory fate cells in the upper crypt, in response to changes in the secretory cell contribution parameter, $Status_{sec}$.

geneous conditions (of the order of several hours) are consistent with observations of recovery from cell fate disruption treatments described in the biological literature [83].

5.12.2 Applicability to Other Biological Scenarios

Crosstalk between the Notch and Wnt pathways in the NWODE model creates a gradual transition between the transit and priming regions, because Notch-Wnt interaction modulates the level of β-catenin within a cell, thus varying the height at which cells become primed for a given fate. Local variation in Notch activity in the population is therefore transmitted to the Wnt pathway too. This could prove useful in exploring the progression of a single cancer cell in a given tissue, since the modulation of Wnt behaviour by the Notch pathway might exert some influence upon the mitotic activity of the rogue cell, or alternatively upon its healthy neighbours.

The Buske model offers a faster means of simulating the crypt epithelium and exhibits a larger variance in its numbers of specialised cell types, suggesting a broader range of patterning than the NWODE model. Nonetheless, its strong dependence on initial conditions and its block oscillations in the priming region need to be addressed prior to its use in scenarios where stable, robust patterning is a required feature. For example, in its current form it is unlikely to prove successful in modelling the *de novo* cryptogenesis experiments of Sato *et al.* and Ootani *et al.* [1, 2], in which colony growth is initiated from a single stem cell.

The suitability of the Buske and NWODE models for simulating a variety of different situations is summarised in Table 5.2 and reflects the current capabilities of the models. Some of the shortcomings highlighted here could be remedied by further development. For instance, introduction of additional binary activity states into the Buske model, representing biochemical entities such as Hes1 and Hath1, could be used to create a subcellular network with associated update rules. This would facilitate investigation of subcellular dysregulation. Refinement of the Notch-Wnt ODE system

associated with the NWODE model might employ saturating feedback terms similar to those used by Owen *et al.* [127, 128] to increase the growth of higher-lengthscale patterning modes and hence extend the range of patterns which can be generated.

Buske Model	Modelling Scenario	NWODE Model
✘	Subcellular dysregulation	✔
✔	Fast simulation required	✘
✘	Local variation in Notch-Wnt interaction	✔
✘	Target pattern not known	✔
✘	Growth from a single cell	✔
✔	Flexibility of patterning required	✘

Table 5.2: Applicabilty of the Buske and NWODE models for particular modelling situations, based upon the implementations explored in this chapter.

5.12.3 Final Comments

This chapter has focused on modelling homeostasis in a healthy crypt. However, colorectal cancer disrupts the dynamic equilibrium of the crypt epithelium and is associated with rewiring of subcellular biochemistry [64, 65].

The embedded ODEs of the NWODE model already provide the necessary biochemical detail for the exploration of subcellular knockouts in mutant phenotypes and for modelling therapeutic interventions at the biochemical scale; the Buske model would require further development to model such situations. We therefore continue using the NWODE model for studies of subcellular disruption and treatment, and equip it for studying a cancerous crypt environment in Chapter 6.

6 In Silico Modelling of Clinical Treatments

Chapter Summary

Does the Notch pathway offer a viable route for the treatment of CRC? Here we extend the NWODE crypt framework developed in Chapter 5, explore the tissue-level effects of introducing mutation to the Wnt pathway, and compare the performance of two proposed Notch-targeted treatments for a mutant phenotype: the first reduces Notch fragmentation at the cell surface, and the other stabilises Hath1. Our results suggest a synergy between the two approaches and highlight the role of the β-catenin/Hes1 crosstalk hub in shaping the tissue response to CRC therapies.

6.1 Introduction

The dysregulation of Wnt signalling in intestinal tumourigenesis has proven a major focus for clinical and biological research over the past two decades. We saw in the biological review of Chapter 1 how disruption of the canonical Wnt pathway in CRC leads to accumulation of nuclear β-catenin and ultimately to hyperproliferation of the cell. Despite this, clinical efforts targeting the Wnt pathway have not proven successful, largely because the section of the pathway downstream of the β-catenin destruction complex is driven by protein-protein interactions, which are more difficult to intercept therapeutically [91].

By contrast, the Notch pathway is not wholly reliant upon protein-protein interaction. Furthermore, it is frequently co-activated with Wnt in CRC [91] and – as described in the construction of our ODE model in Chapter 3 – is involved in crosstalk with the Wnt pathway. *Given the role of Notch in cell fate selection, is it possible to reduce the proliferation of Wnt-aberrant tumour cells by targeting the Notch pathway instead?*

Setting and Outline

Such a proposition provides an excellent subject for investigation using the NWODE model developed in Chapter 5. The subcellular equations of this model detail the function and crosstalk of the Notch and Wnt pathways; these can be modified to mimic the effects of mutation and/or clinical treatment in individual cells, allowing us to observe how these changes impact upon tissue-scale function. As discussed in Chapter 5, the Buske model would require considerable extension for application to problems involving subcellular dysregulation; we therefore retain the NWODE model for all simulations in this chapter.

We begin by outlining a specific mutant phenotype in Section 6.2 and characterise its behaviour in the NWODE crypt model for patches of mutant cells (Section 6.3.1) and entirely mutant crypts (Section 6.3.2). These studies lead into a discussion of clinical treatments in Section 6.4, where we introduce two clinical therapies: one targets the ligand binding capacity of the Notch pathway; the other stabilises the cell fate specifier, Hath1. Results of the clinical scenario tests are presented for mutant cells with regular and elevated adhesion levels (Sections 6.7 and 6.8 respectively).

The simulations in this chapter may be considered as a proof-of-concept study, demonstrating the power of our crypt model for exploring clinically relevant questions. Indeed, our chosen study represents only one of a vast number of questions which could be addressed with this framework.

6.2 Defining A Mutant Phenotype

Mutations to the components of the β-catenin destruction complex are commonly implicated in oncogenic transformation; a malformed destruction complex offers a reduced binding affinity for β-catenin. In particular, mutations to the APC subunit of the destruction complex are observed in around 85% of spontaneous and familial colorectal tumours [119]. APC is coded for genetically by two alleles, each of which is either healthy or mutated; the majority of CRC tumours display inactivation of both APC alleles [248]. The prevalence of this mutation justifies its incorporation into the 'mutant phenotype' of our study.

APC is not represented explicitly in the model described in Chapter 3; its presence is implicit in the formation of the destruction complex C. We therefore emulate APC mutation by reducing the rate of formation of the destruction complex, through use of a multiplier $\rho_{APC} \in [0, 1]$, which modifies Equations (3.10) and (3.11) for G and C as follows:

$$\frac{dG}{dt} = -\mu_G G + (1 + W(t))\alpha_2 + \mu_C C - \rho_{APC}\alpha_5 \Psi_{W,A} G\,,$$

$$\frac{dC}{dt} = -\mu_C C + \rho_{APC}\alpha_5 \Psi_{W,A} G + \mu_{I_2} I_2 - \alpha_3 B \cdot C\,.$$

Healthy cells possess two normal copies of the APC allele and therefore have $\rho_{APC} = 1.0$. A single-hit APC mutation, in which one allele is mutated, is modelled by taking $\rho_{APC} = 0.5$, whilst a two-hit mutation completely removes the capacity to generate a functional destruction complex and sets $\rho_{APC} = 0.0$.

This mutation has already been studied for a two-cell system in Figures 4.14 and 4.15 of Chapter 4. The two-cell studies indicate that APC mutants express more Hes1 and less Hath1 than their healthy counterparts, thereby assisting the maintenance of the mutant in a mitotically active state by retaining high Notch activation alongside

elevated levels of β-catenin. These behaviours become more pronounced as a cell progresses from a single-hit to a two-hit mutant state.

β-Catenin Expression

Transition to the crypt appears to attenuate the β-catenin response in mutant cells. Figure 6.1 depicts the response of a cell pair initialised at a homogeneous equlibrium with a $W = 0$ or $W = 1$ stimulus. The second cell acquires a two-hit APC mutation at $t = 8h$; results from a healthy cell pair are shown in red for comparison. Although the mutant cells still overexpress β-catenin, the difference in expression between the healthy and mutant cases is substantially smaller than in the studies of Chapter 4.

This behaviour may indicate a need for a more detailed parameter analysis of the Notch-Wnt model in future. Alternatively, the attenuated response could be an artefact of the minimal approach to representing the Wnt pathway, since the formation of the destruction complex is currently subsumed into the function $\Psi_{W,A}$. A more nuanced representation of the processes involved, perhaps by introducing the subunits of the destruction complex into the Wnt submodel, might enable the Notch-Wnt model to better encapsulate the behaviour of an aggressive cancerous phenotype.

Focus on the Two-Hit APC Mutant

Our clinically-relevant studies in the later sections of this chapter focus on the efficacy of two treatments for CRC; the first of these, γ-secretase inhibition, interferes with the ligand binding activity of the Notch pathway. In anticipation of this, and given the assertion of Peignon *et al.* [77] that γ-secretase inhibitors may fail for more aggressive mutants, we focus on the two-hit rather than single-hit APC mutant throughout this chapter.

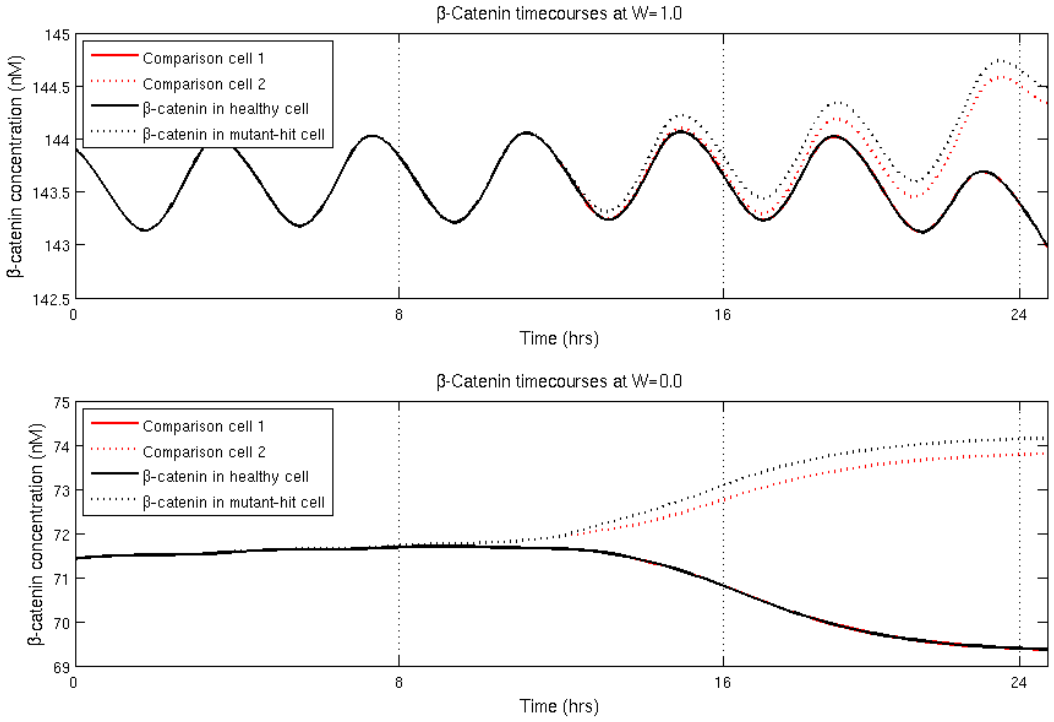

Figure 6.1: Attenuation of the β-catenin response to APC mutation, shown for (top) $W = 1.0$ and (bottom) $W = 0.0$, for two cell pairs: a test pair (shown in black), the second cell of which mutates at $t = 8$h to acquire two APC knockouts; and a healthy pair (shown in red). Cell pairs are initialised at a homogeneous state derived from the crypt conditions of Appendix A, Table A.5, for the given Wnt stimulus. Although the mutant cell expresses higher levels of β-catenin, this increase on the healthy state is substantially smaller than in the two-cell studies of Figures 4.14 and 4.15, which employ initial conditions from Hernández *et al.* [167].

6.3 Mutant Behaviour in a Crypt Setting

It now remains to define the tissue-level behaviour of the mutant phenotype. Mutant cells typically display altered adhesion properties compared to healthy cells [52]. Some models of the Wnt pathway, such as that of van Leeuwen *et al.* [155], explicitly represent the cadherin-binding arm of the pathway commonly associated with intercellular adhesion. Such a model can be used in a crypt embedding to derive variation in adhesion levels directly from cellular Wnt activity [175]. By contrast, our Wnt model represents the canonical form of the pathway only and does not offer as broad a scope for direct coupling to the cellular drag parameters of the underlying tissue framework.

We therefore adopt a simpler approach in this chapter: cells with an APC mutant phenotype may be assigned a drag coefficient ten times that of their healthy counterparts. This is implemented by increasing the parameter μ_i in Equation (2.6), which characterises the forces governing the spring connection between neighbouring cells in the underlying tissue model. Mutant cells with this modification consequently have increased drag and offer a greater resistance to forces imposed upon them by neighbouring healthy cells; this is consistent with the magnitude of drag variation observed *in vivo* [155] and computational implementations in the literature [195].

We mirror the approach of Osborne *et al.* [195] and Mirams *et al.* [176] in decoupling the adhesive and proliferative processes in our crypt model; however, we differ from these studies in deriving mitotic activity from embedded ODEs, rather than a simple proliferative height threshold. Mutant cells in the NWODE framework have an altered biochemistry, but are still subject to the same local concentration of Wnt as healthy cells at the same height and their proliferative power may therefore reduce on ascending the crypt. By contrast, tumour cells in Mirams *et al.* and Osborne *et al.* are assumed to remain mitotically active throughout the crypt, in contrast to healthy phenotypes, which only proliferate in the bottom 30% of the domain.

Some simulations in this chapter examine a mutant phenotype with the same adhesion parameter as healthy cells, in order to determine the effects arising solely from the altered biochemistry of the mutant cells. Others employ the 'elevated adhesion' behaviour described above, in line with existing computational work in the field [195, 175, 176]; this also provides a more accurate depiction of the associated biology. Whether regular or adhesive mutant cells are employed is clearly stated alongside the simulations and discussion in each case. Aside from these considerations, all other aspects of implementation are as described for the NWODE model in Chapter 5.

6.3.1 Observations of Mutant Cell Patches

Our first case study is that of a patch of mutant cells within the crypt. Healthy instances of the NWODE crypt are established and run for 100 crypt hours to ensure attainment of dynamic equilibrium. A mutant patch is then introduced into the crypt, by spontaneously assigning a two-hit phenotype to all cells within 3.0 distance units of a given location. This establishes a roughly circular mass of around $15-16$ mutant cells about the specified point. Crypts are allowed to evolve for a further 40 hours.

Computational studies by Osborne *et al.* [195] and Mirams *et al.* [176] demonstrate the influence of the initial location and relative adhesion level of a mutant cell, or patch of mutants, upon its tendency to fixate within the crypt. In particular, the probability of a mutation eventually dominating the crypt increases with its relative adhesion level [176] and with a lower initial position in the crypt [195, 176].

We therefore examine two different locations for the mutant region: a '*low patch*' scenario, generated around the point with Cartesian coordinate $(5.0, 5.0)$, and a '*high patch*' scenario, which starts from the point $(5.0, 10.0)$. The low patch is therefore placed near the boundary between the transit and priming regions of the crypt, while the 'high patch' lies in the mid-crypt, near to the priming-differentiated divide. Each of these cases is run for mutants with either regular or elevated adhesion; results

presented in this section represent the mean of 100 simulation runs.

Mutant Transit Up the Crypt

The screenshots of Figure 6.2 depict the typical journey of a mutant patch through the crypt, for each of the four main cases (patch high or low; mutants with regular or elevated adhesion). Each of the cases has been run using the same random number seeding and therefore differences between them can be attributed to either the initial location of the mutant patch or its cells' drag coefficient.

These examples suggest that higher patches are flushed out of the crypt sooner, and that patches formed from more adhesive mutants are able to persist for longer. For instance, comparison between the high patch cases (1) and (2) indicates that a tenfold increase in the drag coefficient increases the exit time of the mutant patch from around 25 hours to around 50 hours. Comparison of (2) and (4) suggests that initiation of a low, rather than high, region of mutants with elevated adhesion enables the rogue progeny to extend across the transit, priming and differentiated regions at the 75 hour mark, rather than being flushed out at around 50 hours. Such observations are corroborated by the timecourses of Figure 6.3 and are consistent with similar studies in the literature [195, 176].

Increased adhesion levels enable the mutant cells to move more slowly and persist for longer in the crypt, by allowing the mutants to better resist the proliferative force exerted on them by healthy cells below [195]. A tenfold increase in adhesion levels is not sufficient to prevent a mutant patch from being pushed up the crypt by mitotic pressure from below, but does at least reduce the vertical velocity of the patch. Osborne *et al.* [195] report that a fourteen-fold increase in relative adhesion is necessary for mutant patches to exhibit downward invasion; we would therefore expect upwards movement only for the scenarios explored here, and this is indeed the case.

High patches do not generate the same extent of vertical spread throughout the

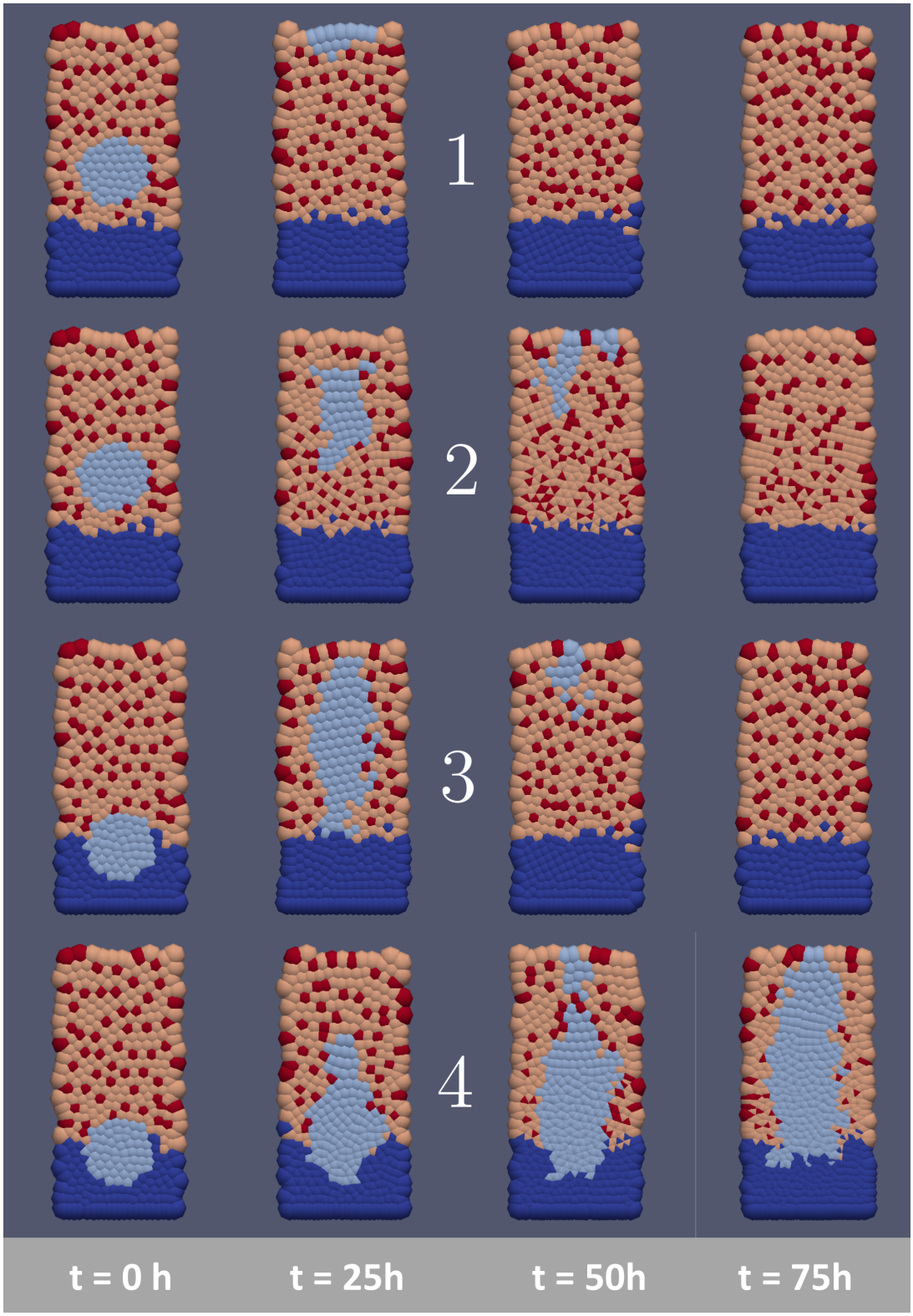

Figure 6.2: Temporal evolution of mutant cell patches: (1) High patch with regular adhesion; (2) High patch with elevated adhesion; (3) Low patch with regular adhesion; (4) Low patch with elevated adhesion. Healthy cells are shown in dark blue (transits), red (secretory) and peach (absorptive), and mutant cells in pale blue. Apparent 'triangular cells' in cases 2 and 4 are visualisation artefacts, arising from compression in and around the mutant patch: these are actually small cells of higher-polygonal form.

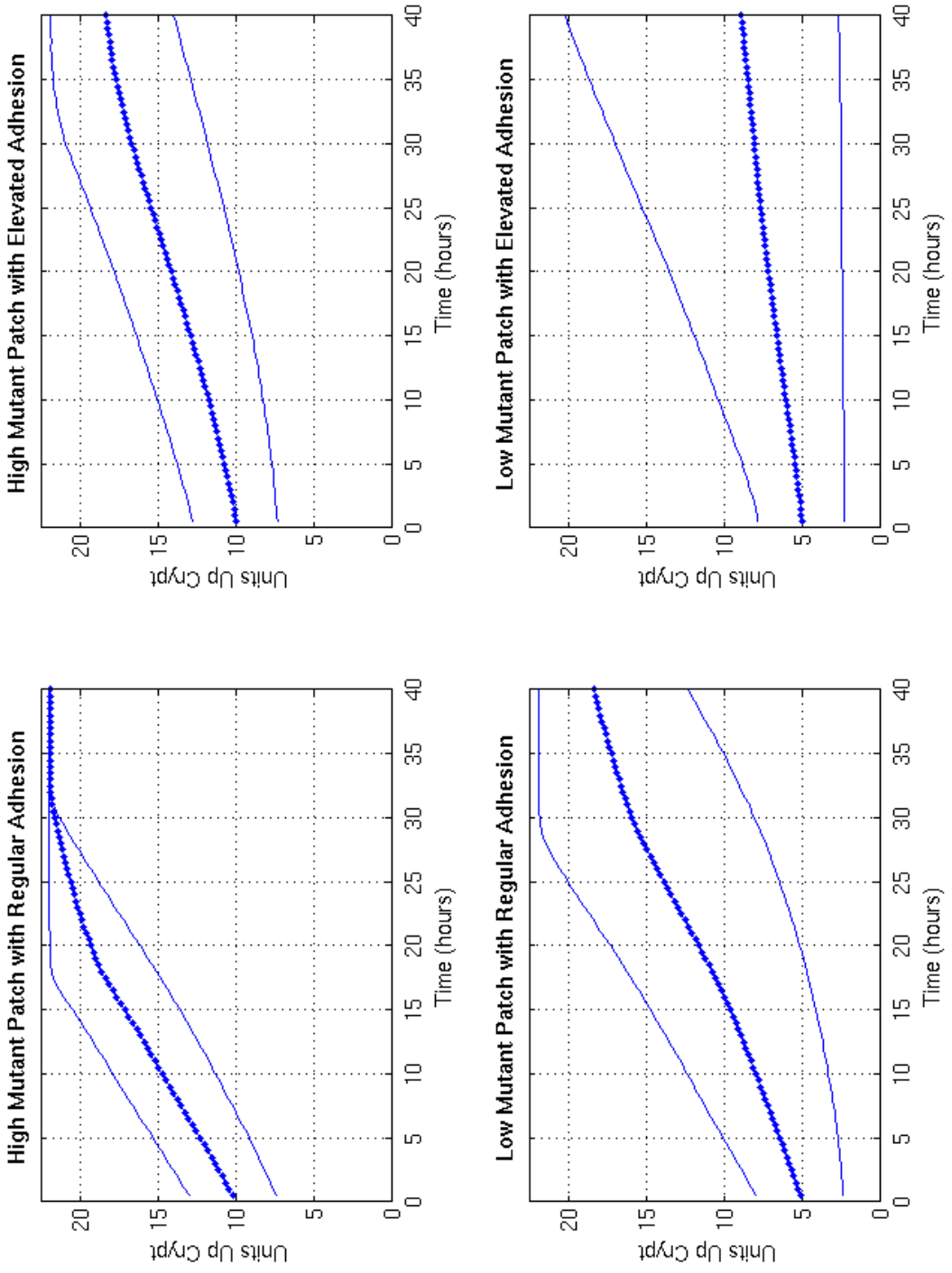

Figure 6.3: Mean timecourses for the transit of mutant cell patches up the crypt, shown for high and low patches, and for mutants with regular and elevated adhesion. Solid lines indicate the position of the highest and lowest mutant cells; the dotted line indicates the height of the centroid of the mutant population.

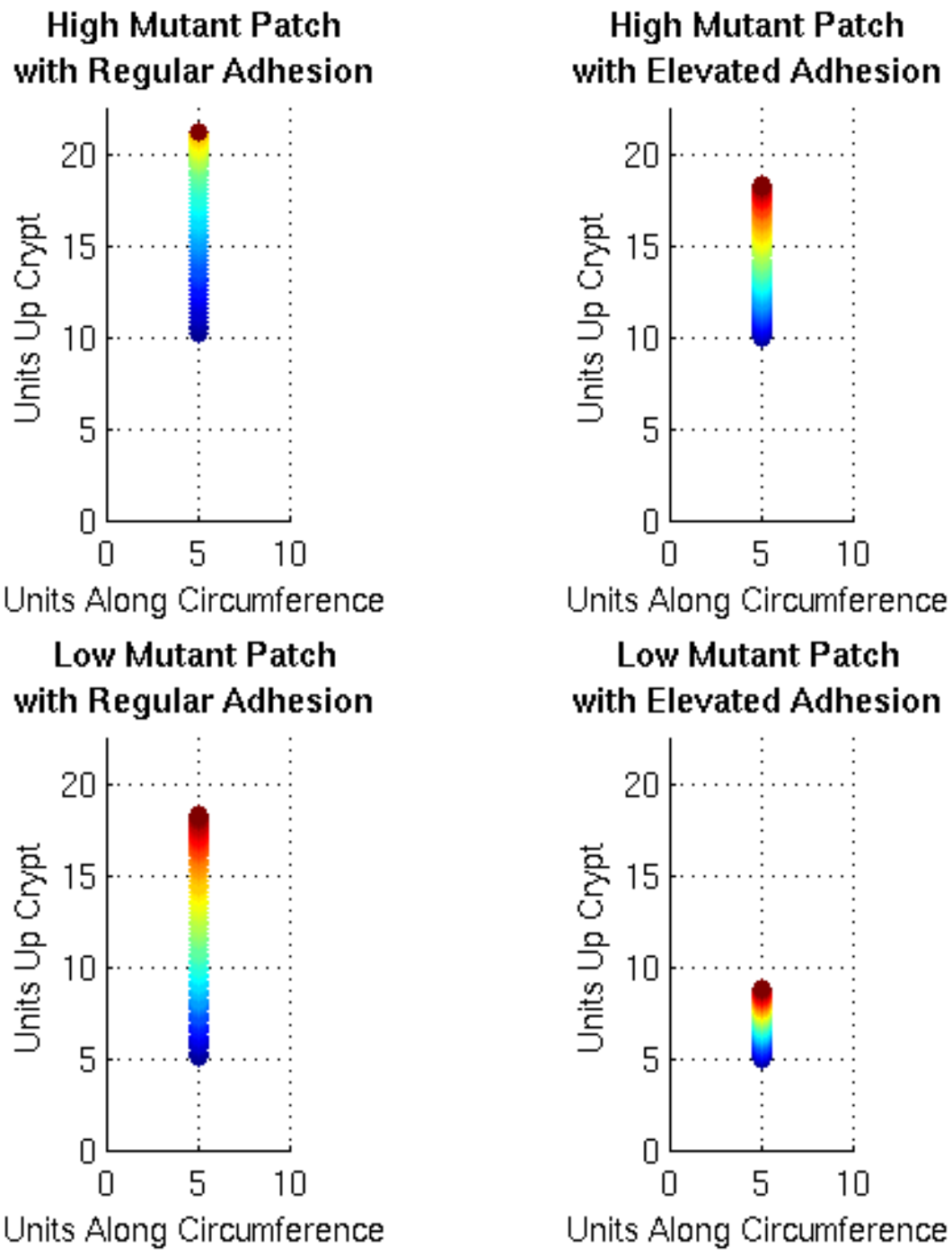

Figure 6.4: Mean path of the centroid of mutant cell patches in the NWODE crypt, averaged over 100 simulations. Colours indicate the time of the given position, ranging from dark blue ($t = 0h$) to dark red ($t = 40h$). Clustering of dark red points in the plot for the high patch with regular adhesion indicates the patch having been completely flushed from the crypt.

crypt, possibly because they have less time to remain in the crypt and expand by proliferation. Although reduced exposure to extracellular Wnt in the upper crypt may also be a factor, Mirams *et al.* [176] suggest that this 'proliferative ceiling' has only a weak influence on the tenacity of mutant cells. Vertical movement dominates the journey of the mutant region up the crypt, as in the mean centroid courses of Figure 6.4. There appears to be almost no lateral movement, except when the mutants are sloughed from the crypt mouth (e.g. high patch with regular adhesion).

Patches with regular adhesion produce longer traces over the 40-hour assessment period than those with elevated adhesion: the low patch with regular adhesion moves further than the high patch with elevated adhesion. Relative adhesion therefore has a stronger influence on the vertical velocity than the initial height of the mutant patch, in accordance with the 'proliferative ceiling' discussion of Mirams *et al.* [176].

Biochemical Impact of Mutant Cells

The screenshots of Figure 6.2 offer a vignette of typical cell behaviour in each of the four mutant patch cases. Although these are only individual examples, they suggest little change to the number and distribution of secretory cells when a mutant region with regular adhesion levels is introduced into the crypt. However, the scenarios with more adhesive mutants demonstrate a marked reduction in the number of secretory cells. Here, compression may effect a biochemical shift in the cells by increasing the number of cell neighbours in the compressed regions; these areas of tissue are then driven to a lower stable state, or even homogeneity, associated with lower Hath1 expression. Reduced expression of Hath1 in turn reduces the number of secretory cells. Similar behaviour has also been observed for the Delta-Notch model of Collier *et al.* [125] in the dynamic crypt studies of Appendix B, Section B.4.3.

Figure 6.5 depicts the mean concentrations of β-catenin and Hath1 in wild-type cells, mutant cells and wild-types neighbouring a mutant cell, for each of the four main

zones of the crypt (according to the partition diagram of Figure 5.3). Although it is possible to calculate these readouts for all the mutant patch scenarios, we focus only on the low patch with elevated adhesion here, in order to further explore the behaviour noted for Case 4 of the screenshots in Figure 6.2.

Perhaps surprisingly, the presence of mutant cells does not have a discernible effect on the mean subcellular concentrations of wild-type cells, or even on the mutant neighbours. The only obvious difference between the plots for each of the three cell classes is the phasing in and out of concentrations for the mutant and neighbour classes, as the mutant patch journeys up the crypt.

It is possible that the attenuation of β-catenin overexpression in mutant cells on going from the two-cell to the crypt-based scenario, as described in Section 6.2, reduces the biochemical impact of the mutants in the crypt setting. Alternatively this could be the result of the robustness of the underlying ODE system, which may compensate for small perturbations inflicted by the mutant cells on the rest of the population.

Although the screenshots of Figure 6.2 suggest that the presence of mutants can cause changes in the cell fate pattern, further studies might examine how much more aggressive a mutant must be to effect noticeable biochemical changes in the surrounding cells in a majority of cases. It would also be informative to explore the cell fate outcome if the NWODE model were extended to include contact inhibition of proliferation.

6.3.2 Differences Between Healthy and Mutant Crypts

We now examine crypts which are comprised entirely of: healthy cells; mutant cells with regular levels of adhesion; and mutant cells with elevated adhesion. Simulation results for the first two cases reflect the mean of 100 simulation runs for each scenario and are shown from the start of simulation, including the equilibration phase. However, compression effects associated with elevated adhesion cause significant lengthening of

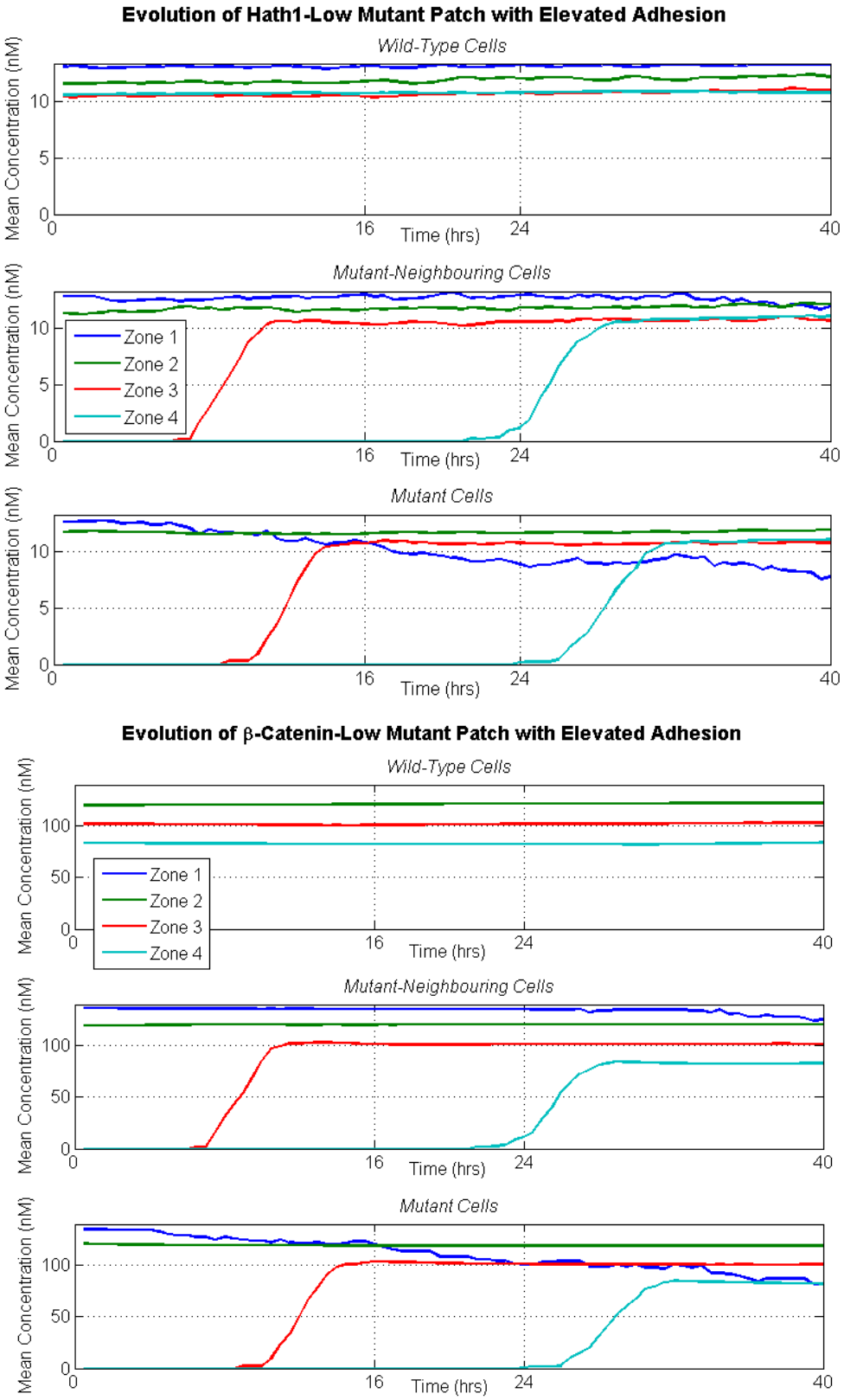

Figure 6.5: Expression timecourses of (upper) Hath1 and (lower) β-catenin, for a crypt with a low mutant patch with elevated adhesion levels. Separate plots are provided for wild-type cells, mutant cells and mutant neighbours. Zone partitions of the crypt are as shown in Figure 5.3.

the runtime, requiring over a week to simulate 100 hours of crypt time for a single random number seeding. This extent of compression is not physiologically realistic and is an artefact of the model; future work might remedy this via the inclusion of contact inhibition of proliferation in the underlying tissue framework. Results for this case represent the mean over four simulation runs.

Response of Cell Totals

The upper plots of Figure 6.6, representing the healthy and mutant crypts with regular adhesion levels, are almost identical and reach dynamic equilibrium after 25 crypt hours. The aberrant biochemistry of mutant cells does not cause substantial changes in the cell type composition of the intestinal crypt epithelium.

As for the mutant patch experiments, cellular compression caused by the elevated adhesion of mutant cells imposes a considerable effect on the cell fate outcome. The lower plot of Figure 6.6, showing cell totals for the more adhesive mutants, does not attain equilibrium within the first 100 crypt hours. Proliferative cell types – namely the transit and absorptive cells – are still in an exponential growth phase after this time. Uniformly elevated adhesion levels cause cells to resist the mitotic pressure from lower regions; the absence of contact inhibition from the model allows the cells to compress but continue to divide. Increased cell type totals are therefore a consequence of the mechanical constraints imposed by the increased drag coefficient, and do not arise from the altered biochemistry of the mutant cells.

Response of Cell Fate Patterning

The Ripley analyses shown in Figure 6.7 indicate similar patterning for the healthy and regular mutant cases, except for a slightly longer pattern length in the mid-crypt for the regular mutants. This may indicate a slight tendency to favour an absorptive fate over a secretory one, but only involving the elimination of a small number of

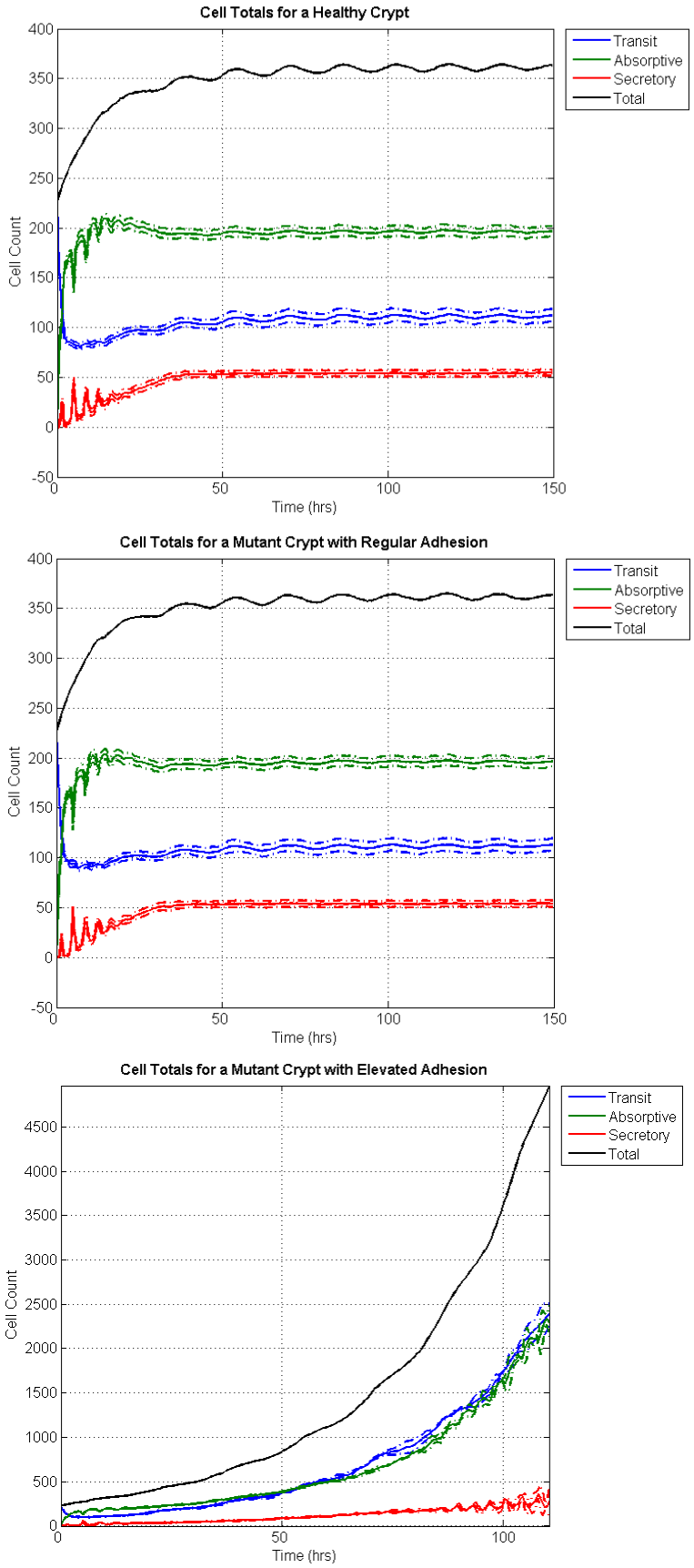

Figure 6.6: Timecourses of the cell totals for crypts comprised entirely of (top) healthy cells; (bottom) mutant cells with regular adhesion levels.

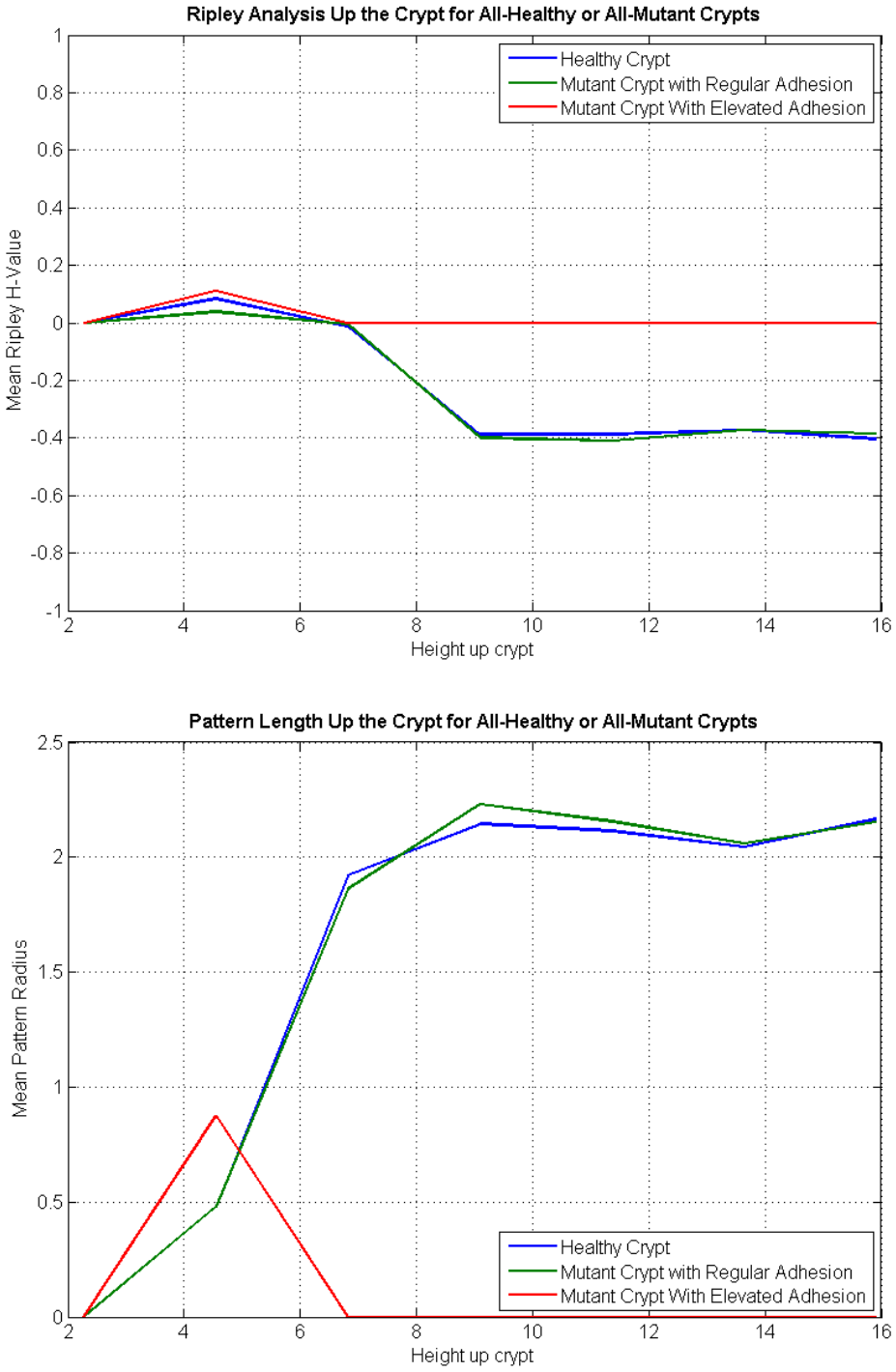

Figure 6.7: Ripley H-Values and pattern length analysis for crypts comprised entirely of healthy cells, or entirely of tumour cells with either regular or elevated adhesion.

secretory cells compared to the normal case. By contrast, the adhesive mutant crypt does not pattern. Example screenshots shown in Figure 6.8 agree with this; cells in the priming zone of the adhesive mutant crypt do not exceed the Hath1 threshold.

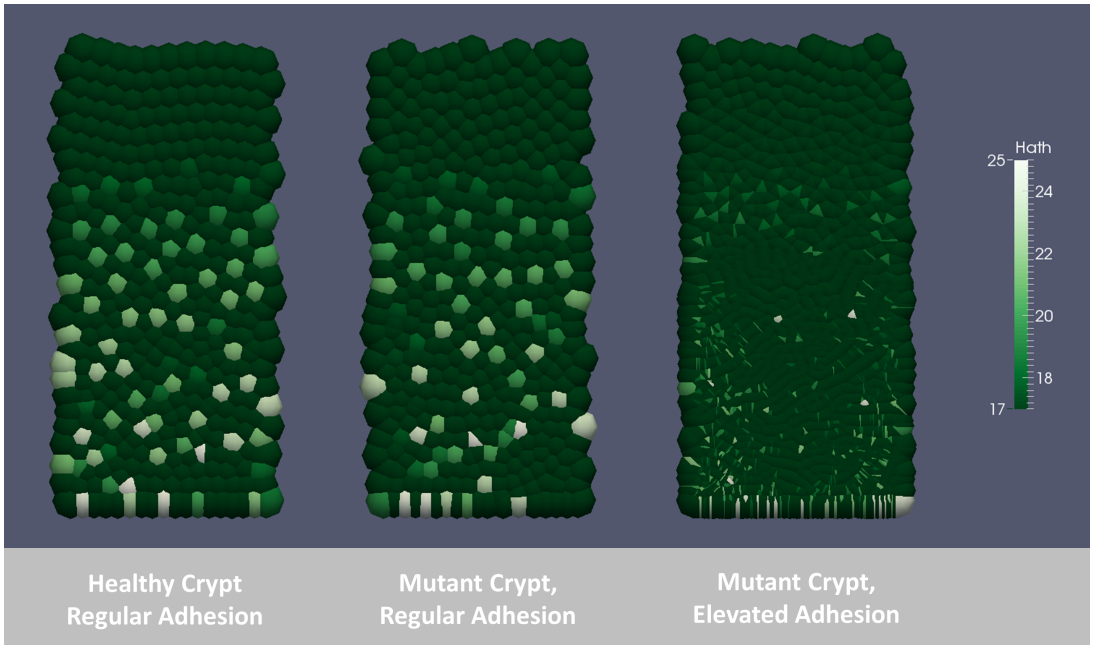

Figure 6.8: Screenshots at $t = 100$h for crypts composed of (L-to-R): normal cells; mutant cells with regular adhesion; mutant cells with elevated adhesion. These images show the concentration of Hath1 rather than cell type. Colour scaling ranges from 17.0nM to 25.0nM to aid identification of cells expressing sufficient Hath1 to surpass the secretory conversion threshold; cells shown in dark green lie below this threshold.

6.3.3 Comments

The crypt setting attenuates the biochemical response of mutant cells, producing less aggressive behaviour than for the two-cell studies of Chapter 4. Although the Wnt activity of neighbouring cells is not directly coupled, it is subject to a secondary form of coupling owing to the subcellular crosstalk with the Notch pathway, which participates in juxtacrine communication. Notch-Wnt crosstalk may therefore serve as a regulatory mechanism in the crypt, in which the local averaging processes characteristic to the Notch pathway serve to guard against perturbations to the Wnt system.

It would be interesting to see whether this behaviour persists after enhancement of the Wnt submodel. The novelty of our Notch-Wnt crosstalk model (using only 5 components in the Wnt system) demanded a simpler approach in Chapter 3; however, it may be that this level of reduction misses some of the subtleties required to produce a more aggressive mutant phenotype in a multicellular setting. Several more detailed models of the Wnt signalling pathway already exist, including those of Lee *et al.* [161] (15 components), van Leeuwen *et al.* [155] (11 components) and Kogan *et al.* [172] (13 components), some of which have been used in crypt embeddings [175]. It would be informative to couple these Wnt models to our Notch submodel to see whether the attenuation effects persist.

Having explored the behaviour of mutant cells in our NWODE model, we now progress to a study of CRC treatments, and examine the performance of two competing therapies proposed for cell fate conversion in the colorectal epithelium.

6.4 Exploring Clinical Treatments

Notch-targeted therapies for CRC employ the pathway's role in cell fate selection to induce cell-cycle exit. This strategy aims to regain control of Wnt-aberrant cells by inducing differentiation into mitotically inactive, secretory phenotypes, but achieves this by modulating the activity of the Notch, rather than the dysregulated Wnt, pathway. Although enforced differentiation does not kill the mutant cells, it inhibits their propagation through the surrounding tissue, enabling containment of the tumour and facilitating its eradication through either surgery or targeted radiotherapy.

High levels of Notch activity are associated with the maintenance of a mitotically active state; conversely, the expression of Hath1 in a low-Notch state induces cell-cycle exit and commitment to the secretory lineage. Possible strategies for forced selection of a secretory phenotype include a reduction in the strength of the Notch signal through

the cell, or an increase in the longevity of Hath1. Two clinical treatments have been proposed to perform this forced selection:

- *γ-secretase inhibitors* reduce the activity of γ-secretase at the cell surface membrane. Under normal conditions, γ-secretase performs a vital cleavage of the Notch receptor, enabling its fragmentation and the transduction of the Notch signal into the recipient cell by means of the NICD fragment. In the presence of an inhibitor, γ-secretase cannot perform the cleavage and the Notch signal is substantially reduced;
- *Hath1 stabilisers* reduce the decay rate of Hath1, thereby facilitating its accumulation within the cell.

γ-secretase inhibitors have been shown to deliver substantial conversion of crypt cells into secretory goblet phenotypes in the intestinal epithelia of mice carrying an APC knockout [91]. Further studies of intestinal tumours in both mice and humans suggest that γ-secretase inhibition is only effective for treating less aggressive tumours and propose stabilisation of Hath1 as a more viable route for CRC therapy, because this is downstream of the interactions between the Notch and Wnt pathways. [77].

Comparison of these two approaches in a computational setting should provide timely and relevant insights into the clinical treatment of CRC. Our examination of potential therapies in this chapter encompasses four distinct treatment strategies:

A No treatment;

B Application of Hath1 stabilisers;

C Application of γ-secretase inhibitors;

D Combined treatment: simultaneous application of B and C.

Modification of Equations

Given the interference of γ-secretase inhibitors with the fragmentation of the Notch receptor, we represent the effects of γ-secretase treatment through use of a multiplier $\rho_{GSI} \in [0, 1]$, applied to the evolution equations for N and F. Stabilisation of Hath1 is effected via the modifier $\rho_{Hath} \in [0, 1]$, applied to the Hath1 decay term in the equation for Hath1 evolution.

These two treatments result in the following modifications to the Notch system ODEs:

$$\frac{dN}{dt} = -\rho_{GSI}\mu_N N + \frac{\theta_1 \bar{D}^{m_1}}{\kappa_1^{m_1} + \bar{D}^{m_1}} ,$$

$$\frac{dF}{dt} = -\mu_F F + \rho_{GSI}\alpha_{\text{frag}}\mu_N N - \alpha_1 B \cdot F ,$$

$$\frac{dH_2}{dt} = -\rho_{Hath}\mu_{H_2} H_2 + \frac{\xi_5 \sigma_5^{n_5}}{\sigma_5^{n_5} + H_1^{n_5}} .$$

Discussion of these approaches in the literature focuses on their qualitative effects upon crypt tissue, rather than a quantitative assessment of the extent to which the associated reaction rates are altered. We adopt the expediency of selecting the largest possible values for ρ_{Hath} and ρ_{GSI} which still yield noticeable effects in the two-cell systems of Figure 6.9 for separately-dosed therapies. This is analogous to a clinical approach of dosing the patient with the smallest amount of drug that will deliver the required effect, given the desire to minimise side effects in the patient [249].

Consequently we use the values $\rho_{Hath} = 0.5$, $\rho_{GSI} = 0.9$ during our simulations to implement dosing of Hath1 stabilisers or γ-secretase inhibitors respectively. Both values are adopted when representing a dual-treatment scenario, and we set $\rho_{Hath} = 1.0$, $\rho_{GSI} = 1.0$ when no treatment is being administered.

We apply some simplifying assumptions, namely that: the effects of dosing occur instantaneously on application of a treatment; that these effects remain constant

throughout the dosing window; and that the dosing parameters return immediately to their normal, non-dosing values on removal of the treatment. Although the pattern of treatment could take many different forms – including intermittent dosing, alternation of treatments and variation in the length of the dosing and recovery windows – we focus only on the constant case here. The more complicated regimes would be more useful in a clinical setting, but the simple, single-dosing window scenario is a necessary starting point for our investigations, and provides the foundation for more sophisticated extensions in the future.

6.5 Two-Cell Studies

Before studying the effects of γ-secretase inhibition and Hath1 stabilisation within the crypt environment, we present some two-cell studies in which the first cell of the pair is healthy and the second is either healthy, a single-hit mutant or a two-hit mutant according to the phenotypes outlined in Section 6.2.

In each case, the ODEs for the cell pair are solved for the first 16 hours without any treatment; treatment is applied continuously for the next 8 hours; and the cellular response is monitored after the end of the treatment window for a further 16 hours. Results for the therapies B, C and D are shown in Figure 6.9. Each cell pair in these simulations starts from typical crypt concentrations at $W = 0.5$, and is set off from a homogeneous state. We note the following observations:

Mutant cells are less susceptible to treatment: Expression of Hath1 is always higher in the healthy cell; elevated concentrations of β-catenin in the mutants enable them to upregulate Hes1 and suppress Hath1. This biochemical rewiring renders the mutant cells less susceptible to the effects of the treatments than their healthy counterparts. One would anticipate crypt-wide dosing to have profound effects on the healthy cells in the intestinal epithelium.

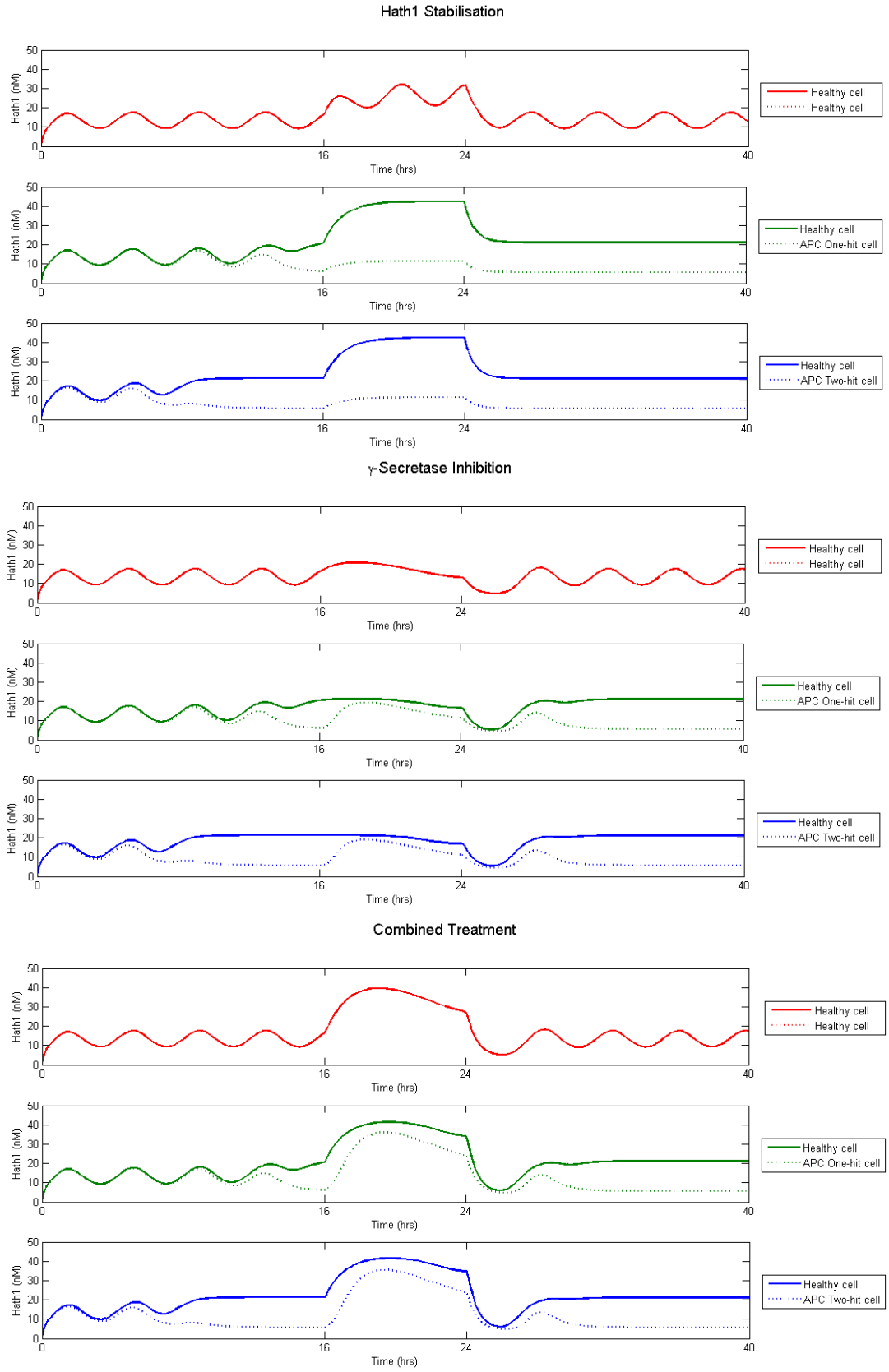

Figure 6.9: Investigation of clinical treatments in a two-cell pair, shown for $W = 0.5$. The top graph set shows the effects of Hath1 stabilisation; the middle set depicts the response to γ-secretase inhibitors; and the lower set is for a combination of the two. Simulations start from homogeneous crypt initial conditions, as listed in Table A.5.

Downstream intervention is more effective: Dosing with Hath1 stabilisers appears to maintain the elevation of Hath1 expression throughout the dosing window; however, γ-secretase inhibitors prove more effective at the start of treatment than towards the end. This may be due to the crosstalk between the Notch and Wnt pathways, which occurs downstream from the point of action of γ-secretase inhibitors. Reduced production of NICD lowers the amount of binding between β-catenin and NICD, thereby leaving more β-catenin available for direct binding with the Hes1 promoter.

Combination therapy has a synergistic effect: Combination of the treatments yields a synergy, and proves the most effective way to force differentiation of the mutant cell. Combined treatment induces a significant increase in the Hath1 expression of the mutant and healthy cells, and although there is some fall-off in expression towards the end of the dosing window, the absolute Hath1 concentrations in the mutant cell represent a two-and-a-half- to three-fold increase during the dosing window, compared to the effects of either of the single treatments.

The observations for the two-cell case are encouraging as regards the apparent synergy between Hath1 stabilisation and γ-secretase inhibition. It remains to investigate whether cells in the crypt environment display a similar response.

6.6 Crypt Implementation

The NWODE framework presented in Chapter 5 was shown to offer a means of simulating robust patterning and consistent cell proportions in a healthy crypt. We have seen in Sections 6.2 and 6.3 how the framework can be extended to accommodate mutant cells. However, studying the effects of clinical treatments introduces new ranges of cellular behaviour, which necessitate minor extensions to the model.

Hath1 thresholding: The secretory conversion threshold $H_2 = 17.0nM$ is retained for the priming region of the crypt. However, treatments B–D induce higher expression of Hath1 than in a healthy crypt and so we impose forced differentiation to the secretory phenotype for any cell in the transit or priming regions whose Hath1 concentration satisfies $H_2 > 28.0nM$[1].

Dosing windows: All crypts are initially run for 100 hours of simulation time to ensure attainment of dynamic equilibrium; this period is not recorded in the results. Data collection begins after this point, which we term $t = 0h$, when a region of mutant cells is introduced into the crypt. The system evolves spontaneously for 16 hours, during which time all mitotically active cells in the crypt divide once on average. Treatment commences at $t = 16h$ and continues until $t = 24h$. Each simulation progresses through a post-dosing 'recovery period' after the treatment is removed, until the end of simulation at $t = 40h$. The use of an eight-hour dosing window is compatible with known half-lives for γ-secretase inhibitors, which range from $t_{1/2} = 0.6$hrs to $t_{1/2} = 15$hrs [250, 249].

All other features of the crypt implementation remain as described in Chapter 5. The basic pattern of *equilibration – mutant growth window – dosing window – recovery window* described in Section 6.3 is applied to all simulations in this study. All results presented here represent mean values taken over all 100 simulations in a given class.

Assessment Criteria

As discussed in Section 6.4, the objective of these treatments is to halt the progress of, rather than kill, the tumour cells. Our assessment of which treatment is 'best' is therefore measured according to the following criteria:

- How successful is the treatment at converting tumour cells to a secretory fate?

[1] This value has been selected following the NWODE threshold variation results from Section 5.11.

- To what extent do cells retain this cell fate conversion?
- How does the therapy affect the progression of tumour cells through the crypt?

We assess these criteria by tracking the relative numbers of transit, secretory and absorptive cells in the healthy and mutant populations at each stage of the treatment process, and also gather data pertaining to the height and spread of tumour cells through the crypt. Where appropriate, these metrics are also compared against the outcomes in a healthy crypt. Our criteria thus established, we now evaluate our results and identify the main features of crypt behaviour in response to the four treatments.

6.7 Mutant Phenotype with Regular Adhesion

Simulations of mutant patches and whole-crypt mutation in Section 6.3 have provided valuable insights into the movement of tumour cells through the crypt. Models involving elevated adhesion provide a closer approximation to the biological reality; however, models endowing tumour cells with normal levels of adhesion allow us to observe the cell fate response arising purely from altered biochemistry. Our initial clinical simulations therefore focus on this approach.

The spatial location of tumour cells within the crypt at the start of dosing strongly influences the interpretation of results. In particular, the NWODE model assumes fixed cell fate within the differentiated region; only cells in the transit and priming regions are susceptible to cell fate conversion. Observations of the crypt response fall into one of two categories: first, the direct effect of the clinical treatments on mutant cells; secondly, indirect effects on the mutant patch arising from cell fate response of healthy cells, which affects the mitotic pressure exerted by lower crypt regions.

The screenshots of Figure 6.10 show the response of a low patch with regular adhesion, to treatments A – D; the mean height of the centroid and vertical bounds of the patch in both high and low cases are shown in Figure 6.11. The lower half of the low

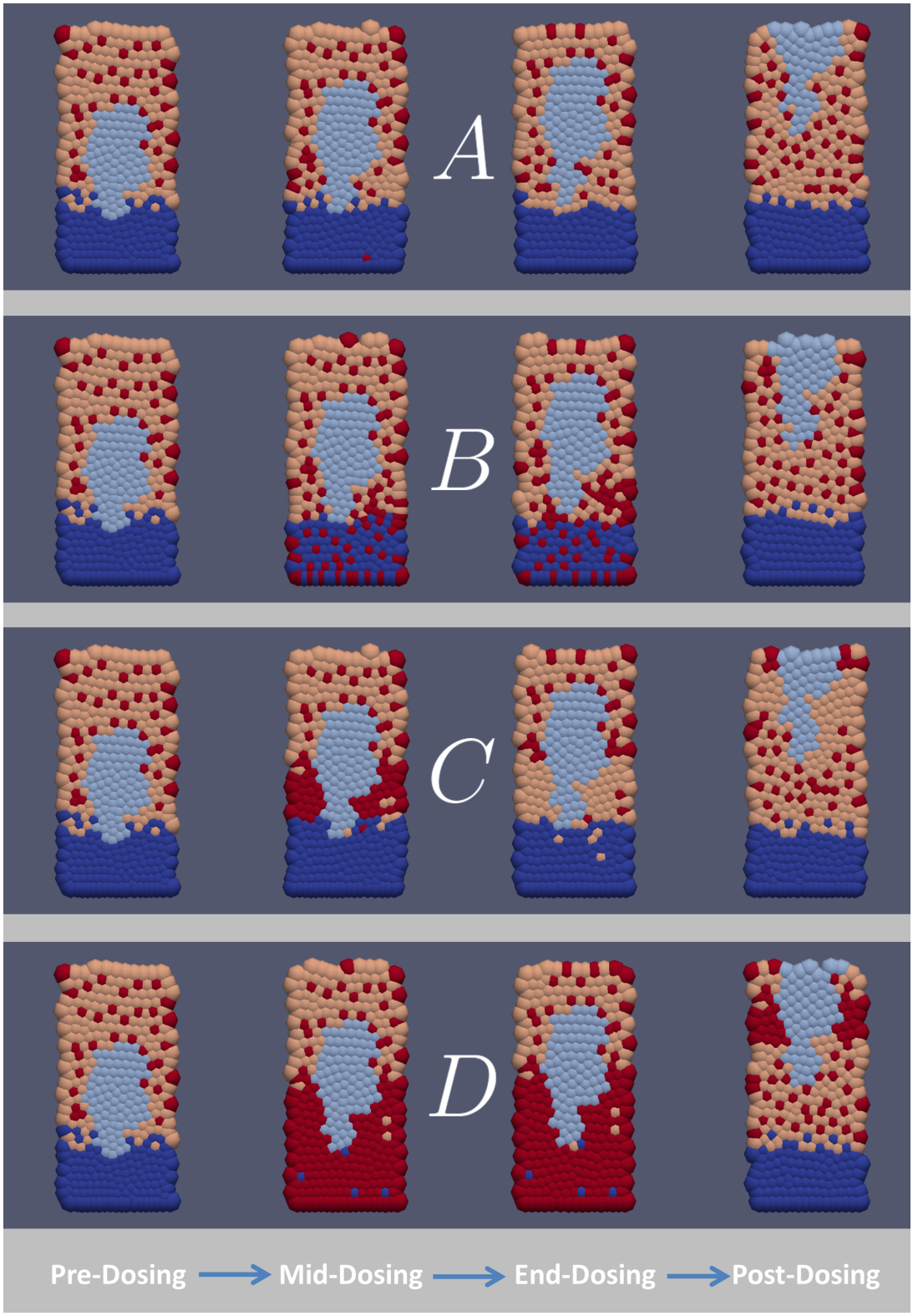

Figure 6.10: Screenshots of the cell type response to treatments A – D, for the low patch case with regular adhesion. Colours represent transit cells (dark blue), absorptive cells (peach) and secretory cells (red), with mutant cells shown in pale blue. Mutants can undergo cell fate switching in response to clinical treatment: their phenotypes are not depicted but are discussed in the graphs of Figures 6.13 and 6.14.

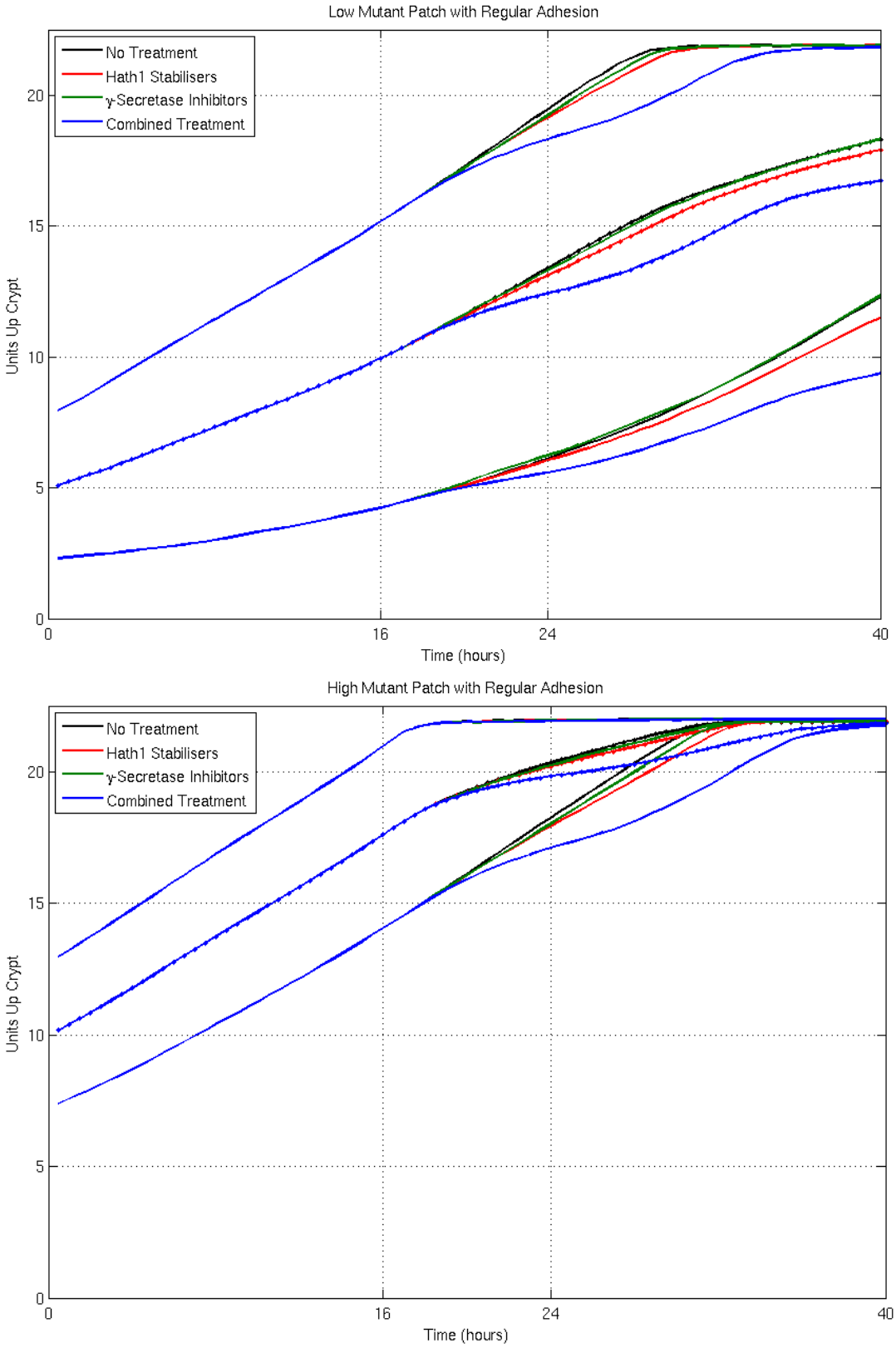

Figure 6.11: Mean transit of regular mutant patches through the crypt during the pre-dosing $(0-16h)$, dosing $(16-24h)$ and recovery $(24-40h)$ windows. Solid lines indicate the position of the highest and lowest mutant cells; the dotted line indicates the height of the centroid of the mutant population.

patch lies within the priming region at $t = 16$h, whereas the high patch is completely in the differentiated zone. Results for the high patch are therefore more indicative of the response of healthy, rather than tumour, cells to the clinical treatments.

Inhibition of the Notch Signal Yields Short-Term Effects

γ-secretase inhibition delivers only short-term cell fate conversion. The graphs of Figure 6.12 show a faster initial response to dosing with γ-secretase inhibitors than with Hath1 stabilisers; however, this response is short-lived and the extent of secretory conversion falls sharply before the end of the dosing window.

This may be due to the feed-forward loop upstream of the β-catenin-Hes1 crosstalk hub. β-catenin can upregulate Hes1 directly, by binding to the promoter in Step (14) of Figure 3.1, or indirectly, by forming an intermediate with NICD in step (3). Impairment of the Notch signal reduces the formation of NICD; this reduces β-catenin-mediated regulation by the indirect route and yields a short-term reduction in the transcription of Hes1, resulting in cells' temporary conversion to a secretory phenotype. However, reduced β-catenin-NICD binding increases the levels of β-catenin available for direct upregulation of Hes1; the feed-forward motif therefore serves to counteract small perturbations in the Notch signal. Future studies might examine whether the Hes1 autoinhibition motif (Step (5) of Figure 3.1) also contributes to this response.

Such behaviour is also visible on the screenshots of Figure 6.10; series C for γ-secretase inhibition converts most cells in the priming region by the middle of the dosing window, but these revert to absorptive type before the end of dosing. By contrast, series B for Hath1 stabilisation demonstrates scattered conversion across the transit and priming regions throughout the dosing window, although this conversion is reversed upon removal of treatment. Hath1 is downstream of the crosstalk hub, so interference at this point is less susceptible to effects from the feed-forward loop.

Although these results pertain largely to healthy cells, the same behaviour is also

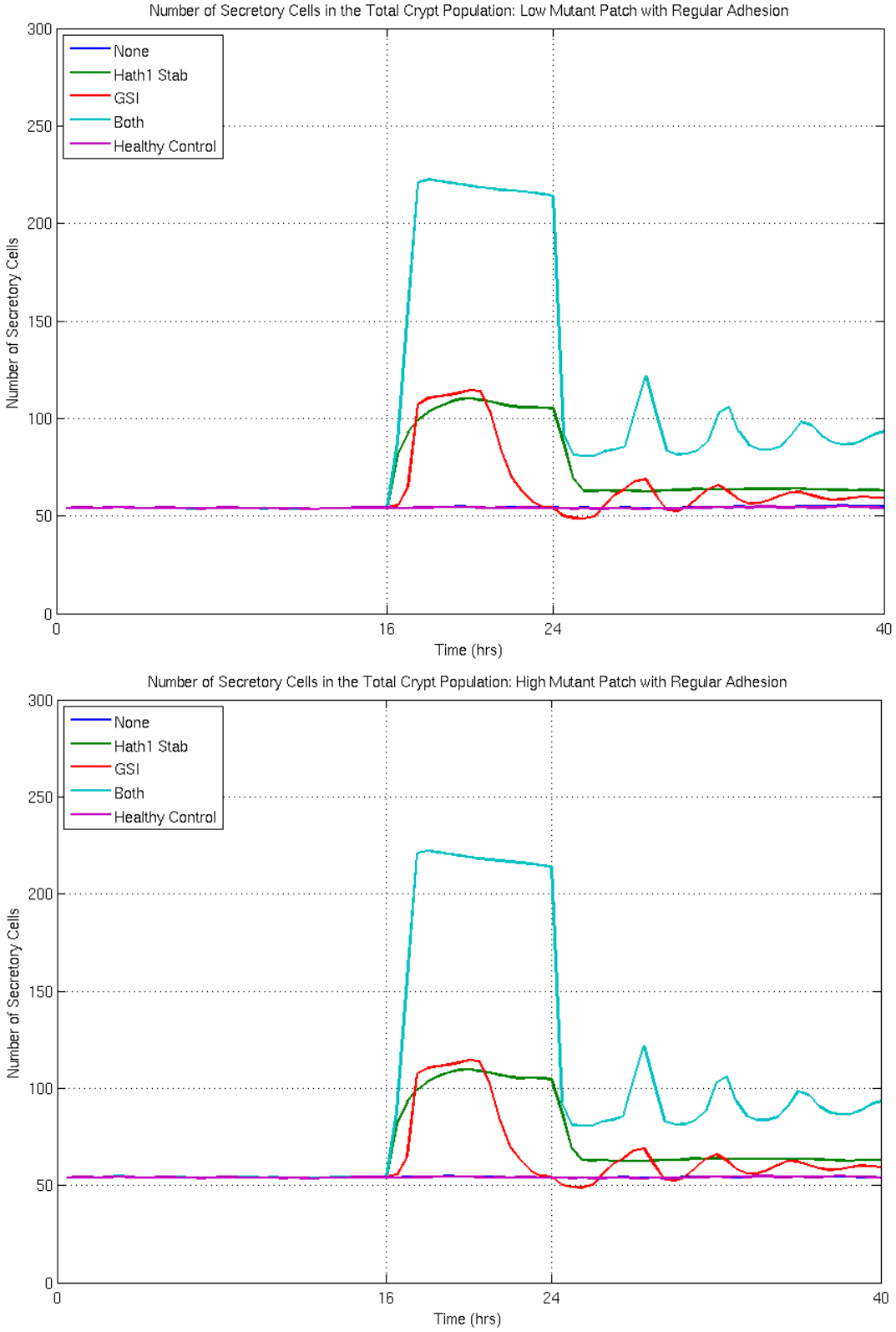

Figure 6.12: Mean timecourses for the number of secretory cells in the crypt population, shown for (upper) a low-placed, and (lower) a high-placed mutant patch; both produce near-identical profiles. Mutant cells have regular adhesion levels in both cases. Results are shown for the four treatment strategies A–D over the course of the pre-dosing $(0-16h)$, dosing $(16-24h)$ and recovery $(24-40h)$ windows.

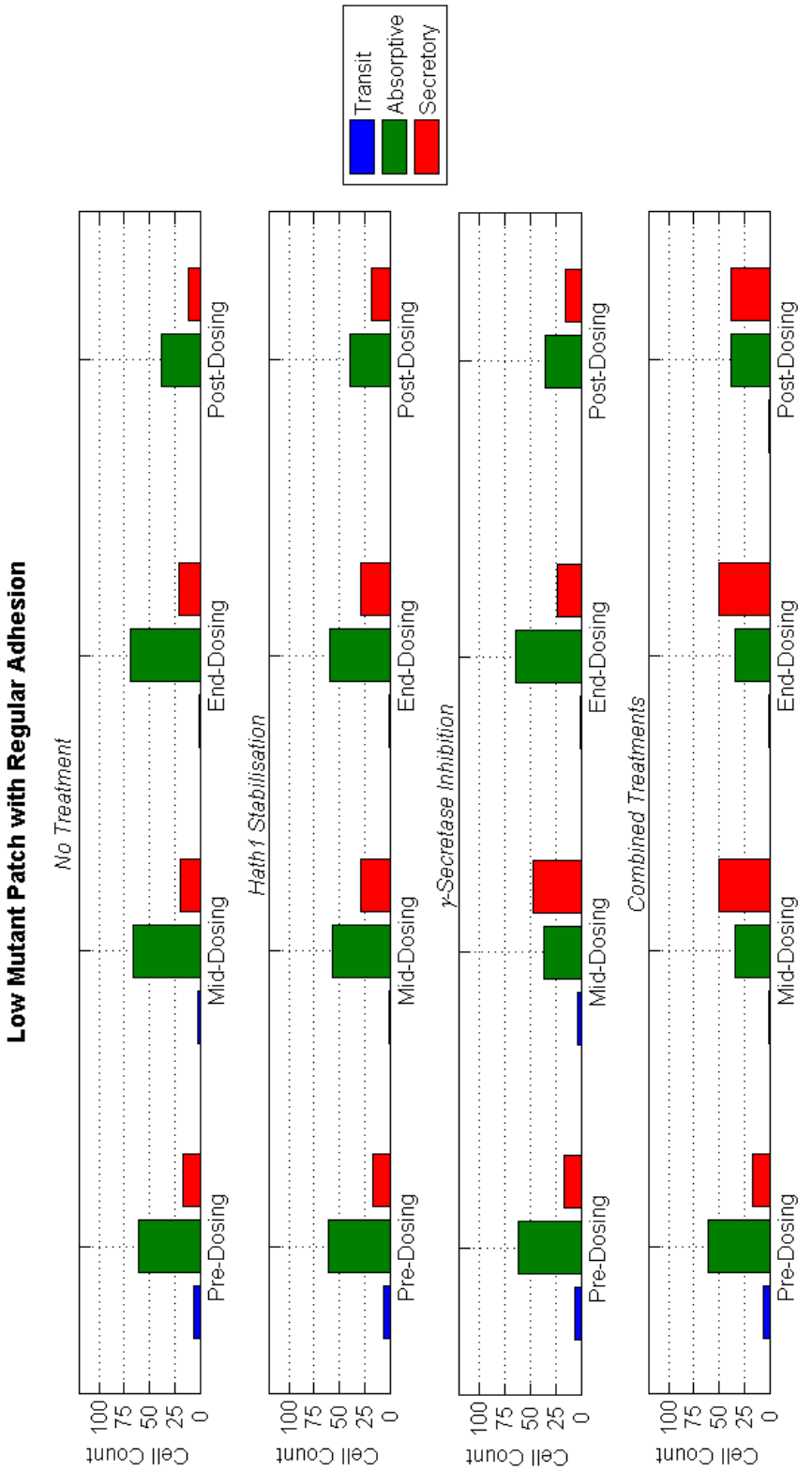

Figure 6.13: Bar graph showing the mean number of mutant cells of transit, absorptive and secretory type at each stage of the four treatment series, for a low-placed mutant patch with regular adhesion. Totals are shown for the end of the pre-dosing ($16h$), dosing ($24h$) and recovery ($40h$) windows, along with results from the midpoint of the dosing window ($20h$).

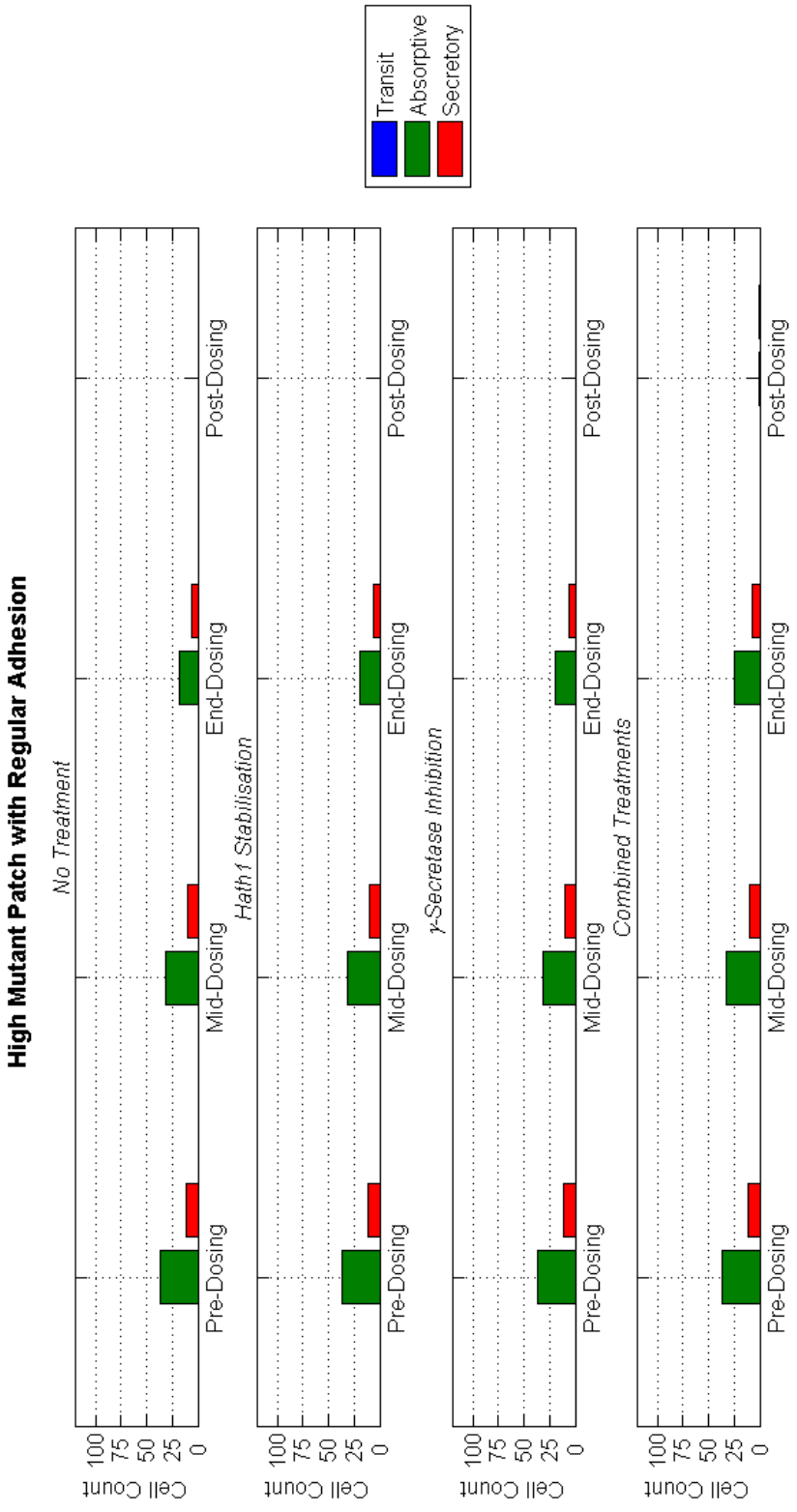

Figure 6.14: Bar graph showing the mean number of mutant cells of transit, absorptive and secretory type at each stage of the four treatment series, for a high-placed mutant patch with regular adhesion. Totals are shown for the end of the pre-dosing ($16h$), dosing ($24h$) and recovery ($40h$) windows, along with results from the midpoint of the dosing window ($20h$). Mutant cells have been eliminated from the crypt by $t = 40$h.

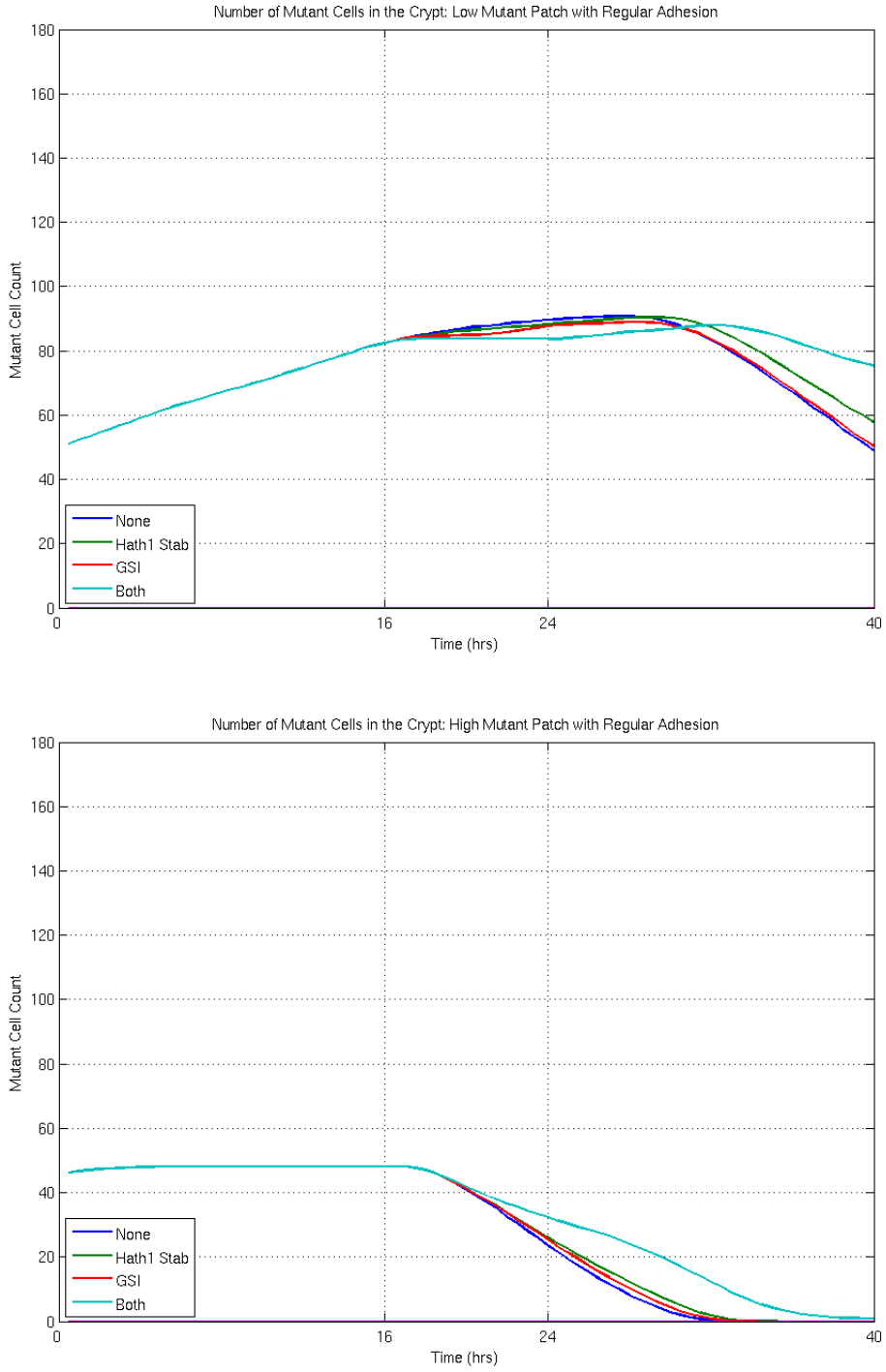

Figure 6.15: Mean total of mutant cells in the crypt population over the course of the pre-dosing $(0-16h)$, dosing $(16-24h)$ and recovery $(24-40h)$ windows.

evident for small numbers $(20-25)$ of tumour cells in the low patch, as can be seen from the bar graphs of Figure 6.13. Mutant conversion does not occur in the high patch case (Figure 6.14), owing to its location in the crypt at the time of dosing.

Hes1 Activity Shapes the Recovery Dynamics

The upstream nature of γ-secretase inhibition is also responsible for the oscillations of the number of secretory cells during the recovery period, in treatments C and D (see Figure 6.12). These are due to the increase in, and subsequent equilibration of, the Notch signal after the γ-secretase inhibitors are removed. These oscillations are similar to those depicted in Figures 4.12 and 4.13 of Chapter 4, and are produced by the autoregulation of Hes1. Hath1 stabilisation does not interfere with Hes1 regulation and so does not produce similar post-dosing oscillations.

Synergy Between γ-secretase Inhibition and Hath1 Stabilisation

Combination treatment inhibits the fall-off of γ-secretase inhibition during the dosing window; the graphs of Figure 6.12 suggest that secretory conversion persists for longer following the combined treatment. Indeed the mutant cell totals for the 'low patch' results of Figure 6.15 suggest that, although each of treatments B, C and D slows mutant population growth compared to the untreated case A, only the combined treatment induces complete mitotic arrest of tumour cells throughout dosing.

Combined Treatment Converts Both the Transit and Priming Regions

Observations of the pattern radius estimates (data not shown) at the end of the dosing window indicate a small lengthscale (< 0.5 cell diameters) for the secretory cell distribution in the lower crypt when using the combined treatment, suggesting substantial conversion of the transit and priming regions. By comparison, the estimate for treatment B lies at around $1.0-1.5$ cell diameters, suggesting a less comprehensive

conversion.

Combined Treatment Increases Mutant Retention

One caveat for the combined treatment is the greater retention of mutant cells in the crypt, owing to the mitotic arrest of both healthy and mutant cells. Indeed, the final bar graph of Figure 6.13 indicates the presence of tumour cells in the transit region of the crypt at the end of the recovery window for treatment D. This is not the case for any of the other therapies.

This outcome is due to the efficiency of the combined treatment at forcing secretory conversion, and hence cell-cycle exit. Wholesale conversion of healthy cells in the transit and priming regions completely removes the mitotic pressure which usually forces cells up the crypt. This enhances the retention of aberrant cells within the crypt, which continue to propagate after the effects of the dosing have subsided. Careful management of the post-dosing period would be required, either by removal of the tumour cells while still in the secretory state, or use of repeat dosing to maintain their mitotic inactivity.

Certainly this finding motivates future work on the length and nature of the dosing window, and suggests that the investigation of mutants with increased adhesion presented below is a useful next step in exploring the efficacy of clinical therapies.

6.8 Mutant Phenotype with Elevated Adhesion

We now incorporate mutant cells with increased adhesion levels into an otherwise healthy crypt[2]. Case studies using regular adhesion offer insights into the behaviour of healthy cells and also of mutants in the priming region; however, the increased fixation associated with more adhesive tumour cells allows us to examine the response

[2]We retain the approach of Section 6.3 and adjust the drag parameter, μ_i, of mutant cells to ten times its value in healthy cells.

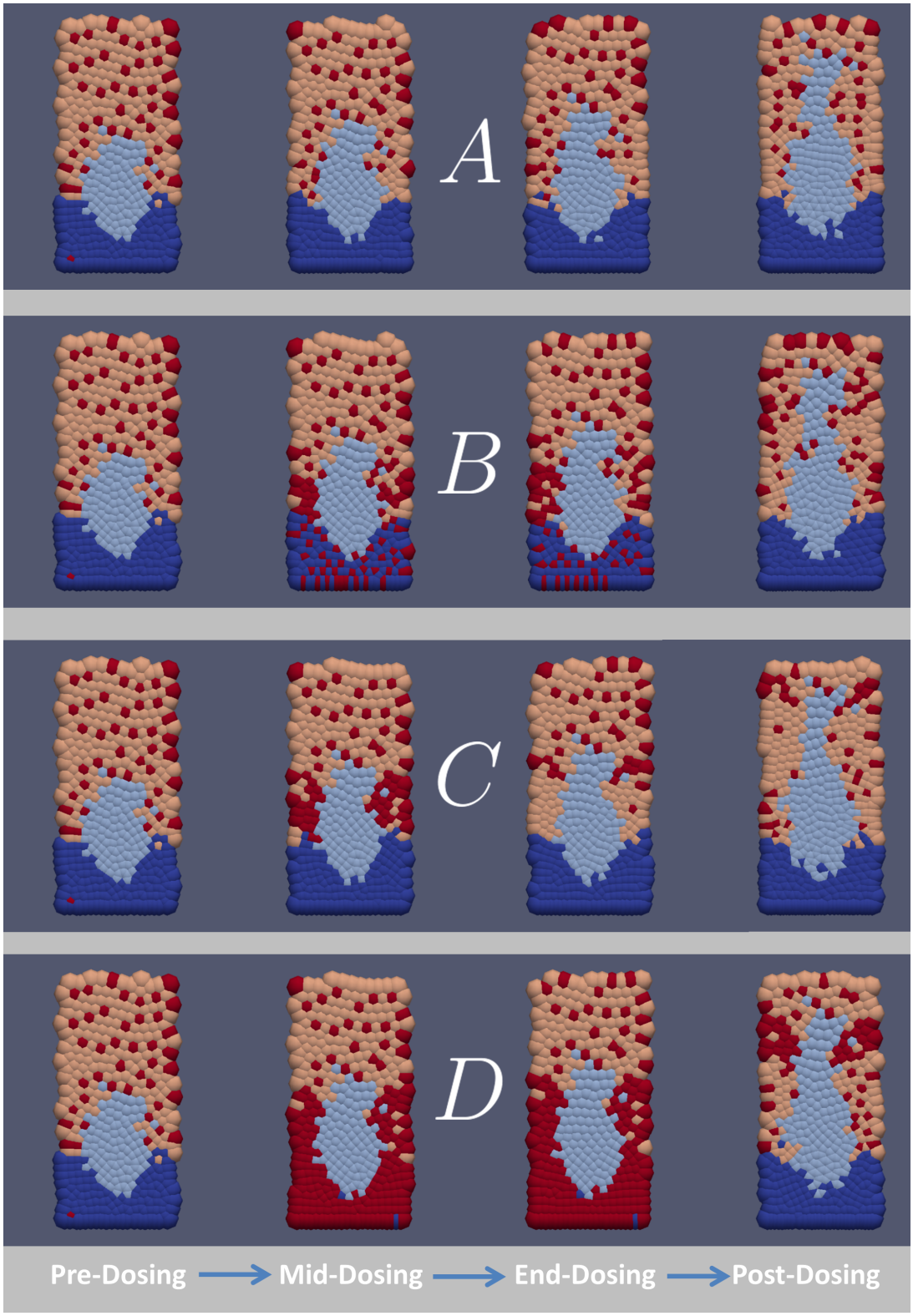

Figure 6.16: Screenshots of the cell fate response to treatments A – D, for a low patch case with elevated adhesion. Colours represent transit cells (dark blue), absorptive cells (peach) and secretory cells (red), with mutant cells shown in pale blue. Mutant cells may also undergo cell fate switching as a result of the clinical treatment: mutant phenotypes are not depicted but are discussed in the graphs of Figures 6.19 and 6.20.

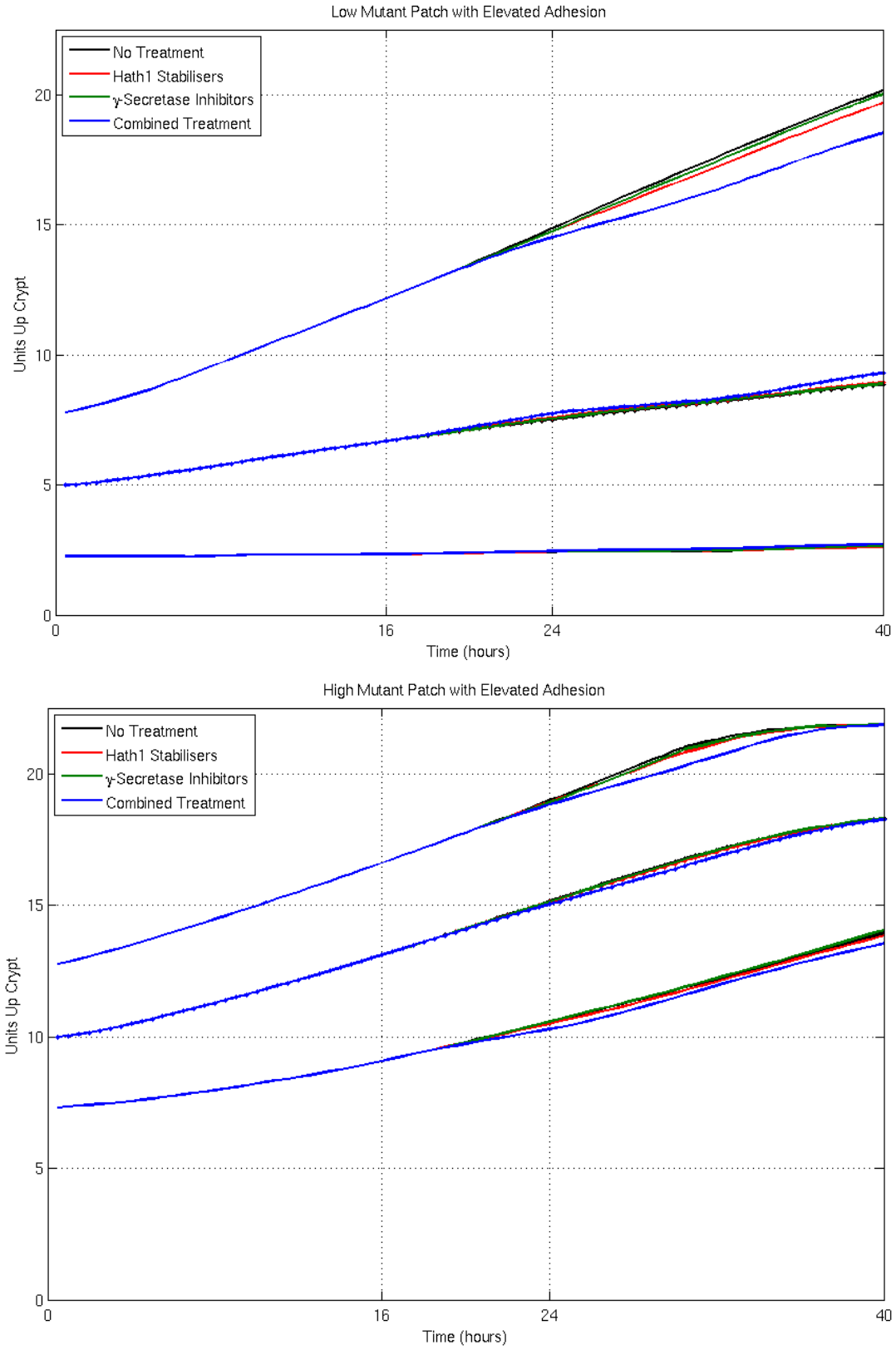

Figure 6.17: Mean transit of adhesive mutant patches through the crypt during the pre-dosing $(0-16h)$, dosing $(16-24h)$ and recovery $(24-40h)$ windows. Solid lines indicate the position of the highest and lowest mutant cells; the dotted line indicates the height of the centroid of the mutant population.

of mutants in the transit region of the crypt. The screenshots of Figure 6.16 depict crypt evolution for clinical treatments A – D, for a low mutant patch with elevated adhesion. These, and the centroid plots of Figure 6.17, confirm that this case spans the transit, priming and differentiated regions at the start of the dosing window.

Therapeutic Intervention is More Effective Downstream of the Notch-Wnt Crosstalk Hub

Adhesive mutants experience a similar recovery from interventions upstream of the β-catenin-Hes1 crosstalk hub, as for their less adhesive counterparts: γ-secretase inhibition does not deliver lasting secretory conversion throughout the dosing window. This is apparent in the secretory cell totals of Figure 6.18, in which γ-secretase inhibition initially converts cells more quickly than the Hath1 stabilisation, before falling sharply to a level not much above that of the untreated case.

Our finding that therapeutic intervention is more effective downstream of the principal Notch-Wnt crosstalk hub also corroborates the experimental findings of Peignon *et al.* [77], who question the use of γ-secretase inhibitors in isolation, owing to the counter-effect of β-catenin-mediated regulation of Hes1.

Combined Therapy Enables Mutant Conversion in the Transit Region

Inspection of the mutant demographic for each stage of the four 'low patch' treatments – summarised in the bar graphs of Figure 6.19 – demonstrates complete conversion of all transit mutants throughout the dosing phase for the combined treatment. The spatial summaries provided by Figures 6.16 and 6.17 confirm that the acquisition of secretory cells at this point is the result of biochemical adjustment from the clinical treatments, rather than the departure of mutants from the transit region. The high patch cases summarised in Figure 6.20 cannot demonstrate this effect, owing to the placement of the patch above the transit region at the start of dosing.

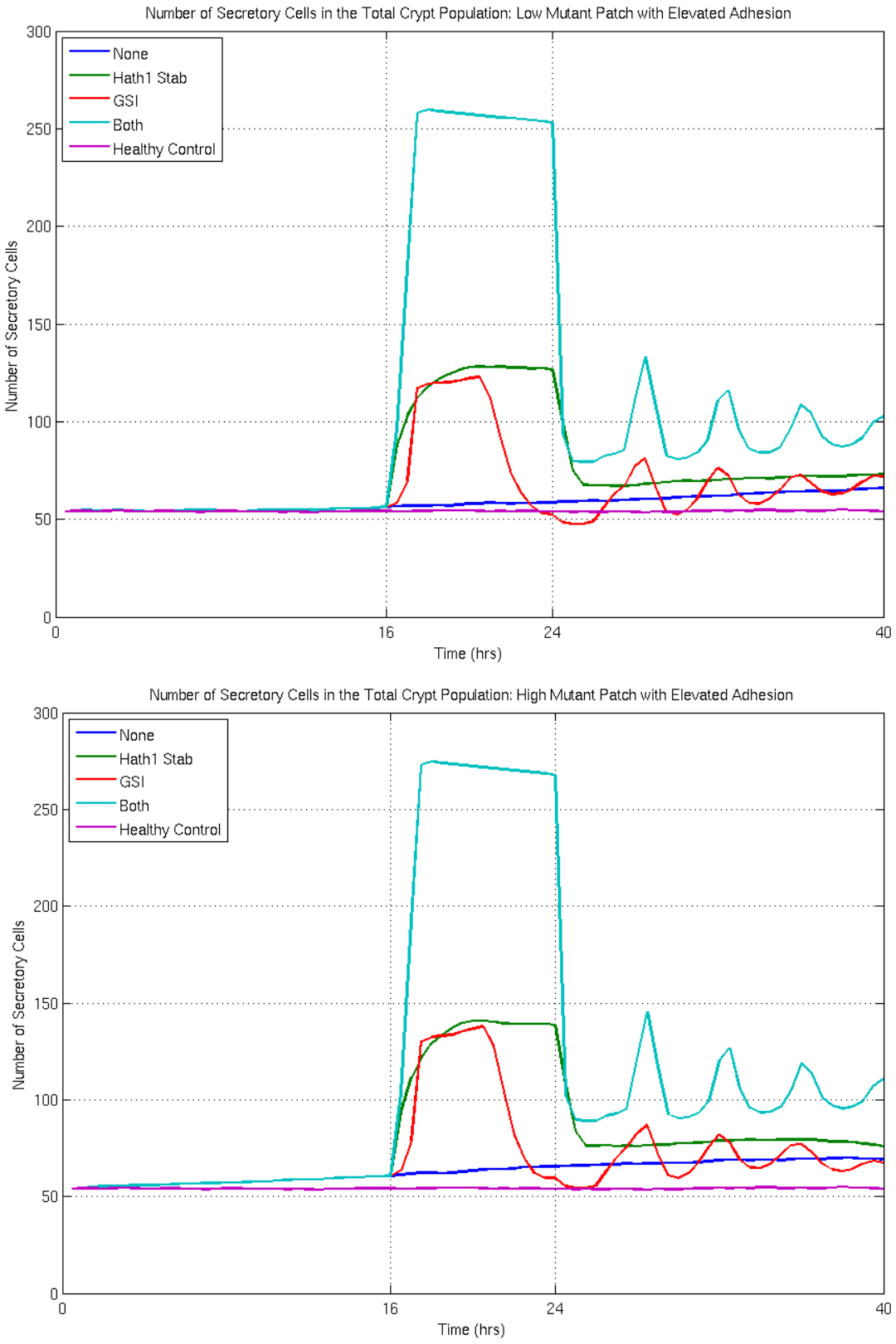

Figure 6.18: Mean timecourses for the number of secretory cells in the crypt population, shown for (upper) a low-placed, and (lower) a high-placed mutant patch; mutant cells have elevated adhesion levels in both cases. Results are shown for the four treatment strategies A–D over the course of the pre-dosing $(0-16h)$, dosing $(16-24h)$ and recovery $(24-40h)$ windows.

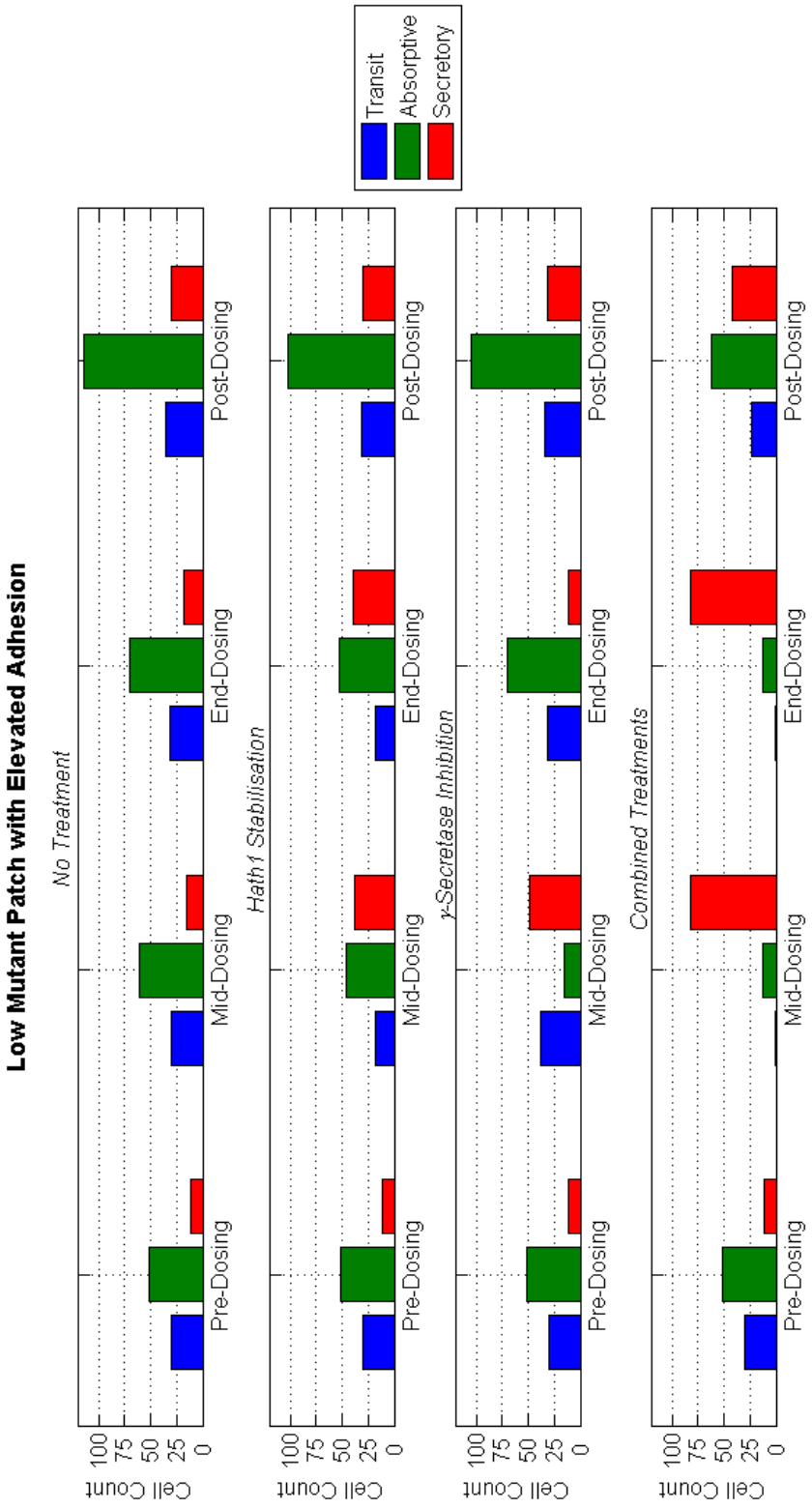

Figure 6.19: Bar graph showing the mean number of mutant cells of transit, absorptive and secretory type at each stage of the four treatment series, for a low-placed mutant patch with elevated adhesion. Totals are shown for the end of the pre-dosing ($16h$), dosing ($24h$) and recovery ($40h$) windows, along with results from the midpoint of the dosing window ($8h$).

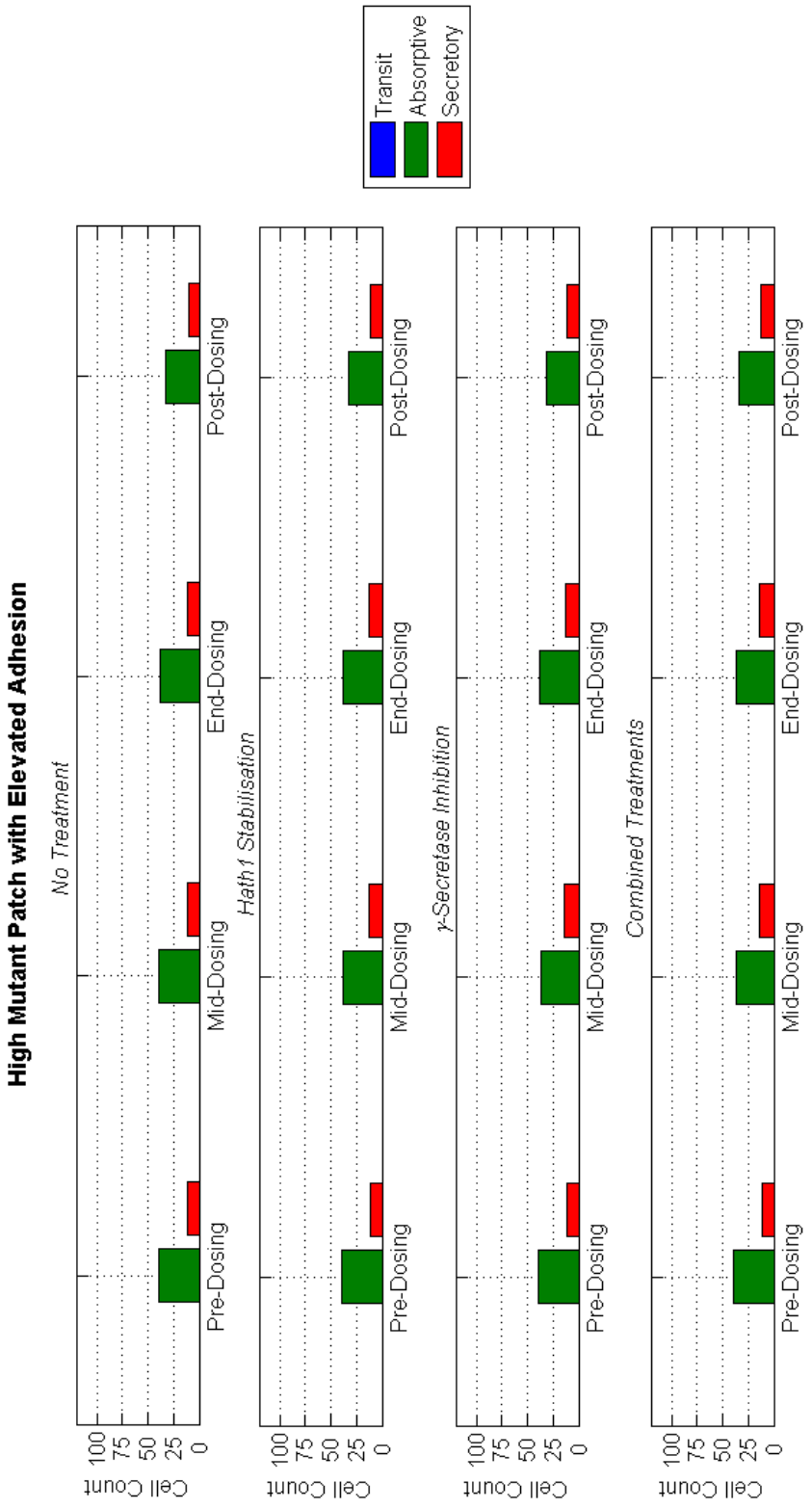

Figure 6.20: Bar graph showing the mean number of mutant cells of transit, absorptive and secretory type at each stage of the four treatment series, for a low-placed mutant patch with elevated adhesion. Totals are shown for the end of the pre-dosing ($16h$), dosing ($24h$) and recovery ($40h$) windows, along with results from the midpoint of the dosing window ($8h$).

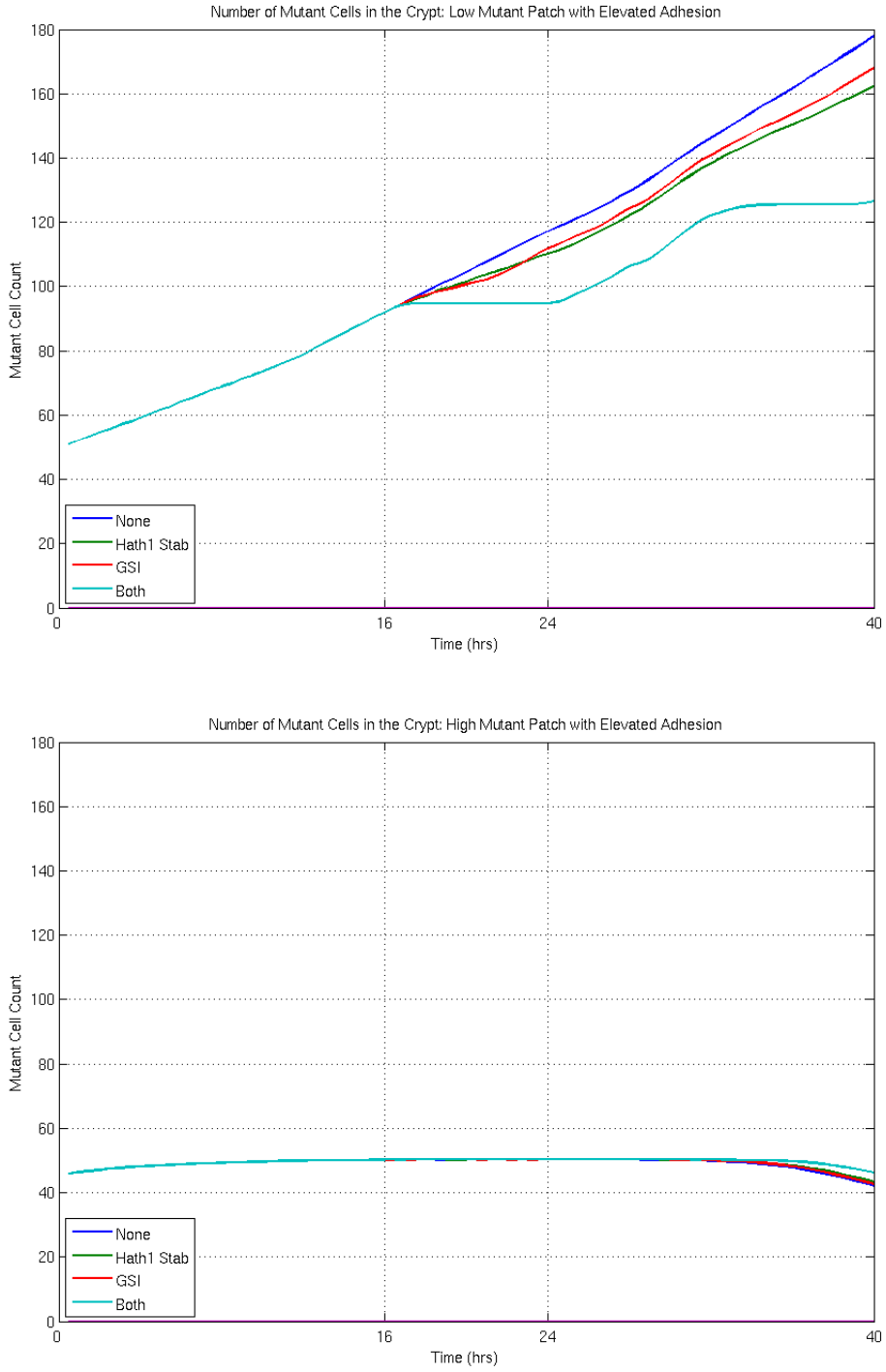

Figure 6.21: Total number of mutant cells in the crypt population over the course of the pre-dosing $(0-16h)$, dosing $(16-24h)$ and recovery $(24-40h)$ windows.

By contrast, the single-therapy treatments for the low-patch case do not convert all transit mutants. This agrees with the regular adhesion case as regards the sustainability of conversion: treatment B maintains a constant conversion throughout dosing, but does not sustain this in the recovery window, while treatment C demonstrates an initial surge in secretory conversion, which has already been curtailed by the end of the dosing window. The elevated adhesion case confirms the synergy between the two treatments initially observed in Section 6.7.

Combined Treatment Restricts Growth of the Tumour Cell Population

The strong mitotic arrest associated with the combined treatment completely halts mutant proliferation (see the upper timecourses of Figure 6.21). Although the single treatments deliver some reduction in the number of mutant cells compared to the untreated case, the total number of tumour cells continues to rise throughout the dosing period. The combined treatment, on the other hand, prevents any increase in the mutant cell total throughout this window. Furthermore, the induced halt in mutant cell proliferation has additional effects upon the recovery phase: crypts for the combined treatment contain $35 - 40$ fewer mutant cells at $t = 40$h on average than crypts treated with individual therapies.

6.9 Conclusions

Development of the NWODE model to incorporate mutant cells, in some cases with elevated adhesion levels, has enabled us to investigate the interplay between mechanical and biochemical effects associated with the formative stages of colorectal cancer.

6.9.1 Mutant Behaviour in the NWODE Model

Our assessment of mutant cell transit through the crypt is consistent with existing studies [195, 176, 175] as regards the fixation of tumour cells within the crypt. Both the relative adhesion and initial location of the mutant cells are important factors in determining their persistence within the tissue. However, extension of the NWODE model to include contact inhibition of proliferation would facilitate the modelling of mutant cells with a high relative adhesion. Notably, the use of a coupled Notch-Wnt ODE model in the subcellular embedding of the NWODE framework has allowed us to extend the current literature, by examining the impact of mutation upon the interplay between proliferation and cell fate specification within the colorectal epithelium, deriving cell types directly from the underlying biochemistry. Key findings include:

- **Cell fate is subject to both biochemical and mechanical influences:** Cellular compression increases the number of cell neighbours; averaging processes within the Notch system thus favour a low-Hath state and absorptive, rather than secretory, cell types;
- **Mutant cells can effect small-scale conversion of neighbours to an absorptive phenotype:** Observations of mutant patch studies and whole-crypt mutation indicate a weak tendency towards the formation of mitotically active, absorptive cell types;
- **The multicellular setting damps perturbations in Wnt:** Biochemical effects associated with mutant cells are less pronounced in the crypt than the two-cell scenario. We hypothesise that the juxtacrine signalling of the Notch pathway employs crosstalk to stabilise small perturbations in the Wnt system. This may guard against less aggressive, low-level mutations in the Wnt pathway.

Refinement of the Wnt ODE submodel would be a useful extension and would allow further exploration of the 'biochemical regulation' hypothesis described above.

6.9.2 Evaluation of Clinical Therapies

The later studies of this chapter have exploited the subcellular detail of the NWODE model to pursue clinically relevant, open hypotheses in the biological literature, assessing the viability of two biochemical interventions in the Notch system as CRC therapies. Our findings suggest cause for optimism as regards the prospects for treating CRC via the Notch, rather than the Wnt, pathway, but highlight the location of intervention as a key factor in the extent and maintenance of the cell fate response.

Crosstalk between the Notch and Wnt pathways is instrumental in shaping the tissue-level dynamics of the treatment response. Of particular note is the β-catenin/Hes1 crosstalk hub, the chief point of interaction between the two networks. The existence of a feed-forward loop surrounding the hub, in which β-catenin can upregulate Hes1 either directly or indirectly, allows the system to compensate for upstream interventions and steer the biochemistry back to its prior state. This is consistent with theoretical analyses of such motifs in the literature [239, 240]. Our key findings include:

- **Downstream intervention is more effective:** γ-secretase inhibitors reduce the strength of the Notch signal upstream of the hub, by impairing fragmentation of the Notch receptor. This temporarily reduces the Notch signal, but β-catenin acts downstream to restore expression of Notch targets and so any cell fate conversion is short-lived. By contrast, Hath1 stabilisers force secretory conversion of the cell by enabling the accumulation of Hath1 downstream of the crosstalk hub. The resulting cell fate conversion lasts for the duration of dosing;

- **γ-secretase inhibitors and Hath1 stabilisers produce a synergistic effect:** Combined application of both treatments delivers wholesale conversion of the transit and priming regions of the crypt. This synergy completely halts expansion of the mutant population during dosing and reduces the growth of the mutant population even after treatment has finished;

- **Combined treatment may aid retention of tumour cells:** The efficacy of the combined treatment at halting cell division, and hence removing the mitotic pressure from the lower crypt, may assist the retention of tumour cells. This localises malignancies but a suitable dosing regimen would need to be identified in order to avoid further spread of the tumour cells after treatment is removed.

We have restricted our attention to patches of mutant cells in the treatment scenarios explored in Section 6.4, as these enable us to study the effects on the transit of tumour cells, as well as any changes to their cell fate. Nonetheless, future work may wish to apply the same treatments to individual crypts composed entirely of mutant cells, such as those detailed in Section 6.3.2, or even to groups of interconnected crypts, some of which are healthy, and some mutant: such clusters have already been implemented computationally by Mirams *et al.* [247]. Such extensions would provide a closer approximation to the polyp formation stage of CRC, in which the tumour propagates via the fission of monoclonal, mutant crypts [62].

Our assertion that downstream intervention is more effective supports the hypothesis of Peignon *et al.* [77] that any Notch-targeted CRC therapies need to consider the location of the crosstalk hub, rather than just a reduction in the strength of the Notch signal. To our knowledge, the synergy between the two treatments explored here has not been reported to date in the literature, and therefore offers valuable possibilities for further computational and experimental study in the future.

7 Conclusions

Chapter Summary

With the chief theoretical and computational studies now complete, we return to the original, guiding questions of our thesis. How is the interplay between proliferation and cell fate selection employed in the maintenance of a healthy crypt, and what role does this crosstalk adopt during the process of CRC? We summarise the main contributions of this work to the field, and outline potential avenues for further study, encompassing mathematical, computational and biological disciplines.

Our Introduction asked whether the interaction between the pathways for proliferation and cell fate selection could be employed to gain insights into the workings of the attainment and maintenance of the healthy intestinal epithelium, and how such a model might be used to identify targeted therapies for treating colorectal cancer.

The ODE realisation of the Notch and Wnt pathways presented in Chapter 3 offers the capacity to study such questions, and has been applied successfully to both two-cell scenarios and cell-based crypt environments in Chapters 4 – 6. It now remains to summarise our key findings and predictions, and to outline the directions in which this work could be extended through further experimental or theoretical endeavour.

7.1 Findings and Insights

Theoretical and computational investigation of our ODE model in Chapters 4 – 6 has identified some recurring themes relating to the interplay of Notch and Wnt processes.

Subcellular Behaviour

Wnt is largely an upstream regulator of Notch and exerts a stabilising influence upon the Notch system, serving to dampen its characteristic oscillations. This behaviour is borne out by chemical reaction network analyses, bifurcation analyses and two-cell simulations. Discussion of the supporting evidence for our model in Chapter 3 also highlighted the role of Hes1 as a key liaison between the two pathways: it is subject to direct and indirect regulation by β-catenin and this facet equips the cell with a means of self-regulation in response to chemical perturbation, as observed in the crypt response to γ-secretase inhibitors in Chapter 6.

Indeed, any approach to treating CRC via forced differentiation methods should consider the crosstalk between the Notch and Wnt pathways, and target interventions at points downstream of the major β-catenin/Hes1 crosstalk hub. Once the downstream targets are guaranteed, addition of upstream targets can be used to improve the efficacy of conversion.

Tissue-Level Modelling

We have also gained insights into *how* Notch and Wnt processes can be modelled at the tissue scale: the ODE embedding provided by the NWODE model offers robust pattern generation and is less sensitively dependent upon the initial conditions of simulation. Without further extension, the rule-based model of Buske *et al.* [5] lacks the capacity for detailed biochemical studies and is prone to clustering of primary fate cells in the mid-crypt, which is an artefact of the summation of discrete activity states

employed by the framework.

Prediction Challenges

The range of insights yielded by our model has generated some testable predictions for exploration by the biological community. These indicate how the ODE model and its associated crypt embedding could be used to guide future experimental work.

TESTABLE PREDICTIONS

- *Chapter 4:* Blocking the direct binding site for NICD on the Hes1 promoter should eradicate oscillations in the Notch system;
- *Chapter 4:* Stronger binding between β-catenin and NICD should attentuate the response of the Wnt system to extracellular stimuli;
- *Chapter 5:* Secretory goblet cells in the intestinal epithelium should appear approximately 2.2 cell diameters apart and yield a dispersed Ripley H-Value of -0.4 in the upper crypt;
- *Chapter 6:* Treatment of CRC in a crypt with a combination of Hath1 stabilisers and γ-secretase inhibitors should induce cell-cycle arrest throughout the crypt and effect $60-70\%$ conversion to a secretory phenotype.

7.2 Future Work

Our work in this thesis poses many questions and challenges in areas biological, mathematical and computational. We summarise the main points here as proposed avenues for future work.

7.2.1 Biological Extensions

The testable predictions stated in Section 7.1 already provide excellent subjects for further biological work. Nonetheless, one of the main problems for a computational biologist is the relative paucity of data with which to parametrise and validate mathematical models. This motivates the following ideas for further experimental study:

Parameter Estimation

We would hope that the potential demonstrated by our Notch-Wnt model and subsequent crypt embedding could provide the stimulus for a thorough investigation of its parameters in a single, human intestinal, cell line. Nonetheless, there are inherent difficulties associated with this, because cell lines from healthy human intestinal tissue do not typically yield stable cultures *in vitro*. At present, our Notch-Wnt model relies upon data drawn from human, murine, rat and frog cell lines. Further experimental work should seek to reduce the number of parameter estimates taken from non-human or non-intestinal cell lines, and to minimise the use of data fitting procedures to estimate unknown parameters.

Crypt Imaging

The comparative study presented in Chapter 5 provides an assessment of the spacing of secretory goblet cells in the crypt. Although the Ripley metric enables a comparison between computational models, it is difficult to assess how well these outputs capture the spacing observed *in vivo*. Existing sources in the biological literature focus on a qualitative, rather than quantitative, assessment of the cell distribution.

If good-quality stills of crypts could be obtained, the images could be sharpened and the coordinates of individual goblet cells determined using image processing software, e.g. MATLAB's Image Processing Toolbox. These coordinates could then be used to estimate the Ripley H-Value for secretory cell distribution, thus providing a benchmark

against which the performance of the computational representations could be assessed.

Such imaging work would require the use of mucin staining to detect the goblet cells, with light microscopy used to produce the stills. Careful staining and fixing would be required, to avoid distortion of the crypt and to ensure that the stained secretory cells lie in the same tissue plane. *In vitro* crypt organoids, of the kind cultured by Ootani *et al.* [2] and Sato *et al.* [1], may prove a viable means of obtaining such data from individual crypts and would reduce the tissue preparation artefacts associated with samples obtained *in vivo*.

7.2.2 Mathematical and Computational Extensions

Although our Notch-Wnt ODE model in its present form has a good capacity for exploring crosstalk of the two pathways, extensions of either submodel could extend this capacity still further.

Notch Model Development

The prominence of the β-catenin/Hes1 crosstalk hub in shaping the system dynamics may justify further refinement of this area of the model. A great deal of the literature discussed in Section 2.1.4 could provide inspiration for this. For example, the addition of Hes1 mRNA and Hes1 dimerisation could enable closer matching of the amplitude and timescale of oscillation against the data of Hirata *et al.* [142] and permit more detailed studies of activity around the Hes1 promoter. Alternatively the system could be realised as a series of delay differential equations, as in Monk [143].

Wnt Model Development

Reappraisal of the Wnt model would bring two major benefits: first, a reduction in the reliance upon data fitting to obtain the form of $\Psi_{W,A}$; secondly, an increase in the versatility of the ODE system by expanding the range of mutants and therapies which

it can represent. The attenuation within the crypt setting of the β-catenin response of APC mutants in Figure 6.1 may be partly a consequence of the minimality of our Wnt model. The inclusion of more nuanced interactions between the components of the destruction complex may be needed to model a more aggressive phenotype.

The model of Lee *et al.* [161] includes details of the APC, Axin and GSK subunits as well as their phosphorylation states; extension of our Wnt model to include some of these elements might inform as to which are vital parts of the tumourigenic response. Alternatively, our Wnt submodel could be extended to address non-canonical branches of the pathway, such as the cadherin-binding arm associated with intercellular adhesion (as, for example, in the ODE model of van Leeuwen *et al.* [155]); such extensions could also facilitate the modelling of contact inhibition within the NWODE crypt framework.

Parameter Investigation

An in-depth analysis of parameter space would prove beneficial, either with or without the above refinements to the Notch-Wnt ODE system. Examples of possible methods to consider for exploring or sampling the response across global parameter space include Gaussian process modelling [251, 252], or Latin hypercube sampling allied with a correlation coefficient [253]. These refinements of the parametrisation approach would represent considerable improvements on the methods described in Chapter 4.

7.2.3 Further Studies

Application of our model to two-cell studies in Chapters 4 and 6 and to a multicellular crypt setting in Chapters 5 and 6 has also raised many interesting questions about the underlying biology our model aims to capture:

Dosing Strategies for Combined Therapy

Simultaneous dosing of Hath1 stabilisers and γ-secretase inhibitors proved the most effective method for enforcing secretory conversion of APC-mutant crypt cells in the studies of Chapter 6. However, its efficacy at the fate conversion of both healthy and mutant cells removes mitotic pressure from the crypt and may therefore aid the retention of tumour cells after the dosing period. These studies could be extended to determine the effects of alternative dosing patterns – such as intermittent or prolonged dosing – upon the localisation of tumour cells within the crypt.

Cancer Stem Cell Hypothesis

The two-cell experiments depicted in Figure 4.16 examine the behaviour of a mutant cell with a 'hyperstimulated' Wnt phenotype. This mutant cell produces a more exaggerated response to local Wnt levels than a corresponding healthy cell. This mutant phenotype displays an ability in two-cell simulations to force elevated Hes1 expression in a neighbouring healthy cell, which would typically maintain the healthy cell in a mitotically active state. This merits further attention through multicellular studies, as it may indicate that the Cancer Stem Cell Hypothesis is an emergent feature of our ODE model.

Control of the Hes1 Promoter

Chemical network analysis, along with the two-cell studies of Chapter 4 and the crypt experiments of Chapter 6, has highlighted activity around the Hes1 promoter and the β-catenin/Hes1 crosstalk hub as a key influence upon the dynamics of subcellular processes and tissue-level behaviour. In particular, the relative strengths of Steps (4) and (14) upon the Hes1 promoter have been shown to determine the driving or damping of oscillations in the Notch system. Given that the proof-of-concept study of Chapter 6 has made the case for the utility of our embedded Notch-Wnt crypt

model as a testbed for biological and clinical questions, a study of the crypt-wide effects of manipulating Hes1 promoter activity is feasible and could provide insights into how spatial constraints in the crypt influence Notch-Wnt crosstalk. In addition, the simulated application of Wnt inhibitors could yield some valuable insights into the role of spatial variation of Wnt upon Wnt- or β-catenin-mediated regulation of the Hes1 promoter.

7.3 Closing Remarks

The research presented in this thesis offers several new developments in intestinal crypt modelling and the study of colorectal cancer:

First, by its coupled representation of two major cell processes. Historically, mathematical models for the Notch and Wnt pathways have largely focused on either one network or the other, examining typical '*Notch function*' or typical '*Wnt function*', rather than a combination of the two. By contrast, our ODE model of Chapter 3 has been developed specifically to examine the effects of pathway crosstalk and so delivers a joint perspective on proliferation *and* cell fate specification. It could therefore be applied to a broad range of situations in both oncogenesis and developmental biology, from studies of tumour cells in intestinal tissue to the modelling of *de novo* cryptogenesis [1, 2].

Secondly, by its approach to quantifying cell dispersal. Notch-driven cell fate selection is a highly spatial process, yet the metrics of existing studies fail to take this into account. Our use of statistical measures such as the Ripley H-Value represents an advance in accurately measuring the spatial output of models for cell fate selection and should facilitate experimental validation of cell fate models in the future.

Thirdly, through its creation of a computational test-bed for exploring multiscale effects of the Notch and Wnt pathways in the intestinal crypt. At present the main

example of Notch-Wnt enabled crypt framework in the computational literature is that of Buske *et al.* [5], with its simple, rule-based representation of pathway activity. Our ODE-based crypt embedding permits the study of subcellular scale phenomena in crypt tissue and hence enables the study of a broader range of biological questions. It has also been shown in Chapter 5 to possess a more consistent patterning mechanism, less dependent upon initial conditions than that of Buske *et al.*

Finally, in its exploration of clinically relevant hypotheses. The mechanisms of Notch-Wnt crosstalk have raised many questions in the experimental literature about therapeutic Notch-Wnt control in oncogenesis. The putative CRC treatments explored in Chapter 6 have corroborated current lines of biological thought [77] and identified potential routes – and challenges – for development of successful CRC therapies.

And Finally

It must of course be remembered that the Notch and Wnt pathways are but two parts of a highly intricate biochemical network within the cell. The models presented here aim to capture what we believe to be the salient points as regards the depiction of cellular proliferation and differentiation.

Further adaptation of our model and crypt framework offers the potential to guide experimental direction for countless other unanswered questions, and to open up exciting new avenues of thought in the future, as we attempt to comprehend the nuanced roles of proliferation and cell fate selection in an organic system of such formidable complexity.

Part D

Appendices

A

Model Parameters

Appendix Summary

We present a full list of parameter values for the ODE model of Chapter 3, along with further details of the sensitivity analysis used in Chapter 4.

In Chapter 3, we presented a new ODE model for studying Notch-Wnt crosstalk. Dimensional values for all parameters, along with the references used as data sources, are shown in the following tables:

- **Half-lives and decay rates**: Table A.1;
- **Hill parameters**: Table A.2;
- **Hyperbola parameters**: Table A.3;
- **Other parameters**: Table A.4;
- **Initial conditions**: Table A.5.

Suitable experimental data are not currently available for all of the rate constants in our model. Where appropriate data were lacking, a parameter estimation was performed as described in Sections 4.3.2 and 4.3.3; numerically fitted values are indicated by a '*PF*'.

Parameter	Half-Life (min)	Source	Estimated Value (min^{-1})
μ_N	40.0	Logeat *et al.* [244], human CRC cells	0.017
μ_F	180.0	Foltz *et al.* [254], murine fibroblasts	0.00385
μ_{I_1}	-	*PF*	0.04
μ_{H_1}	22.3	Hirata *et al.* [142], murine myoblasts	0.065[a]
μ_P	14.4	Roark *et al.* [255], *Xenopus laevis*	0.035[b]
μ_D	-	Collier *et al.* [125], Logeat *et al.* [244]	0.049[c]
μ_{H_2}	-	*PF*	0.0311[d]
μ_G	900.0	Cole *et al.* [256], *HEK*293 cells	9.36×10^{-4}[e]
μ_C	-	Lee *et al.* [161], *Xenopus* oocytes	1.061[f]
μ_B	104.0	Hernandez *et al.* [167], *RKO* cells	0.00636[g]
μ_A	480.0	Yamamoto *et al.* [257], *COS* cells	6.23×10^{-4}[h]
μ_{I_2}	-	Lee *et al.* [161], *Xenopus* oocytes	4.204[i]

Table A.1: Dimensional parameter estimates for the decay rate constants of the ODE model presented in Chapter 3. Owing to the lack of data for some species, parameters such as μ_{H_2} and μ_D have been estimated using other known decay rates. Such approximations are based on factors such as the molecular size of a species and its location and function within the cell. *PF* indicates numerically fitted parameters, described in Section 4.3.2.

[a] Value derived by parameter fitting, using the estimate of 0.0311 as a starting value.
[b] Value derived by parameter fitting, using the estimate of 0.0481 as a starting value.
[c] Value derived by parameter fitting from the Notch data of Logeat *et al.* [244], using $\mu_D = \mu_N$ as in the model of Collier *et al.* [125].
[d] In the absence of data for μ_{H_2}, a starting value was based upon that for μ_{H_1} from the data of Hirata *et al.* [142].
[e] Value derived by parameter fitting, using the estimate of 7.7×10^{-4} as a starting value.
[f] Value derived by parameter fitting, using the estimate of 0.909 as a starting value.
[g] Value derived by parameter fitting, using the estimate of 0.00666 as a starting value.
[h] Value derived by parameter fitting, using the estimate of 0.00144 as a starting value.
[i] Value derived by parameter fitting, using the estimate of 210.0 as a starting value.

Parameter	Units	Dimensional Value	Source
θ_1	nM min^{-1}	0.06[a]	Agrawal *et al.* [151]
θ_2	dim'less	0.75	Agrawal *et al.* [151], Cinquin *et al.* [258]
θ_4	nM min^{-1}	0.4	*PF*
θ_6	nM min^{-1}	1.64×10^{-4}[b]	Lee *et al.* [161]
θ_7	dim'less	0.25	Agrawal *et al.* [151], Cinquin *et al.* [258]
κ_1	nM	0.6	*PF*
κ_2	nM	0.9	*PF*
κ_4	nM	14.7	*PF*
κ_6	nM	0.026	*PF*
κ_7	nM	10.0	*PF*
$m_i, i = 1, 2, 4, 6, 7$	dim'less	3	-

Table A.2: Dimensional parameters for the Hill functions used in the Notch-Wnt ODE model presented in Chapter 3. The θ_i are maximal rates; the κ_i are the Hill coefficients; and the m_i are the Hill exponents. *PF* indicates numerically fitted parameters, described in Section 4.3.2.

[a] Value derived by parameter fitting, using the estimate of 0.055 from the calculations of Agrawal *et al.* [151] as an initial estimate.
[b] Value derived by parameter fitting, using the estimate of 8.2×10^{-5} as a starting value.

Parameter	Units	Dimensional Value	Source
ξ_2	nM min^{-1}	0.5	Agrawal *et al.* [151]
ξ_3	nM min^{-1}	0.9	*PF*
ξ_5	nM min^{-1}	0.9	*PF*
σ_2	nM	3.5	*PF*
σ_3	nM	1.21	*PF*
σ_5	nM	1.7	*PF*
$n_i, i = 2, 3, 5$	dim'less	3	-

Table A.3: Dimensional parameters for the hyperbola functions used in the Notch-Wnt ODE model presented in Chapter 3. The ξ_i are maximal rates; the σ_i are constants of inhibition; and the n_i are the exponents. *PF* indicates numerically fitted parameters, described in Section 4.3.2.

Parameter	Units	Dimensional Value	Source
α_1	$\text{nM}^{-1}\ \text{min}^{-1}$	6.8	*PF*
α_2	$\text{nM}\ \text{min}^{-1}$	0.0174	*PF*[a]
α_3	$\text{nM}^{-1}\ \text{min}^{-1}$	1.465×10^{-4}	*PF*[b]
α_4	$\text{nM}\ \text{min}^{-1}$	0.472	*PF*[c]
α_5	$\text{nM}^{-1}\ \text{min}^{-1}$	0.1044	*PF*[d]
σ_K	dim'less	1.0	Collu *et al.* [222]
α_{frag}	dim'less	0.8	*PF*

Table A.4: Miscellaneous rate parameters used in the Notch-Wnt ODE model presented in Chapter 3. *PF* indicates numerically fitted parameters, described in Sections 4.3.2 and 4.3.3.

[a] In the absence of any experimental data, a starting value of 0.01 was used in parameter fitting
[b] Value derived by parameter fitting against the β-catenin timecourses of Hernandez *et al.* [167], initial estimate 1.028×10^{-4}
[c] Value derived by parameter fitting against the β-catenin timecourses of Hernandez *et al.* [167], initial estimate 0.3
[d] Starting value of 0.091, from the model of Lee *et al.* [161]

Variable	Description	Two-cell ICs (nM)	Crypt ICs (nM)
N	Membrane-bound Notch receptor	0.5	0.5 (r)
F	Notch Intracellular Domain (NICD)	0.5	0.5 (r)
H_1	Hes1	0.5	0.5 (r)
P	Ngn3	0.5	0.5 (r)
D	Delta ligand	0.5	0.5 (r)
H_2	Hath1	0.5	0.5 (r)
G	GSK3β	30.0	49.84
C	Destruction complex	25.0	0.67
B	Active β-catenin	9.0	140.17
A	Axin	27.0	1.29
I_1	Intermediate 1 (NICD/β-catenin)	0.5	0.5 (r)
I_2	Intermediate 2 (GSK3β/β-catenin)	30.0	0.0033

Table A.5: Initial conditions (ICs) for the variables in the dimensional Notch-Wnt ODE model of Chapter 3. Except where stated otherwise, all two-cell simulations start from the concentrations in the penultimate column. Motivation for these values is described in Section 4.3. Crypt simulations adopt the concentrations of the final column; these are based upon original observations of the Wnt-system steady state in a crypt setting, for Wnt stimulus $W = 1$. An (r) indicates randomisation around the stated value, within a tolerance of $\pm 5\%$

A.1 Parameter Sensitivity Analysis

The parameter sensitivity analyses of Chapter 4 were performed using the Systems Biology Toolbox, an add-on kit for MATLAB. Results from the preliminary sensitivity analyses, which were used to create a priority ordering of the parameters for the fitting procedure, are shown in Figures A.1 and A.2. The information provided here is intended to supplement the descriptions provided in the main text; sensitivity analysis is discussed within the context of the parameter fitting as a whole in Sections 4.3.2 and 4.3.3.

Sensitivity Equations for Hes1 Oscillation Analysis

Parameter fitting for the Notch system uses the two-hour Hes1 oscillation period, measured experimentally by Hirata *et al.* [142], as the target data. The parameter analysis for the Notch system therefore calculates the sensitivity of this oscillation period to changes in each of the parameters. The sensitivities shown in Figure A.1 have been generated using the dimensional Notch submodel, defined by Equations (3.3) – (3.9).

The sensitivity, S_p, for the Hes1 oscillation period with respect to an individual parameter p is calculated using the following formula:

$$S_p = \frac{|T(p+\delta_p) - T(p)|}{\delta_p}$$

where δ_p is the incremental change in the parameter p and $T(p)$ is the Hes1 oscillation period for the given parameter set using parameter p. This is converted into the *normalised sensitivity index*, NS_p, by

$$NS_p = \frac{p}{T(p)} \times S_p$$

Normalised sensitivity indices for the Notch model are shown in Figure A.1.

Sensitivity analysis of the Hes1 oscillation period yields the following parameter ordering, with parameters listed in order of decreasing oscillation period sensitivity: $\kappa_7, \theta_1, \alpha_{frag}, \xi_3, \theta_4, \mu_{H_1}, \xi_2, \mu_N, \alpha_1, \kappa_4, \mu_P, \xi_5, \mu_F, \sigma_5, \mu_{H_2}, \sigma_2, \mu_{I1}, \mu_D, \kappa_1, \sigma_3, \kappa_2$.

Sensitivity Equations for β-catenin Steady-State Analysis

In contrast to the Notch system, the Wnt model does not exhibit oscillations and so its parameter analysis measures the sensitivity of the β-catenin steady state value, B^*, to changes in each of the parameters. Datapoints from the β-catenin timeseries of

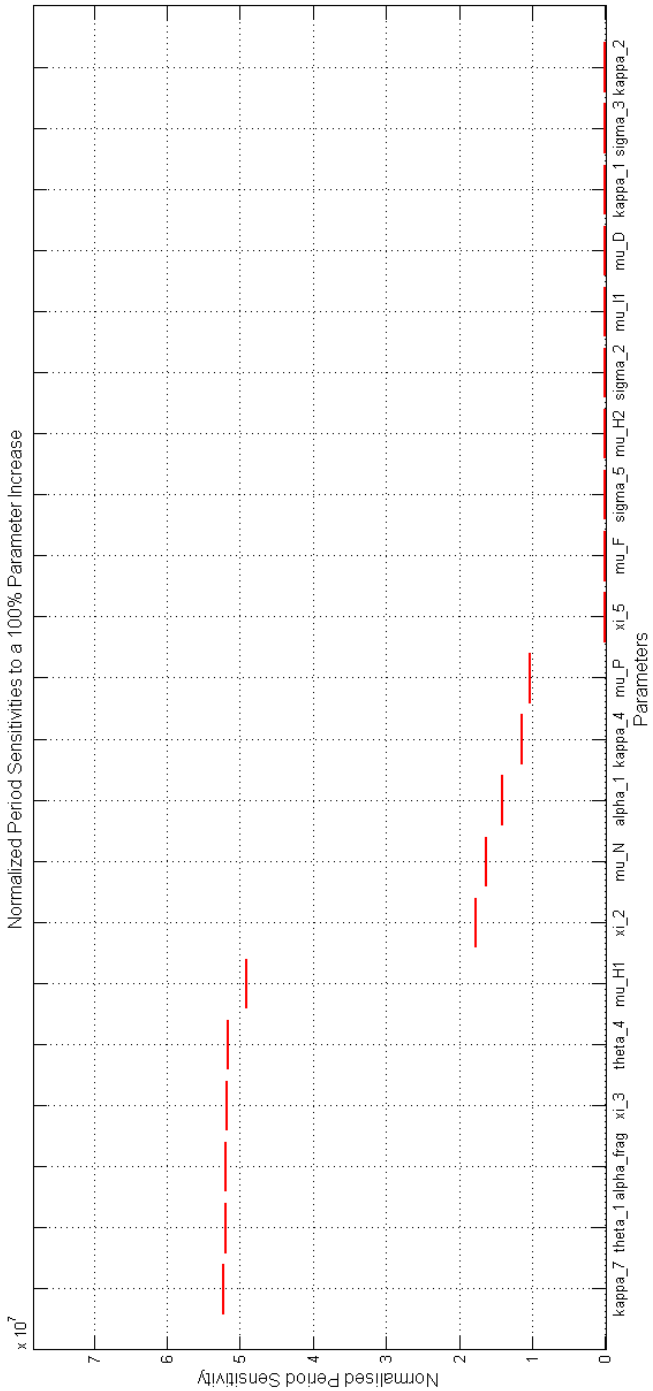

Figure A.1: Results from a preliminary sensitivity analysis on the oscillation period of Hes1 in the Notch system, showing normalised sensitivities for a 100% increase in the value of each parameter in turn. These results were used to create an ordering for the parameter fitting exercise described in Section 4.3.2.

Hernandez *et al.* [167] are used as the target data. The sensitivities shown in Figure A.2 have been generated using the dimensional Wnt submodel, defined by Equations (3.10) – (3.14).

The sensitivity, S_p, of the β-catenin steady state B^* to a given parameter p is defined by:

$$S_p = \frac{|B^*(p + \delta_p) - B^*(p)|}{\delta_p}$$

where δ_p is the incremental change in the parameter p. This is converted into the *normalised sensitivity index*, NS_p, by

$$NS_p = \frac{p}{B^*(p)} \times S_p$$

Normalised sensitivity indices for the Wnt model are shown in Figure A.2.

Sensitivity analysis of the β-catenin steady state yields the following parameter ordering, with parameters listed in order of decreasing steady-state sensitivity: $\alpha_4, W, \mu_B, \mu_A, \mu_G, \mu_C, \kappa_6, \mu_{I_2}, \alpha_3, \alpha_2, \alpha_5, \theta_6$.

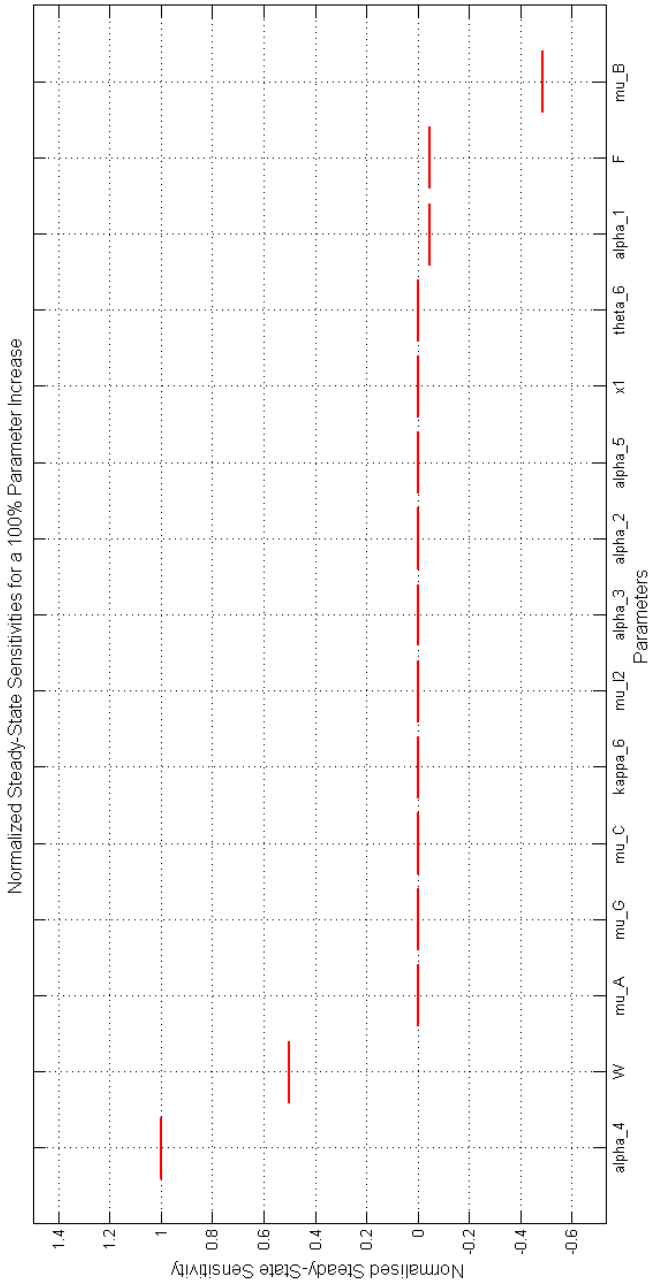

Figure A.2: Results from a preliminary sensitivity analysis for the steady state of β-catenin in the Wnt system, showing normalised sensitivities for a 100% increase in the value of each parameter in turn. These results were used to create an ordering for the parameter fitting exercise described in Section 4.3.3. Values for W and F are included here as a comparison, as they are held constant within the decoupled Wnt system; however they are not varied during parameter fitting, as they are variables rather than parameters in the full system. $x1$ is the multiplier for the Wnt response function $Psi_{W,A}$, described in Section 3.3; α_1 is fitted using the Notch-only system and is not varied during parameter fitting for the Wnt system.

B

Point Dispersal Measures

Appendix Summary

The study of cell fate patterns in biological tissues requires us to observe the number and spatial distribution of a range of cell types. Here we explore two methods for measuring point dispersal on two-dimensional cell monolayers: Ripley's H-statistic and an O-measure pair correlation function. The runtime and accuracy of these methods is compared over three different cell-based tissue models, and the metric outputs analysed for static (non-dividing) and dynamic (mitotically active) scenarios.

Full characterisation of cell fate dispersal within a biological tissue requires two pieces of information: first, the total count of each cell type; secondly, the distribution of each cell type throughout the region of interest. The first of these is generally trivial to ascertain in computational simulations; however, the second is a more complicated statistic, requiring knowledge of the spatial location of cells of a given type and their relative positions to one another.

Point dispersal analyses are required in Chapters 5 and 6 in order to quantify the effects of Notch-Wnt crosstalk upon cell type distributions in a tissue domain. In anticipation of this, we now develop and analyse methods for measuring cell fate distributions in two-dimensional cell monolayers. Section B.2 introduces two candidate metrics, namely the Ripley measure and the pair correlation function (PCF). A

performance analysis on static monolayers in Section B.2.4 yields insights into the relative merits of each method, provides experience in the interpretation of each metric in the context of a simulated tissue and explores their runtime on a variety of types of tissue model. Our study of point dispersal measures culminates in simulations of a dynamically growing, cylindrical crypt in Section B.4, which enables us to show how the output of the Ripley measure can provide valuable information about the changing lengthscale and character of cellular patterning over the course of a simulation.

B.1 Subcellular Model

Throughout this Appendix, we represent cellular Notch activity using the model of Collier *et al.* [125], which provides a simple ODE representation of lateral inhibition in Delta-Notch signalling. This '*Collier model*', described in Section 2.1.1, provides a robust mechanism for cell fate selection which is easy to implement for the purpose of testing our point dispersal metrics.

Equations (2.1) and (2.2), along with a simple, stochastic depiction of proliferation, therefore constitute our model for Notch and Wnt activity throughout this chapter. Here, these two 'pathways' (inasmuch as this simple representation of proliferation can be so considered) are biochemically decoupled. Except where stated otherwise, all simulations use the standard parameters listed in Table 2.1.

The cell cycle model employs a simple, phase based framework provided in *Chaste*, the `SimpleWntCellCycleModel`. In this representation, the cell cycle is partitioned into four phases: M, $G1$, S and $G2$, as shown in Figure 1.7. During *Chaste* simulations, the cell cycle model is initialised and its phase lengths assigned to an individual cell at its point of birth. The M, $G2$ and S phases are given predetermined, constant values (1, 4 and 5 hours respectively), while the $G1$ phase length is variable, being determined by a random number generator on the normal distribution $N(2, 1)$,

truncated to exclude negative and very small values.

In this simple model, cells are assumed to lie in a predefined chemical gradient of the extracellular factor Wnt and can detect the local concentration to which they are subjected. If the local Wnt concentration exceeds a certain threshold, cells can cycle and proliferate; otherwise they adopt a differentiated phenotype and do not undergo mitosis. Individual molecular entities in the intercellular Wnt pathway are not depicted in this model. Specific parameters governing the Wnt concentration are specified in Section B.4.1 when outlining conditions for the dynamic simulations.

B.2 Point Dispersal Metrics in Two Dimensions

Qualitative assessment of cell patterning has been well studied in the mathematical literature, including the juxtacrine signalling mechanisms exhibited by Notch [125, 131, 134]. Analytic methods usually identify the dominant patterning mode(s) of such systems [131] and assess their stability [126]. Deviations from the global pattern remain difficult to analyse however, and their study demands statistical, rather than mathematical, analysis.

Suppose we have a series of cells lying in a tissue domain Ω, each cell expressing a certain amount of protein, p, which induces differentiation into cell type T when $p \geq p_{\text{threshold}}$. If we are interested in how cells of type T are distributed within Ω, we need to identify the '*threshold cells*' for which $p > p_{\text{threshold}}$ and provide a numerical assessment of their spatial dispersal or clustering.

The quantification of local defects in a pattern rests on the measurement of spatial correlations of point dispersal and/or clustering. This requires so-called *second order statistics*, which assess the distribution across the tissue domain (or a subsection thereof) of distances between pairs of threshold cells. The two main statistical techniques of this kind are the *pair correlation functions* (PCFs) [259] and *Ripley's*

measures [246], which we shall describe in Sections B.2.1 and B.2.2. An example of pattern length detection using these methods is depicted in Figure B.1, along with images of the cellular pattern at different stages along the timecourse.

The advantages and disadvantages of Ripley measures and PCFs are discussed at length in the review by Wiegand *et al.*[260], along with suggestions for their numerical implementation. In the interests of selecting an appropriate method for use in our own studies, we now proceed to a comparison between the two methods. For clarity we describe only the two-dimensional version of these methods here.

B.2.1 Ripley's Values

Ripley's K-value is a statistical estimator which analyses the locations of events in two-dimensional space and contrasts this with the dispersal associated with a fully random (Poisson) distribution [246]. Ripley's K-value is defined as

$$K(r) = \frac{A}{N} \sum_{i} \sum_{j \neq i} \frac{w(i,j) I(d_{ij} < r)}{N}, \tag{B.1}$$

where A is the area of the study region Ω, N is the observed number of threshold points (cells) and both summations are taken over the set of threshold cells in Ω (the summation over j excepting the cell of interest, i). I represents an indicator function, denoting whether the distance d_{ij} between points i and j is less than the Ripley radius r. Finally, $w(i,j)$ is a weighting function: given a circle C with centre i and radius d_{ij}, w is the reciprocal of the proportion of the circumference of C that lies within the domain of interest Ω. An example of this construction is shown on the left-hand side of Figure B.2. This weighting serves to mitigate edge effects in the calculation and is described in full in Section B.2.3. K has been shown to be an unbiased estimator of point dispersal [246].

The construction of the Ripley K-Value as a comparison against a Poisson process,

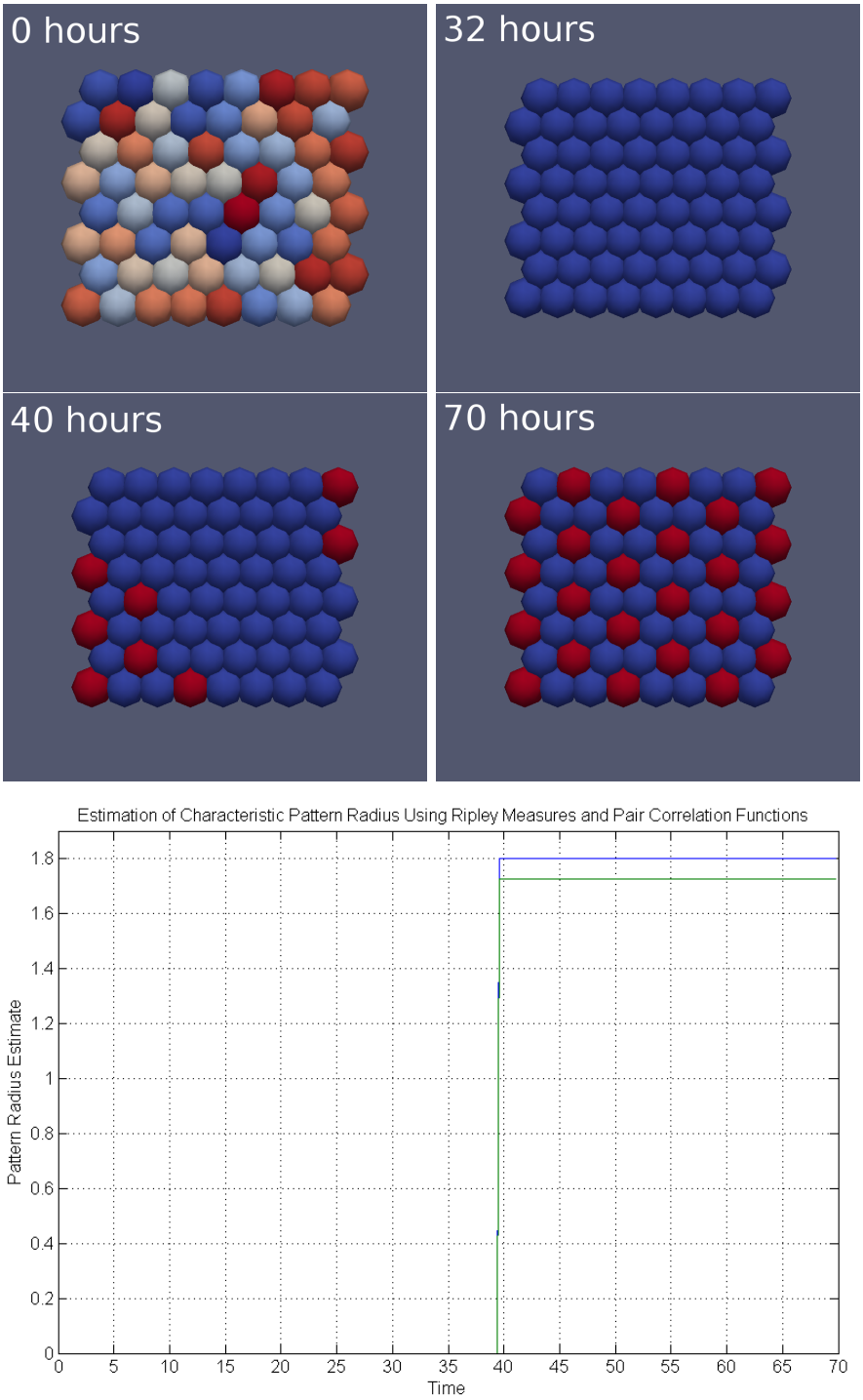

Figure B.1: Evolution of the pattern radius estimate on a node-based monolayer; cells are coloured on a scale of dark blue to dark red, low-to-high according to their Delta concentration. The four images depict the development of a pattern of primary fate cells, from random initial conditions. Initially, primary fate cells have yet to form and so the pattern radius is zero. By 40h some primary fate cells have formed and the radial assessment jumps from zero to 1.8, where it remains as the pattern continues to develop.

along with its circular weighting topology, intuitively yields an expected value of πr^2. Linearisation of the K-Value produces the *Ripley L-Value*, defined as

$$L(r) = \sqrt{K(r)/\pi}\,. \tag{B.2}$$

This transformation serves to remove the dependence upon the scale of the domain, whilst also stabilising the variance [260, 261]. Normalisation of the L-Value yields the *Ripley H-Value*, with expected value zero:

$$H(r) = L(r) - r. \tag{B.3}$$

Consequently, $H(r) \in [-1, 1]$, where positive values of $H(r)$ indicate point *clustering* over spatial scale r: that is, there are more points in the locality than would be expected from a random pattern. Negative values, on the other hand, represent *dispersal*: fewer such points than might be expected.

Ripley Catchment Zone

Use of a circular topology for the Ripley catchment zones can cause the measure to confound small- and large-scale effects [262, 263]. Ripley's values are therefore recommended for use in studying small-distance phenomena, where this accumulation effect is reduced [260]. The Ripley H-Value provides a measure of clustering or dispersal, and consequently does not directly yield a pattern length scale.

Much attention has been given to translating the behaviour of Ripley H-Values of a range of r into a conclusion about the characteristic pattern radius across a domain [260, 264]. Several studies take the maximum value of $H(r)$ over a given range of Ripley radii as the characteristic radius [265, 266, 267]. The accuracy of using the radius r_{max} which yields the maximum Ripley value has been disputed, owing to the accumulative effects associated with the measure. Kiskowski *et al.* [262] instead use the derivative

of $H(r)$ to determine the Ripley radius at which the point density estimate suddenly falls. Under this approach, the first radius $r > r_{max}$ for which $H'(r) \leq -1$ is taken to be the pattern length scale.

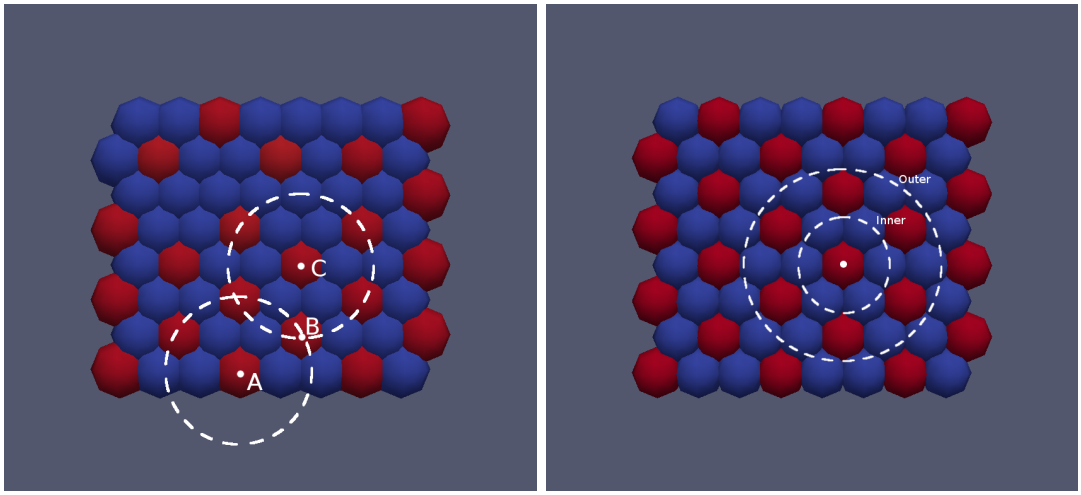

Figure B.2: Examples of weighting constructions for our 2D point dispersal measures, assessing the distribution of the red primary fate cells. (L) Ripley catchment: when weighting for cell C's neighbours, the cell pair C-B is assessed by drawing a circle centred on C and passing through B. This lies completely inside the domain, so contributes a weighting of 1.0 to the summation of $w(i, j)$ in equation (B.1). The circle from cell pair A-B only lies partly in the domain and yields a 'partial' weighting $w > 1.0$. (R) Annular zone for the PCF: this entails a count of the number of threshold cells (in this case six) lying in an annular region centred on cell X, bounded by the inner and outer circles shown. Weighting for the annulus is based on the proportion of the outer radius lying within the domain.

B.2.2 Pair Correlation Functions

Pair correlation functions (PCFs) are an alternative means of assessing point dispersal in two dimensions and have been used to assess the dispersal of multiple cell types and to quantify cell patterning [259]. The PCF, $a(r_k)$, at radius r_k is defined to be:

$$a(r_k) = \sum_i \sum_{j \neq i} \frac{w(i, r_k) I(r_{k-1} \leq d_{ij} < r_k)}{N}, \tag{B.4}$$

where $w(i, r_k)$ is the weighting function described in Section B.2.1, but implemented for the annulus centred on i with outer radius r_k; an example of this is shown on the right-hand side of Figure B.2. $I(r_{k-1} \leq d_{ij} < r_k)$ is an indicator function, in which r_{k-1} is the inner radius of the annulus and d_{ij} is the distance between the centres of cells i and j; it equals 1 when cell j lies within the annular catchment, and 0 otherwise. $a(r_k)$ is typically normalised over the area of the annulus as

$$P(r) = \frac{A}{N} \frac{a(r)}{\pi(r_k^2 - r_{k-1}^2)}, \tag{B.5}$$

for A the area of the domain. Weighting functions $w(i, r_k)$ for annular regions are discussed further in Section B.2.3.

PCF Catchment Zone

In contrast to Ripley's measure, the PCF readily yields a measure of pattern radius. This is due to the use of annular rather than circular catchment zones when calculating the PCF, which avoids the accumulative effects associated with the Ripley measure. The width of the catchment annulus must be carefully chosen however; a too-broad band will fail to accurately detect the pattern length, whilst a too-narrow band will not catch a sufficient number of points to allow the extent of dispersal to be detected [260]. In light of this, our simulations with the PCF metric in Section B.3 take the annular thickness to be the same value as the stepsize between successive catchment zones.

Figure B.4 demonstrates the difference between Ripley and PCF measures on the same cell domain. In practice, $P(r)$ is measured over a range of r and the pattern length is taken to be the radius $r = \text{MAX}(P(r))$.

B.2.3 Weighting at Domain Edges

Weighting functions $w(i,j)$ attempt to mitigate edge effects in dispersal calculations, in cases where a portion of the catchment zone falls outside the domain. Point dispersal measures such as Ripley and the PCF base their comparisons of totals of point events against the randomised event count associated with a Poisson distribution over the same area. Catchment areas at the edge of a domain cannot draw point counts from a full circle or annulus and must have their totals scaled accordingly. Methods for mitigation of edge effects are discussed extensively in [268, 269, 270].

In the case of a *circular catchment zone*, an approximation for the ratio of the viable zone to that of the full circle area is given by

$$\frac{\text{Area(Major segment } XOY)}{\text{Area(Full circle)}} = \frac{\frac{1}{2}r^2\theta}{\pi r^2} = \frac{\theta}{2\pi},$$

where θ is the angle formed by the two radii extending from the centre of cell i to the contact points X and Y with the edge of the domain, as shown in Figure B.3. This does not account for the shaded zone Z shown in Figure B.3, but has been shown by Ripley [246] to provide an unbiased estimate of point dispersal. Consequently, the accepted practice for Ripley calculations is to take the reciprocal value

$$w(i,j) = \frac{2\pi}{\theta} \tag{B.6}$$

as the weighting function, using the circle centred on cell i and whose radius passes through the centre of cell j. $w(i,j)$ is in fact the ratio of the circumference of C to the major arclength XY.

A similar expression can be derived for the *annular catchment zone* used by the PCF, starting from area calculations on the annulus, as shown on the right-hand side of Figure B.3. An approximation for the ratio of the viable zone to the full annulus is

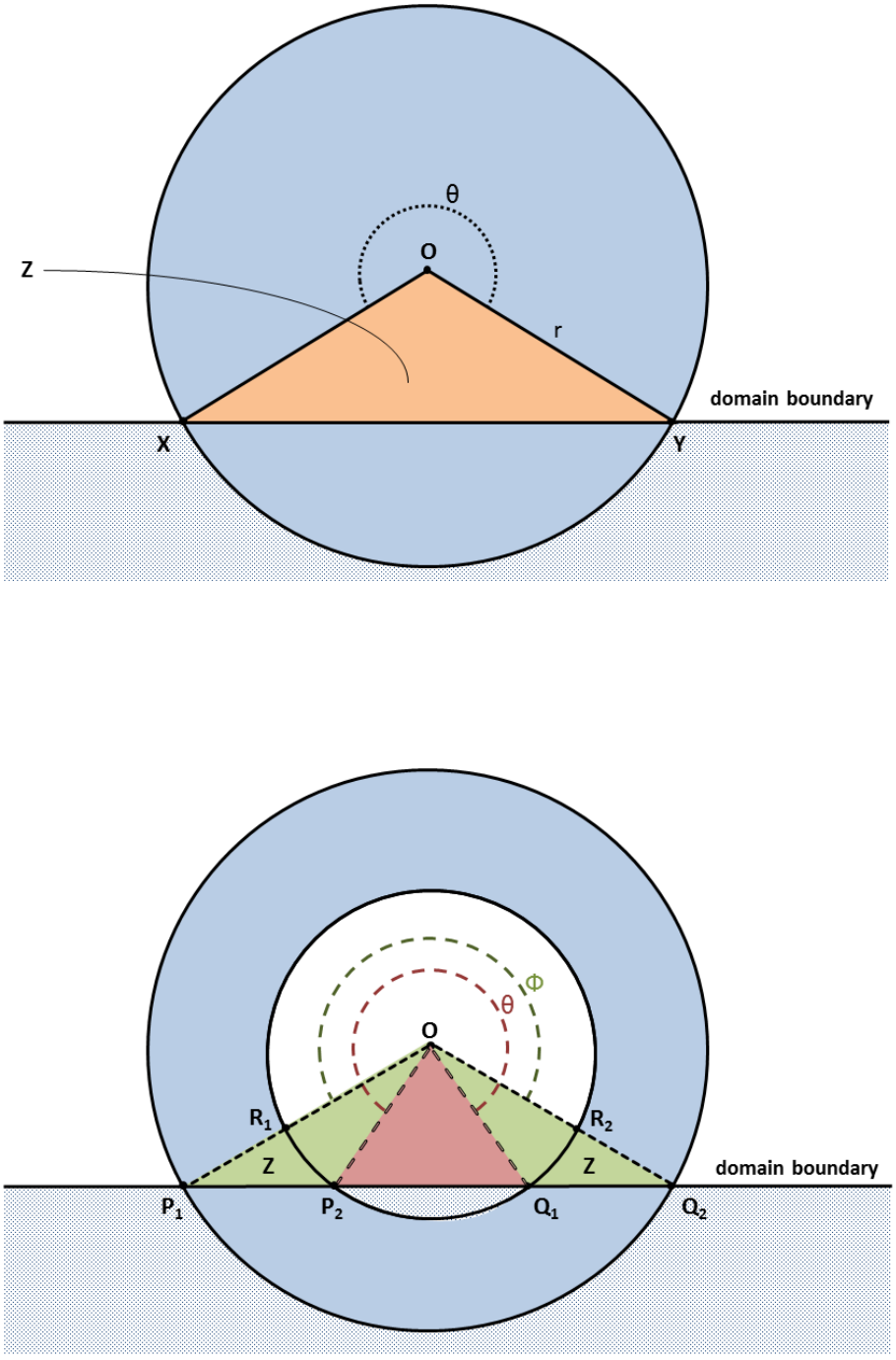

Figure B.3: Derivation of the weighting functions $w(i, j)$ used in the point dispersal calculations to mitigate edge effects at boundaries. (Top) Circular assessment zone for the Ripley measure. (Bottom) Annular zone used in PCF calculations; the zone Z is formed from the portions of the green area that lie within the annulus.

given by

$$\frac{\text{Area(Major section bounded by } P_1R_1 \text{ and } R_2Q_2)}{\text{Area(Full annulus)}} = \frac{\frac{1}{2}r_\phi^2\phi - \frac{1}{2}r_\theta^2\phi}{\pi(r_\phi^2 - r_\theta^2)} = \frac{\phi}{2\pi},$$

where ϕ is the angle spanned by the major arclength P_1OQ_2 and r_ϕ, r_θ are, respectively, the outer and inner radii of the annulus. The weighting function is therefore taken to be

$$w(i, r_k) = \frac{2\pi}{\phi}, \tag{B.7}$$

for the annulus centred on cell i with inner and outer radii r_{k-1}, r_k. As with the Ripley weighting (B.6), the PCF weighting (B.7) does not account for the shaded zone Z (as shown in Figure B.3). Nonetheless, the weighting $w(i, r_k)$ is only intended as an approximation and provides an appropriate correction where the stepsize $r_k - r_{k-1}$ for successive annular radii is taken to be sufficiently small, particularly on large domains where few catchment zones intersect with the domain boundary.

Edge effect compensations in Ripley and PCF calculations will always produce heavier weightings for border cells. To reduce the number of such approximations required during point dispersal calculations, the condition $r < \text{MIN}(\Omega_l, \Omega_w)$ is applied, where r is the radius of the catchment zone and Ω_l, Ω_w are the length and width of Ω respectively.

Typical output from the Ripley and PCF metrics is shown in Figure B.4, which demonstrates the variation in raw Ripley and PCF values over a range of catchment zone radii.

B.2.4 Implementation

Studies from the existing literature discussed in Section 2.1 have shown how the definition of a 'neighbouring cell' in a tissue framework exerts significant influence on the

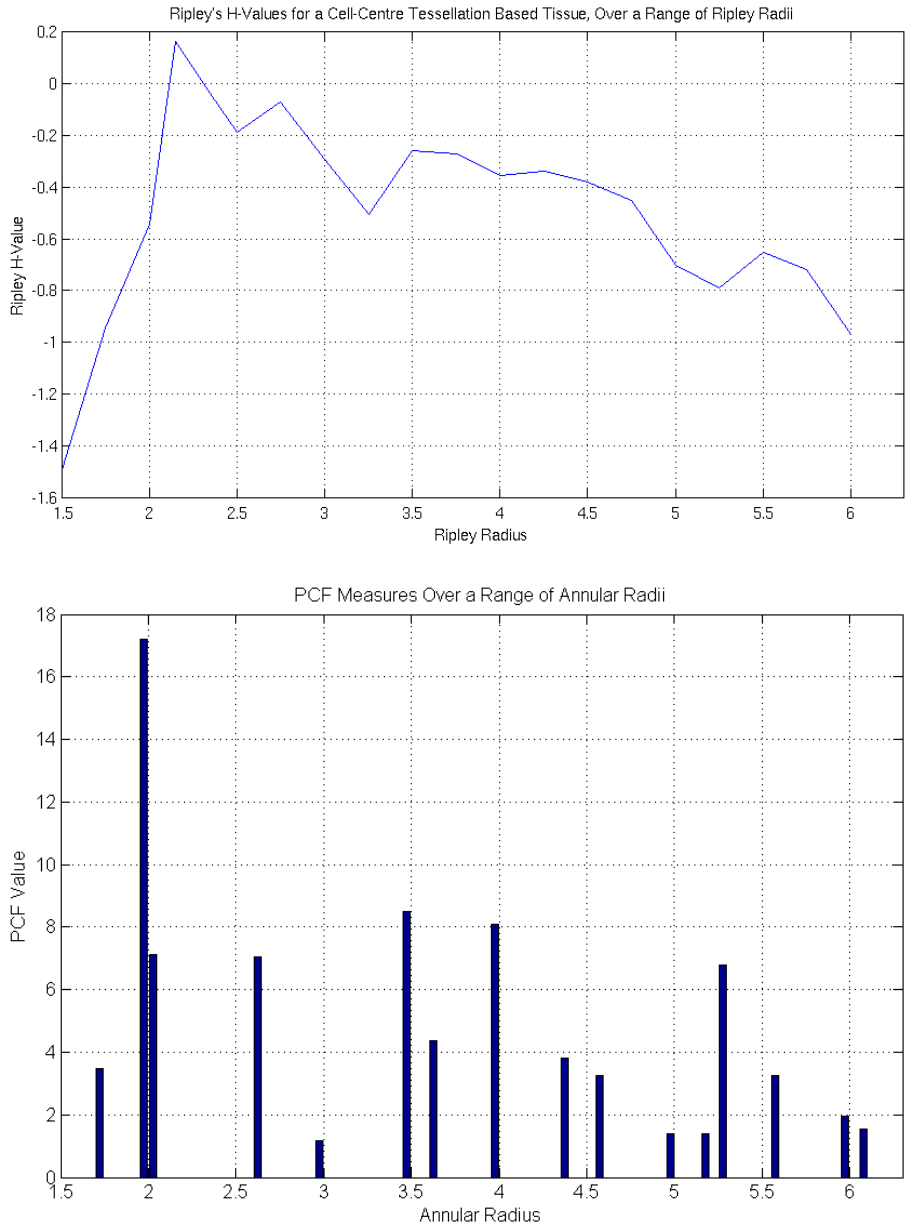

Figure B.4: Pattern assessment measures for the cell-centre, tessellation-based tissue depicted on the left-hand side of Figure B.2. (Upper) Ripley H-Values over a range of Ripley radii. The H-Value increases once the Ripley zone is large enough to capture threshold cells which are pairwise close, thereafter falling once the radius significantly exceeds the pattern radius of the domain. (Lower) PCF assessment for the same domain over a range of annular radii. The PCF histogram spikes at particular cellular length scales, falling to zero in between these values when no cells lie within the annular catchment zone.

patterning of a juxtacrine signalling model such as the Collier model, in which the rate of change of one or more species depends on an averaging process taken over nearby cells. The nuances of neighbour selection, cell spacing and force representation in a computational tissue model may each affect the outcome of spatial statistical analysis. Point dispersal measures must therefore be carefully interpreted in the context of the underlying tissue model if they are to lead to valid conclusions.

Our objective in this chapter is to select an appropriate point dispersal measure for our later studies and to understand its interpretation in the context of a given tissue modelling framework. To this end, we now carry out a comparison of the Ripley and PCF metrics across several different tissue models. The tissue modelling frameworks of interest are: cell-centre, vertex-based and node-based models, all of which were described in Section 2.4.1. This comparison requires us to consider several aspects of implementation, which we now describe.

Threshold Cells

We define '*threshold cells*' to be those cells expressing a Delta level greater than 0.9. A value of this magnitude provides sufficient separation between the high-Notch and high-Delta cells for us to adequately identify the primary fate cells.

Neighbour Selection

The definition of a 'neighbouring cell' affects the Delta averaging processes of the Collier system ($\bar{D}$ in Equation (2.1)) and can have a significant impact on the pattern and number of threshold cells obtained[1]. The three tissue models we initially explore in this study, all described in Section 2.4, differ in their neighbour selection methods, as follows:

[1]For example, the lattice-based simulations of Webb *et al.* [134], described in Section 2.1, demonstrate that increasing perturbations from a regularised placement of cell neighbours give rise to increasingly irregular patterning on a hexagonal mesh.

1. *Cell-centre tessellation models* are arranged around a mesh-based Voronoi tessellation. Neighbours are therefore defined by the cells which share an attached spring according to the geometry of the underlying tessellation.

2. *Vertex-based models* are similarly space-filling and a cell's neighbours can be accessed from its associated vertex mesh. The boundary-dynamic nature of the vertex method means that neighbouring cells are defined as those which share a perimeter element.

3. By contrast, *node-based frameworks* are not associated with an underlying mesh: a pair of cells neighbour one another if the sum of their assigned cell radii exceeds the Euclidean distance between the two points which denote the cell locations (that is, the circular zones swept out by the cell radii overlap).

Chaste implementations of these three methods differ in their treatment of neighbour selection at the edge of the tissue domain, as shown in Figure B.5. Both the vertex- and node-based methods adopt the arrangement shown in the lower image, while the cell-centre method adopts the upper arrangement. Some modifications to the implementation of the cell-centre mesh in *Chaste* are therefore required to bring the neighbour selection processes in line with this; we refer to this altered version as a "*modified cell-centre mesh*". In Section B.3, we present results for both the original and modified versions of the cell-centre mesh, to demonstrate the difference that neighbour selection can make upon the resulting pattern. This also enables us to establish how a difference in patterning translates into variation in PCF or Ripley values.

Standardisation Process

Absolute cell spacing is not the same for all models in a *Chaste* implementation and varies over the course of a simulation if cells are allowed to move and divide. This does not affect the output from static monolayers in Section B.3, since cells are spatially

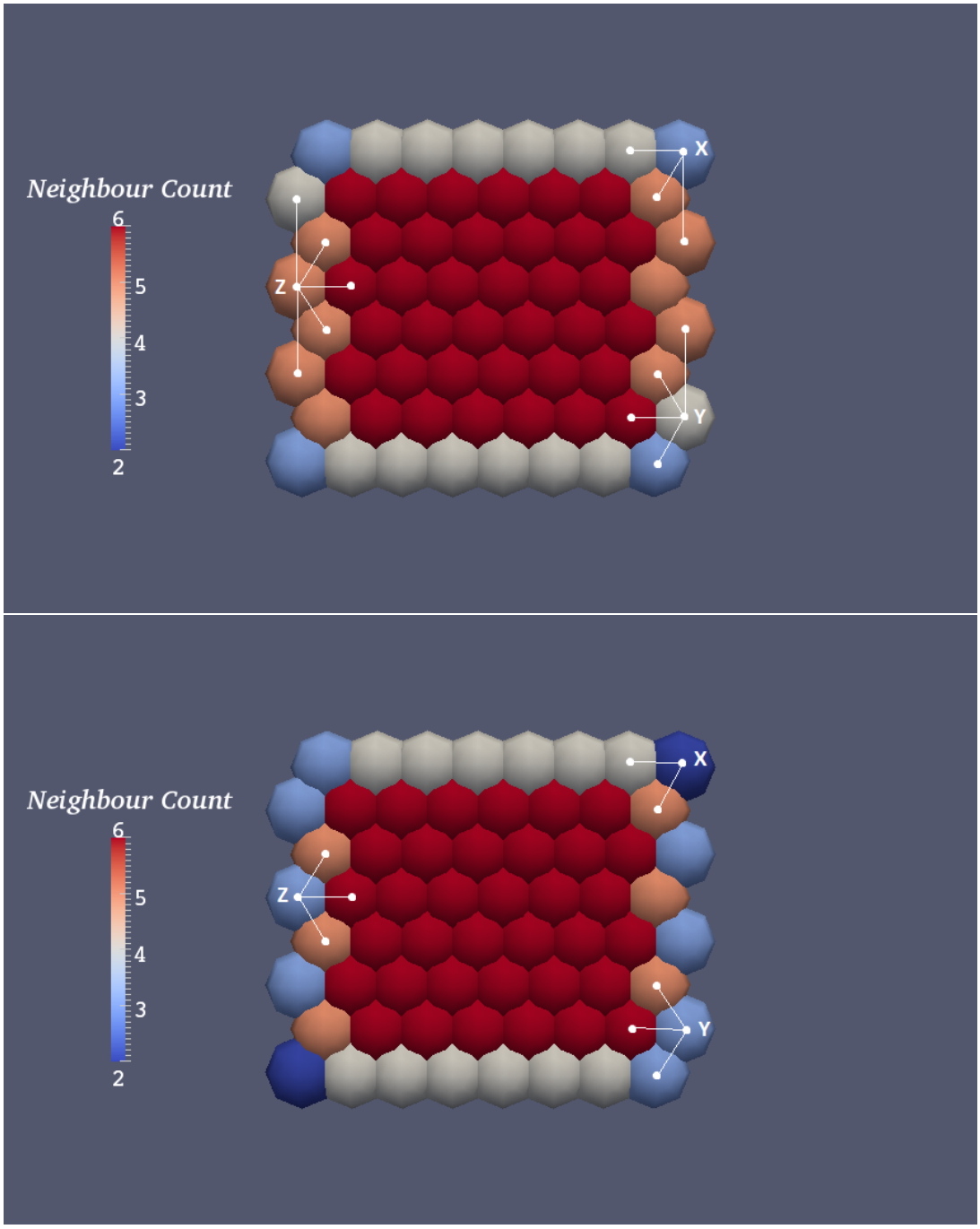

Figure B.5: Neighbour selection using (top) the original *Chaste* cell-centre mesh, in which cell X has three neighbours, Y four and Z five, against (bottom) the modified version in line with the Vertex and Node implementations, in which cells X, Y and Z have two, three and three neighbours respectively.

fixed and arrested in $G0$ phase, hence an equal spacing at the outset remains fixed throughout. However, it does need to be addressed in the dynamic experiments of Section B.4.

When calculating point dispersal metrics in dynamic simulations, the mean cell spacing is calculated for the entire cell population (or, where appropriate, for the cell population of a subdomain) and used to standardise the characteristic radius with respect to the underlying tissue framework. This yields a dispersal measure in terms of mean cell lengths, rather than absolute distance. Mean cell spacing is calculated according to the formula

$$\text{Mean cell spacing} = \sqrt{\frac{A}{N_{\text{total}}}}, \tag{B.8}$$

where A is the area of the domain and N_{total} is the total number of cells (threshold and non-threshold). This construction accounts for domain periodicity within our dynamic scenarios.

Estimation of Pattern Radius

The formulation of the Ripley metric as a measure of clustering or dispersal does not yield a pattern radius directly. Furthermore, artefacts arising from the circular topology of its catchment zone (see Section B.2.1) make it difficult to ascertain the radius of maximal aggregation from the maximum of H(r) alone. Here we adopt the approach of Kiskowski *et al.* [262] and employ a numerical method to estimate the derivative $H'(r)$. Using a five-point approximation for the derivative, we take the pattern radius to be the first value r for which the derivative $H'(r) = -1$.

By contrast, the annular structure of the PCF catchment zone encapsulates how the count of local threshold cells varies with distance from a specified cell. The outer radius at the maximum value of $P(r)$ is therefore used to estimate the pattern radius

from the PCF.

B.3 Static Monolayers

In static monolayers, all cells are arrested in the non-dividing $G0$ phase and the removal of intercellular forces in the underlying tissue model constrains cells to remain spatially fixed. This provides an excellent test scenario for the Ripley and PCF metrics, allowing for the investigation of runtime, metric stepsize and metric catchment zone without the added concerns of coordinating the ODE system with the phases of the cell cycle. Studies in this section will inform us as to the advantages and disadvantages of each method and indicate which is most suitable for analysing our own model of Notch-Wnt interaction, in Chapters 5 and 6.

Test Conditions

All static simulations employ an 8×8 grid of cells, set up in *Chaste* using one of the four main tissue models discussed in Section B.2.4. Simulations to evaluate CPU time and metric stepsize all use a flat monolayer, owing to its straightforward implementation. The equilibration time studies of Section B.3.2 use a vertex-based toroidal mesh in order to circumvent the need for boundary conditions.

Notch activity is modelled using a cellular embedding of the model of Collier *et al.*, using the conditions detailed in Section B.1; all cells are assigned a differentiated phenotype, so that they do not cycle or divide. Initial conditions for the Collier system vary between the simulations, whether due to the use of randomised values across a cell population, or to testing a scenario over a series of fixed values. Initial conditions are therefore stated alongside simulations, either in the figure captions or in the main text.

B.3.1 CPU Time and Metric Stepsize

Sections B.2.1 and B.2.2 described how the radius of the catchment zone of a point dispersal metric is successively increased and the dispersal measure calculated at each of these radii in order to determine the lengthscale of the cell pattern. The difference between successive radii is the metric stepsize; a smaller stepsize should produce more accurate lengthscale estimates but usually requires a longer runtime, because a smaller stepsize will require calls to the metric calculation function at a greater number of radii.

To evaluate the trade-off between accuracy and computational time, a runtime assessment is performed on the two functions which carry out the PCF calculation, `CalculateAnnularPatternRadius()`, and the Ripley calculation, `CalculateCircularPatternRadius()`. Simulations are established using standard conditions on each of the four tissue types for stepsizes ranging from 0.1 to 0.01. These are run for 70 simulation hours to ensure each domain has patterned; then a single call is made to each of the pattern analysis functions and the CPU time and numerical outputs are recorded. Results from these simulations are depicted in Figures B.6 and B.7.

Discussion

It is clear from the CPU times shown in Figure B.6 that the PCF is the faster method on all the tissue models tested. Although the exact ratio of Ripley:PCF CPU time varies between the tissue models and stepsizes, the PCF generally requires around $60 - 75\%$ of the runtime of the Ripley function. Much of this improvement is due to the PCF yielding a pattern estimate directly, whereas the Ripley measure must employ numerical differentiation to determine its radial estimate.

Both metrics have a longer runtime on the vertex based model, as a result of the cell IDs being accessed via a different method to those of cell-centre or node populations. When operating on a vertex mesh, each metric must make two function calls to the

underlying cell population, rather than one, in order to identify the threshold cells.

Stepsizes in the range $[0.01, 0.075]$ yield accurate pattern detection, with the precision largely limited by the magnitude of the stepsize, as shown on Figure B.7. However, the Ripley metric fails to produce a good estimate at the larger stepsize 0.1, possibly because the stepsize is too large to yield a good approximation of the derivative $H'(r)$ at a given radius. Figure B.7 also confirms that the circular topology of the Ripley measure tends to overestimate slightly the pattern lengthscale: its estimates converge from above as the stepsize is decreased. This effect is substantially reduced when a smaller catchment zone stepsize is used.

Examining the results of Figures B.6 and B.7, the 0.05 stepsize between successive catchment zones delivers a suitable compromise between accuracy and runtime. PCF runtime for calculation of a lengthscale estimate at the 0.05 stepsize is ≤ 0.25 seconds, while for the Ripley measure it is ≤ 0.4 seconds.

Notably, the non-modified cell-centre model yields the same lengthscale estimate as the other models, as it only carries a single pattern defect, which is not sufficient to affect the pattern length estimate. In such cases, the presence of defects becomes apparent on examining the raw totals for each metric, listed for the 0.05 stepsize in Table B.1. The raw PCF and Ripley values are significantly lower for the cell-centre population than for the ideal, flawless domains produced by the other models. Indeed, these statistics could be used as comparison data for any static studies on an 8×8 domain. Subtraction of a simulation's raw dispersal metrics from these 'canonical' values for node, modified cell-centre and vertex-based tissues would yield a measure of the pattern deviation from a perfectly patterned domain.

Moreover, the Ripley H-Value provides further information by charaterising the degree of clustering or dispersal in the domain. As discussed in Section B.2.1, $H(r) \in [-1, 1]$, such that positive values represent clustering, negative values represent dispersal and a score of zero indicates a completely random pattern. The Ripley values

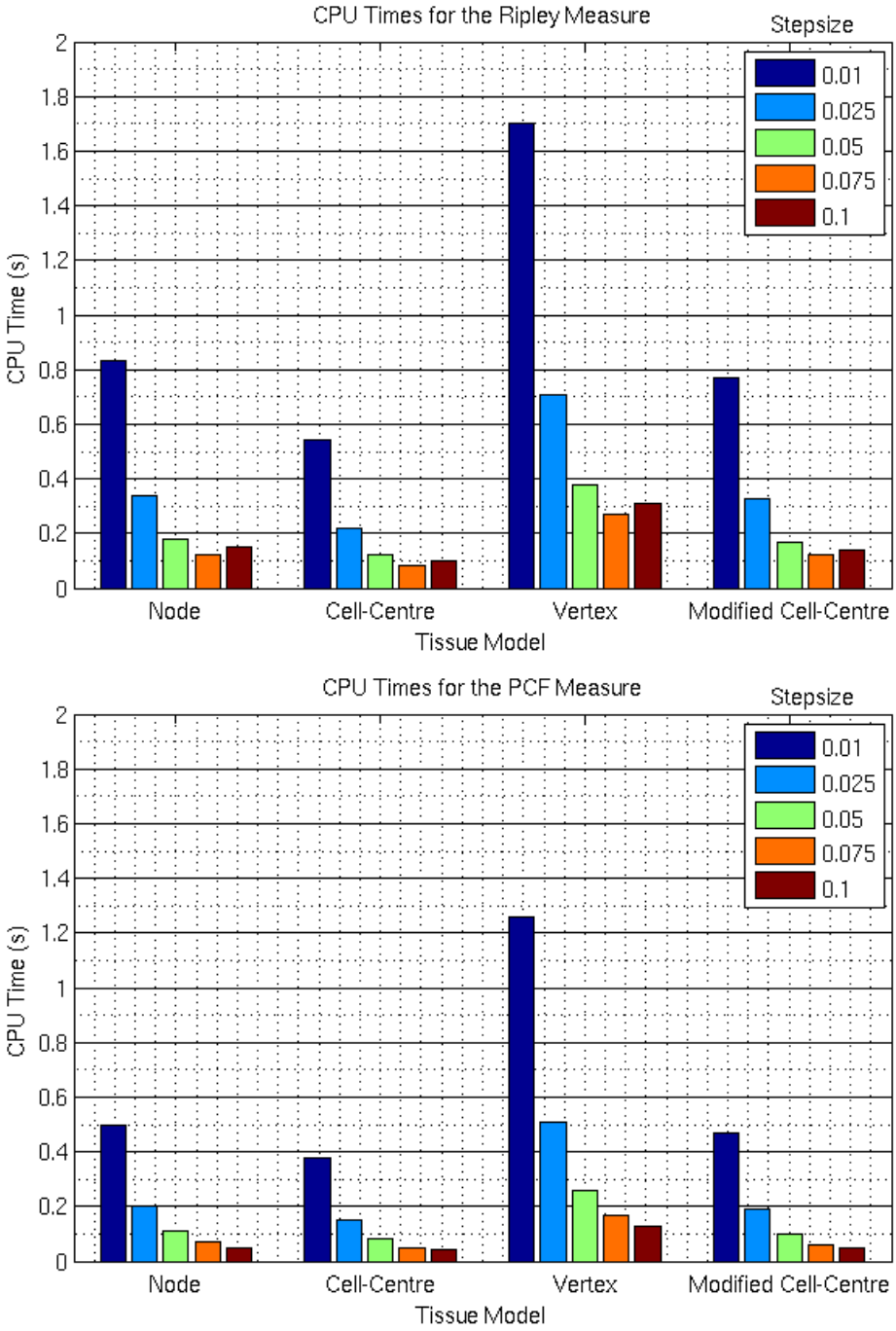

Figure B.6: CPU time for a single call to the Ripley and PCF metrics over five different catchment zone stepsizes, run in *Chaste* on the four different tissue models detailed in Section B.2.4. Machine specifications: Intel Core 2 Quad CPU 8300 @ 250 GHz×4.

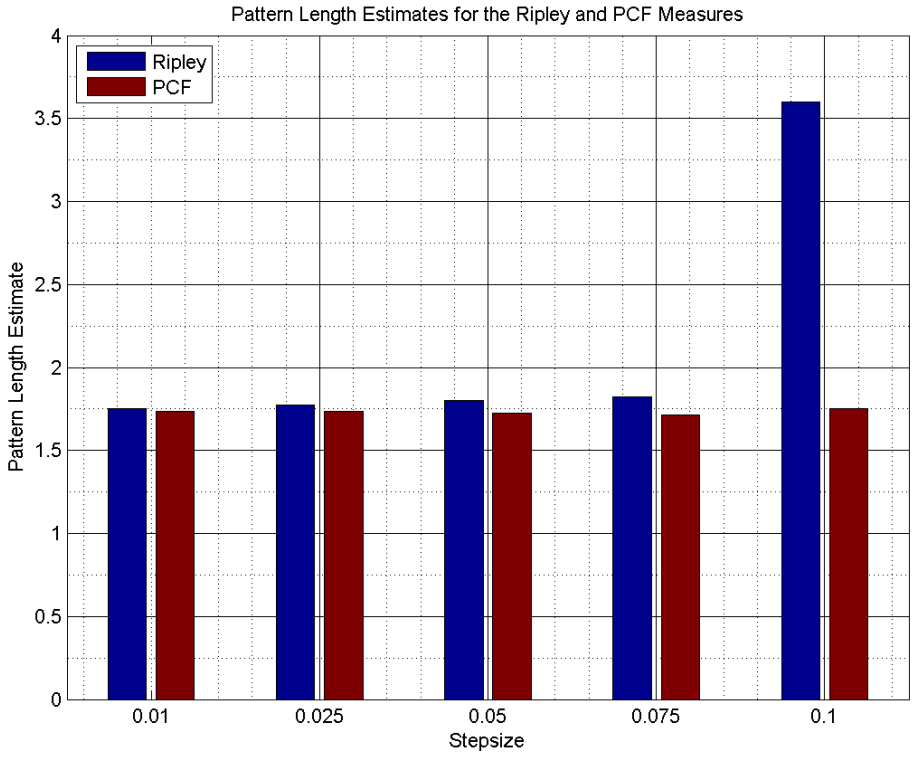

Figure B.7: Pattern length estimates from the PCF and Ripley measures at five different stepsizes over the range $[0.01, 0.1]$. Each of the four tissue models yields the same pattern length estimate and so the graph only displays a single set of bars for each stepsize.

in Table B.1 indicate an H-Value of 0.211226 for the original cell-centre model, whilst the modified equivalent yields an H-Value of 0.348976. The lower H-Value for the original model indicates that this pattern is closer to a random distribution than that generated by the modified cell-centre model. This suggests the presence of one or more defects in the pattern associated with the original cell-centre model, as is indeed the case.

Although the raw PCF values for these simulations also differ, these cannot provide the insight into clustering, dispersal or randomness that the Ripley H-Value is able to. Raw values from the Ripley metric therefore provide finer-grained detail of patterning behaviour than a simple lengthscale estimate can supply.

Metric	**Cell-Centre**	**Node**	**Vertex**	**Modified Cell-Centre**
Ripley H-Value	0.211226	0.348976	0.327826	0.348976
PCF	26.5788	29.2562	29.2562	29.2562

Table B.1: Raw output of Ripley and PCF values from the pattern analysis functions, run with a stepsize of 0.05. The cell-centre model operates with a different neighbour selection rule from the other models and exhibits a pattern defect. This results in substantially different raw PCF and Ripley values, compared to the remaining three models. The slightly lower Ripley value for the vertex mesh is due to this model having slightly different absolute spacing between cells than the node and cell-centre models.

If an overall pattern length is the key feature of interest, the PCF would be the best metric to use, owing to its significantly shorter runtime. If, on the other hand, a more nuanced assessment of the pattern defects is required, then the Ripley measure would prove the better option, as it characterises the degree of dispersal or clustering of the threshold cells. In such circumstances, this extra information justifies the longer runtime required to implement the Ripley measure.

B.3.2 Application to a Static Cell-Based Monolayer

Section B.3.1 assessed basic properties of the two point dispersal metrics, such as runtime and dependence upon the catchment zone stepsize. We now progress to studying the metric outputs over the course of a series of cell simulations, in order to demonstrate how these outputs can be used to illustrate the temporal evolution of patterning on a cell-based monolayer.

One of the main quantities of interest in this section is the *equilibration time* of the Notch system: that is, the time (in simulation hours) required for the cell population to settle on a stable, patterned state. Variation in equilibration time becomes important when working with dynamic systems in Section B.4, as patterning may not occur if cells do not attain heterogeneous equilibrium within the timescale of one cell cycle.

Variation with Decay Ratio, ν

Patterning in a cell-based domain is indicated by a nonzero estimate for the pattern lengthscale. Postprocessing of timeseries for the point dispersal metrics readily yields the equilibration time, by detecting the time at which the metric values settle on a constant state. We now demonstrate this through a series of simulations which vary the decay ratio, ν, and examine its effect upon the equilibration time.

Figure B.8 shows the variation in equilibration time as the decay ratio, ν, is varied over the range $(0, 1]$. All simulations are run for 500 simulation hours to give ample chance for a global pattern to emerge. Initial conditions i_{init} for Notch and Delta are randomised around each of $[0.0, 0.25, 0.5, 0.75, 1.0]$ in turn, within a tolerance of ± 0.05. Owing to the randomisation of the initial conditions, ten different random number seedings are run for each pair of values (ν, i_{init}) and used to calculate a mean value for the equilibration time. A periodic, toroidal vertex mesh is used, in order to eliminate dependence on boundary conditions.

There is a nonlinear decrease in equilibration time with an increase in ν. A lower

value of ν reduces the rate of change of Delta, thus weakening the positive feedback loop which provides the patterning mechanism. $\nu = 0$ would give Delta a zero rate of change, locking the Delta values and preventing any pattern from developing.

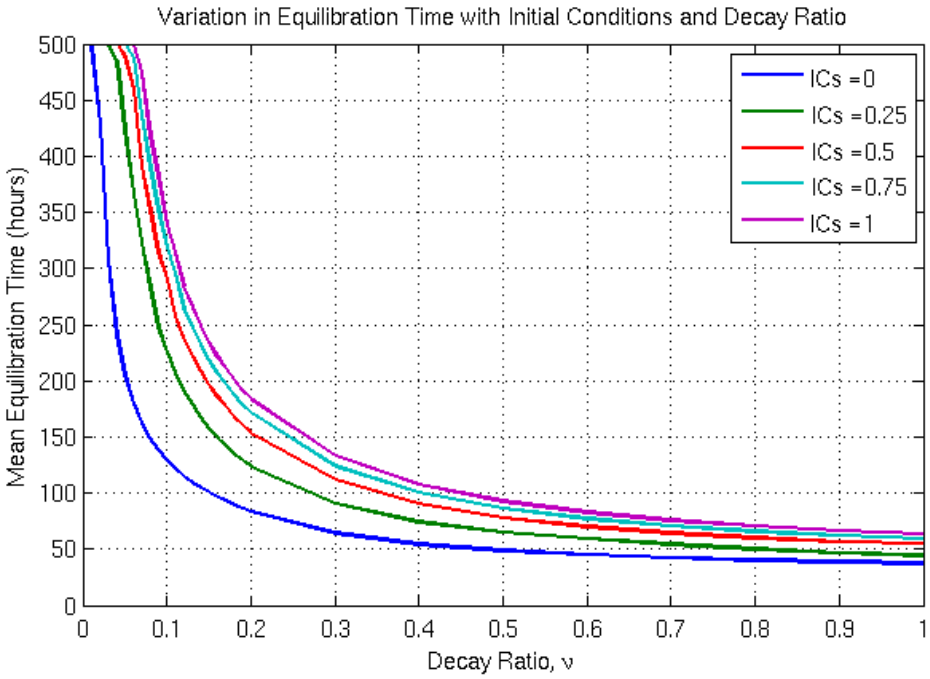

Figure B.8: Variation in equilibration time over a range of decay ratios ν. Each data point is a mean value taken over ten separate simulations, each performed with a different random number seeding.

Timecourses for the raw Ripley and PCF metrics are depicted in Figure B.9, for the specific example of $\nu = 0.8$. A clear contrast is evident between a completely unpatterned state at the very beginning (zero values), followed by a patterning phase involving a progressive increase in the raw metric values, before the system settles on its equilibrial state. These features hold true for both metrics and indeed follow a similar pattern, although the Ripley metric provides a specific assessment of randomised spread within the domain. Ripley's H-Value provides more detailed information about the pattern evolution, for example indicating that the $i_{init} = 0$ and $i_{init} = 0.5$ cases peak at the same degree of dispersal.

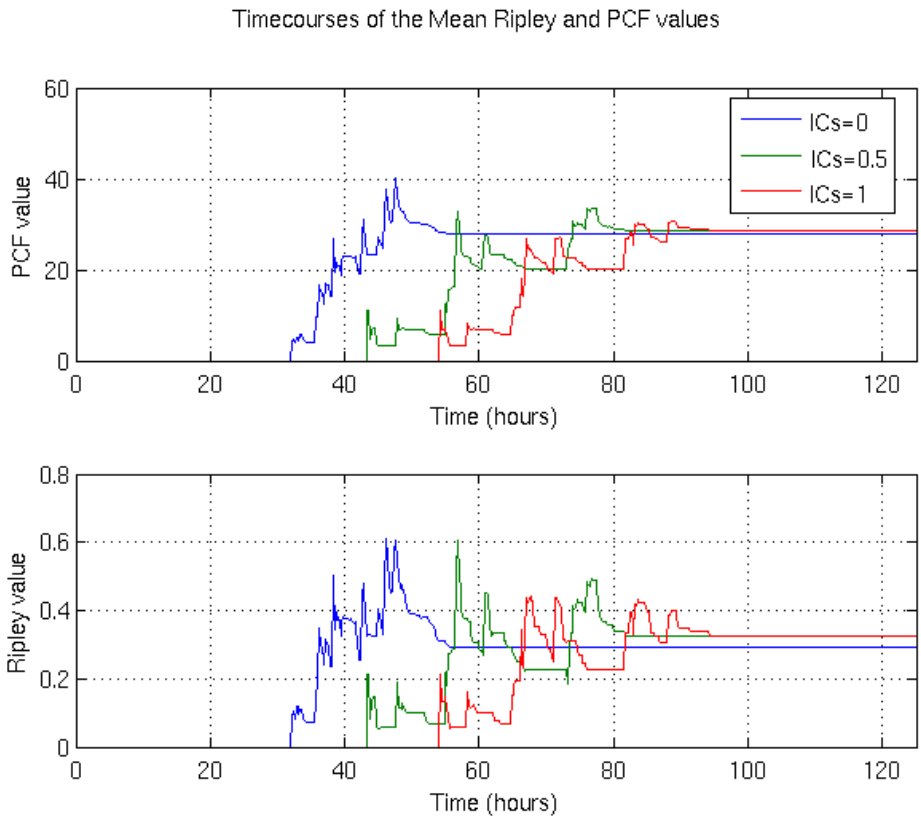

Figure B.9: Evolution of raw PCF and Ripley values for $\nu = 0.8$, with initial conditions for Notch and Delta randomised about $0.0, 0.5, 1.0$. These timecourses are averaged over ten separate simulations, each performed with a different random number seeding.

Discussion

Lower values of ν would be unlikely to yield patterning within the timescale of a typical cell cycle, if these simulations were being run within a dynamic setting. Initial conditions clearly have some influence upon the equilibration time, but the decay ratio provides the stronger control over the timescale of pattern development, as a result of the latter's role in determining the strength of the positive feedback loop within the Notch system (as discussed in Section 2.1.1).

Raw Ripley values provide a useful measure of the pattern development within the

domain, beyond that provided by simple estimates of the dominant pattern length. For example, the Collier model simulations depicted in Figure B.9 show less randomised point dispersal as the domain approaches its equilibrial configuration. Timecourses of raw metric values might be employed in tracking pattern evolution within several subregions of a given domain, which could prove particularly useful in dynamic simulations for measuring cellular response to spatially varying stimuli. Consequently, we focus solely on the Ripley measure for our dynamic crypt simulations in Section B.4.

B.4 Dynamic Simulations

Focus on static monolayers has provided valuable insights into the implementation and interpretation of point dispersal metrics in two dimensions. Nonetheless, our overall objective in this work is to understand the interplay of proliferation and cell fate selection in dynamically evolving crypts. This section sees the application of point dispersal metrics to banded sections of the domain, to observe the effects of a spatially varying Wnt stimulus upon the cell fate pattern.

B.4.1 Crypt Simulation Conditions

All simulations in this section model the crypt as a two-dimensional, cylindrical surface, with a circumference of 10 cells and a height of 20. This is represented using a cell-centre tessellation, mesh-based model in *Chaste*, owing to the quicker runtime of this model and its ease of implementation. Each simulation is run for 300 crypt hours.

As with the static simulations of Section B.3, we implement the decoupled model of Notch and cell-cycle activity outlined in Section B.1. Initial conditions of Delta are set at 0.5 for all cells; Notch conditions are randomised over the range 0.5 ± 0.05 using a random number generator on a uniform distribution. Inheritance of Notch and Delta at mitosis is implemented asymmetrically, using a random number generator to

determine the amounts received by the two daughter cells.

An external Wnt stimulus is supplied to the domain; its strength and spatial extent are determined by two parameters: the *Wnt concentration parameter*, and the *Wnt cut-off*. The stimulus takes its specified maximum at the crypt base, and declines linearly up the crypt until reaching zero at the cut-off, according to the formula

$$\text{Local Wnt stimulus} = 1.0 - \frac{\text{current height}}{\text{concentration parameter} \times \text{cut-off}}. \tag{B.9}$$

Any point lying above the cut-off is subject to a Wnt stimulus of zero. Cells are mitotically active if they are subject to a Wnt stimulus of 0.65 and become differentiated when the stimulus is below this threshold. Cell division therefore occurs at the crypt base; cells are pushed upwards into a reduced Wnt concentration and eventually become differentiated. Sloughing is modelled by the removal of cells beyond a height of 20.0 units.

Ripley analyses for all crypt simulations are presented in terms of zones, numbered $1-7$ as shown in Figure 5.3 of the main text. Zones $1-4$ are formed from a direct partition of the crypt domain into horizontal, rectangular bands of equal height. Zones $5-7$ are the same height as $1-4$, but sit within the overlap between the midpoints of zones $1-4$. This enables us to see how the pattern length and Ripley H-Value vary on ascending the crypt, as shown in Figure B.12.

B.4.2 Graded Wnt Concentration

Here we examine four crypt scenarios, each with different Wnt parameters. The case studies are detailed in Table B.2.

Each of these cases adopts the conditions described in Section B.4.1. To mitigate influence from randomised aspects of the initial conditions and Notch inheritance, each case is run over 100 different random number seedings and these results used to

Case Study	Cut-off	Concentration Parameter	Mitotic threshold
A	5.0	1.0	1.75
B	5.0	0.5	0.875
C	10.0	1.0	3.5
D	10.0	0.5	1.75

Table B.2: Wnt parameters for the studies of dynamic crypt cylinders described in Section B.4.2. The second and third columns indicate assigned parameters, whilst the final column indicates the resulting height at which cell division ceases; this is calculated using Equation (B.9). Case studies A and D generate identical Wnt stimulus profiles but are included to demonstrate matching of the point dispersal outputs.

calculate mean values for the pattern lengthscale estimates and the Ripley H-Values.

Inspection of Equation (B.9) and Table B.2 indicates that case studies A and D deliver the same Wnt profile; both these cases are included as a demonstration of how the Ripley measure can identify this similarity, in contrast to cases B and C.

As with the static simulations depicted in Figure B.9, we include Ripley readouts from the beginning of the simulation, rather than just the dynamic equilibrium. This serves to illustrate the capacity of point dispersal metrics for tracking pattern evolution over time, and to show how distinct regions of the tissue domain can influence one another. Results from case studies A and B are shown in Figure B.10; those from case studies C and D are shown in Figure B.11.

B.4.3 Results and Discussion

Cases A and B, depicted on Figure B.10, and the case D, shown as the lower plots of Figure B.11, develop a patterned state in their dynamic equilibrium. The correspondence between the graphs of cases A and D is immediately apparent, and the pattern length readings and Ripley values of all three cases share certain features.

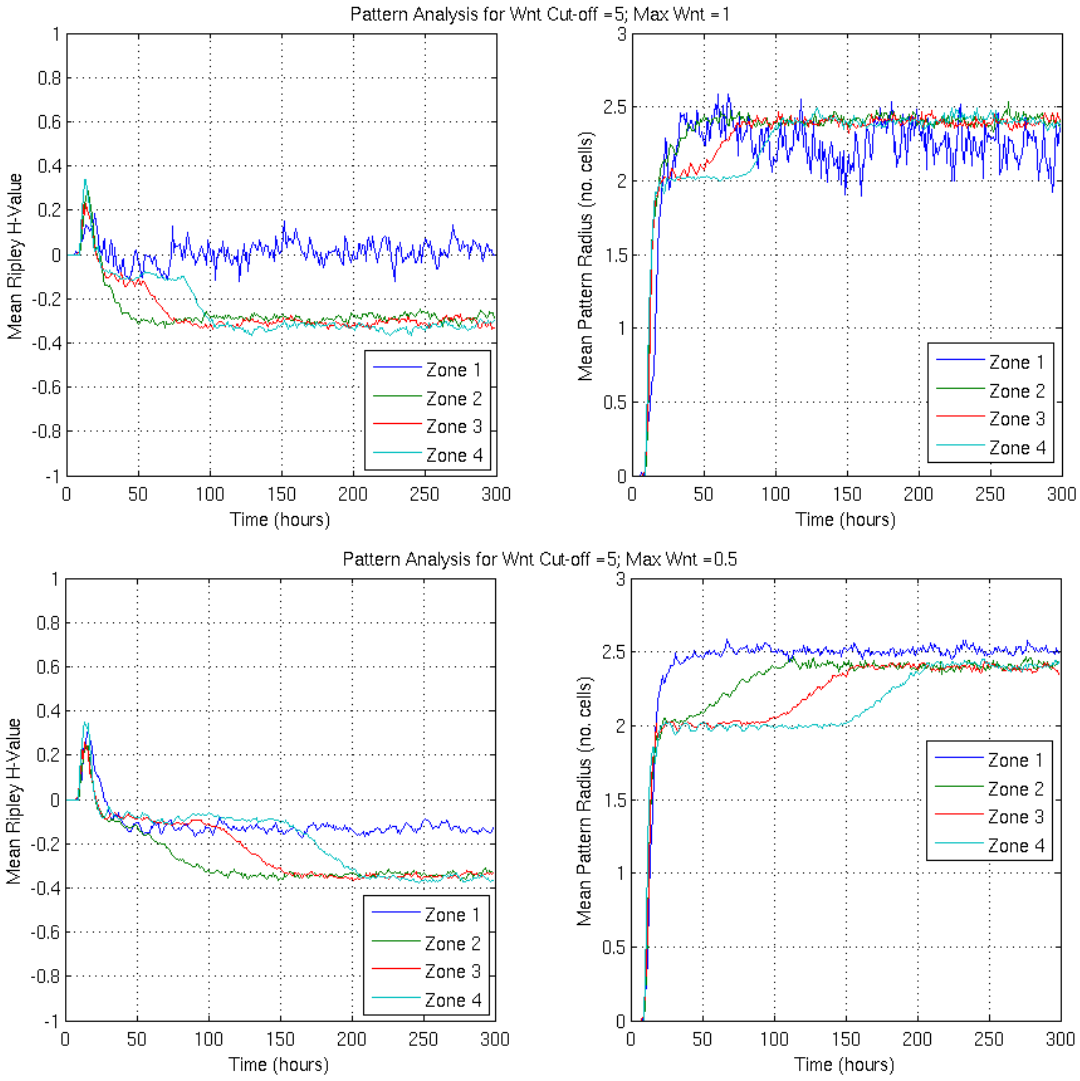

Figure B.10: Trans-domain variation in patterning, subject to a graded Wnt concentration. (Top) Case study A; (Bottom) Case study B. The right-hand plots show the pattern lengthscale estimate, normalised over the mean cell spacing; the left-hand graphs indicate the raw Ripley H-Values. Separate timecourses are shown for each of the four zones of assessment.

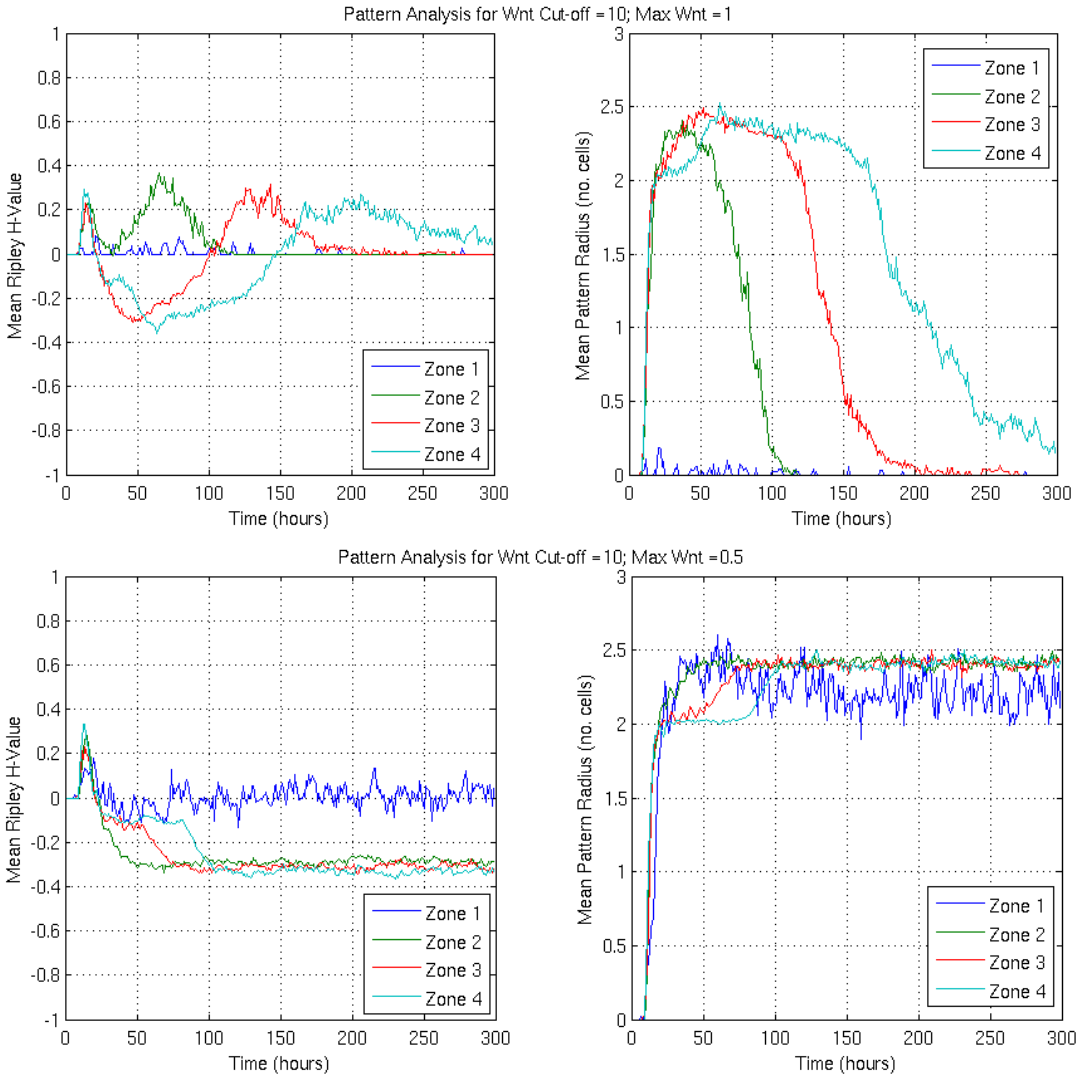

Figure B.11: Trans-domain variation in patterning, subject to a graded Wnt concentration. (Top) Case study C; (Bottom) Case study D. The right-hand plots show the pattern lengthscale estimate, normalised over the mean cell spacing; the left-hand graphs indicate the raw Ripley H-Values. Separate timecourses are shown for each of the four zones of assessment.

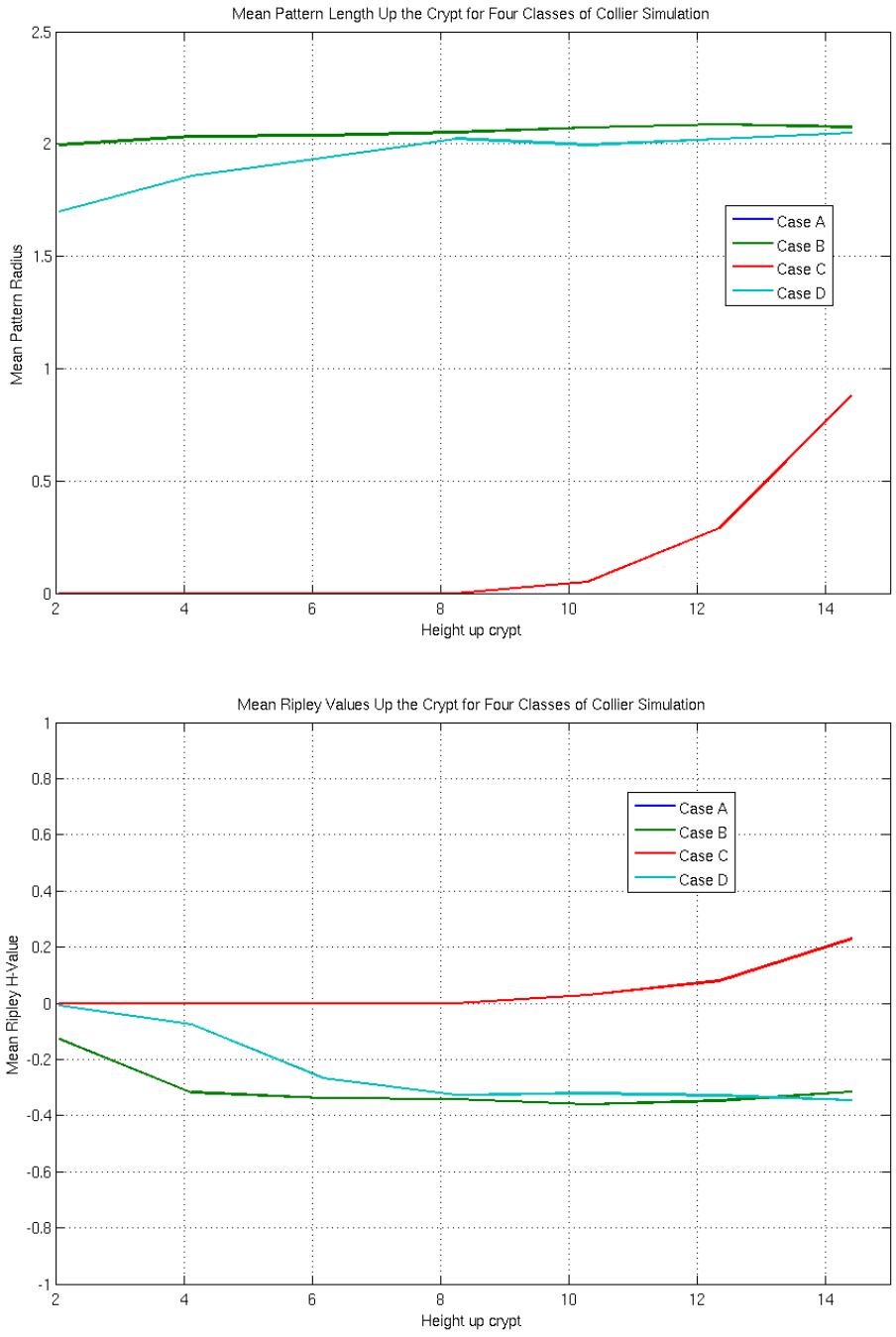

Figure B.12: (Bottom) Ripley and (Top) pattern length analyses for the Collier crypt embedding at dynamic equilibrium, showing the variation in these metrics on ascending the crypt. Graph lines for cases A and D coincide.

Initial patterning: All simulations initially yield an arc of positive H-Values on the Ripley graph. This is due to the randomised initial conditions giving rise to small islands of patterning, which the Ripley measure identifies as point clusters. Juxtacrine signalling then causes the pattern to spread out, creating a more even pattern which is characterised as dispersal. Although pattern length outputs can be used to identify when the pattern forms, the subtle details of its development are only apparent from examining the Ripley H-Values.

Very little patterning in Zone 1: A non-zero pattern length estimate in all three cases suggests that Zone 1 contains some primary fate cells. However, the corresponding Ripley value remains close to zero, indicating a random distribution of primary fate cells. Zone 1 is the mitotically active region and frequent division events regularly change each cell's network of neighbours. In many cases, this keeps the cells close to the homogeneous state. As the cells move into the upper part of the zone, fewer cells divide and patterning can develop.

Patterning in the upper crypt: With the exception of some lower-placed cells in Zone 2, the cells in Zones 2 to 4 lie above the mitotically active region and behave as terminally differentiated cells. The identity and number of cell neighbours do not change dramatically, allowing time for the trajectories of the Collier model described in Figures 2.2 and 2.3 to emerge from the homogeneous state and settle upon the patterned state.

Upwards propagation of pattern: The equilibration process in the crypt is driven by cell division in Zone 1 and sloughing at the top of Zone 4. As the crypt equilibrates from its starting configuration, we observe an upwards propagation of patterning; cells leave Zone 1, become differentiated in Zone 2 and move upwards due to displacement by the cells being produced in Zone 1. In keeping with this, the graphs for pattern length and Ripley measure indicate that Zone

2 equilibrates first, followed by Zone 3, and finally Zone 4.

The remaining case, C, shown as the top two plots on Figure B.11, displays substantially different features. Of all four case studies, it involves the strongest Wnt stimulus at the crypt base (1.0) and the highest cut-off for Wnt (10.0 units). Like the other cases, it has an upwards propagation of the dynamic equilibrium; however, its other features are as follows:

No pattern in Zone 1: The mean pattern length from Zone 1 remains close to zero in the early part of the timecourse, before settling on a constant zero from around $t = 130$. This indicates a lack of patterning and is due to the presence of many dividing cells (a consequence of the high Wnt cut-off and high maximum Wnt stimulus). This is effectively a more extreme version of the lack of patterning in the other three cases.

Successive loss of primary fate cells in Zones 2 to 4: Ultimately, the pattern length estimates and Ripley H-Values for each of Zones 2 to 4 fall to zero, creating a crypt with no primary fate cells. This is again due to the large number of cell divisions in this scenario. Prolific mitosis leads to cell compression, increases the mean number of cell neighbours and locks the Collier dynamics into the homogeneous state. As with the other three experiments, the lower the zone (and hence the closer it is to the mitotically active region), the earlier it attains its dynamic equilibrium.

The contrast between patterned and unpatterned cases is evident in Figure B.13. The image on the left shows a patterned dynamic equilibrium from case study A, in which the non-dividing regions adopt the heterogeneous state. By contrast, the image on the right, from case study C, is almost devoid of patterning. Excessive cell division in the lower half of the crypt leads to compression and loss of patterning. Ultimately the primary fate cells in the uppermost region will be sloughed off and the crypt will

attain an unpatterned dynamic equilibrium. Pattern analysis via metrics such as the Ripley H-Value and PCF measure highlights the discrepancy between the patterned cases A, B and D and the unpatterned case C and motivates use of these metrics in future for identifying non-physical parameter regimes in a simulation.

These findings are reiterated by the results of Figure B.12, which shows the variation in the Ripley H-Value and pattern length estimate on ascending the crypt, for the four case studies. Case C settles on a pattern length and H-Value of zero throughout the crypt, the result of complete loss of primary fate cells. By contrast, the other cases feature zero Ripley values at the very base of the crypt, where mitosis prevents cell patterning from occurring, before attaining fairly constant pattern lengths (around 2 cell diameters) above this region. The lower Wnt cut-off and concentration parameter in Case B ensures patterning lower down the crypt than for Cases A and D.

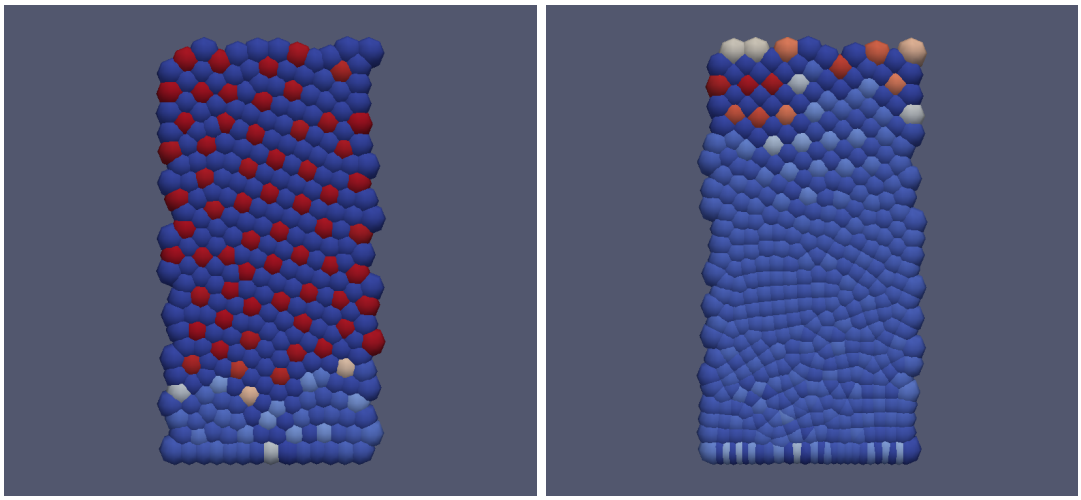

Figure B.13: Screenshots of two dynamic crypt cylinders, at time $t = 300$. (L) Case study A: Max Wnt 1.0, cut-off 5.0. Sufficient balance between cell division at the base and sloughing at the crypt mouth enables clear patterning to emerge in the dynamic equilibrium. (R) Case study C: Max wnt 1.0, cut-off 10.0. Here, the higher Wnt cut-off leads to higher numbers of dividing cells; more cells are born per timestep than are sloughed at the crypt mouth. This leads to compression in lower crypt regions and patterning is lost in the equilibrial state.

Estimates of the pattern lengthscale are therefore useful in characterising many key features of primary fate cell dispersal. The Ripley H-Value allows for more subtle interpretation of this information and can be used in tandem with lengthscale estimates to successfully characterise the cell fate distribution within a dynamically evolving tissue.

B.5 Discussion and Conclusions

The simulations in this appendix, both static and dynamic, have proved successful in using point dispersal measures to analyse the temporal evolution of cellular patterning and its spatial variation across a tissue domain.

The PCF is somewhat quicker to calculate than the Ripley measure and its annular measurement of point-to-point distances readily yields the length scale of a pattern, simply the radial value at which the PCF is maximised. However, the pattern length estimate fails to capture the fine-grained detail of the dispersal of threshold cells. For example, two domains may yield the same pattern length estimate without being identically patterned, or having the same number of pattern defects, as was shown in Section B.3.1.

The Ripley measure is better equipped to address this. Although its runtime is longer than that of the PCF, the raw Ripley H-Value explicitly characterises the degree of clustering or dispersal in the domain. Pattern defects create irregular gaps between threshold cells, altering the degree of dispersal or clustering and hence the raw H-Value. In circumstances where finer-grained detail is required, the useful, additional information provided by the Ripley metric should outweigh the drawback of its longer runtime.

Simulations on dynamically evolving crypts in Section B.4 demonstrated how pattern lengthscale estimates can be used in tandem with the Ripley H-Value to track

changes to the cellular composition of, and its distribution within, a biological tissue. Insights from the unpatterned crypt scenario (case study C in Table B.2) also indicate the need to balance the processes of cell division and sloughing for a given crypt size, if a biologically realistic crypt (i.e. containing both primary and secondary fate cells) is to be obtained. This should be taken into consideration when calibrating the crypt embedding of our own model for Notch-Wnt interaction, in Chapter 6.

Fine-grained details of patterning are valuable when exploring the crypt embedding of our ODE model for Notch-Wnt interaction in Chapters 5 and 6. Since early-stage CRC is the main biological motivation for this thesis, we need to explore the behaviour of small groups of mutant cells, or even individual cells, as they move and proliferate within the colorectal crypt. A nuanced measure of clustering and dispersal is therefore more suitable for analysing the spread of mutant cells. The findings of this chapter therefore suggest that the Ripley measure, rather than the PCF, be used in the simulations of the later chapters of this thesis, and that it be implemented with a catchment zone stepsize of 0.05.

C

Additional Simulations of the Buske and NWODE Models

Appendix Summary

Comparison of the Buske and NWODE models in Chapter 5 required use of normally-distributed phase lengths. This approach differs from the Gamma-distributed lengths used in Buske *et al.* [5] and we present additional simulations using this distribution to demonstrate its minimal influence on the results obtained.

C.1 Buske Model with Gamma-Distributed G1 Phases

Comparison between the Buske and NWODE models in Chapter 5 required a unified approach to the modelling of the cell-cycle phase lengths, to ensure a fair comparison of the two different models for cell fate selection. Our decision to generate G1 phase lengths from the normal distribution $N(2, 1)$, truncated to discard negative or very small values, represent a departure from the approach of Buske *et al.* [5], in which the G1 phase lengths are drawn from a Gamma distribution.

To determine whether this change may have affected the performance of the Buske model, we now run simulations of the model using G1 phase lengths drawn from the distribution $Gamma(4, 0.5)$, which has the same mean and variance as the $N(2, 1)$ distribution. As in Section 5.3, the distribution is truncated to discard any negative or very small phase lengths.

This new batch of simulations is established and conducted using identical conditions to those described in Sections 5.2, 5.3 and 5.5, save for the implementation of G1 phase lengths. As with the simulations of Chapter 5, the Gamma-distributed case is run for 100 separate simulations, each at a different random number seeding. All timecourses and states shown in this Appendix reflect the mean of these aggregated results.

C.1.1 Results and Discussion

The results from Ripley analysis of these simulations are shown in Figure C.1, which provides timeseries for zones $1-4$ of the crypt. The upper results, arising from a system with normally distributed phase lengths, are almost indistinguishable from the lower plots, which are from a Buske model using Gamma-distributed phase lengths.

A seven-zone assessment of the pattern radius and Ripley values up the crypt at dynamic equilibrium are shown in Figure C.2. Although some slight variation is apparent, there is very little difference between the two outcomes.

Given the minimal differences between the patterning obtained when deriving G1 phase lengths from a truncated Gamma or truncated normal distribution, we conclude that the use of normal values does not compromise the behaviour of the Buske model, and that the comparison of Chapter 5 presents a fair assessment of the Buske and NWODE modelling frameworks.

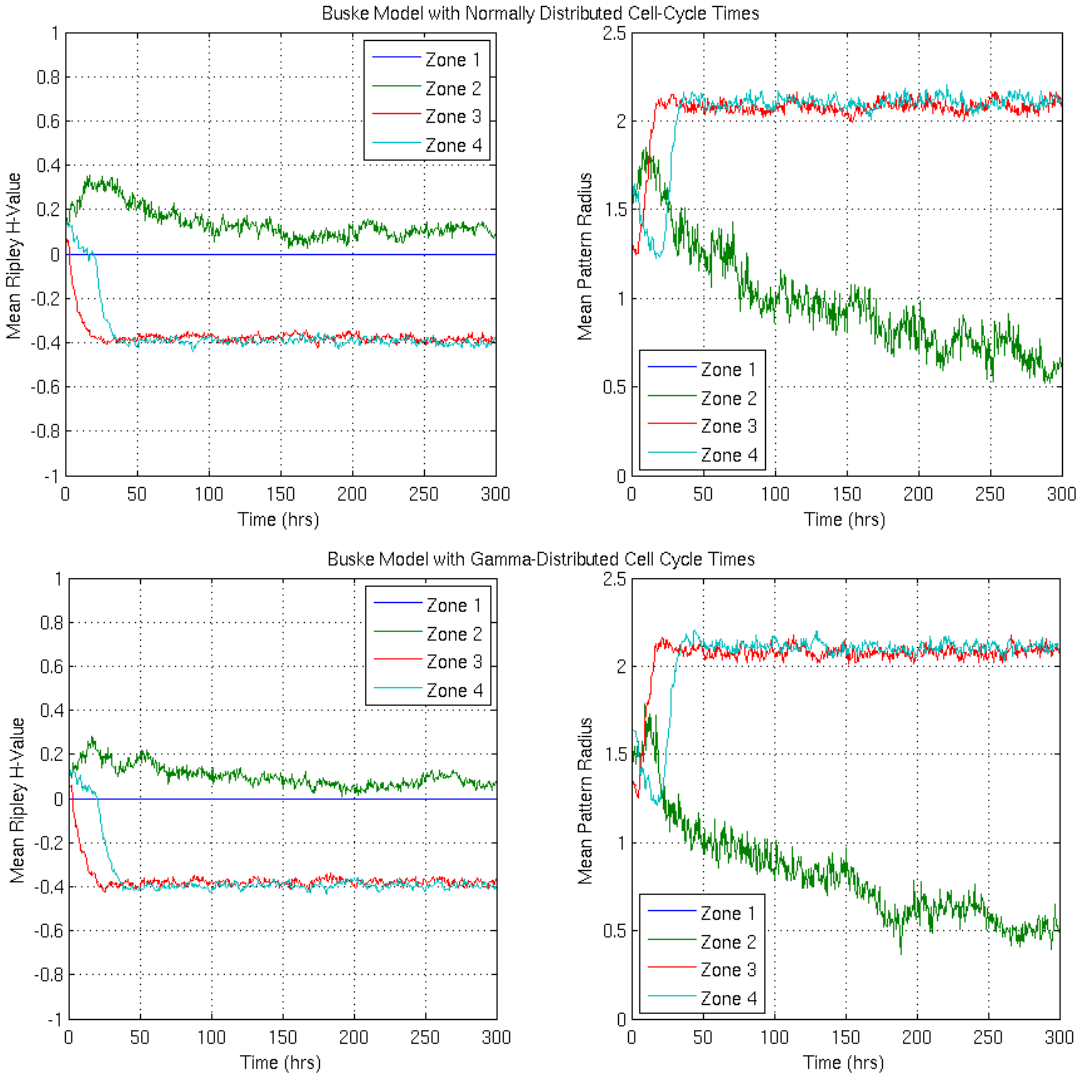

Figure C.1: Ripley timecourses for zones $1-4$ of the crypt, generated from 100 simulations of the Buske model using (top) normally distributed G1 phase lengths and (bottom) Gamma-distributed phase lengths.

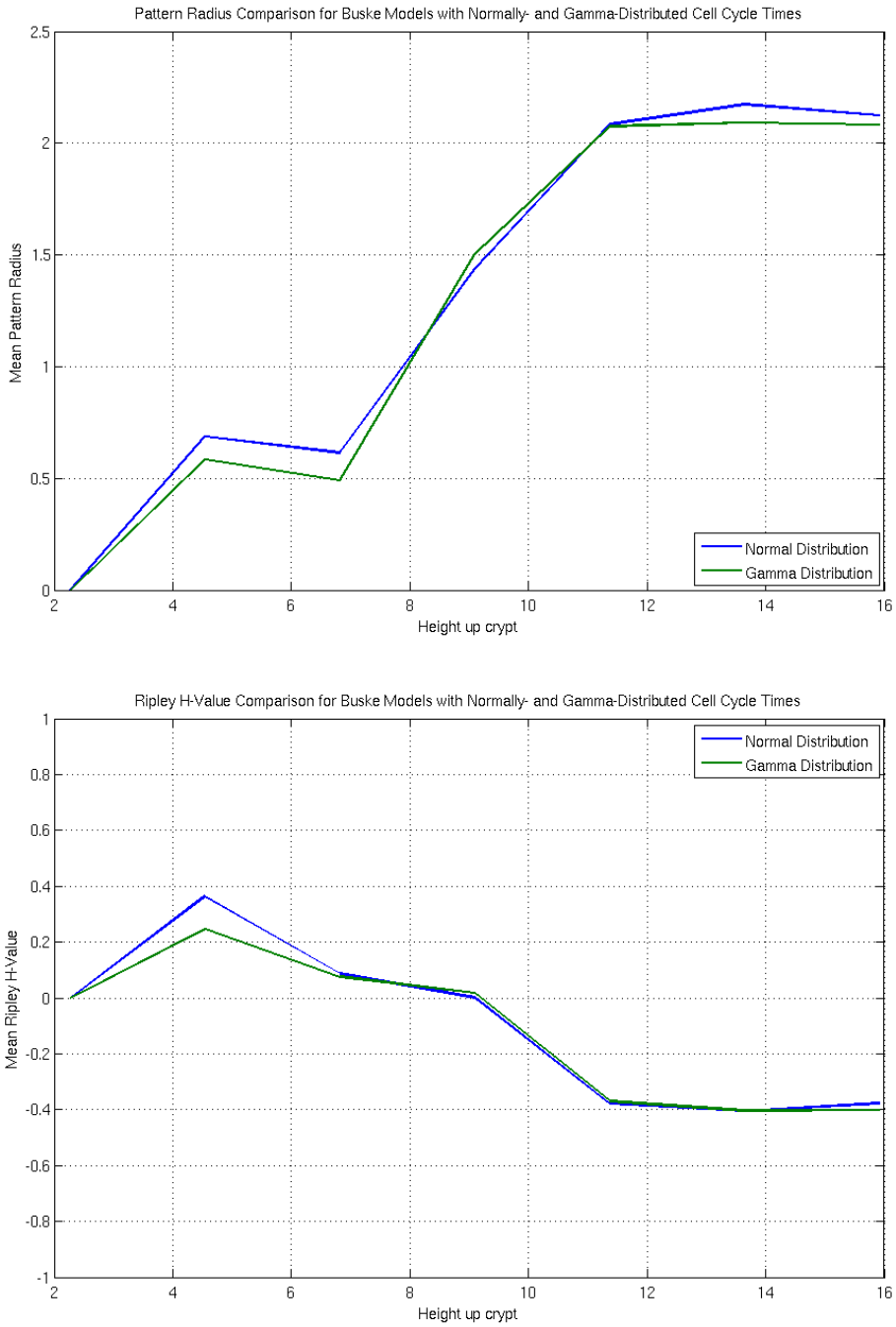

Figure C.2: (Bottom) Ripley and (Top) pattern length analyses for the Buske crypts at dynamic equilibrium, shown for simulations run with either Gamma- or normally-distributed G1 phase lengths. Crypt subregions used to generate these results are as shown in Figure 5.3.

Bibliography

[1] Sato, T., Vries, R., Snippert, H., van de Wetering, M., Barker, N., Stange, D., van Es, J., Abo, A., Kujala, P., Peters, P. Single Lgr5 stem cells build crypt-villus structures in vitro without a mesenchymal niche. Nature 2009;459:262–266.

[2] Ootani, A., Li, X., Sangiorgi, E., Ho, Q., Ueno, H., Toda, S., Sugihara, H., Fujimoto, K., Weissman, I., Capecchi, M., Kuo, C. Sustained *in vitro* intestinal epithelial culture within a Wnt-dependent stem cell niche. Nat. Med. (N. Y., NY, U. S.) 2009;15(6):701–706.

[3] Garcia, M., Jemal, A., Ward, E., Center, M., Hao, Y., Siegel, R., Thun, M. Global cancer facts and figures 2007 Tech. Rep.; American Cancer Society; 2007.

[4] Qureshi, A., Verma, A., Ross, P., Landau, D. Colorectal cancer treatment. Clinical Evidence 2010;04(401).

[5] Buske, P., Galle, J., Barker, N., Aust, G., Clevers, H., Loeffler, M., Lauffenburger, D. A comprehensive model of the spatio-temporal stem cell and tissue organisation in the intestinal crypt. PLoS Comput. Biol. 2011;7(1):1332–1336.

[6] De Rodriguez, M., Sunter, J., Watson, A., Wright, N., Appleton, D. Cell population kinetics in the mucosal crypts of the descending colon of the mouse. Virchows Arch. B 1979;29(1):351–361.

[7] Nicolas, P., Kim, K., Shibata, D., Tavaré, S. The stem cell population of the human colon crypt: analysis via methylation patterns. PLoS Comput. Biol. 2007;3(3):e28.

[8] Sunter, J., Appleton, D., Dé Rodriguez, M., Wright, N., Watson, A. A comparison of cell proliferation at different sites within the large bowel of the mouse. J. Anat. 1979;129(Pt 4):833.

[9] Gray, H. Anatomy: descriptive and surgical. John W. Parker and Son, London, U.K.; 1858.

[10] Reizel, Y., Chapal-Ilani, N., Adar, R., Itzkovitz, S., Elbaz, J., Maruvka, Y.E., Segev, E., Shlush, L.I., Dekel, N., Shapiro, E. Colon stem cell and crypt dynamics exposed by cell lineage reconstruction. PLoS Genet. 2011;7(7):e1002192.

[11] van der Wath, R.C., Gardiner, B.S., Burgess, A.W., Smith, D.W. Cell organisation in the colonic crypt: a theoretical comparison of the pedigree and niche concepts. PLoS One 2013;8(9):e73204.

[12] Bizzozero, G. Ueber die schlauchformigen Drusen des Magendarmkanals und die Beziehungen ihres Epithels zu dem Oberflachenepithel der Schleimhaut. Arch. Mikros. Anat. 1892;40(1):325–375.

[13] Friedman, N. Cellular dynamics in the intestinal mucosa: the effect of irradiation on epithelial maturation and migration. J. Exp. Med. 1945;81(6):553.

[14] Quastler, H., Sherman, F. Cell population kinetics in the intestinal epithelium of the mouse. Exp. Cell Res. 1959;17(3):420.

[15] Cheng, H., Leblond, C. Origin, differentiation and renewal of the four main epithelial cell types in the mouse small intestine: V. Unitarian theory of the origin of the four epithelial cell types. Am. J. Anat. 1974;141(4):537–561.

[16] Cairnie, A., Lamerton, L., Steel, G. Cell proliferation studies in the intestinal epithelium of the rat: I. Determination of the kinetic parameters. Exp. Cell Res. 1965;39:528–538.

[17] Porter, E., Bevins, C., Ghosh, D., Ganz, T. The multifaceted Paneth cell. Cell. Mol. Life Sci. 2002;59(1):156–170.

[18] Cairnie, A., Lamerton, L., Steel, G. Cell proliferation studies in the intestinal epithelium of the rat: II. Theoretical aspects. Exp. Cell Res. 1965;39(2-3):539–553.

[19] Yeung, T., Chia, L., Kosinski, C., Kuo, C. Regulation of self-renewal and differentiation by the intestinal stem cell niche. Cell. Mol. Life Sci. 2011;68:2513–2523.

[20] Moore, K., Lemischka, I. Stem cells and their niches. Science 2006;311(5769):1881–1885.

[21] Potten, C., Loeffler, M. Stem cells: attributes, cycles, spirals, pitfalls and uncertainties. Lessons for and from the crypt. Development 1990;110(4):1001.

[22] Murray, P., Kang, J., Mirams, G., Shin, S., Byrne, H., Maini, P., Cho, K. Modelling spatially regulated β-catenin dynamics & invasion in intestinal crypts. Biophys. J. 2010;99(3):716–725.

[23] Loeffler, M., Stein, R., Wichmann, H., Potten, C., Kaur, P., Chwalinski, S. Intestinal cell proliferation. I: A comprehensive model of steady-state proliferation in the crypt. Cell Proliferation 1986;19(6):627–645.

[24] Loeffler, M., Potten, C., Paulus, U., Glatzer, J., Chwalinski, S. Intestinal crypt proliferation. II: Computer modelling of mitotic index data provides further evidence for lateral and vertical cell migration in the absence of mitotic activity. Cell Proliferation 1988;21(4):247–258.

[25] Paulus, U., Potten, C., Loeffler, M. A model of the control of cellular regeneration in the intestinal crypt after perturbation based solely on local stem cell regulation. Cell Proliferation 1992;25(6):559–578.

[26] Barker, N., Van Es, J., Kuipers, J., Kujala, P., Van Den Born, M., Cozijnsen, M., Haegebarth, A., Korving, J., Begthel, H., Peters, P., Clevers, C. Identification of stem cells in small intestine and colon by marker gene Lgr5. Nature 2007;449(7165):1003–1007.

[27] Jones, P. Stem cell fate in proliferating tissues: equal odds in a game of chance. Dev. Cell 2010;19(4):489–490.

[28] Sangiorgi, E., Capecchi, M. Bmi1 is expressed *in vivo* in intestinal stem cells. Nat. Genet. 2008;40(7):915–920.

[29] Kim, J., Yoon, S., Kim, C., Joo, J., Moon, S., Choe, I., Choe, Y., Kim, J. The Bmi-1 oncoprotein is overexpressed in human colorectal cancer and correlates with the reduced p16INK4a/p14ARF proteins. Cancer Lett. (N. Y., NY, U. S.) 2004;203(2):217–224.

[30] Li, D., Tang, H., Fan, J., Yan, D., Zhou, C., Li, S., Wang, X., Peng, Z. Expression level of Bmi-1 oncoprotein is associated with progression and prognosis in colon cancer. J. Cancer Res. Clin. Oncol. 2010;136(7):997–1006.

[31] Lopez-Garcia, C., Klein, A., Simons, B., Winton, D. Intestinal stem cell replacement follows a pattern of neutral drift. Science 2010;330(6005):822.

[32] Snippert, H., van der Flier, L., Sato, T., van Es, J., van den Born, M., Kroon-Veenboer, C., Barker, N., Klein, A., van Rheenen, J., Simons, B., Clevers, H. Intestinal crypt homeostasis results from neutral competition between symmetrically dividing Lgr5 stem cells. Cell 2010;143(1):134–144.

[33] Gavrieli, Y., Sherman, Y., Ben-Sasson, S. Identification of programmed cell death *in situ* via specific labeling of nuclear DNA fragmentation. J. Cell Biol. 1992;119(3):493.

[34] Potten, C., Booth, C. The role of radiation-induced and spontaneous apoptosis in the homeostasis of the gastrointestinal epithelium: a brief review. Comp. Biochem. Physiol., Part B: Biochem. Mol. Biol. 1997;118(3):473–478.

[35] Frisch, S., Francis, H. Disruption of epithelial cell-matrix interactions induces apoptosis. J. Cell Biol. 1994;124(4):619.

[36] Strater, J., Wedding, U., Barth, T., Koretz, K., Elsing, C., Moller, P. Rapid onset of apoptosis in vitro follows disruption of β1-integrin/matrix interactions in human colonic crypt cells. Gastroenterology 1996;110(6):1776–1784.

[37] Hughes, W., Bond, V., Brecher, G., Cronkite, E., Painter, R., Quastler, H., Sherman, F. Cellular proliferation in the mouse as revealed by autoradiography with tritiated thymidine. Proc. Natl. Acad. Sci. U. S. A. 1958;44(5):476.

[38] Cheng, H., Leblond, C. Origin, differentiation and renewal of the four main epithelial cell types in the mouse small intestine I. Columnar cell. Am. J. Anat. 1974;141(4):461–479.

[39] Tsubouchi, S. Theoretical implications for cell migration through the crypt and the villus of labelling studies conducted at each position within the crypt. Cell Tissue Kinet. 1983;16(5):441.

[40] Kaur, P., Potten, C. Circadian variation in migration velocity in small intestinal epithelium. Cell Proliferation 1986;19(6):591–599.

[41] Wong, S., Chiam, K., Lim, C., Matsudaira, P. Computational model of cell positioning: directed and collective migration in the intestinal crypt epithelium. J. R. Soc., Interface 2010;7(Suppl 3):S351.

[42] Kaur, P., Potten, C. Effects of puromycin, cycloheximide and noradrenaline on cell migration within the crypts and on the villi of the small intestine. Cell Proliferation 1986;19(6):611–625.

[43] Ijiri, K., Potten, C. Response of intestinal cells of differing topographical and hierarchical status to ten cytotoxic drugs and five sources of radiation. Br. J. Cancer 1983;47(2):175.

[44] Ijiri, K., Potten, C. Further studies on the response of intestinal crypt cells of different hierarchical status to eighteen different cytotoxic agents. Br. J. Cancer 1987;55(2):113.

[45] Kaur, P., Potten, C. Cell migration velocities in the crypts of the small intestine after cytotoxic insult are not dependent on mitotic activity. Cell Proliferation 1986;19(6):601–610.

[46] Potten, C., Chwalinski, S., Swindell, R., Palmer, M. The spatial organization of the hierarchical proliferative cells of the crypts of the small intestine into clusters of 'synchronized' cells. Cell Proliferation 1982;15(4):351–370.

[47] Potten, C., Booth, C., Pritchard, D. The intestinal epithelial stem cell: the mucosal governor. Int. J. Exp. Pathol. 1997;78(4):219–243.

[48] Fearon, E., Vogelstein, B. A genetic model for colorectal tumorigenesis. Cell 1990;61(5):759–767.

[49] Salama, P., Platell, C. Colorectal cancer stem cells. Aust. N. Z. J. Surg. 2009;79(10):697–702.

[50] Papailiou, J., Bramis, K., Gazouli, M., Theodoropoulos, G. Stem cells in colon cancer: a new era in cancer theory begins. Int. J. Colorectal Dis. 2010;26(1):1–11.

[51] Pritchett, C., Senior, P., Sunter, J., Watson, A., Appleton, D., Wilson, R. Human colorectal tumours in short-term organ culture: a stathmokinetic study. Cell Proliferation 1982;15(5):555–564.

[52] Dalerba, P., Dylla, S., Park, I., Liu, R., Wang, X., Cho, R., Hoey, T., Gurney, A., Huang, E., Simeone, D., Shelton, A., Parmiani, G., Castelli, C., Clarke, M. Phenotypic characterization of human colorectal cancer stem cells. Proc. Natl. Acad. Sci. U. S. A. 2007;104(24):10158–10163.

[53] Todaro, M., Alea, M., Di Stefano, A., Cammareri, P., Vermeulen, L., Iovino, F., Tripodo, C., Russo, A., Gulotta, G., Medema, J., Stassi, G. Colon cancer stem cells dictate tumor growth and resist cell death by production of interleukin-4. Cell Stem Cell 2007;1(4):389–402.

[54] Roncucci, L., Scalmati, A., De Leon, M. Pattern of cell kinetics in colorectal mucosa of patients with different types of adenomatous polyps of the large bowel. Cancer 1991;68(4):873–878.

[55] Cheng, H., Bjerknes, M., Amar, J., Gardiner, G. Crypt production in normal and diseased human colonic epithelium. Anat. Rec. (1906-2002) 1986;216(1):44–48.

[56] Cairnie, A., Millen, B. Fission of crypts in the small intestine of the irradiated mouse. Cell Proliferation 1975;8(2):189–196.

[57] Hagemann, R., Sigdestad, C., Lesher, S. Intestinal crypt survival and total and per crypt levels of proliferative cellularity following irradiation: single X-ray exposures. Radiat. Res. 1971;46(3):533–546.

[58] Withers, H., Elkind, M. Radiosensitivity and fractionation response of crypt cells of mouse jejunum. Radiat. Res. 1969;38(3):598–613.

[59] Araki, K., Ogata, T., Kobayashi, M., Yatani, R. A morphological study on the histogenesis of human colorectal hyperplastic polyps. Gastroenterology 1995;109(5):1468–1474.

[60] Brackett, K., Townsend, S. Organogenesis of the colon in rats. J. Morphol. 1980;163(2):191–201.

[61] Bjerknes, M., Cheng, H., Erlandsen, S. Functional gap junctions in mouse small intestinal crypts. Anat. Rec. (1906-2002) 1985;212(4):364–367.

[62] Preston, S., Wong, W., Chan, A., Poulsom, R., Jeffery, R., Goodlad, R., Mandir, N., Elia, G., Novelli, M., Bodmer, W., Tomlinson, I., Wright, N. Bottom-up histogenesis of colorectal adenomas. Cancer Res. 2003;63(13):3819–3825.

[63] Appleton, P., Quyn, A., Swift, S., Nathke, I. Preparation of wholemount mouse intestine for high-resolution three-dimensional imaging using two-photon microscopy. J. Microsc. (Oxford, U. K.) 2009;234(2):196–204.

[64] Hanahan, D., Weinberg, R. The hallmarks of cancer. Cell 2000;100(1):57–70.

[65] Hanahan, D., Weinberg, R. Hallmarks of cancer: the next generation. Cell 2011;144(5):646–674.

[66] Greenman, C., Stephens, P., Smith, R., Dalgliesh, G., Hunter, C., Bignell, G., Davies, H., Teague, J., Butler, A., Stevens, C. Patterns of somatic mutation in human cancer genomes. Nature 2007;446(7132):153–158.

[67] Artavanis-Tsakonas, S., Rand, M., Lake, R. Notch signaling: cell fate control and signal integration in development. Science 1999;284(5415):770–776.

[68] Massague, J. Transforming growth factor-alpha. A model for membrane-anchored growth factors. J Biol Chem 1990;265(35):21393–21396.

[69] Bray, S. Notch signalling: a simple pathway becomes complex. Nat. Rev. Mol. Cell Biol. 2006;7(9):678–689.

[70] Wharton, K.A., Johansen, K.M., Xu, T., Artavanis-Tsakonas, S. Nucleotide sequence from the neurogenic locus notch implies a gene product that shares homology with proteins containing EGF-like repeats. Cell 1985;43(3):567–581.

[71] Radtke, F., Raj, K. The role of Notch in tumorigenesis: oncogene or tumour suppressor? Nat. Rev. Cancer 2003;3(10):756–767.

[72] Heitzler, P., Simpson, P. The choice of cell fate in the epidermis of *Drosophila*. Cell 1991;64(6):1083–1092.

[73] Artavanis-Tsakonas, S., Matsuno, K., Fortini, M. Notch signaling. Science 1995;268(5208):225.

[74] Sancho, E., Batlle, E., Clevers, H. Signaling pathways in intestinal development and cancer. Annu. Rev. Cell Dev. Biol. 2004;20:695–723.

[75] Zhou, S., Fujimuro, M., Hsieh, J.J.D., Chen, L., Miyamoto, A., Weinmaster, G., Hayward, S.D. SKIP, a CBF1-associated protein, interacts with the ankyrin repeat domain of NotchIC to facilitate NotchIC function. Mol. Cell. Biol. 2000;20(7):2400–2410.

[76] Kurooka, H., Honjo, T. Functional interaction between the mouse notch1 intracellular region and histone acetyltransferases PCAF and GCN5. J. Biol. Chem. 2000;275(22):17211–17220.

[77] Peignon, G., Durand, A., Cacheux, W., Ayrault, O., Terris, B., Laurent-Puig, P., Shroyer, N., Van Seuningen, I., Honjo, T., Perret, C., Romagnolo, B. Complex interplay between β-catenin signalling and Notch effectors in intestinal tumorigenesis. Gut 2011;60(2):166–176.

[78] Jensen, J., Pedersen, E., Galante, P., Hald, J., Heller, R., Ishibashi, M., Kageyama, R., Guillemot, F., Serup, P., Madsen, O. Control of endodermal endocrine development by Hes-1. Nat. Genet. 2000;24(1):36–44.

[79] Qu, X., Afelik, S., Jensen, J., Bukys, M., Kobberup, S., Schmerr, M., Xiao, F., Nyeng, P., Veronica Albertoni, M., Grapin-Botton, A., Jensen, J. Notch-mediated post-translational control of Ngn3 protein stability regulates pancreatic patterning and cell fate commitment. Dev. Biol. (Amsterdam, Neth.) 2013;376:1–12.

[80] Rangarajan, A., Talora, C., Okuyama, R., Nicolas, M., Mammucari, C., Oh, H., Aster, J., Krishna, S., Metzger, D., Chambon, P., Miele, L., Aguet, M., Radtke, F., Dotto, G. Notch signaling is a direct determinant of keratinocyte growth arrest and entry into differentiation. The EMBO Journal 2001;20(13):3427–3436.

[81] Treff, N.R., Vincent, R.K., Budde, M.L., Browning, V.L., Magliocca, J.F., Kapur, V., Odorico, J.S. Differentiation of embryonic stem cells conditionally expressing neurogenin-3. Stem Cells 2006;24(11):2529–2537.

[82] Gasa, R., Mrejen, C., Leachman, N., Otten, M., Barnes, M., Wang, J., Chakrabarti, S., Mirmira, R., German, M. Proendocrine genes coordinate the pancreatic islet differentiation program in vitro. Proc. Natl. Acad. Sci. U. S. A. 2004;101(36):13245–13250.

[83] Hartenstein, V., Posakony, J. A dual function of the Notch gene in *Drosophila* sensillum development. Dev. Biol. (Amsterdam, Neth.) 1990;142(1):13–30.

[84] Vässin, H., Bremer, K., Knust, E., Campos-Ortega, J. The neurogenic gene Delta of *Drosophila melanogaster* is expressed in neurogenic territories and encodes a putative transmembrane protein with EGF-like repeats. The EMBO Journal 1987;6(11):3431–3440.

[85] Louvi, A., Artavanis-Tsakonas, S. Notch signalling in vertebrate neural development. Nat. Rev. Neurosci. 2006;7(2):93–102.

[86] Lowell, S., Benchoua, A., Heavey, B., Smith, A.G. Notch promotes neural lineage entry by pluripotent embryonic stem cells. PLoS Biol. 2006;4(5):e121.

[87] De Celis, J., Bray, S. Feed-back mechanisms affecting Notch activation at the dorsoventral boundary in the *Drosophila* wing. Development 1997;124(17):3241–3251.

[88] Lewis, J. Notch signalling and the control of cell fate choices in vertebrates In: Semin. Cell Dev. Biol.; vol. 9. London: Academic Press, c1996-; 1998, p. 583–590.

[89] Bjerknes, M., Cheng, H. Clonal analysis of mouse intestinal epithelial progenitors. Gastroenterology 1999;116(1):7–14.

[90] Yang, Q., Bermingham, N., Finegold, M., Zoghbi, H. Requirement of Math1 for secretory cell lineage commitment in the mouse intestine. Science 2001;294(5549):2155–2158.

[91] van Es, J., Clevers, H. Notch and Wnt inhibitors as potential new drugs for intestinal neoplastic disease. Trends Mol. Med. 2005;11(11):496–502.

[92] Fre, S., Huyghe, M., Mourikis, P., Robine, S., Louvard, D., Artavanis-Tsakonas, S. Notch signals control the fate of immature progenitor cells in the intestine. Nature 2005;435(7044):964–968.

[93] Nakamura, T., Tsuchiya, K., Watanabe, M. Crosstalk between Wnt and Notch signaling in intestinal epithelial cell fate decision. J. Gastroenterol. 2007;42(9):705–710.

[94] van de Wetering, M., Sancho, E., Verweij, C., de Lau, W., Oving, I., Hurlstone, A., van der Horn, K., Batlle, E., Coudreuse, D., Haramis, A. The β-catenin/TCF-4 complex imposes a crypt progenitor phenotype on colorectal cancer cells. Cell 2002;111(2):241–250.

[95] Behrens, J., Lustig, B. The Wnt connection to tumorigenesis. Int. J. Dev. Biol. 2004;48:477–488.

[96] Bienz, M., Clevers, H. Linking colorectal cancer to Wnt signaling: a review. Cell 2000;103:311–320.

[97] Lustig, B., Behrens, J. The Wnt signaling pathway and its role in tumor development. J. Cancer Res. Clin. Oncol. 2003;129(4):199–221.

[98] van Amerongen, R. Alternative Wnt pathways and receptors. Cold Spring Harbor Perspect. Biol. 2012;4(10):a007914.

[99] Korswagen, H.C. Canonical and non-canonical Wnt signaling pathways in *Caenorhabditis elegans*: variations on a common signaling theme. Bioessays 2002;24(9):801–810.

[100] Strutt, D. Frizzled signalling and cell polarisation in *Drosophila* and vertebrates. Development 2003;130(19):4501–4513.

[101] Veeman, M.T., Axelrod, J.D., Moon, R.T. A second canon: functions and mechanisms of β-catenin-independent Wnt signaling. Dev. Cell 2003;5(3):367–377.

[102] Tanaka, K., Kitagawa, Y., Kadowaki, T. *Drosophila* segment polarity gene product porcupine stimulates the posttranslational N-glycosylation of wingless in the endoplasmic reticulum. J. Biol. Chem. 2002;277(15):12816–12823.

[103] Clevers, H., Nusse, R. Wnt/β-catenin signaling and disease. Cell 2012;149(6):1192–1205.

[104] Franch-Marro, X., Wendler, F., Griffith, J., Maurice, M.M., Vincent, J.P. In vivo role of lipid adducts on Wingless. J. Cell Sci. 2008;121(10):1587–1592.

[105] Willert, K., Brown, J.D., Danenberg, E., Duncan, A.W., Weissman, I.L., Reya, T., Yates, J.R., Nusse, R. Wnt proteins are lipid-modified and can act as stem cell growth factors. Nature 2003;423(6938):448–452.

[106] Logan, C., Nusse, R. The Wnt signaling pathway in development and disease. Annu. Rev. Cell Dev. Biol. 2004;20(1):781–810.

[107] Zeng, L., Fagotto, F., Zhang, T., Hsu, W., Vasicek, T.J., Perry I, W.L., Lee, J.J., Tilghman, S.M., Gumbiner, B.M., Costantini, F. The mouse $fused$ locus encodes Axin, an inhibitor of the Wnt signaling pathway that regulates embryonic axis formation. Cell 1997;90(1):181–192.

[108] Behrens, J., Jerchow, B.A., Würtele, M., Grimm, J., Asbrand, C., Wirtz, R., Kühl, M., Wedlich, D., Birchmeier, W. Functional interaction of an Axin homolog, conductin, with β-catenin, APC, and GSK3β. Science 1998;280(5363):596–599.

[109] Aberle, H., Bauer, A., Stappert, J., Kispert, A., Kemler, R. β-catenin is a target for the ubiquitin–proteasome pathway. The EMBO Journal 1997;16(13):3797–3804.

[110] Marikawa, Y., Elinson, R.P. β-TrCP is a negative regulator of the Wnt/β-catenin signaling pathway and dorsal axis formation in *Xenopus* embryos. Mech. Dev. 1998;77(1):75–80.

[111] Axelrod, J.D., Miller, J.R., Shulman, J.M., Moon, R.T., Perrimon, N. Differential recruitment of Dishevelled provides signaling specificity in the planar cell polarity and Wingless signaling pathways. Genes Dev. 1998;12(16):2610–2622.

[112] Behrens, J. and von Kries, J.P. and Kühl, M. and Bruhn, L. and Wedlich, D. and Grosschedl, R. and Birchmeier, W., Functional interaction of β-catenin with the transcription factor LEF-1. Nature 1996;382(6592):638–642.

[113] Tetsu, O., McCormick, F. β-Catenin regulates expression of cyclin D1 in colon carcinoma cells. Nature 1999;398(6726):422–426.

[114] He, T., Sparks, A., Rago, C., Hermeking, H., Zawel, L., da Costa, L., Morin, P., Vogelstein, B., Kinzler, K. Identification of c-MYC as a target of the APC pathway. Science 1998;281(5382):1509–1512.

[115] Leow, C., Romero, M., Ross, S., Polakis, P., Gao, W. Hath1, down-regulated in colon adenocarcinomas, inhibits proliferation and tumorigenesis of colon cancer cells. Cancer Res. 2004;64(17):6050–6057.

[116] Li, V., Ng, S., Boersema, P., Low, T., Karthaus, W., Gerlach, J., Mohammed, S., Heck, A., Maurice, M., Mahmoudi, T., Clevers, H. Wnt signaling through inhibition of β-catenin degradation in an intact Axin1 complex. Cell 2012;149(6):1245–1256.

[117] Gilbert, S. Developmental Biology. Sinauer Associates Inc., Sunderland, MA., U.S.A.; 2003.

[118] Schneikert, J., Behrens, J. The canonical Wnt signalling pathway and its APC partner in colon cancer development. Gut 2007;56(3):417–425.

[119] Kinzler, K.W., Vogelstein, B. Lessons from hereditary colorectal cancer. Cell 1996;87(2):159–170.

[120] Baylin, S., Ohm, J. Epigenetic gene silencing in cancer – a mechanism for early oncogenic pathway addiction? Nat. Rev. Cancer 2006;6(2):107–116.

[121] Walker, F., Zhang, H., Odorizzi, A., Burgess, A. Lgr5 is a negative regulator of tumourigenicity, antagonizes Wnt signalling and regulates cell adhesion in colorectal cancer cell lines. PLoS One 2011;6(7):e22733.

[122] Fre, S., Pallavi, S., Huyghe, M., Laé, M., Janssen, K., Robine, S., Artavanis-Tsakonas, S., Louvard, D. Notch and Wnt signals cooperatively control cell proliferation and tumorigenesis in the intestine. Proc. Natl. Acad. Sci. U. S. A. 2009;106(15):6309–6314.

[123] Shin, S., Rath, O., Zebisch, A., Choo, S., Kolch, W., Cho, K. Functional roles of multiple feedback loops in extracellular signal-regulated kinase and Wnt

signaling pathways that regulate epithelial-mesenchymal transition. Cancer Res. 2010;70(17):6715–6724.

[124] Rodilla, V., Villanueva, A., Obrador-Hevia, A., Robert-Moreno, A., Fernandez-Majada, V., Grilli, A., Lopez-Bigas, N., Bellora, N., Alba, M., Torres, F., Dunach, M., Sanjuan, X., Gonzalez, S., Gridley, T., Capella, G., Bigas, A., Espinosa, L. Jagged1 is the pathological link between Wnt and Notch pathways in colorectal cancer. Proc. Natl. Acad. Sci. U. S. A. 2009;106(15):6315–6320.

[125] Collier, J., Monk, N., Maini, P., Lewis, J. Pattern formation by lateral inhibition with feedback: a mathematical model of Delta-Notch intercellular signalling. J. Theor. Biol. 1996;183(4):429–446.

[126] Plahte, E. Pattern formation in discrete cell lattices. J. Math. Biol. 2001;43(5):411–445.

[127] Owen, M.R., Sherratt, J.A. Mathematical modelling of juxtacrine cell signalling. Math. Biosci. 1998;153(2):125–150.

[128] Owen, M., Sherratt, J., Wearing, H. Lateral induction by juxtacrine signaling is a new mechanism for pattern formation. Dev. Biol. (Amsterdam, Neth.) 2000;217(1):54–61.

[129] Wearing, H., Owen, M., Sherratt, J. Mathematical modelling of juxtacrine patterning. Bull. Math. Biol. 2000;62(2):293–320.

[130] Webb, S.D., Owen, M.R. Oscillations and patterns in spatially discrete models for developmental intercellular signalling. J. Math. Biol. 2004;48(4):444–476.

[131] O'Dea, R., King, J. The isolation of spatial patterning modes in a mathematical model of juxtacrine cell signalling. Math. Med. Biol. 2011;(30):95–113.

[132] Owen, M.R., Sherratt, J.A., Myers, S.R. How far can a juxtacrine signal travel? Proc. R. Soc. London, Ser. B 1999;266(1419):579–585.

[133] Savill, N., Sherratt, J. Control of epidermal stem cell clusters by Notch-mediated lateral induction. Dev. Biol. (Amsterdam, Neth.) 2003;258(1):141–153.

[134] Webb, S., Owen, M. Intra-membrane ligand diffusion and cell shape modulate juxtacrine patterning. J. Theor. Biol. 2004;230(1):99–117.

[135] Sprinzak, D., Lakhanpal, A., LeBon, L., Santat, L.A., Fontes, M.E., Anderson, G.A., Garcia-Ojalvo, J., Elowitz, M.B. Cis-interactions between Notch and Delta generate mutually exclusive signalling states. Nature 2010;465(7294):86–90.

[136] Marnellos, G., Deblandre, G., Mjolsness, E., Kintner, C. Delta-notch lateral inhibitory patterning in the emergence of ciliated cells in *Xenopus*: experimental observations and a gene network model. In: Pac. Symp. Biocomput. 2000; vol. 5. 2000, p. 329–340.

[137] Ghosh, R., Tomlin, C. Lateral inhibition through Delta-Notch signaling: a piecewise affine hybrid model. Hybrid Systems: Computation and Control 2001;2034:232–246.

[138] Ghosh, R., Tomlin, C. Symbolic reachable set computation of piecewise affine hybrid automata and its application to biological modelling: Delta-Notch protein signalling. Syst. Biol. 2004;1(1):170–183.

[139] Pin, C., Watson, A., Carding, S. Modelling the spatio-temporal cell dynamics reveals novel insights on cell differentiation and proliferation in the small intestinal crypt. PLoS One 2012;7(5):e37115.

[140] Goodwin, B.C. Oscillatory behavior in enzymatic control processes. Adv. Enzyme Regul. 1965;3:425–437.

[141] Griffith, J. Mathematics of cellular control processes I. Negative feedback to one gene. J. Theor. Biol. 1968;20(2):202–208.

[142] Hirata, H., Yoshiura, S., Ohtsuka, T., Bessho, Y., Harada, T., Yoshikawa, K., Kageyama, R. Oscillatory expression of the bHLH factor Hes1 regulated by a negative feedback loop. Sci. Signaling 2002;298(5594):840–843.

[143] Monk, N.A. Oscillatory expression of Hes1, p53, and NF-κB driven by transcriptional time delays. Curr. Biol. 2003;13(16):1409–1413.

[144] Momiji, H., Monk, N.A. Dissecting the dynamics of the Hes1 genetic oscillator. J. Theor. Biol. 2008;254(4):784–798.

[145] Momiji, H., Monk, N.A. Oscillatory Notch-pathway activity in a delay model of neuronal differentiation. Phys. Rev. E: Stat., Nonlinear, Soft Matter Phys. 2009;80(2):021930(13).

[146] Lewis, J. Autoinhibition with transcriptional delay: a simple mechanism for the zebrafish somitogenesis oscillator. Curr. Biol. 2003;13(16):1398–1408.

[147] Goldbeter, A., Pourquié, O. Modeling the segmentation clock as a network of coupled oscillations in the Notch, Wnt and FGF signaling pathways. J. Theor. Biol. 2008;252(3):574–585.

[148] Murray, P.J., Maini, P.K., Baker, R.E. The clock and wavefront model revisited. J. Theor. Biol. 2011;283(1):227–238.

[149] Murray, P.J., Maini, P.K., Baker, R.E. Modelling Delta-Notch perturbations during zebrafish somitogenesis. Dev. Biol. (Amsterdam, Neth.) 2013;373(2):407–421.

[150] Kageyama, R., Ohtsuka, T., Shimojo, H., Imayoshi, I. Dynamic Notch signaling in neural progenitor cells and a revised view of lateral inhibition. Nat. Neurosci. 2008;11(11):1247–1251.

[151] Agrawal, S., Archer, C., Schaffer, D. Computational models of the Notch network elucidate mechanisms of context-dependent signaling. PLoS Comput. Biol. 2009;5(5):e1000390.

[152] Kiparissides, A., Koutinas, M., Moss, T., Newman, J., Pistikopoulos, E., Mantalaris, A., Monk, N. Modelling the Delta1/Notch1 pathway: in search of the mediator(s) of neural stem cell differentiation. PLoS One 2011;6(2):770–776.

[153] Kirnasovsky, O., Kogan, Y., Agur, Z. Analysis of a mathematical model for the molecular mechanism of fate decision in mammary stem cells. Math. Modell. Nat. Phenom. 2008;3(07):78–89.

[154] Agur, Z., Kirnasovsky, O., Vasserman, G., Tencer-Hershkowicz, L., Kogan, Y., Harrison, H., Lamb, R., Clarke, R. Dickkopf1 regulates fate decision and drives breast cancer stem cells to differentiation: An experimentally supported mathematical model. PLoS One 2011;6(9):e24225.

[155] van Leeuwen, I., Byrne, H., Jensen, O., King, J. Elucidating the interactions between the adhesive and transcriptional functions of β-catenin in normal and cancerous cells. J. Theor. Biol. 2007;247(1):77–102.

[156] Basan, M., Idema, T., Lenz, M., Joanny, J.F., Risler, T. A reaction-diffusion model of the cadherin-catenin system: A possible mechanism for contact inhibition and implications for tumorigenesis. Biophys. J. 2010;98(12):2770–2779.

[157] Ramis-Conde, I., Drasdo, D., Anderson, A.R., Chaplain, M.A. Modeling the influence of the E-cadherin β-catenin pathway in cancer cell invasion: a multiscale approach. Biophys. J. 2008;95(1):155–165.

[158] Kim, D., Rath, O., Kolch, W., Cho, K. A hidden oncogenic positive feedback loop caused by crosstalk between Wnt and ERK pathways. Oncogene 2007;26(31):4571–4579.

[159] Kofahl, B., Wolf, J. Mathematical modelling of Wnt/β-catenin signalling. Biochem. Soc. Trans. 2010;38(5):1281–1285.

[160] Lloyd-Lewis, B., Fletcher, A.G., Dale, T.C., Byrne, H.M. Toward a quantitative understanding of the Wnt/β-catenin pathway through simulation and experiment. Wiley Interdiscip. Rev.: Syst. Biol. Med. 2013;5(4):391–407.

[161] Lee, E., Salic, A., Kruger, R., Heinrich, R., Kirschner, M. The roles of APC and Axin derived from experimental and theoretical analysis of the Wnt pathway. PLoS Biol. 2003;1(1):116–132.

[162] Tan, C.W., Gardiner, B.S., Hirokawa, Y., Layton, M.J., Smith, D.W., Burgess, A.W. Wnt signalling pathway parameters for mammalian cells. PLoS One 2012;7(2):e31882.

[163] Tolwinski, N., Wieschaus, E. Rethinking Wnt signaling. Trends Genet. 2004;20(4):177–181.

[164] Goentoro, L., Kirschner, M. Evidence that fold-change, and not absolute level, of β-catenin dictates Wnt signaling. Mol. Cell 2009;36(5):872–884.

[165] Kruger, R., Heinrich, R. Model reduction and analysis of robustness for the Wnt/β-catenin signal transduction pathway. Genome Inf. Ser. 2004;15(1):138–148.

[166] Mirams, G., Byrne, H., King, J. A multiple timescale analysis of a mathematical model of the Wnt/β-catenin signalling pathway. J. Math. Biol. 2010;60(1):131–160.

[167] Hernández, A.R., Klein, A.M., Kirschner, M.W. Kinetic responses of β-catenin specify the sites of Wnt control. Science 2012;338(6112):1337–1340.

[168] Wawra, C., Kühl, M., Kestler, H.A. Extended analyses of the Wnt/β-catenin pathway: robustness and oscillatory behaviour. FEBS Lett. 2007;581(21):4043–4048.

[169] Cho, K., Baek, S., Sung, M. Wnt pathway mutations selected by optimal β-catenin signaling for tumorigenesis. FEBS Lett. 2006;580(15):3665–3670.

[170] Mazemondet, O., John, M., Leye, S., Rolfs, A., Uhrmacher, A.M. Elucidating the sources of β-catenin dynamics in human neural progenitor cells. PLoS One 2012;7(8):e42792.

[171] Schmitz, Y., Rateitschak, K., Wolkenhauer, O. Analysing the impact of nucleo-cytoplasmic shuttling of β-catenin and its antagonists APC, Axin and GSK3 on Wnt/β-catenin signalling. Cell. Signalling 2013;25(11):2210–2221.

[172] Kogan, Y., Halevi-Tobias, K., Hochman, G., Baczmanska, A., Leyns, L., Agur, Z. A new validated mathematical model of the Wnt signaling pathway predicts effective combinational therapy by sFRP and Dkk. Biochem. J. 2012;444:115–125.

[173] Benary, U., Kofahl, B., Hecht, A., Wolf, J. Modeling Wnt/β-catenin target gene expression in APC and Wnt gradients under wild type and mutant conditions. Frontiers in Physiology 2013;4(21):1–18.

[174] Song, J.H., Huels, D., Ridgway, R., Sansom, O., Kholodenko, B., Kolch, W., Cho, K.H. The APC network regulates the removal of mutated cells from colonic crypts. Cell Rep. 2014;7:94–103.

[175] van Leeuwen, I., Mirams, G., Walter, A., Fletcher, A., Murray, P., Osborne, J., Varma, S., Young, S., Cooper, J., Doyle, B., Pitt-Francis, J., Momtahan, L., Pathmanathan, P., Whiteley, J., Chapman, S., Gavaghan, D., Jensen, O., King, J., Maini, P., Waters, S., Byrne, H. An integrative computational model for intestinal tissue renewal. Cell Proliferation 2009;42(5):617–636.

[176] Mirams, G., Fletcher, A., Maini, P., Byrne, H. A theoretical investigation of the effect of proliferation and adhesion on monoclonal conversion in the colonic crypt. J. Theor. Biol. 2012;312:143–156.

[177] Fletcher, A., Breward, C., Chapman, S. Mathematical modeling of monoclonal conversion in the colonic crypt. J. Theor. Biol. 2012;300:118–133.

[178] Zhang, L., Lander, A.D., Nie, Q. A reaction–diffusion mechanism influences cell lineage progression as a basis for formation, regeneration, and stability of intestinal crypts. BMC Syst. Biol. 2012;6(1):93.

[179] Turing, A. The chemical basis of morphogenesis. Philos. Trans. R. Soc., B 1952;237:37–72.

[180] Pitt-Francis, J., Pathmanathan, P., Bernabeu, M., Bordas, R., Cooper, J., Fletcher, A., Mirams, G., Murray, P., Osborne, J., Walter, A., Chapman, S., Garny, A., van Leeuwen, I., Maini, P., Rodriguez, B., Waters, S., Whiteley, J., Byrne, H., Gavaghan, D. Chaste: a test-driven approach to software development for biological modelling. Comput. Phys. Commun. 2009;180(12):2452–2471.

[181] Cohen, S.D., Hindmarsh, A.C. CVODE, a stiff/nonstiff ODE solver in C. Comput. Phys. 1996;10(2):138–143.

[182] Shampine, L.F., Reichelt, M.W. The Matlab ODE suite. SIAM J. Sci. Comp. 1997;18(1):1–22.

[183] Schmidt, H., Jirstrand, M. Systems Biology Toolbox for MATLAB: a computational platform for research in systems biology. Bioinformatics 2006;22(4):514–515.

[184] Ji, H., Ellison, P., Knight, D., Feinberg, M. A guide to the Chemical Reaction Network Toolbox, version 2.2a www.crnt.osu.edu/CRNTWin; 2013.

[185] Ji, H. Uniqueness of equilibria for complex chemical reaction networks Ph.D. thesis; Ohio State University; 2011.

[186] Armitage, P., Doll, R. The age distribution of cancer and a multi-stage theory of carcinogenesis. Br. J. Cancer 1954;8(1):1.

[187] Armitage, P., Doll, R. A two-stage theory of carcinogenesis in relation to the age distribution of human cancer. Br. J. Cancer 1957;11(2):161.

[188] Tomlinson, I., Bodmer, W. Failure of programmed cell death and differentiation as cause of tumors: some simple mathematical models. Proc. Natl. Acad. Sci. USA 1995;92:11130–11134.

[189] d'Onofrio, A., Tomlinson, I. A nonlinear mathematical model of cell turnover, differentiation and tumorigenesis in the intestinal crypt. J. Theor. Biol. 2007;244(3):367–374.

[190] Johnston, M., Edwards, C., Bodmer, W., Maini, P., Chapman, S. Mathematical modeling of cell population dynamics in the colonic crypt and in colorectal cancer. Proc. Natl. Acad. Sci. U. S. A. 2007;104(10):4008.

[191] Boman, B., Fields, J., Cavanaugh, K., Guetter, A., Runquist, O. How dysregulated colonic crypt dynamics cause stem cell overpopulation and initiate colon cancer. Cancer Res. 2008;68(9):3304.

[192] Edwards, C., Chapman, S. Biomechanical modelling of colorectal crypt budding and fission. Bull. Math. Biol. 2007;69(6):1927–1942.

[193] Figueiredo, I., Leal, C., Leonori, T., Romanazzi, G., Figueiredo, P., Donato, M. A coupled convection-diffusion level set model for tracking epithelial cells in colonic crypts. Proc. Comp. Sci. 2010;1(1):961–969.

[194] Nelson, M., Howard, D., Jensen, O., King, J., Rose, F., Waters, S. Growth-induced buckling of an epithelial layer. Biomech. Model. Mechanobiol. 2010;10:883–900.

[195] Osborne, J., Walter, A., Kershaw, S., Mirams, G., Fletcher, A., Pathmanathan, P., Gavaghan, D., Jensen, O., Maini, P., Byrne, H. A hybrid approach to multi-scale modelling of cancer. Philos. Trans. R. Soc., A 2010;368(1930):5013–5028.

[196] Murray, P., Walter, A., Fletcher, A., Edwards, C., Tindall, M., Maini, P. Comparing a discrete and continuum model of the intestinal crypt. Phys. Biol. 2011;8:026011.

[197] Meinzer, H., Sandblad, B. A simulation model for studies of intestine cell dynamics. Comp. Meth. Prog. Biomed. 1985;21(2):89–98.

[198] Meinzer, H., Sandblad, B. Evidence for cell generation controlled proliferation in the small intestinal crypt. Cell Proliferation 1986;19(6):581–590.

[199] Meinzer, H., Sandblad, B., Baur, H. Generation-dependent control mechanisms in cell proliferation and differentiation – the power of two. Cell Proliferation 1992;25(2):125–140.

[200] Potten, C., Loeffler, M. A comprehensive model of the crypts of the small intestine of the mouse provides insight into the mechanisms of cell migration and the proliferation hierarchy. J. Theor. Biol. 1987;127(4):381–391.

[201] Paulus, U., Loeffler, M., Zeidler, J., Owen, G., Potten, C. The differentiation and lineage development of goblet cells in the murine small intestinal crypt: experimental and modelling studies. J. Cell Sci. 1993;106(2):473.

[202] Kershaw, S.K., Byrne, H.M., Gavaghan, D.J., Osborne, J.M. Colorectal cancer through simulation and experiment. IET Systems Biology 2013;7(3):57–73.

[203] De Matteis, G., Graudenzi, A., Antoniotti, M. A review of spatial computational models for multi-cellular systems, with regard to intestinal crypts and colorectal cancer development. J. Math. Biol. 2012;66(7):1409–1462.

[204] Meineke, F., Potten, C., Loeffler, M. Cell migration and organization in the intestinal crypt using a lattice-free model. Cell Proliferation 2001;34(4):253–266.

[205] Pathmanathan, P., Cooper, J., Fletcher, A., Mirams, G., Murray, P., Osborne, J., Pitt-Francis, J., Walter, A., Chapman, S. A computational study of discrete mechanical tissue models. Phys. Biol. 2009;6(3):036001.

[206] Nagai, T., Honda, H. A dynamic cell model for the formation of epithelial tissues. Philos. Mag. B 2001;81(7):699–719.

[207] Fletcher, A.G., Osborne, J.M., Maini, P.K., Gavaghan, D.J. Implementing vertex dynamics models of cell populations in biology within a consistent computational framework. Prog. Biophys. Mol. Biol. 2013;113(2):299–326.

[208] Feder, J.N., Li, L., Jan, L.Y., Jan, Y.N. Genomic cloning and chromosomal localization of HRY, the human homolog to the *Drosophila* segmentation gene, hairy. Genomics 1994;20(1):56–61.

[209] Pourquié, O. The segmentation clock: converting embryonic time into spatial pattern. Sci. Signaling 2003;301(5631):328–330.

[210] Kageyama, R., Ohtsuka, T., Kobayashi, T. Roles of Hes genes in neural development. Dev., Growth Differ. 2008;50:S97–S103.

[211] Seo, S., Lim, J.W., Yellajoshyula, D., Chang, L.W., Kroll, K.L. Neurogenin and NeuroD direct transcriptional targets and their regulatory enhancers. The EMBO Journal 2007;26(24):5093–5108.

[212] Leow, C., Polakis, P., Gao, W. A role for Hath1, a bHLH transcription factor, in colon adenocarcinoma. Ann. N. Y. Acad. Sci. 2005;1059(1):174–183.

[213] Tsuchiya, K., Nakamura, T., Okamoto, R., Kanai, T., Watanabe, M. Reciprocal targeting of Hath1 and β-catenin by Wnt glycogen synthase kinase 3β in human colon cancer. Gastroenterology 2007;132(1):208–220.

[214] Van Es, J., Van Gijn, M., Riccio, O., van den Born, M., Vooijs, M., Begthel, H., Cozijnsen, M., Robine, S., Winton, D., Radtke, F., Clevers, C. Notch/γ-secretase inhibition turns proliferative cells in intestinal crypts and adenomas into goblet cells. Nature 2005;435(7044):959–963.

[215] Clevers, H. Wnt/β-catenin signaling in development and disease. Cell 2006;127(3):469–480.

[216] Jho, E.h., Zhang, T., Domon, C., Joo, C.K., Freund, J.N., Costantini, F. Wnt/β-catenin/Tcf signaling induces the transcription of Axin2, a negative regulator of the signaling pathway. Mol. Cell. Biol. 2002;22(4):1172–1183.

[217] Tax, F.E., Yeargers, J.J., Thomas, J.H. Sequence of *C. elegans* lag-2 reveals a cell-signalling domain shared with Delta and Serrate of *Drosophila*. Nature 1994;368:150–154.

[218] Fortini, M.E. γ-secretase-mediated proteolysis in cell-surface-receptor signalling. Nat. Rev. Mol. Cell Biol. 2002;3(9):673–684.

[219] Yamamizu, K., Matsunaga, T., Uosaki, H., Fukushima, H., Katayama, S., Hiraoka-Kanie, M., Mitani, K., Yamashita, J.K. Convergence of Notch and β-catenin signaling induces arterial fate in vascular progenitors. J. Cell Biol. 2010;189(2):325–338.

[220] Jin, Y., Kim, H., Ki, H., Yang, I., Yang, N., Lee, K., Kim, N., Park, H., Kim, K. Beta-catenin modulates the level and transcriptional activity of Notch1/NICD through its direct interaction. Biochim. Biophys. Acta, Mol. Cell Res. 2009;1793(2):290–299.

[221] Espinosa, L., Inglés-Esteve, J., Aguilera, C., Bigas, A. Phosphorylation by glycogen synthase kinase-3β down-regulates Notch activity, a link for Notch and Wnt pathways. J. Biol. Chem. 2003;278(34):32227–32235.

[222] Collu, G., Hidalgo-Sastre, A., Acar, A., Bayston, L., Gildea, C., Leverentz, M., Mills, C., Owens, T., Meurette, O., Dorey, K., K., B. Dishevelled limits Notch signalling through inhibition of CSL. Sci. Signaling 2012;139(23):4405–4415.

[223] Takebayashi, K., Sasai, Y., Sakai, Y., Watanabe, T., Nakanishi, S., Kageyama, R. Structure, chromosomal locus, and promoter analysis of the gene encoding the mouse helix-loop-helix factor Hes-1. Negative autoregulation through the multiple N-box elements. J. Biol. Chem. 1994;269(7):5150–5156.

[224] Iso, T., Kedes, L., Hamamori, Y. HES and HERP families: multiple effectors of the Notch signaling pathway. J. Cell. Physiol. 2003;194(3):237–255.

[225] Kageyama, R., Ohtsuka, T., Kobayashi, T. The Hes gene family: repressors and oscillators that orchestrate embryogenesis. Development 2007;134(7):1243–1251.

[226] Ishibashi, M., Ang, S.L., Shiota, K., Nakanishi, S., Kageyama, R., Guillemot, F. Targeted disruption of mammalian hairy and enhancer of split homolog-1 (HES-1) leads to up-regulation of neural helix-loop-helix factors, premature neurogenesis, and severe neural tube defects. Genes Dev. 1995;9(24):3136–3148.

[227] Sasai, Y., Kageyama, R., Tagawa, Y., Shigemoto, R., Nakanishi, S. Two mammalian helix-loop-helix factors structurally related to *Drosophila* hairy and enhancer of split. Genes Dev. 1992;6(12b):2620–2634.

[228] Ueo, T., Imayoshi, I., Kobayashi, T., Ohtsuka, T., Seno, H., Nakase, H., Chiba, T., Kageyama, R. The role of Hes genes in intestinal development, homeostasis and tumor formation. Development 2012;139(6):1071–1082.

[229] Sikandar, S.S., Pate, K.T., Anderson, S., Dizon, D., Edwards, R.A., Waterman, M.L., Lipkin, S.M. Notch signaling is required for formation and self-renewal of tumor-initiating cells and for repression of secretory cell differentiation in colon cancer. Cancer Res. 2010;70(4):1469–1478.

[230] Lee, J.C., Smith, S.B., Watada, H., Lin, J., Scheel, D., Wang, J., Mirmira, R.G., German, M.S. Regulation of the pancreatic pro-endocrine gene neurogenin3. Diabetes 2001;50(5):928–936.

[231] Ohtsuka, T., Ishibashi, M., Gradwohl, G., Nakanishi, S., Guillemot, F., Kageyama, R. Hes1 and Hes5 as Notch effectors in mammalian neuronal differentiation. The EMBO Journal 1999;18(8):2196–2207.

[232] Jenny, M., Uhl, C., Roche, C., Duluc, I., Guillermin, V., Guillemot, F., Jensen, J., Kedinger, M., Gradwohl, G. Neurogenin3 is differentially required for endocrine cell fate specification in the intestinal and gastric epithelium. The EMBO Journal 2002;21(23):6338–6347.

[233] Leung, J.Y., Kolligs, F.T., Wu, R., Zhai, Y., Kuick, R., Hanash, S., Cho, K.R., Fearon, E.R. Activation of Axin2 expression by β-catenin T-cell factor: a feedback repressor pathway regulating Wnt signaling. J. Biol. Chem. 2002;277(24):21657–21665.

[234] Fodde, R., Brabletz, T. Wnt/β-catenin signaling in cancer stemness and malignant behavior. Curr. Opin. Cell Biol. 2007;19(2):150–158.

[235] Taelman, V., Dobrowolski, R., Plouhinec, J.L., Fuentealba, L., Vorwald, P., Gumper, I., Sabatini, D., De Robertis, E. Wnt signaling requires sequestration of glycogen synthase kinase-3 inside multivesicular endosomes. Cell 2010;143(7):1136–1148.

[236] Reya, T., Clevers, H. Wnt signalling in stem cells and cancer. Nature 2005;434(7035):843–850.

[237] Buceta, J., Herranz, H., Canela-Xandri, O., Reigada, R., Sagués, F., Milán, M. Robustness and stability of the gene regulatory network involved in DV boundary formation in the *Drosophila* wing. PLoS One 2007;2(7):e602.

[238] Shepherd, S. Computational modelling of neurogenesis; 2010 Unpublished research, University of Nottingham.

[239] Alon, U. Network motifs: theory and experimental approaches. Nat. Rev. Genet. 2007;8(6):450–461.

[240] Mangan, S., Alon, U. Structure and function of the feed-forward loop network motif. Proc. Natl. Acad. Sci. U. S. A. 2003;100(21):11980–11985.

[241] Shinar, G., Feinberg, M. Concordant chemical reaction networks. Math. Biosci. 2012;240(2):92–113.

[242] Harrington, H.A., Feliu, E., Wiuf, C., Stumpf, M.P. Cellular compartments cause multistability and allow cells to process more information. Biophys. J. 2013;104(8):1824–1831.

[243] Shiu, A. The smallest multistationary mass-preserving chemical reaction network. In: Algebraic Biology. Springer; 2008, p. 172–184.

[244] Logeat, F., Bessia, C., Brou, C., LeBail, O., Jarriault, S., Seidah, N.G., Israël, A. The Notch1 receptor is cleaved constitutively by a furin-like convertase. Proc. Natl. Acad. Sci. U. S. A. 1998;95(14):8108–8112.

[245] Gregorieff, A., Pinto, D., Begthel, H., Destrée, O., Kielman, M., Clevers, H. Expression pattern of Wnt signaling components in the adult intestine. Gastroenterology 2005;129(2):626–638.

[246] Ripley, B. Modelling spatial patterns. J. Royal Stat. Soc. B 1977;39(2):172–212.

[247] Mirams, G.R., Arthurs, C.J., Bernabeu, M.O., Bordas, R., Cooper, J., Corrias, A., Davit, Y., Dunn, S.J., Fletcher, A.G., Harvey, D.G., et al. Chaste: an open source C++ library for computational physiology and biology. PLoS Comput. Biol. 2013;9(3):e1002970.

[248] Nagase, H., Nakamura, Y. Mutations of the APC (adenomatous polyposis coli) gene. Human Mutation 1993;2(6):425–434.

[249] LoConte, N.K., Razak, A.R., Ivy, P., Tevaarwerk, A., Leverence, R., Kolesar, J., Siu, L., Lubner, S.J., Mulkerin, D.L., Schelman, W.R., et al. A multicenter phase 1 study of γ-secretase inhibitor RO4929097 in combination with capecitabine in refractory solid tumors. Invest. New Drugs 2014;1:1–8.

[250] Krop, I., Demuth, T., Guthrie, T., Wen, P.Y., Mason, W.P., Chinnaiyan, P., Butowski, N., Groves, M.D., Kesari, S., Freedman, S.J., et al. Phase I pharmacologic and pharmacodynamic study of the γ-secretase (Notch) inhibitor MK-0752 in adult patients with advanced solid tumors. J. Clin. Oncol. 2012;30(19):2307–2313.

[251] Jones, D.R. A taxonomy of global optimization methods based on response surfaces. Journal of global optimization 2001;21(4):345–383.

[252] Picheny, V. A stepwise uncertainty reduction approach to constrained global optimization. In: Proceedings of the Seventeenth International Conference on Artificial Intelligence and Statistics. 2014, p. 787–795.

[253] Huntington, D., Lyrintzis, C. Improvements to and limitations of Latin hypercube sampling. Probabilistic Engineering Mechanics 1998;13(4):245–253.

[254] Foltz, D.R., Santiago, M.C., Berechid, B.E., Nye, J.S. Glycogen synthase kinase-3β modulates Notch signaling and stability. Curr. Biol. 2002;12(12):1006–1011.

[255] Roark, R., Itzhaki, L., Philpott, A. Complex regulation controls Neurogenin3 proteolysis. Biol. Open 2012;1(12):1264–1272.

[256] Cole, A., Frame, S., Cohen, P. Further evidence that the tyrosine phosphorylation of glycogen synthase kinase-3 (GSK3) in mammalian cells is an autophosphorylation event. Biochem. J 2004;377:249–255.

[257] Yamamoto, H., Kishida, S., Kishida, M., Ikeda, S., Takada, S., Kikuchi, A. Phosphorylation of Axin, a Wnt signal negative regulator, by glycogen synthase kinase-3β regulates its stability. J. Biol. Chem. 1999;274(16):10681–10684.

[258] Cinquin, O. Repressor dimerization in the zebrafish somitogenesis clock. PLoS Comput. Biol. 2007;3(2):e32.

[259] Fozard, J., Kirkham, G., Buttery, L., King, J., Jensen, O., Byrne, H. Techniques for analysing pattern formation in populations of stem cells and their progeny. BMC Bioinf. 2011;12(1):1–16.

[260] Wiegand, T., A Moloney, K. Rings, circles, and null-models for point pattern analysis in ecology. Oikos 2004;104(2):209–229.

[261] Ripley, B. Spatial Statistics. Wiley; 1981.

[262] Kiskowski, M., Hancock, J., Kenworthy, A. On the use of Ripley's K-function and its derivatives to analyse domain size. Biophys. J. 2009;97:1095–1103.

[263] Freeman, E., Ford, E. Effects of data quality on analysis of ecological pattern using the K(d) statistical function. Ecology 2002;83(1):35–46.

[264] Stoyan, D., Penttinen, A. Recent applications of point process methods in forestry statistics. Statistical Science 2000;15(1):61–78.

[265] Parton, R., Hancock, J. Lipid rafts and plasma membrane microorganization: insights from Ras. Trends Cell Biol. 2004;14(3):141–147.

[266] Hancock, J., Prior, I. Electron microscopic imaging of Ras signaling domains. Methods 2005;37(2):165–172.

[267] Zhang, J., Leiderman, K., Pfeiffer, J., Wilson, B., Oliver, J., Steinberg, S. Characterizing the topography of membrane receptors and signaling molecules from spatial patterns obtained using nanometer-scale electron-dense probes and electron microscopy. Micron 2006;37(1):14–34.

[268] Ripley, B.D. Edge effects in spatial stochastic processes. In: Statistics in Theory and Practice. Swedish University of Agricultural Sciences, Umea, Sweden; 1982, p. 247–262.

[269] Haase, P. Spatial pattern analysis in ecology based on Ripley's K-function: Introduction and methods of edge correction. J. Veg. Sci. 1995;6(4):575–582.

[270] Goreaud, F., Pélissier, R. On explicit formulas of edge effect correction for Ripley's K-function. J. Veg. Sci. 1999;10(3):433–438.